Modulating Protein-Protein Interactions Through Peptidomimetics Utilizing Thioether Oxidation States, Noncovalent Interactions & Epigenetic Regulation

A DISSERTATION
SUBMITTED TO THE FACULTY OF
UNIVERSITY OF MINNESOTA
BY

Gabriella T. Perell

IN PARTIAL FULFILLMENT OF THE REQUIREMENTS
FOR THE DEGREE OF
DOCTOR OF PHILOSOPHY

ADVISOR:
Dr. William C. K. Pomerantz

September 2017

Acknowledgements

For their time, mentorship, and intellect I acknowledge the many scientists I have encountered through this research including all members of the Pomerantz lab, and the many talented researchers at the University of Minnesota. For his guidance, knowledge, and patience, I acknowledge my advisor Willam C. K. Pomerantz.

Abstract

Interactions among proteins play a fundamental role in regulating all biological processes. Such interactions that dictate disease progression are viable regions to target with chemical probes and inhibitors. With an array of interacting sites that vary in size, polarity, and structure, these intransigent chemical targets have been termed *undruggable* due to the difficulties to target; however, advancements in the area of chemical biology now allow for exploration and progress of this formidable territory. With an estimated 650,000 protein-protein interactions (PPIs) found in the human interactome, probes that can target such interactions are highly sought after due to their significance in disease suppression. In Chapter 2, we explore the importance of a new non-covalent interaction between aromatic π-systems and sulfoxide moieties that contribute to binding energy. With an enrichment of aromatic amino acids at protein interfaces, the utility of this interaction can be exploited at protein interaction sites. We further probe protein interfaces in Chapter 3 by incorporating oxidizable thioether-bridged α-helical peptidomimetics. These probes modulate the polarity, structure, stability, affinity, and permeability, thereby allowing the mimetics to disrupt native PPIs. We utilized a specific Protein Observed ^{19}F (PrOF) NMR technique to monitor crosslinked peptide affinity, as well as circular dichroism, tryptic

digests, HPLC, fluorescence microscopy, fluorescence polarization, and computational calculations to evaluate biophysical characteristics. We further probe perfluorinated sulfone crosslinks in collaboration with Ratimir Derda in Chapter 3 for interactions with human serum albumin. By using two different methods to incorporate thioether crosslinks, either with an S_N2 dibromoalkylation or a thiol-ene reaction as discussed in Chapter 4, we can alter the oxidation states of either one or two sulfur groups within the macrocycle. Chapter 5 is an assessment of a histone variant, H2A.Z for specific acetylation patterns to interact with certain bromodomains, BPTF and *Pf*GCN5. Using PrOF NMR, a ligand observed NMR technique CPMG, and photo-crosslinking, we identify from of a series of various acetylation patterns, that H2A.Z Ack4,11 shows the highest affinity towards the bromodomain BPTF. We further investigate a different bromodomain, CBP in collaboration with Stuart Conway for interactions with five previously identified small molecules. Using PrOF NMR, and fluorescence polarization, we identify affinity towards three bromodomains: CBP, Brd4 and BrdT.

Table of Contents

List of Figures

List of Tables

Citations from previously published work in this dissertation are as follows:

Chapter 2: “Oxidation increases the strength of the methionine-aromatic interaction” Andrew K Lewis, Katie M Dunleavy, Tiffany L. Senkow Cheng Her, Benjamin T. Horn, Mark A. Jersett, Ryan Mahling, Megan R. McCarthy, Gabriella T. Perell, Christopher C. Valley, Christine B. Karim, Jiali Gao, William C. K. Pomerantz, David D. Thomas, Alessandro Cembran, Anne Hinderliter, and Jonathan N. Sachs. *Nature Chemical Biology* **2016**, 12, 860-866.

Chapter 3: “Tuning Sulfur Oxidation States on Thioether-Bridged Peptide Macrocycles for Modulation of Protein Interactions” Gabriella T. Perell, Rachel L. Staebell, Mehrdad Hairani, Alessandro Cembran, William C. K. Pomerantz, *ChemBioChem* **2017**, Accepted Author Manuscript.

Chapter 5: “Specific Acetylation Patterns of H2A.Z Form Transient Interactions with the BPTF Bromodomain” Gabriella T Perell, Neeraj K. Mishra, Babu Sudhamalla, Peter D. Ycas, Kabirul Islam, William C. K. Pomerantz, *Biochemistry* **2017**, Accepted Author Manuscript.

Chapter 1. Introduction

1.1 **Introduction to peptide mimetics**

Protein-protein interactions (PPIs) play a central role orchestrating biological processes. While necessary, they have also been implicated in disease progression. Targeting of PPIs using small molecules has been a great challenge that has puzzled researchers, but development of molecules into useful probes could expand our understanding of biological processes, uncover new therapeutics, and discover novel diagnostics. Emerging advances in the field of chemical biology strive to mediate disease progression with PPI-targeted chemical probes. It is estimated to be >100,000 Protein-protein interactions (PPIs)[1]; therefore, they are to be critical points of which manipulation may be possible. While there are numerous PPIs, not all are equally targetable. Small molecules have been able to target clustered regions with increased binding affinity, termed 'hot spots', **Figure 1.1**. 'Hot spot' regions of high binding affinity bind well to small molecule inhibitors, but unfortunately many 'hot spot' regions can expand over a significant portion of the PPI interface (1940 ± 760 $Å^2$). This area is typically too large for small molecules to effectively inhibit with protein-small molecule binding areas of ~300-1,000 $Å^2$. Many weak binding interactions throughout a PPI that accumulate to a large binding energy attenuate further the difficulty small molecules face in modulating the expansive area. With the topology of many PPIs having vast hydrophobic, flat regions, researchers have turned their attention toward alternative approaches, taking inspiration from the protein structure to create peptide mimics.

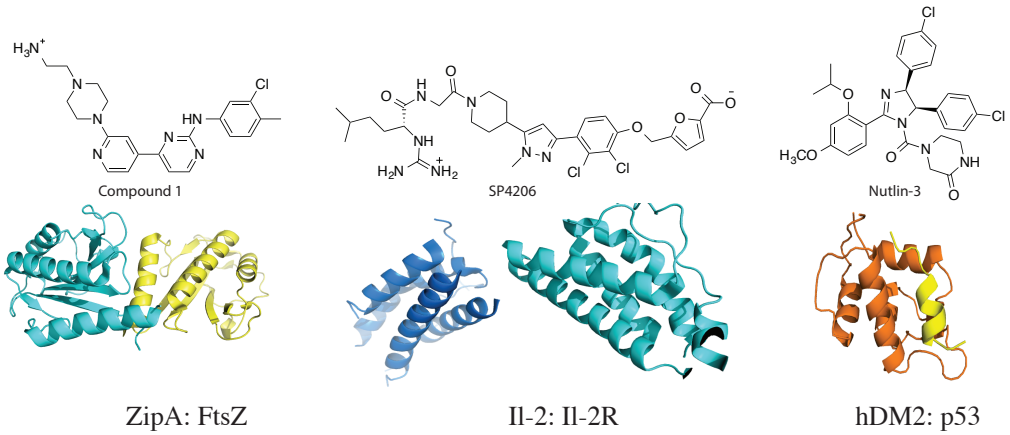

Figure 1.1 Three complexes with discontinuous protein-protein interfaces that have been targeted with small molecule inhibitors, shown above the respective PPI. (PDB: ZipA:FtsZ-1Y2F; IL2:IL2R-1PY2; hDM2: p53-1YCR).

1.2 **Defining characteristics of protein-protein interactions (PPIs)**

PPIs are notoriously difficult to target and inhibit. The term *undruggable* has been used to name the extensive area of molecular targets not able to be targeted by either small molecules.[2] This daunting title expresses the difficult problem researchers are facing. PPIs with weak binding interactions (K_D >200 nM) and extensive binding surfaces (>2,500 Å^2) prove to be the most challenging.[3,4] While small molecules can be optimized to fit into deep pockets, or mimic certain 'hot spot' residues[5], the flat, hydrophobic landscape of many protein targets prove to be inaccessible to most small molecule inhibitors[6]. Unfortunately, small molecules are only able to target ~10% of the proteins encoded in the human genome, designating the majority of PPIs as currently *undruggable*.[7,8] Moving

beyond small molecule inhibitors, several promising methods have been developed to disrupt PPIs using peptidomimetics and α-helical mimicry.

1.3 **Role of the α-Helix in PPIs**

With 62% of all protein-protein interfaces mediated by an α-helix, the desire to exploit this ubiquitous secondary structure is evident.[9] Peptides mimicking an α-helical binding surface allows for direct competition with the native protein. A disruption of the native PPI is achieved by designing stabilized α-helical peptidomimetics. With enhanced binding affinity, proteolytic stability and cell penetration, a disruption of the native activity can be achieved.

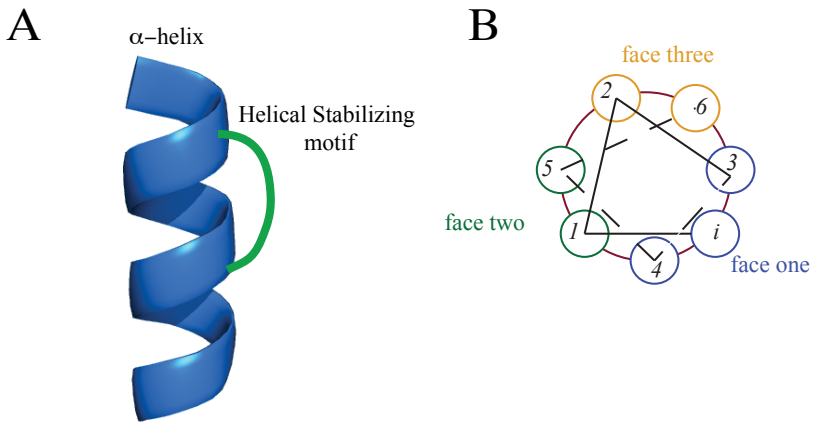

Figure 1.2 A. α-helix construct with synthetic stabilizing motif encompassing one face of helix. B. Helical wheel with three faces separated.

While diverse topographies characterize PPIs, there is a high frequency of α-helices at the binding site.[9] Researchers have begun to exploit this ubiquitous secondary structure

by mimicking the natural α-helix (α-helical peptidomimetics), and stabilizing the helix with conformationally constraining crosslinks that expand over one face of the helix, **Figure 1.2**. A variety of modulations can dramatically enhance the mimetic compared to the native protein by crosslinking the peptide.

1.4 **Structural Effects**

The α-helix is a ubiquitous structure within proteins that is characterized by a rotation of the backbone with 3.6 amino acids within each turn. Defined torsion angles of the α-helix backbone, with phi (NH—Cα) being −57.8° and psi (Cα—C=O) being −47.0°, have been well defined using X-ray crystal structures.[10] This turn creates three separate faces of the α-helix (**Figure 1.2**). An interesting feature of this secondary structure was first elucidated by Isabella Karle and colleagues where they determined an unstructured peptide could transform into an α-helix upon conformational nucleation.[11] This allows for only a portion of the α-helix to be synthetically constrained which ultimately leads to a fully structured α-helix.

Understanding the natural helical structure of peptides within the binding site is the first step in identifying potential utility of the cross-link motif. If the peptide does not have a natural propensity to fold into an α-helix when it is in the active state, an installed crosslink may not achieve enhanced affinity. It has been identified that robust ring-closing metathesis reactions with full conversion typically confers a high degree of helicity.[12,13] Certain amino acids have less propensity to fold into the α-helical secondary structure.[14] The bulky character of β-branched residues (threonine, valine, isoleucine) often reduces helicity. A variety of studies have assessed crosslinked helical peptides for an optimal

structural design. To perturb side chain interactions as little as possible, crosslinking motifs have been added to only one face of an α-helix, usually away from the binding side and solvent exposed. Synthetic constraints are placed at an initial position (*i)* and either 3 or 4 residues away to encompass one helical turn. To expand over two helical turns, *i, i+7* positions are utilized. These sites are somewhat near in space, spanning 6.7-10 Å in distance, **Figure 1.3**. Recently, 'stitched' peptides have been identified as having even more stability.[15] Two hydrocarbon constraints are placed adjacently, e.g. *i,i+4+7*. These 'stitched' peptides have shown significant thermal stability as well as cell penetration capabilities.

Stereochemistry of the amino acids used in appending constraints can greatly affect the reactivity, depending on the linkage size and the number of helical turns constrained (*i, i+3,4* vs. *i, i+7)*. For an *i, i+3* linkage, D_iL_{i+3} stereochemistry leads to a much higher % product conversion, whereas for *i, i+4,* the same stereochemistry with D_iD_{i+4} or L_iL_{i+4} has more than 98% conversion in a model RNAseA peptide.[12] A follow up study further investigated how stereochemistry affected a stapled BH3 peptide, and identified L_iL_{i+4} to have marked enhancement of not only helicity, but also in vivo reduction of leukemic cell growth.[16] The p53 helical stapled peptide mimics have been identified to incorporate D_iL_{i+7} stereochemistry (SAH p53-5) leading to 20% helicity, cell permeability, and 0.80 ± 0.05 nM.[17] There are several structural changes that can substantially affect the chemistry, as well as the stability, helicity, and permeability of the constructs. Identifying an optimal structural design can influence the effectiveness of the inhibitors, and should be prudently assessed before moving forward.

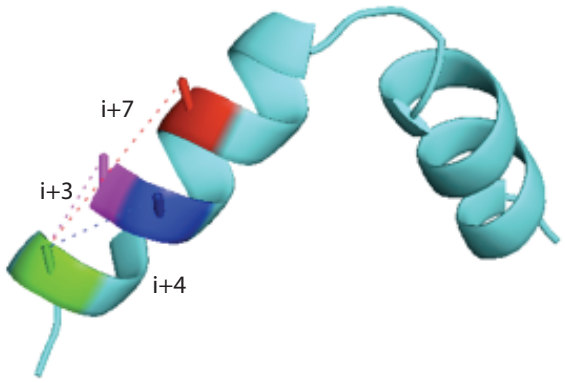

Figure 1.3 Calculated distance between the Cβ of amino acid residues i (green) to i + 3 (magenta), 4 (blue), and 7 (red) amino acids are 5.7 Å, 6.0 Å, and, 10.2 Å respectively. Distances were calculated on the CREB peptide (PDB: 1KDX).

1.5 **Stability**

Identifying the extent of α-helicity achieved with added structural constraints is the first step in achieving potent inhibitors. Circular Dichroism (CD) allows for an assessment of the average α-helical content within the peptides. A generic α-helix displays a double-well minimum at 208 and 222 nm. The degree of helicity utilizes the molar ellipticity at 222 nm, since there is overlap of other structural signatures near 208 nm, such as a random coil. The percent helicity for shorter peptides is the ratio of $[\theta]_{222}/^{max}[\theta]_{222}$ where

$$^{max}[\theta]_{222} = (-40\ 000\ X\ [1 - k/n]),\ k = 2.5,\ n = \text{number of residues.}$$ [18]

1.6 **Solubility**

Achieving highly soluble crosslinked peptide inhibitors can be an issue. With the introduction of a highly hydrophobic cross-linker such as the all-hydrocarbon ‘staples’,

caution needs to be taken towards aggregation. Often synthetic crosslinks are appended onto a face of the helix away from the binding site, typically solvent exposed. The lack of polar substituents may lead to aggregation and inactivation by serum.[19–21] Furthermore, diminished solubility can cause disruptions to precise measurements to fully characterize the properties of potential drug candidates. The problematic nature warrants consideration of more polar crosslinking motifs.

1.7 **Protease Resistance**

Unstructured peptides rapidly undergo proteolytic degradation, but with the addition of a synthetic constraint, they can withstand proteolysis. Trypsin is a serine protease enzyme that identifies peptides with a catalytic triad made up of histidine, aspartate and serine, which recognize and cleave the amide bond on the c-terminal side of lysine and arginine residues. A synthetic crosslink disallows the peptide to unfold into an extended strand, and fit into the binding pocket, thus making it difficult for the protease to cleave the scissile bond. The constrained peptides confer resistance similar to that of small molecule inhibitors, and dramatically increases the stability versus the unconstrained peptide.[18]

1.8 **Intracellular Uptake**

It is still unclear as to what dictates cross-linked peptide's membrane permeability. Typically, unfolded peptides do not readily pass through the membrane, except for a few highly basic peptides, termed cell penetrating peptides (CPPs) (**Figure 1.4**). These include TAT, penetratin, and octa-arginine. While it is not known exactly what makes these arginine rich peptides pass through, we do know the guanidino functional group induces

interactions with the cell surface. Sulfated glycans and other phosphates and carboxylates that have anionic character are present at the cell surface. The guanidino group on arginines can form hydrogen bonds with these molecules to confer an increase in hydrophobicity leading to cell penetration.

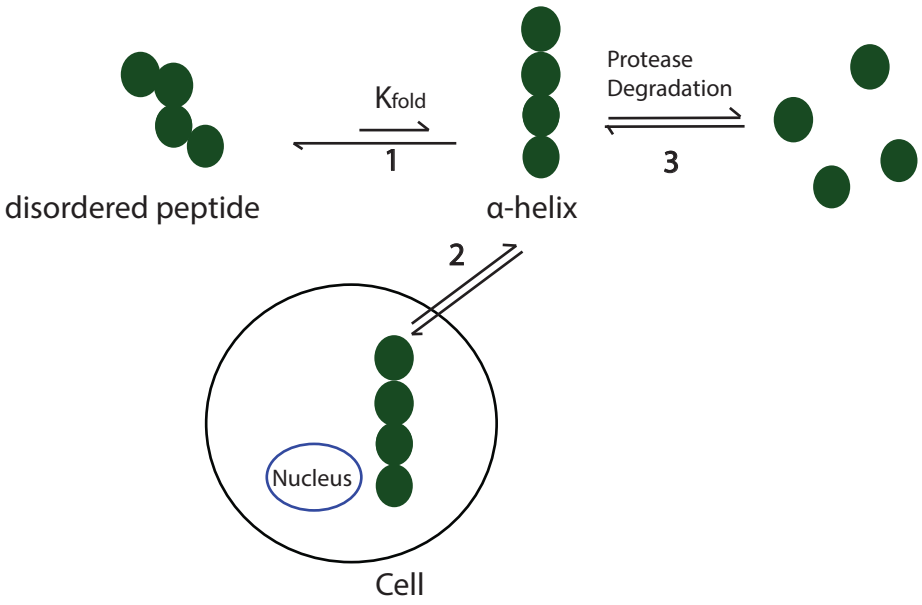

Figure 1.4 Process by which a disordered protein folds into a stable α-helix (1), crosses into the cell membrane (2), and is finally degraded by proteases (3).

Based on the punctate pattern seen on microscopy images, stapled peptides can be taken up actively through endocytosis.[22,23] Export of the peptides from pinosomes into the intracellular matrix has also been observed.[22,24] However, not all stapled peptides confer intracellular uptake.[17,19,25–27] The overall charge, hydrophobicity, and α-helical structure are all believed to affect cellular penetration. Increasing the net charge of the peptide often leads to enhanced permeability, as well as changing the location of the cross-link.[18,19,28,29]

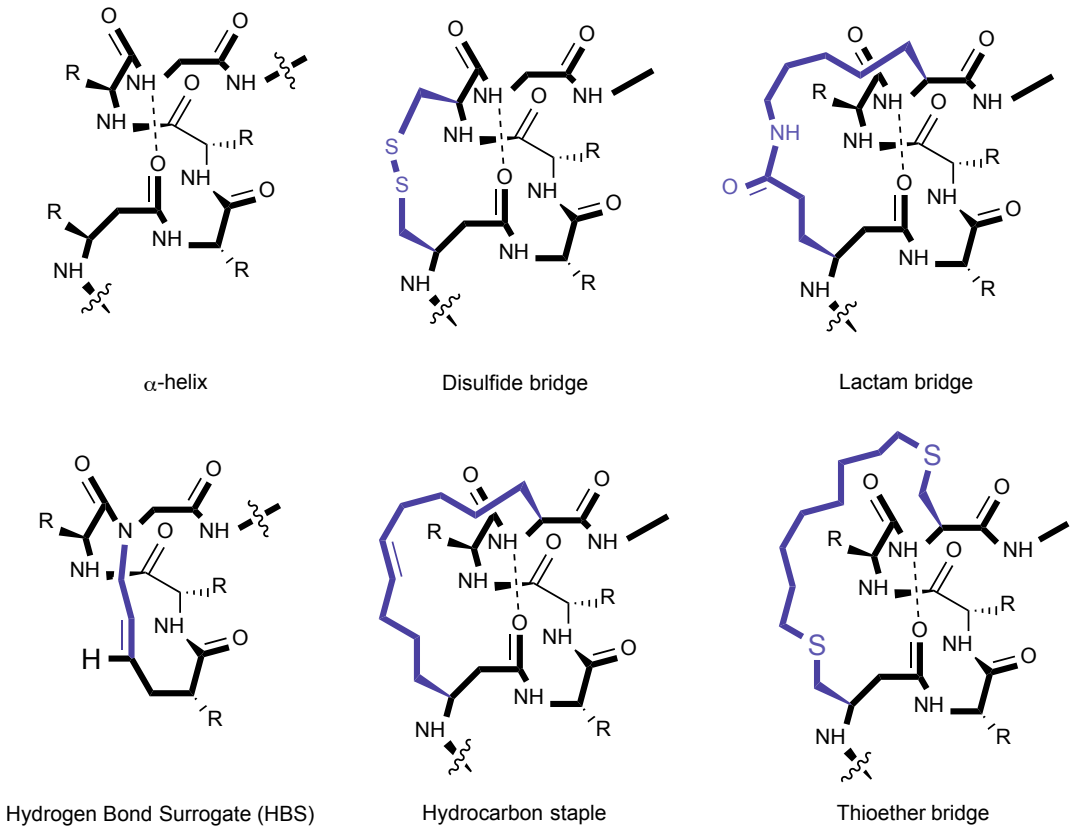

Figure 1.5 α-Helical peptidomimetics, including stapled peptides, hydrogen bond surrogates, lactam linkers, disulfides, and thioether bridges. Image adapted from Azzarito et al.[30]

A variety of clever methods have been employed to add rigidity, stability, and affinity to α-helical peptidomimetics, including stapled peptides, hydrogen bond surrogates, lactam linkers, and thioether bridges, **Figure 1.5.**

1.9 **Disulfide Bridge**

Naturally occurring disulfide motifs inspired the first studies of stabilizing α-helices into locked, rigid structures with disulfide tethers (**Figure 1.5**).[31,32] The work of Schultz, et al. incorporated a disulfide bond into peptides, which resulted in enhanced

helicity compared to reduced, uncyclic analogs. Furthermore, the *L,L* enantiomers had increased helicity versus the *L,D* enantiomers. Few disulfide bridging techniques have been published recently, potentially due to a major drawback of intracellular disulfide reductions. Reducing environments can reverse disulfide bonds back to the unconstrained peptide, limiting their applicability towards intracellular targets. Cystathionine thioethers, where one sulfur atom is replaced by a methylene group has become an alternative strategy that has maintained some structure and activity while eliminating the disulfide bond susceptible to reduction.[33] This strategy has been evaluated on Compstatin, currently in clinical trials for macular degeneration.[34] Compstatin contains a susceptible disulfide bond that was exchanged to a cystathionine thioether. Activity was maintained while increasing biological stability.

1.10 **Lactam Bridge**

Incorporation of a lactam cross-link to stabilize helical mimetics has been researched by several including Fairlie, Osapay, and Taylor.[35–37] Lactamization on one side of an amphiphilic helix showed increased helicity that potentially stabilizes the peptide and increases binding affinity (**Figure 1.5**).[36–38] In work done by Osapay et al., a condensation reaction involving a lysine residue and an oxime resin-bound aspartic acid at the *i, i+4* positions created a lactam crosslink that showed 69% α-helicity via CD. Fairlie has also shown peptides with increased helicity as well as increased binding affinity.[35]

1.11 **Stapled Peptides**

The pioneering work of Grubbs and Blackwell propelled the area of peptide mimetics forward (**Table 1.1**). Using a ruthenium catalyzed ring closing metathesis

reaction (for which Grubbs received the Nobel Prize in Chemistry for), they cross-linked short peptides on resin supports. By introducing allyl-glycine or *O*-allyl serine amino acids, they formed a new C-C bond between the two alkene moieties to afford the macrocycle **(Figure 1.5)**.[13] This work inspired Verdine and colleagues to use the RCM reaction to afford an all-hydrocarbon crosslinked α-helix peptide.[12] Incorporation of α-methyl,α-alkenyl glycines to afford a crosslink over one or two α-helical turns were assessed for the optimal stereochemistry and linker length. This method of 'Stapling Peptides' has been used on a variety of PPIs by numerous laboratories, **Table 1.1**. Recently, Aileron Therapeutics published a potent stapled peptide inhibitor ATSP-7041 that targets the oncogenic proteins MDM2 and MDMX, **Figure 1.6**.[39] With high α-helicity, protease stability, and increased cell penetration coupled with favorable pharmacokinetic properties and in vivo stability, they highlight the capability of stapled peptides developing as pre-clinical drug candidates.

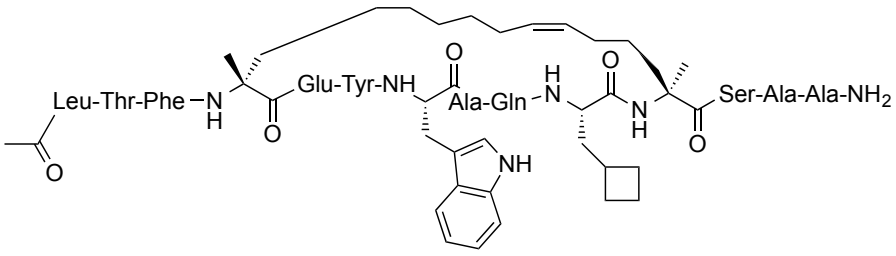

ATSP 7041

Figure 1.6 Peptide inhibitor from Aileron Therapeutics targeting MDM2 (K_i = 0.9 nM) and MDMX (K_i = 6.8 nM)

Table 1.1 A sample of the many targets that have been analyzed with stapled peptides.

Stapled Peptide	Target	PPI target
BID BH3, BIM BH3, BAD BH3, PUMA BH3, MCL-1 BH3	BCL-2 family proteins	Transcriptional machinery[22,25,40–44]
mastermind	NOTCH	Transcriptional machinery [45]
BCL9, axin	β-catenin	Transcriptiona machinery [46]
P53	MDM2/MDMX	Transcriptional machinery [47–50]
EZH2	EED	Enzyme catalytic domain[51]
HIV-1 Integrase	LEDGF/p75	Viral protein and host cell co-factor[52]
lasioglossin III (LL-III) and melectin	bacterial cells	Antimicrobial peptide and bacterial cell surface[53]
NR coactivator peptide 2, SP1	ER- α	Coactivator of estrogen receptors [54,54]
NYAD-1	gag	HIV particle assembly[55]
BAD BH3	glucokinase	Restore mitochondrial respiration[56]
neuropeptide Y	galanin	Anticonvulsant neuropeptides[57]

1.12 **Stapled peptides in clinical trials**

Aileron Therapeutics, a pharmaceutical company exploring constrained peptide inhibitors have begun clinical trials on the stapled peptide, ALRN-6924 recently (Sept. 2016). The peptide targets both MDM2 and MDMX interactions with the suppressor protein, p53. The protein p53 coordinates transcriptional machinery to trigger a cell death response. Small molecule drug targets are only able to target MDM2, making ALRN-6924 potentially beneficial to suppress cancer cell growth.

Aileron has also investigated a stapled peptide—a growth-hormone-releasing hormone agonist targeting an extracellular site, ALRN-5281—for the treatment of endocrine disorders, hormone deficiencies, and human immunodeficiency virus (HIV).[58] The drug has completed phase I clinical trials on 32 subjects with no adverse effects, dose-limiting safety findings or, tolerability problems. The recent clinical studies on stapled peptides underscore the potential utility and applicability of peptides used as inhibitors. The need to further elucidate the role constrained peptides can have as potential clinical candidates is evident.

1.13 **Hydrogen Bond Surrogates**

Arora and colleagues have developed a unique method to confer helicity through nucleation with a covalent crosslink at the N-terminus of the peptide (**Figure 1.5**).[59] By nucleating a helix at the N-terminus with a covalent C-C bond, they can conformationally constrain the full peptide into stable α-helical peptides. Incorporation of pentenoic acid at the first position of the peptide, and an aspartic acid at the fourth residue allows for a ring closing metathesis reaction to afford a stable covalent crosslink. By replacing a hydrogen bond with the covalent crosslink, they are not burdened by a crosslink covering one face of the helix. By freeing all sides of the peptide, they can target deep pockets that surround all sides of the helix. They have been able to target a variety of PPIs including the Bak BH3: Bcl-x_L, where they synthesized a HBS Bak BH3 peptide that bound Bcl-x_L with 69 nM affinity and high proteolytic stability.[60] They have also identified the HBS HIF-1α (hypoxia inducible factor 1 alpha) targets p300 CH1 with K_d of 420 nM.[59] Due to synthesis and purification difficulties, they have incorporated thioether linkages (teHBS) that have

shown similar conformational stability and protein target potential to the hydrocarbon HBS.[61]

1.14 **Cysteine containing crosslinks**

The broad reactivity profile of thiols makes cysteine an excellent functional moiety to develop synthetic peptide constraints. With high nucleophilicity, thiolates can participate in exchange, radical, and atom-, hydride transfer, and metal binding reactions.[62] Thiol incorporation into peptides are as simple as engineering cysteine or methionine residues at sites of interest in the peptide primary sequence. The facile insertion of cysteine coupled with the wide scope of reactivity of sulfur gives this method an advantage over other costly, difficult to synthesize constraints (e.g. disubstituted alkenyl glycines and click reactions).[63]

1.15 **Thioether crosslinks**

Taking advantage of thiol-ene reactivity, Danny Chou and colleagues have used dialkenyl hydrocarbons to react with a thiol on cysteine residues that are either *i, i+4* or *7* residues apart. With both an 8 and 10 carbon linker appended, an increase in helicity and % inhibition of the p53: MDM2 interaction.[64]

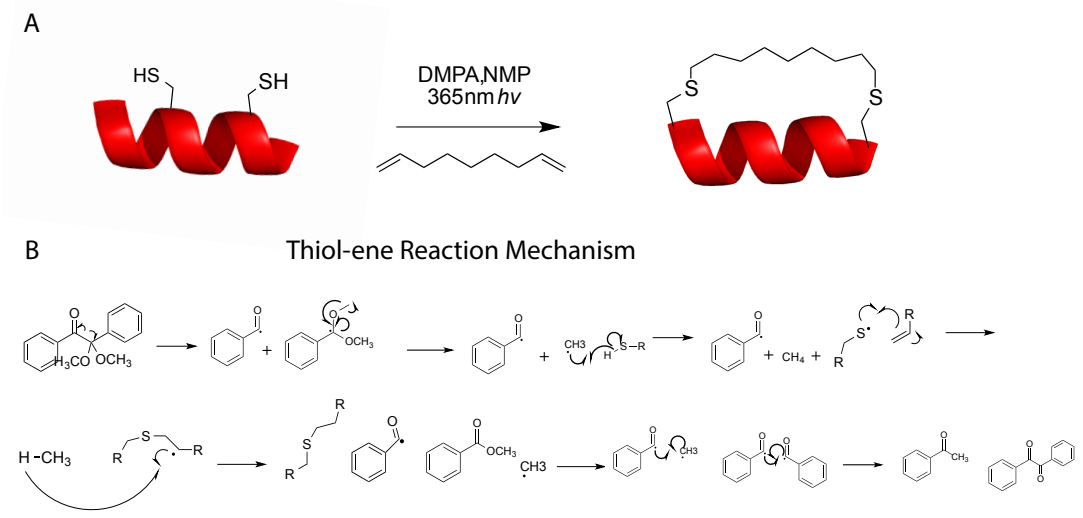

Figure 1.7 Thiol-ene reaction photoinitiated with 2,2-dimethoxy-2-phenylacetophenone (DMPA) reacting a dialkene with thiolyl radicals on two cysteine residues at positions i, i+4 or 7.[64]

Brunel and Dawson have synthesized thioether constraints by reacting a thiol on cysteine with an α-bromoamide.[65] These were shown to have an increase in helicity as well as affinity towards the gp-41 specific antibody 4E10.

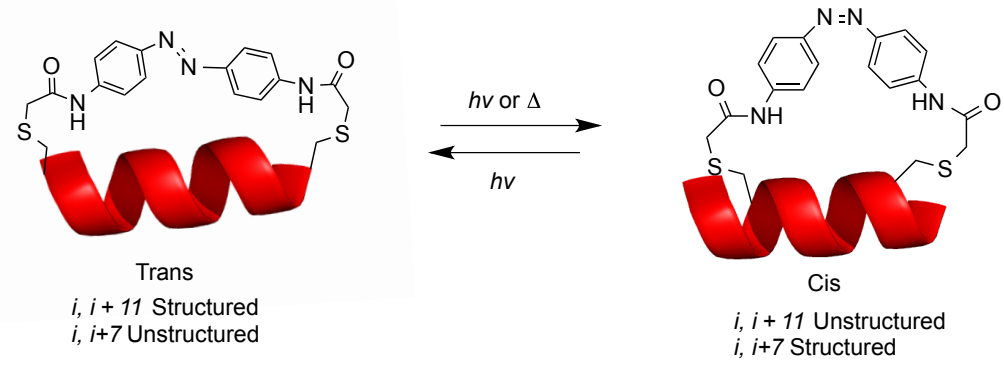

Figure 1.8 Photoisomerization of azobenzene crosslinker leads to structural changes in the helix. When trans, *i, i+11* is stabilized into a helical constraint, whereas i*, i+7* is constrained in the *cis* isomer. [64]

Woolley and colleagues have incorporated photoswitchable azobenzene crosslinkers that result in *trans* to *cis* isomerization which leads to substantial changes in the folding of the peptide (**Figure 1.8**).[66] Nevola and colleagues took photoisomerization further by developing peptides that regulated clathrin-mediated endocytosis, and has made azobenezene crosslinked peptides that can pass through the membrane and target specific PPIs inside the cell.[67]

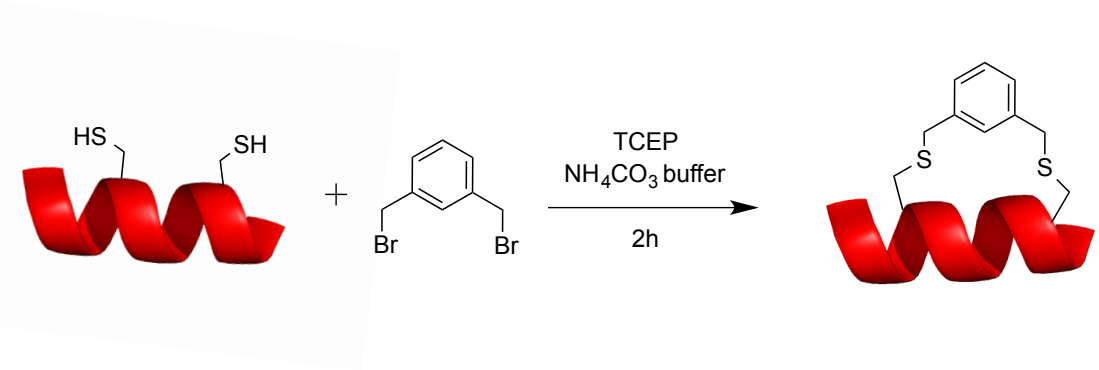

Figure 1.9 Biphenyl thioether staples synthetic scheme with peptide and dibromo-*m*-xylene crosslinker under basic conditions.

Biphenyl staples with *S*-alkylation reactions at positions *i, i+3, 4, 5,* and *6* have been synthesized by Micewicz and co-workers (**Figure 1.9**). They synthesized a library of 60 constructs to identify inhibitors of the p53: MDM2/MDMX interaction.[68] Recently, Pentelute and colleagues have utilized a novel S_NAr bioconjugation approach (**Figure 1.10**).[69] Their approach transfers aryl groups selectively to cysteine thiolates. They have

investigated a variety of perfluoroaromatic species, which can then be monitored with ^{19}F NMR.

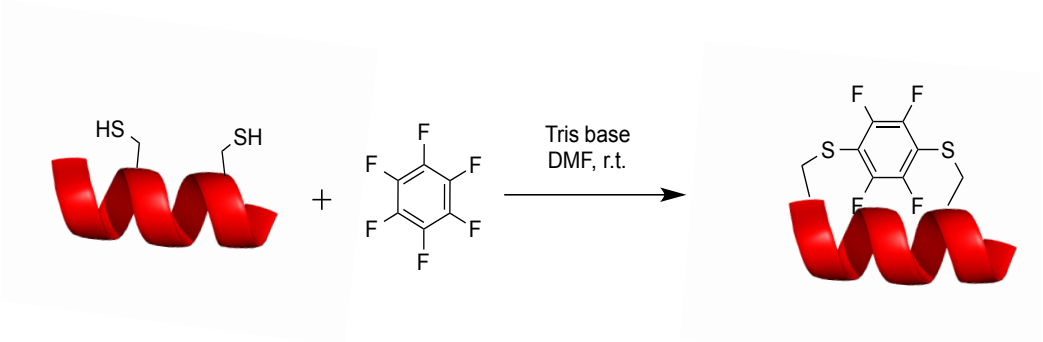

Figure 1.10 Perfluoroaryl thioether constructs utilizing an S_NAr bioconjugation approach

1.16 **Tetrazine staples and tricysteine**

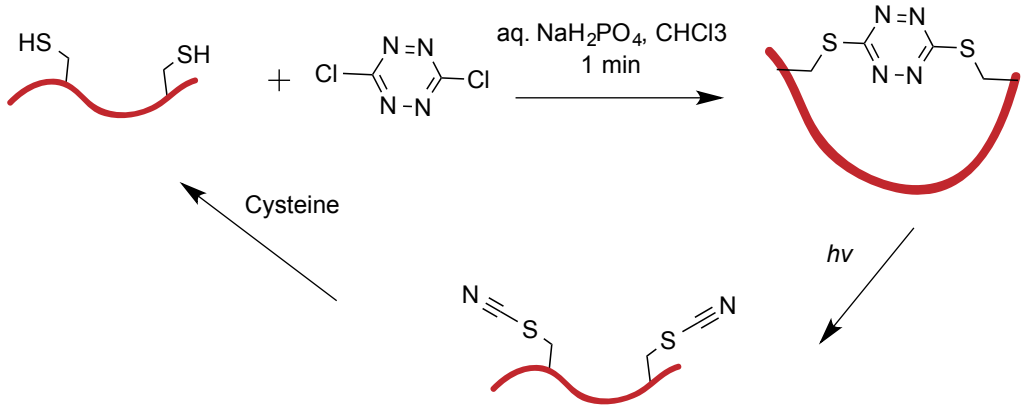

Figure 1.11 S-tretrazine reversible macrocycles able to convert back to initial free thiol peptide with light.

S,S-tetrazine macrocycles have been synthesized using cysteine amino acids positioned 2-27 away from one another (**Figure 1.11**).[70] The constraint can then be broken photochemically to regenerate the free thiol. Furthermore, the tetrazine can be used in an

inverse demand Diels-Alder reaction to append a fluorescein tag. While this conformationally constrains the peptide, it is not stabilized into the specific α-helical structure, but rather a large macrocyclic ring.

The wide variety of sulfur chemistry used to form macrocyclic peptides highlights the vast utility cysteine-based strategies have become. With the growing methods, we can identify bioactive molecules for therapeutic based drugs more readily.

1.17 **Transcription Factors and Coactivators**

Transcription factors can be classified as intrinsically disordered proteins that bind tightly (nM-pM) to a response element on DNA. Once bound, RNA polymerase II is recruited via the transcriptional activation domain, and co-activator complexes. Activation of the promoter then initiates transcription. These dynamic complexes rely on timing, specificity, and coactivators in order to initiate transcription of various genes.[71] One transcription factor may have several coactivators that bind to several areas of the basal transcription machinery.[72,73] These coactivators may be allosterically regulated, such that the binding of one ligand affects the binding of another.[74] CREB binding protein is a large multidomain protein that contains one domain, KIX (kinase-induced domain interacting domain) that can interacts with over a dozen transcriptional activators including CREB, c-Myb, and MLL.[75] The various types of binding affect what genes will be upregulated. The binding of CREB to CBP induces transcription of *cyclin A1*, *B-cell lymphoma 2* (*bcl-2*), and *early growth response gene 1* (*egr-1*) allowing for survival, proliferation, and differentiation, respectively (**Figure 1.12**).[76,77]

1.18 **CREB/MLL-KIX binding interactions**

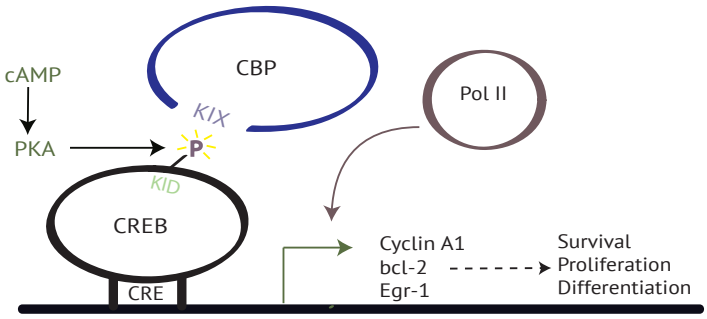

Figure 1.12 Transcriptional activation machinery directed by the CREB:KIX binding interaction upon Ser-133 phosphorylation. Adapted from Sakamoto. [28]

1.18.1 Defining characteristics of the CREB binding protein

A large portion of proteins has been classified as intrinsically disordered proteins (IDPs). IDPs lack a defined structure in native conditions, but are often still able to functionally engage in protein-protein or protein-DNA recognition complexes.[78] Conformational transitions of peptides have great importance on their ability to interact and ultimately activate specific processes, but it is still unclear as to what induces such conformational switches.[79–81] It has been shown that binding precedes folding in the transactivation domain of c-Myb.[78]

The binding of CREB to CBP induces a random coil-to-helix transition that stabilizes binding[82,83] and creates an amphipathic helix with hydrophobic groups lining one face of CREB so as to interact with the shallow groove of KIX through a coupled folding

and binding mechanism[84] (**Figure 1.13A**). About 1200 Å^2 of surface is buried upon pKID: KIX complex formation, and is predominately hydrophobic. To supplement the interaction between the proteins are electrostatic interactions. What seems to be an important interaction is the salt bridge formation of Lys-606 of KIX with Asp-140 of pKID. Acidic residues at this position have also been invariant within the CREB family.[82]

Another proto-oncogene, c-Myb binds at the same site CREB binds on KIX, also via an amphipathic helix.[85] Ongoing research in several laboratories is continuing to elucidate the key components of CREB necessary to bind including Montminy and colleagues.[83] Their discovery of an 8-amino acid synthetic peptide derived from phage display has shown a 16.1 μM affinity towards the KIX domain as well as potent transcriptional activation.[86]

The interactions between KIX and its many binding ligands create a complex system that intertwines dynamic allostery with affinity, **Figure 1.13**. The distal binding site where mixed lineage leukemia (MLL) binds has been shown to affect the pKID: KIX complex with the binding of MLL enhancing KIX interactions with c-Myb and CREB. CREB: KIX or c-Myb: KIX has a 2-fold higher affinity when MLL is also bound compared to the KIX domain alone. However, the complexity of activation in this interaction proves to be difficult to modulate and control.[71,87]

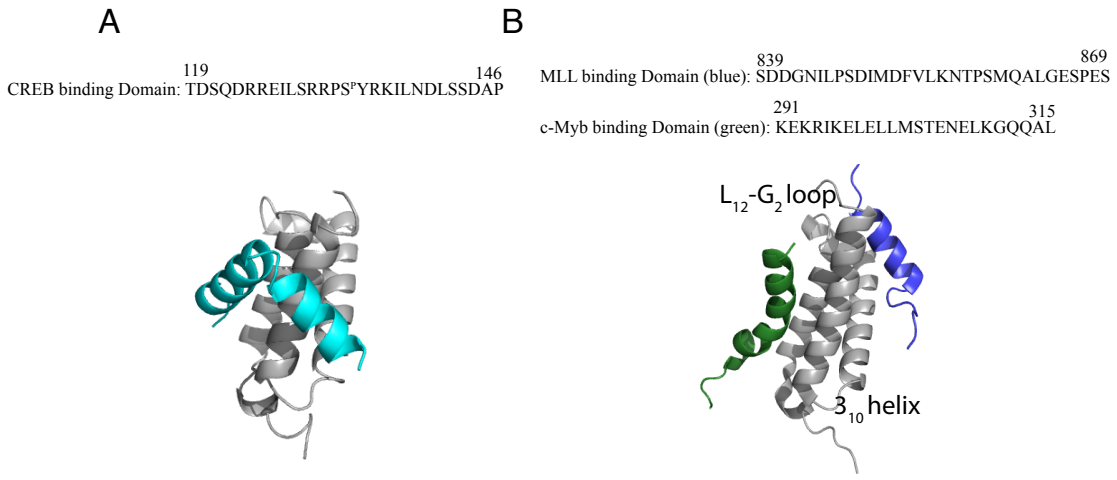

Figure 1.13 3D structure of the KIX complex in solution. A. KIX interaction with CREB (cyan) (PDB: 1KDX) B. KIX binding with two partners, MLL (blue) and c-Myb (green), where c-Myb overlaps in binding site with CREB.

CREB has been found to play a critical role in regulation of several biological processes including circadian rhythms, memory formation, and hematopoiesis.[88] It is also important in normal T-cell formation and the regulation of gluconeogenesis.[89] This 43 kDa basic leucine zipper (bZip) is conserved from *Drosophila* to humans, and is a part of the CREB/ATF-1 transcription factor family.[90] The binding of CREB to KIX is activated through a cascade of signals. Activation of Cyclic AMP leads to the phosphorylation of Ser-133 of CREB via protein kinase A (PKA). Once phosphorylated, CREB induces transcriptional activation by interacting with CREB binding protein (CBP), which acts as a 'bridge' to allow the recruitment of Polymerase II (Pol II), which allows transcription to occur.[76,77,90,91] The transcription of distinct genes is highly regulated by the interactions between CBP and the many transcription coactivators that bind.[92] Transient PPIs, such as

transcription factor binding interactions, are not only central to cell growth and development, but also to the progression of disease, such as acute myeloid leukemia (AML).

1.18.2 Defining characteristics of the MLL binding protein

Mixed lineage leukemia (MLL) binding to KIX induces the formation of the 3_{10}-Helix (residues 591-594) and displaces a loop region (residues 614-621) which allows for hydrophobic contacts with MLL, including F612, and L628, **Figure 1.13B**.[93] L628 has shown to be a critical contact necessary for a conformational transition important for the MLL transcriptional activation domain to bind, as indicated through HSQC NMR studies.[94] The interactions between KIX and MLL create a complex system that intertwines dynamic allostery with affinity, **Figure 1.13**. The distal binding site where MLL binds has been shown to affect the pKID: KIX complex with the binding of MLL enhancing KIX interactions with c-Myb and CREB. CREB: KIX or c-Myb: KIX has a 2-fold higher affinity when MLL is also bound compared to the KIX domain alone.[95] However, the complexity of activation in this interaction proves to be difficult to modulate and control.[71,87]

1.19 **Acute Myeloid Leukemia**

A deadly disease that is characterized by abnormal myoblast cell formation within the blood inside bone marrow has been treated with chemotherapy cocktails, radiation therapy, or bone marrow transplants. The dismal outlook of a 24.2% 5-year disease-free survival rate for AML patients has not changed since 2003.[96,97] This deadly cancer affected 14,000

individuals in 2012, most of which were adults.[96] Children have less than 50% survival rate.[90] A few small molecules are in clinical trials including Dexamethasone, Pomalidomide, and pembrolizumab.[98] None of the options are ideal, as they are either kill numerous healthy cells in the process, or don't target the root cause of the issue.[99] Methods to target specific locations without detrimental off-target effects would allow for a beneficial drug to ease the difficulties AML patients must endure.

While CREB is an important transcription factor for regulating normal processes in the body, over regulation has been implicated in AML. It is thought that if the distinct CREB: KIX binding interaction can be inhibited, then the transcription of cancer cells may be reduced without affecting transcription of other genes. [75,77,90,91,100] Research on AML has shown that CREB is necessary for the proliferation of hematopoietic stem cells as well as leukemia cells.[90] The upregulation of cyclin A1 by overexpression of CREB leads to aberrant cell cycle progression.[77] While CREB is overexpressed in leukemic blast cells in patients with AML, it is not enough to induce leukemia growth in vivo. It is unclear if the activation of CREB drives cancer cell growth, or if it is simply a byproduct of an activated pathway upstream.[76,88] It appears most leukemias are a result of collaborations of several mutations.[77] More research is critical to better understand the role of CREB in acute leukemia progression.

1.20 **Preface to this Dissertation**

The following chapters describe my contribution to the modulation and understanding of interactions between proteins with the use of peptidic probes. Chapter 2 identifies a non-covalent interaction between sulfoxide functional groups and aromatic rings. We first evaluated structural databases to understand the prevalence of the interaction. Experimentally we further confirmed the interaction with NMR, and CD thermal melts to identify the energy associated with the noncovalent interaction to be -1.24 kcal/mol, which correlated with the computational studies. This interaction was further evaluated within the protein calmodulin. Chapter 3 describes the synthesis, and characterization of thio-ether bridged macrocycles. Due to the chemical plasticity of sulfur, we evaluated a variety of oxidation states. The biophysical characteristics including polarity, helical propensity, tryptic stability, and cell permeation were evaluated, as well as affinity towards the KIX protein using Protein Observed ^{19}F (PrOF) NMR and fluorescence polarization. In collaboration with Derda and colleagues, we analyzed a perfluorinated crosslinked peptide for affinity towards human serum albumin using PrOF NMR. To attain varied oxidized sulfur containing peptides, we employ a specific synthetic reaction, the thiol-ene reaction, investigated in Chapter 4. This reaction incorporated non-natural cysteine derivatives that can be incorporated into peptides during solid phase peptide synthesis (SPPS). These cysteine derivatives can be oxidized to various oxidation states, allowing for further elaboration of thioether crosslinked peptides. Chapter 5 investigates epigenetic interactions of a histone variant, H2A.Z that is highly enriched at transcription start sites, and may provide an effective site to suppress specific transcriptional sites. H2A.Z has 5 lysines that can be acetylated an identified by bromodomains. We evaluated

the histone variant H2A.Z for specific acetylation patterns that are necessary to interact with bromodomains. We identify two bromodomains (BPTF and *Pf*GCN5) to have interactions with a diacetylated pattern on H2A.Z—H2A.Z AcK4,11. In Collaboration with Stuart Conway, we investigated series of dihydroquinoxalinone small molecules for their affinity towards three bromodomains: CBP, BrdT, and Brd4. Utilizing both PrOF NMR and FP, we identify small molecules with affinity and specificity towards the bromodomains.

Chapter 2. Sulfoxide-Pi Interactions within biological systems

Motivation:

We collaborated with researchers from the Sachs, Gao, Thomas, Cembran, and Hinderliter labs to identify sulfoxide interactions with aryl rings. While the methionine-π interaction has garnered significant attention, the sulfoxide-π interaction has not been evaluated. The prevalence of the interaction was identified within both the PDB and CSD, computational and experimental work on the energy associated with the interaction, as well as analysis within the Calmodulin protein to provide evidence for the sulfoxide-π non-covalent interaction. The work I contribute to this project includes the CSD data-mining evaluations, as well as the NMR (ROESY and ^{1}H) to identify the sulfoxide-π interaction. To put this work in context, the entire work has been reproduced, and an introductory section expanded on the role of sulfur-aryl noncovalent interactions.

2.1 **Methionine-π interactions**

The role sulfur plays within a biological context is vast, and understood quite well for cysteine residues. Cysteine can partake in catalysis, metal binding, and redox regulation as well as within a structural context through disulfide formation.[101–103] The role methionine plays, however is still emerging. Methionine is highly susceptible to oxidation. The reversible posttranslational modification, methionine sulfoxide, may guard against reactive oxygen species, thus protecting proteins from oxidative damage.[104] Methionine further plays a beneficial role through its contribution to binding energy, such as methionine-π interactions. Due to the high frequency of sulfur contacts with aromatic rings in proteins— 50% of Protein Data Bank have sulfur atoms interacting with aromatic rings[105]— Waters and colleagues evaluated the contribution of energy associated with methionine and a variety of aromatic residues using a double mutant cycle.[106] A double mutant cycle places two residues of interest diagonal to one another within a β-hairpin peptide structure where the side chains are in close proximity. The interaction between either Phe or Trp with methionine stabilized the construct by -0.3 to -0.5 kcal/mol.[106] Serrano and Viguera have also observed increased stabilization between Phe and Met or Cys within an α-helix. By placing residues at an initial position, *i* and four residues away, *i+4* they evaluated the interactions between side chains. With Phe at an *i* position and Met at *i+4,* a free energy of interaction was calculated to be -0.65 kcal/mol.[107] Further validation of methionine stabilization properties were reported by Yamaotsu et al. where substitution of methionine with Leu in staphylococcal nuclease has also been shown to decrease the stability of the protein by 0.8 kcal/mol.[108]

2.2 **Cation-π interactions**

Significant work on cation-π interactions have also been assessed by Dougherty[109,110] and others.[109,111] The interaction is dictated by both an electrostatic interaction and induction effect[112] between the π-system of an aryl group and a positively charged group such as the side chains of lysine and arginine,[113] as well as ammonium and sulfonium substituents.[110,114] While it is observed that methionine oxidation plays a beneficial role within biological systems and the sulfur-π interactions lead to enhanced affinity, no significant work had evaluated sulfoxide prevalence or interaction scope. We sought to further explore how oxidation of methionine plays a critical role in stabilizing protein interactions.

2.3 **Introduction**

The methionine-aromatic motif is a promiscuous, highly stabilizing, and prevalent noncovalent interaction that forms between methionine thioether sulfurs and the aromatic rings of nearby (~5 Å) Tyr, Trp and Phe residues.[105,115–119] Methionine-aromatic interactions have been detected in several bioinformatics studies[118,119] including our exhaustive analysis of the Protein Data Bank (PDB). Sulfur-aromatic (S-Ar) interactions between the C-S-C divalent sulfur motif and aromatic groups have been similarly found in the Cambridge Crystal Structural Database (CSD).[116] The motif is substantially stronger than a purely hydrophobic contact, suggesting that it has a unique role in stabilizing protein structure and ligand-receptor binding. In a thermal unfolding experiment using a synthetic helical peptide, the Met-Phe interaction has been measured to be −0.65 ± 0.15 kcal/mol.[120] Quantum calculations have revealed an interaction energy of 1−3 kcal/mol at a range of 4−6 Å between dimethyl sulfide (DMS) and benzene.[117] Our own quantum calculations

expanded the analysis to include DMS interactions with phenol and indole (Tyr and Trp analogs, respectively) and revealed that dispersion interactions are the major contributor to stability.[115] In addition to forming highly stabilizing interactions with aromatic residues, methionine is uniquely important because its thioether can undergo modification with the addition of one or two sulfonyl oxygens to become methionine sulfoxide (MetOx) or sulfone, respectively, in oxidizing environments.[121] Elevated levels of methionine sulfoxide have been detected in diseased tissues, but methionine sulfone is rare.[122] Methionine sulfoxidation is known to regulate the activity of certain proteins. In other cases, methionine-rich domains protect critical amino acids from oxidation by removing free radicals and regulating the local redox environment.[104] Despite this functional importance, the specific molecular mechanism through which proteins sense and respond to oxidative modification of methionine residues has not been fully characterized. It has been posited that polarization of the methionine thioether by oxidation could weaken the methionine-aromatic interaction by ablating the hydrophobic contribution,[123] but this has never been tested experimentally to our knowledge. In the present study, we found the opposite to be true: that oxidation of methionine strengthened its interaction with aromatic residues, and has the potential to disrupt native conformation and alter protein function. We found that the interaction was strengthened even in the absence of a hydrogen bond between the sulfoxide oxygen (acceptor) and donor hydrogens (on Tyr or Trp). Through quantum mechanical calculations, we showed that the interaction between the dipole moment of dimethyl sulfoxide (DMSO) and the aromatic ring quadrupole moment was the main contribution to the increased stability of the motif. We started by analyzing both the PDB and the CSD to identify and characterize interactions between DMSO (a small-

molecule analog to MetOx) and aromatic groups in the crystal structures of proteins and small molecules. We performed quantum mechanical calculations on model compounds to determine the strength of the sulfoxide-aromatic interaction, and assessed the potential contribution of hydrogen bonding on the motif in a variety of solvent environments. We then isolated and determined the strength of the specific interaction between unoxidized and oxidized methionine, and the side chain of phenylalanine by extending a previously described helix unfolding experiment and performing a double mutant cycle analysis.[120] We investigated the effects of site-specific methionine oxidation on the methionine-aromatic interaction in two biologically important proteins. First, using a combination of electron paramagnetic resonance (EPR) spectroscopy and replica exchange molecular dynamics (REMD) simulations, we probed the effects of oxidation on the structure of calmodulin (CaM). Second, we investigated lymphotoxin-α (LTα) binding to tumor necrosis factor receptor 1 (TNFR1), which we have previously shown is stabilized by a methionine-aromatic interaction between Met120 of LTα and Trp107 of TNFR1.[115]

2.4 **Results and Discussion**

2.4.1 DMSO-aromatic interactions in crystal structure databases

To find examples of sulfoxide-aromatic interactions, we searched the PDB and CSD for occurrences of DMSO molecules near aromatic rings (**Figure 2.1**). The PDB is a repository containing crystal structures of proteins and the CSD is the analogous repository for organic and metal-organic small molecules. DMSO solubilizes tryptophan more readily than leucine, alanine and glycine,[124] so we expected to find that it specifically interacts with aromatic side chains. Our PDB search yielded 205 unique structures containing a total of

872 DMSO molecules. In **Figure 2.1A**, we show a representative DMSO-Tyr interaction. When compared to all amino acids, or just the aliphatic amino acids, aromatic residues were enriched 4−7 Å from DMSO sulfurs, with a maximum at 5 Å, resembling the radial density function for methionine-aromatic interactions from our previous study (**Figure 2.1B**).[115] We found 451 (51.7%) DMSO molecules within 7 Å of the nearest aromatic residue. Only 32 of these (7.1%) were in position to accept a hydrogen bond from either Trp or Tyr. Thus, hydrogen bonding did not drive DMSO-aromatic bonding in the proteins found in the PDB. Our CSD search similarly found ~50% enrichment of DMSO-aromatic contacts (e.g., **Figure 2.1C**) compared to C-CH2-C-aromatic pairs (**Figure 2.1D**), which had been used previously as a noninteracting control to show the enrichment of the Met-aromatic motif.[116] Again, few DMSO-phenol or DMSO-indole pairs in the CSD were in position to form a hydrogen bond (<14%).

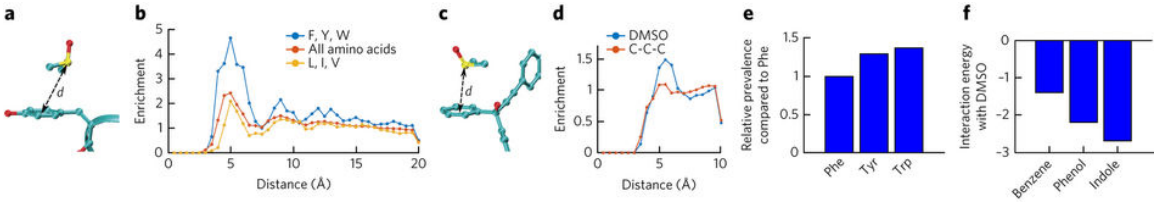

Figure 2.1 (a) Representative snapshot of a DMSO-aromatic interaction taken from the PDB (4KAD). *d*, distance between aromatic center and sulfur atom. (b) Radial distributions of indicated amino acids relative to DMSO. (c) Representative snapshot of a DMSO-aromatic interaction taken from the CSD (AWUHEF[125]). (d) Radial distributions of aromatic groups relative to DMSO sulfur and relative to C-CH_2-C motifs, which are noninteracting. (e) Frequency of DMSO interactions with each aromatic amino acid. These values are normalized against the abundance of each aromatic group in the PDB subset analyzed and shows enrichment of interactions with Tyr and Trp compared to DMSO-phenylalanine interactions. (f) Interaction energies calculated at the MP2/6-311+G(d,p) with CP corrections for the complexes between benzene, phenol and indole, and DMSO. Structures excluded hydrogen bonding and were calculated using ensembles of configurations from the MD simulations.

We then parsed the frequency of methionine-aromatic interactions in the PDB <7 Å between DMSO and the centers of Phe, Tyr and Trp individually. The interaction was more prevalent with Tyr and Trp than with Phe when normalized by the relative abundance of each of these amino acids in the analyzed structures (**Figure 2.1E**). This trend is not explained by relative solvent accessibility, as Trp and Phe have similar solvent accessibilities, whereas that of Tyr is somewhat higher.[126] We calculated a 1.3-fold and 1.4-fold preference for Tyr and Trp over Phe, respectively, translating to a ~0.3 kcal/mol increase in Met^{Ox}-Tyr and Met^{Ox}-Trp stability compared to Met^{Ox}-Phe. Therefore, these database results suggested that, although hydrogen bonding is not common in the interaction motif, DMSO interacts more favorably with Tyr and Trp than with Phe. This has similarly been observed in cation-π interactions in proteins, where the more electron-rich π systems of Trp and Tyr relative to Phe make them more attractive to positively charged ligands.[113]

2.5 **Oxidation strengthened interaction in quantum calculations (Cembran lab)**

We report interaction energies between the reduced (DMS) and oxidized (DMSO) models of methionine with the model aromatic compounds benzene, phenol and indole (**Table 2.3 and Table 2.1**). The data showed that upon oxidation of DMS to DMSO, the complex with benzene was 0.9 kcal/mol more stable. To understand the origin of this stabilization, we first tested the possible contribution of dispersion interactions. Dispersion energy contribution for DMS-benzene was −8.4 kcal/mol, and for DMSO-benzene it was

−8.2 kcal/mol (**Table 2.2**). This change in contribution was small (0.2 kcal/mol), and was more stabilizing for the DMS-benzene interaction than for the DMSO-benzene interaction. Therefore, dispersion interactions were not the source of the stronger interaction energy in the oxidized complex. Rather, the stronger interaction can be explained in terms of the interaction between the dipole moment of DMSO and the aromatic ring quadrupole moment. The calculated dipole moment for DMS was 1.8 Debye, whereas in DMSO the enhanced polarization owing to the presence of oxygen resulted in a dipole moment of 5.0 Debye, roughly aligned along the S=O bond. Both DMS and DMSO maximized dispersion interactions with the benzene ring by aligning the Me-S-Me moiety over the ring plane; as a result, in the DMS-benzene complex the orientation of the small dipole of DMS is orthogonal to the benzene quadrupole moment, whereas in DMSO-benzene, the angle between the S=O bond and the ring is approximately 120°, which is well poised for a favorable dipole-quadrupole interaction. The natural bond orbital (NBO) charge analysis for the complex and isolated species (**Table 2.4** and **Figure 2.2**) supported this explanation, showing a large positive charge (+1.19 e) on the sulfur that can interact with the π electron cloud, balanced by a negative charge (−0.96 e) on the oxygen pointing away from the benzene ring, **Table 2.2**.

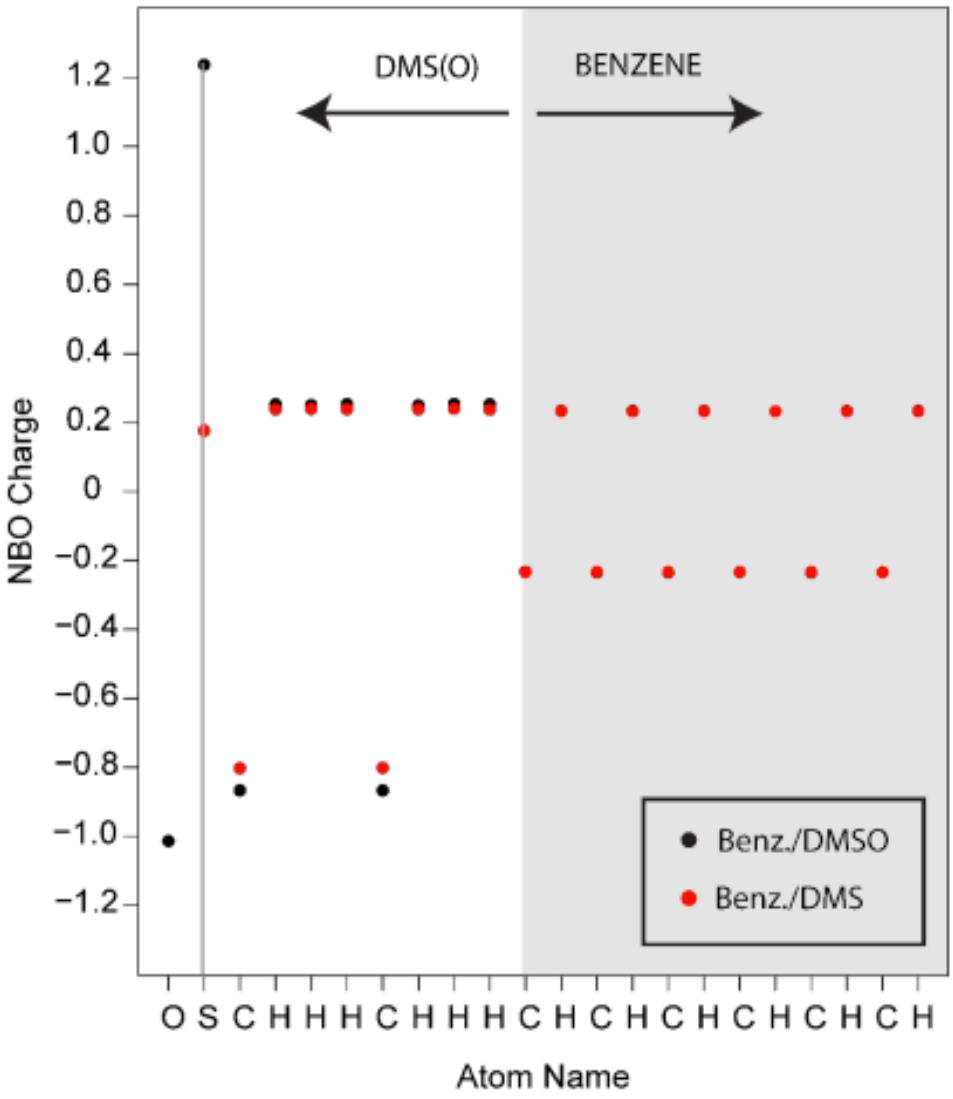

Figure 2.2 NBO average charges for the ABF simulations. NBO charges were computed as the average for the 128 structures for the simulations of DMS/DMSO and benzene in EtOAc using the MP2/6-311+G(d,p) electron density. In red the charges for benzene/DMS are reported, and in black for benzene/DMSO.

Table 2.1 Interaction energies for DMS and DMSO with benzene, phenol, and indole. Computed interaction energies in kcal/mol for the complexes of benzene, phenol, and indole with DMS and DMSO, images shown below table. M06-2X and MP2 data are reported for structures fully optimized at the corresponding levels of theory with the 6-311+G(d,p) basis set. Interaction energies corrected for basis set superposition error are reported in parenthesis.

	Benzene		Phenol		Indole	
Complex	M06-2X	MP2	M06-2X	MP2	M06-2X	MP2
DMS	-4.6 (-4.0)	-6.0 (-2.4)	-8.3 (-7.3)	-9.3 (-4.9)	-7.3 (-6.3)	-9.5 (-4.7)
DMSO	-6.2 (-4.9)	-7.3 (-3.3)	-16.0 (-14.4)	-16.0 (-10.6)	-13.6 (-12.1)	-15.5 (-10.0)

Table 2.2 Dispersion energy interactions. Dispersion energy interactions are calculated in kcal/mol for the complexes of benzene with DMS and DMSO as the difference between the MP2/6-311G(d,p) interaction energies and the HF/6-311+G(d,p) calculated as single point on the MP2 minima**.**

	MP2	HF	Dispersion Energy
DMS	-6.0	2.4	-8.4
DSMO	-7.3	0.9	-8.2

Table 2.3 Interaction energies for DMS or DMSO with benzene, phenol, and indole.

		Benzene	Phenol	Indole
Full Optimization	DMS	-2.4	-4.9	-4.7
	DMSO	-3.3	-10.6	-10.0
Molecular Dynamics Simulations	DMS	-0.9	-1.0	-1.3
	DMSO non-H-bonded	-1.4	-2.2	-2.7
	DMSO H-bonded		-9.0	-7.5

Table 2.4 NBO Charges analysis of the benzene complexes with DMS and DMSO, and of the isolated species based on the MP2/6-311+G(d,p) electron density.

	DMSO/Benzene	DMS/Benzene	DMSO	DMS	Benzene
O	-0.96		-0.96		
S	1.19	0.19	1.18	0.20	
C	-0.77	-0.70	-0.76	-0.70	
H	0.22	0.21	0.22	0.21	
H	0.22	0.21	0.21	0.19	
H	0.21	0.19	0.21	0.19	
C	-0.76	-0.70	-0.76	-0.70	
H	0.22	0.21	0.22	0.21	
H	0.21	0.19	0.21	0.19	
H	0.21	0.19	0.21	0.19	
C	-0.20	-0.20			-0.20
C	-0.21	-0.21			-0.20
C	-0.20	-0.19			-0.20
C	-0.20	-0.21			-0.20
C	-0.21	-0.20			-0.20
C	-0.20	-0.20			-0.20
H	0.21	0.20			0.20
H	0.20	0.20			0.20
H	0.21	0.20			0.20
H	0.21	0.20			0.20
H	0.20	0.20			0.20
H	0.21	0.20			0.20

For phenol and indole, the change in interaction energy upon DMS oxidation (−5.7 kcal/mol and −5.3 kcal/mol, respectively; **Table 2.3**) was of larger magnitude than for benzene. Such a large change cannot be explained in terms of enhanced dipole-quadrupole interactions, and is a result of hydrogen bonding between the DMSO oxygen and the hydrogen of the phenol hydroxyl group or the indole amine (**Figure 2.3**). To determine the relevance of hydrogen bonding in sulfoxide-aromatic interactions in a range of environments, we ran molecular dynamics simulations of DMSO and phenol or indole in hexane, ethyl acetate (EtOAc) and water using the adaptive biasing force (ABF) module in the NAMD parallel molecular dynamics (MD) simulation package. We found (**Figure 2.4**) that DMSO hydrogen-bonded with phenol and indole in hexane. Thus, in this nonpolar

environment, we expect the contribution of the hydrogen bond to outweigh the increased interaction energy of the S-Ar motif. In EtOAc (a polar nonprotic solvent with dielectric constant of 6, representative of the protein interior), hydrogen bonding occurred less frequently. Therefore, the S-Ar motif had a role in the stabilization of the complex in this environment. Finally, in water, hydrogen bonding between DMSO and the aromatic group was essentially absent; rather the sulfonyl and aromatic hydrogens were solvated by water. This environment mimicked interfacial residues on the protein, which are often involved in protein-protein interactions.[127]

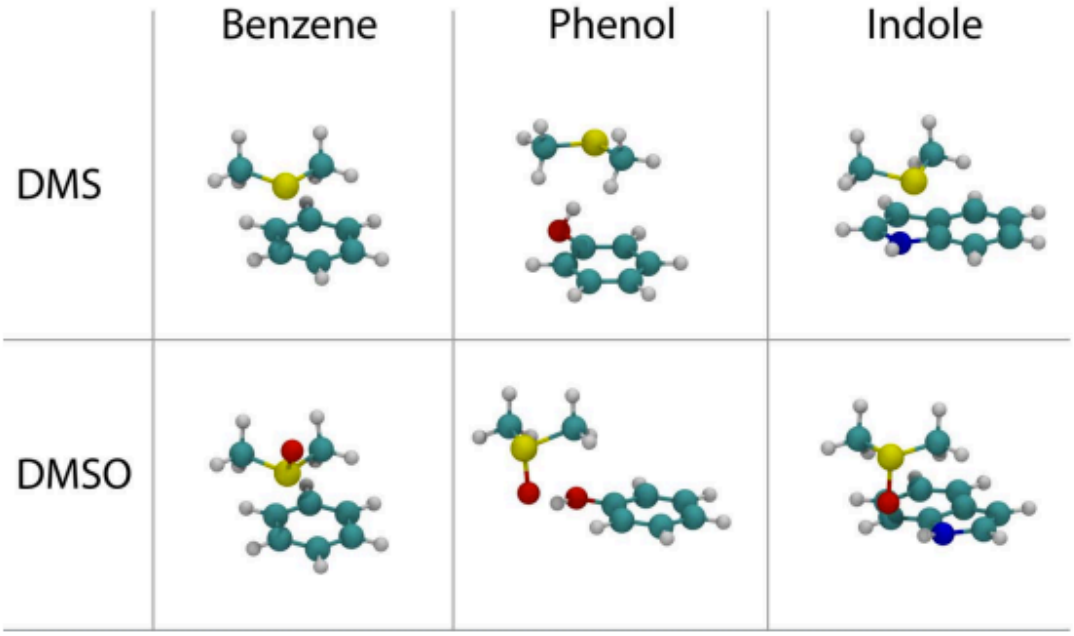

Figure 2.3 Minimum energy structures. The minimum energy structures for the complex between DMS or DMSO and benzene, phenol, and indole, calculated from full optimizations at the MP2/6-311+G(d,p) level.

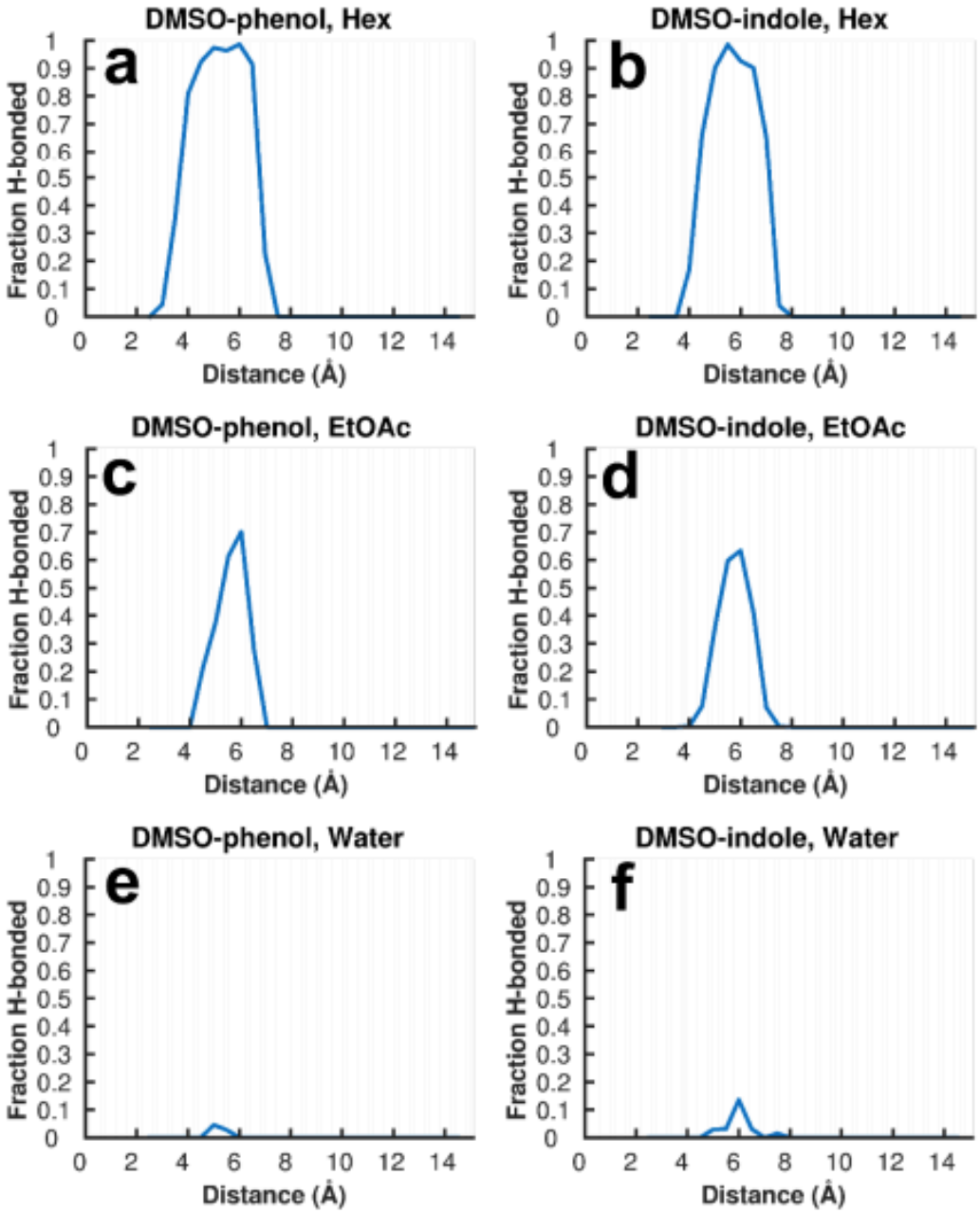

Figure 2.4 Fraction of structures in which the DMSO sulfonyl accepts a hydrogen bond from the aromatic. Structures were extracted from the ABF simulations of DMSO and aromatic amino acid analogs in three solvents. The fraction of structures that are hydrogen bonded (H-acceptor distance < 2.5Å) along all sulfur-aromatic distances is plotted. Hydrogen bonding occurred in nearly all configurations that were in range in hexane (a, b), fewer configurations in EtOAc (the frequency of hydrogen bonding was reduced by ~60%) (c, d), and almost none of the configurations in TIP3P water (e, f). EtOAc is able to accept hydrogen bonds from the aromatic group and TIP3P is able to donate and accept hydrogen bonds, which results in the lower prevalence of bonding between the DMSO and aromatic group.

To disentangle the energy contribution owing to hydrogen bonding from that of sulfur-aromatic interaction, we performed quantum mechanical calculations on configurational ensembles from our simulations in EtOAc for both DMS and DMSO complexes with aromatic residues. The intermediate dielectric constant of EtOAc and its ability to accept hydrogen bonds allowed complexes between DMSO and either phenol or indole to sample hydrogen-bonded and non-hydrogen-bonded conformations with similar probability. We analyzed non-hydrogen-bonded and hydrogen-bonded ensembles as mimics of the interactions on the protein surface and in its hydrophobic core, respectively. The results (**Table 2.1** and **Figure 2.1F**) agreed with the data from the full optimization, and together indicate that (i) in the absence of hydrogen bonding, oxidation of DMS to DMSO strengthened the sulfur-aromatic interaction by 0.5−1.5 kcal/mol, and (ii) in hydrogen-bonded structures (rare in proteins) the complex was stabilized by up to 8 kcal/mol.

2.6 **Evaluation of oxidation in a model peptide scaffold**

To experimentally assess the database findings and quantum results, we used thermal denaturation (monitored with circular dichroism (CD)) and NMR spectroscopy to investigate a previously reported 15-residue peptide scaffold,[120] designed such that the strength of the interaction between i, i + 4 amino acids would determine the thermal stability of the peptide secondary structure. In that study,[120] the Met-Phe pair had been found to interact, with a Gibbs free energy of interaction (ΔG_{int}) of 0.65 kcal/mol. We first confirmed a direct interaction between oxidized Met and Phe (**Table 2.5**) using NMR spectroscopy. We observed the strongest signals from nuclear Overhauser effects (NOEs)

to the aryl hydrogens meta to the side chain methylene (3,5 position) (**Figure 3.9A** and **Figure 2.1**). NOEs to the hydrogen at the 4 and 2,6 positions were present at lower levels and overlap.

Table 2.5 All peptides used in CD thermal studies, their appropriate abbreviation and their sequences. Only residues 9 and 13 were varied, shown in bold.

Peptide	***Abbreviation***	***Construct Sequence***
Phe-Met	FM	YGGSAAEA-**F**-AKA-**M**-AR-NH_2
Phe-Met (ox)	$FM_{(ox)}$	YGGSAAEA-**F**-AKA-**M (ox)**-AR-NH_2
Phe-Ala	FA	YGGSAAEA-**F**-AKA-**A**-AR-NH_2
Ala-Met	AM	YGGSAAEA-**A**-AKA-**M**-AR-NH_2
Ala-Met (ox)	$AM_{(ox)}$	YGGSAAEA-**A**-AKA-**M (ox)**-AR-NH_2
Ala-Ala	AA	YGGSAAEA-**A**-AKA-**A**-AR-NH_2

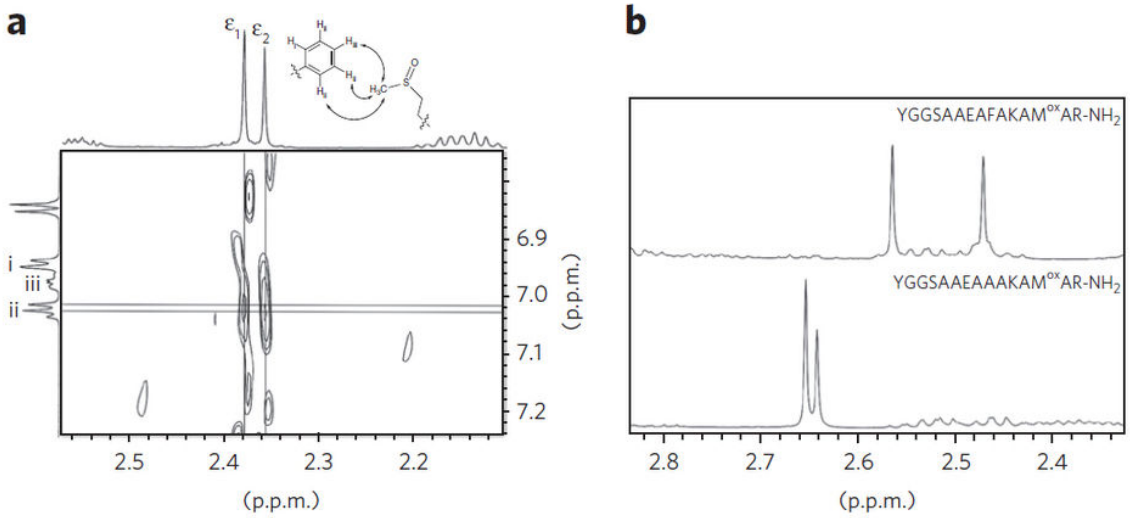

Figure 2.5 ^{1}H-^{1}H rotating frame Overhauser effect NMR spectroscopy (ROESY) and chemical shift analysis of α-helical peptide mixtures of two diasteriomers containing the *R* and *S* sulfoxide of methionine. (a) ^{1}H-^{1}H ROESY NMR spectroscopy correlating NOEs from the two diastereomeric ε-methyls (denoted ε_1 and ε_2) of oxomethionine to the aromatic resonances of phenylalanine. The strongest NOEs correlating with the aryl protons of the phenylalanine 'ii' are indicated by double-headed arrows. (b) Analysis of Phe-Met^{Ox} and Ala-Met^{Ox} ^{1}H NMR spectroscopy experiments indicating an upfield shift of the ε-methyl resonances of oxomethionine when an aromatic ring is present (top) relative to a methyl group (bottom).

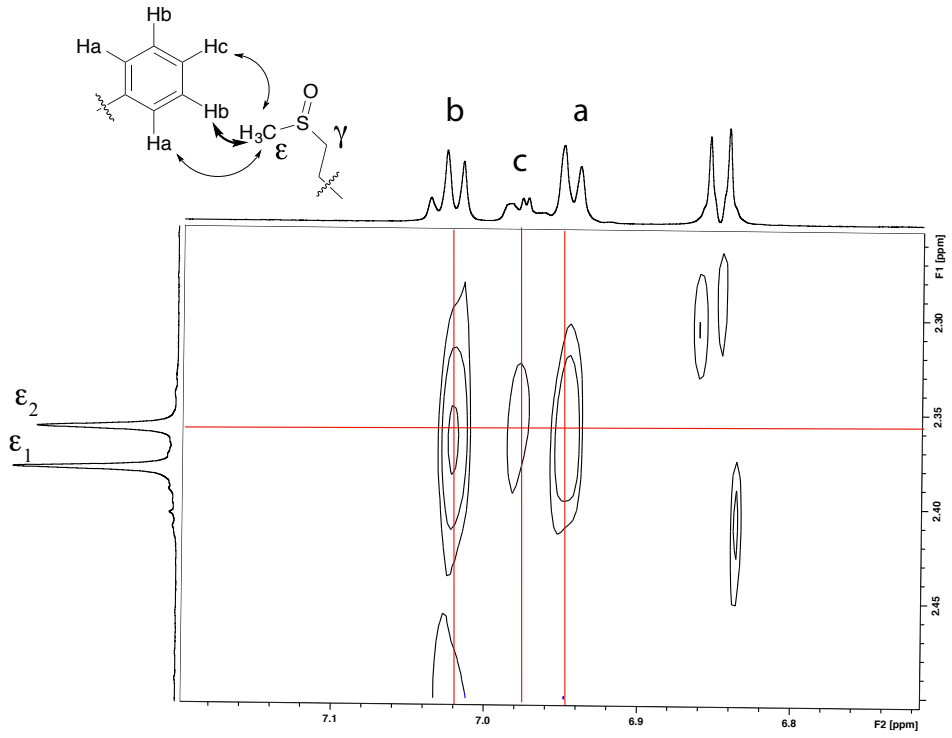

Figure 2.6 A close-up of the Phe-Met^{ox} ^{1}H-^{1}H ROESY NMR spectrum taken in acidic (pH 4.0) D_2O at 4^{o}C with reversed axis. NOEs shown between the ε-S-methyl sulfoxide diasteriomeric resonances and the aromatic protons of phenylalanine. The strongest NOEs are observed with Hb at the 3,5 position of phenylalanine. The upfield doublet is from one of the N-terminal tyrosine resonances.

To further probe the details of the sulfoxide-aromatic (S^{Ox}-Ar) interaction in the helical state, we compared the chemical shift of the ε-S-methyl groups on the sulfoxide-containing peptide when it was in an *i* +4 relationship with phenylalanine (Phe-Met^{Ox}) versus alanine (Ala-Met^{Ox}) in methanol. We purified oxidized peptides as a 1:1 mixture of diastereomers due to the new stereocenter from the sulfoxide. As such, we observed two singlets corresponding to the methyl group of each diastereomer (**Figure 3.9B**). DMSO methyl resonances in methanol have been reported at 2.65 p.p.m.[128] Similarly, in our measurements for Ala-Met^{Ox}, they were at 2.65 p.p.m. and 2.64 p.p.m. However, for Phe-

Met^{Ox}, we observed both ε-S-methyl resonances shifted upfield at 2.57 p.p.m.and 2.47 p.p.m. The chemical shift of the DMSO methyl resonances in benzene has also been shown to be upfield at 1.68 p.p.m.[128] Owing to ring-current shielding effects from aromatic rings, we interpreted these results to be consistent with the ε-S-methyl groups of oxomethionine approaching from above the aromatic ring of phenylalanine (**Figure 2.1 A, C**). Both the NOE experiments and chemical shift information indicated an interaction between the sulfoxide group over top of the aromatic ring.

We then used CD to measure the change in the strength of the S-Ar interaction upon methionine oxidation. Our experiments reproduced the original S-Ar result for Met-Phe (ΔG_{int} = 0.62 kcal/mol). The interaction strength was doubled (strengthened by 0.62 kcal/mol) upon methionine oxidation. Associated with this change in free energy, oxidation increased the enthalpy of the S-Ar interaction by 1.1 kcal/mol (**Figure 2.7**), consistent with the quantum result. We note that although CD spectra had been used in the original S-Ar study to extract energetics of side-chain interactions, it is not possible to draw a direct correlation between peptide helicity and free energy.[120,129] Rather, fitting of the CD spectra is necessary to extract energetics. Two aspects of our approach differed from the original study. First, we performed a double mutant cycle to isolate the methionine-aromatic interaction from possible interference owing to neighboring residues (**Figure 2.15** and **Figure 2.8**). This approach solidified our reported interaction free energies, and was especially important in the case of oxidized methionine because of the increased likelihood of hydrogen bonds and electrostatic interactions with the other residues in the peptide, **Figure 2.7**). We justified applying a two-state approximation and hence using the GHE by:

(i) observation of complete reversibility (overlap) in the heating and cooling curves (**Figure 2.10**), and (ii) the presence of a molar ellipticity isodichroic point in all constructs (**Figure 2.9**).[130] Additionally, principal component analysis[131] of the CD spectra yielded only two components that dominated the CD spectra (**Figure 2.11** and **Figure 2.6**), again consistent with the two-state assumption. Together with the addition of the double mutant cycle, the fact that we obtained nearly identical values for the Met-Phe energy as in the original study[107] (compare 0.62 ± 0.09 kcal/mol to 0.65 kcal/mol) reinforced the robustness of our approach. Thus, our peptide study lends experimental support to the conclusions drawn from the quantum calculations: oxidation increased the strength of the methionine-aromatic interaction.

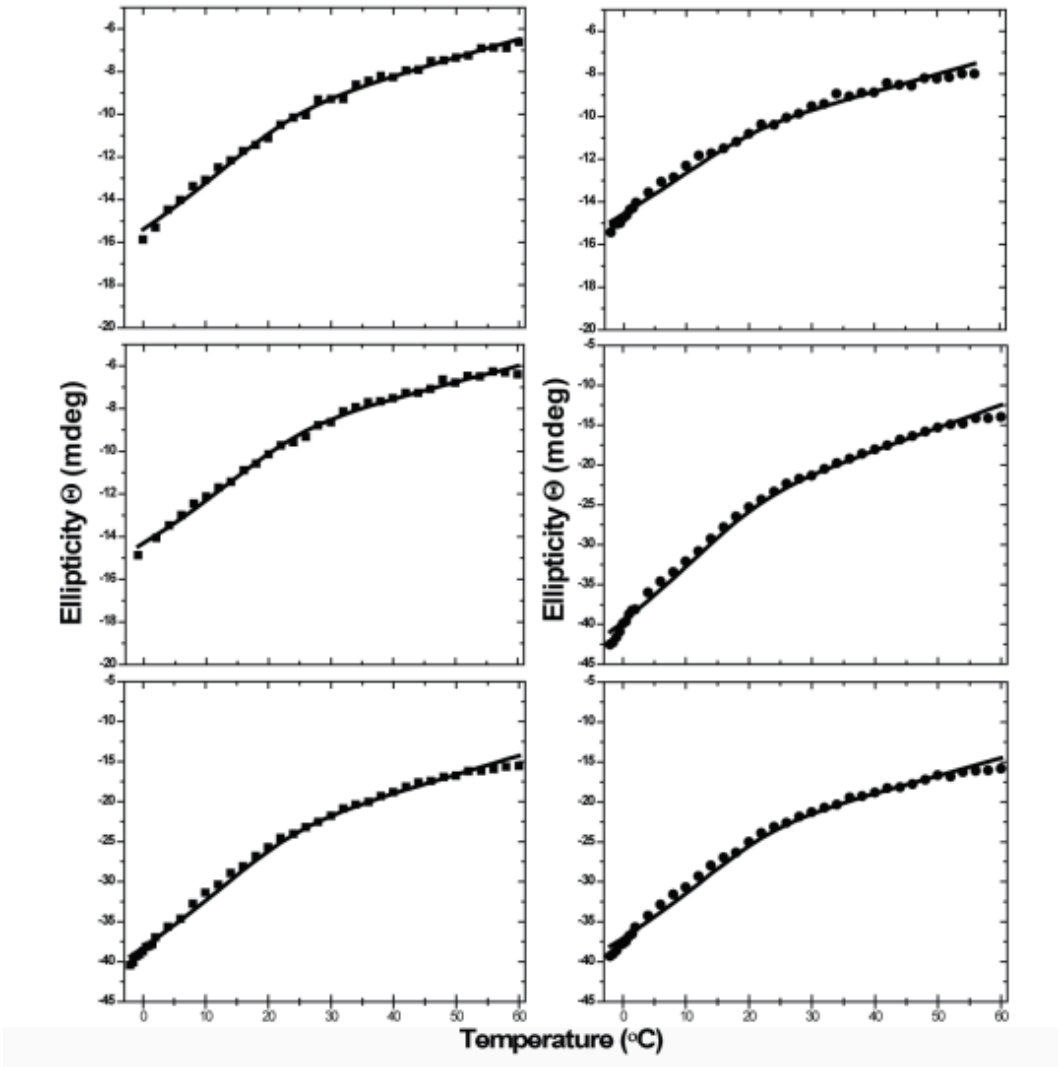

Figure 2.7 Representative data sets and global fits for three replicas of Phe-Met (Left, solid squares) and Phe-MetOx (Right, solid circles). Signal was acquired at 222nm. For each peptide, a black solid line represents the global fit to all three datasets using the Gibbs Helmholtz equation, as described in Methods. The fitting parameters are, for Phe-Met: $\Delta HTm = 26.0 \pm 0.7$ kcal/mol, $\Delta CP = 0.2 \pm 0.2$ kcal/mol°C and $Tm = 18.3 \pm 0.3$ °C; and for Phe-MetOx are: $\Delta HTm = 27.1 \pm 0.1$ kcal/mol, $\Delta CP = 0.21 \pm 0.02$ kcal/mol°C and $Tm = 21 \pm 1$°C were determined for Phe-MetOx peptide. Raw ellipticity signal varies for each peptide sample set due to variations in each individual peptide experiment (~150μM concentration). Free energy values were extracted from the global fit at T=0°C and are presented in **Figure 2.8**.

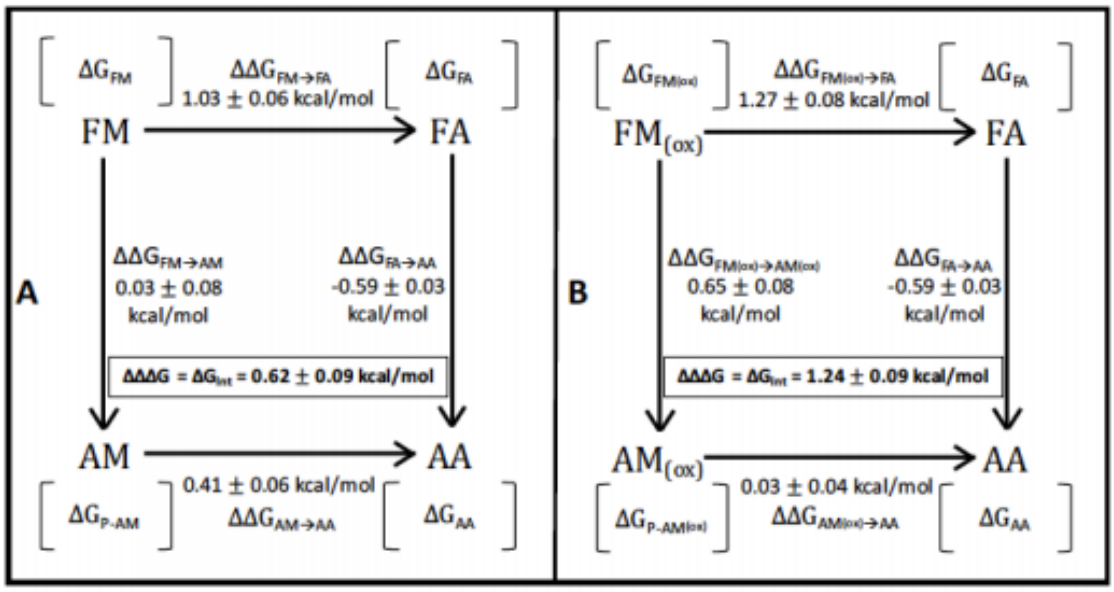

Figure 2.8 Double-mutant cycle. Thermodynamic double mutant cycle of FM (a) and FM(ox) (b) peptides. Nomenclature is: Wild-type peptide (FM and FM(ox)), singly mutated peptide (FA, AM and AM(ox)) and doubly mutated peptide (AA). F, M and A represent phenylalanine, methionine (un-oxidized or oxidized) and alanine, respectively. Free energy of each peptide denaturation is represented as ΔG at each step in the cycle. ΔΔG values are determined by the difference in ΔG denaturation values of peptides at 0°C, which were used to determine the ΔΔΔG. For simplicity, and as described in the Methods, we assign the nomenclature ΔGint to reflect the change in interaction free energy between Met/Phe and Met(ox)/Phe (SOx/Ar- S/Ar = 1.24 - 0.62 = 0.62 kcal/mol). Thus, there is a doubling of the strength of the interaction upon oxidation. Error was calculated through a total differential approach, where the derivatives of the GHE with respect to ΔH, ΔCp and Tm were calculated. The error for each thermal denaturation ΔG is the sum of the products of each derivative and their respective individual error values. Error was then calculated with ΔG values for each side of the thermodynamic cycle for ΔΔG and ΔGInt.

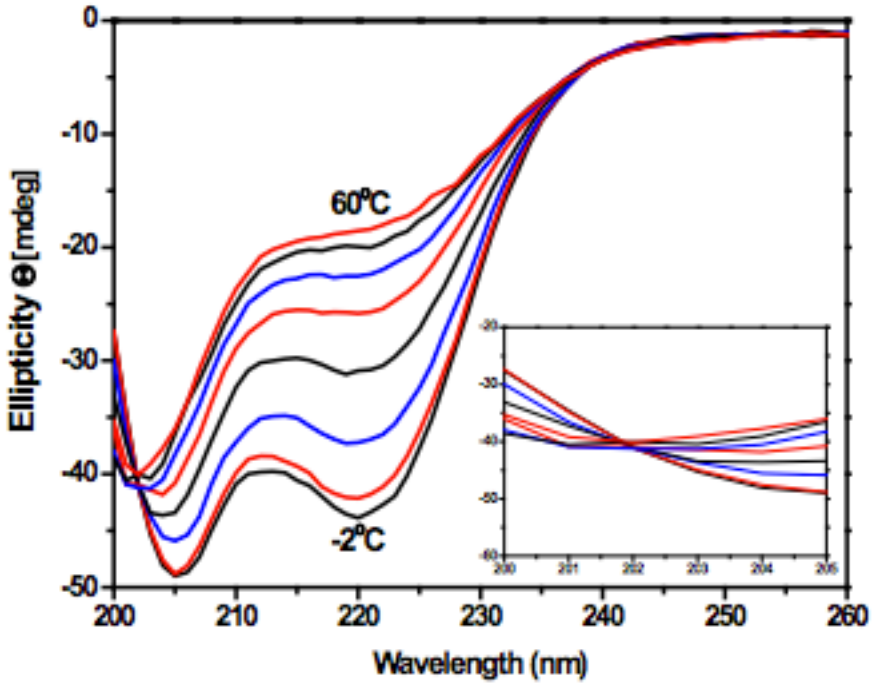

Figure 2.9 Combined Ala-Met spectra observed from 200 to 260nm at increasing temperatures from -2°C to 60°C. Crossing of all spectra at ~202 nm indicates isodichroic point seen in inset plot. This plot is representative of the all peptide constructs used in the double mutant cycle, where an isodichroic point is also observed.

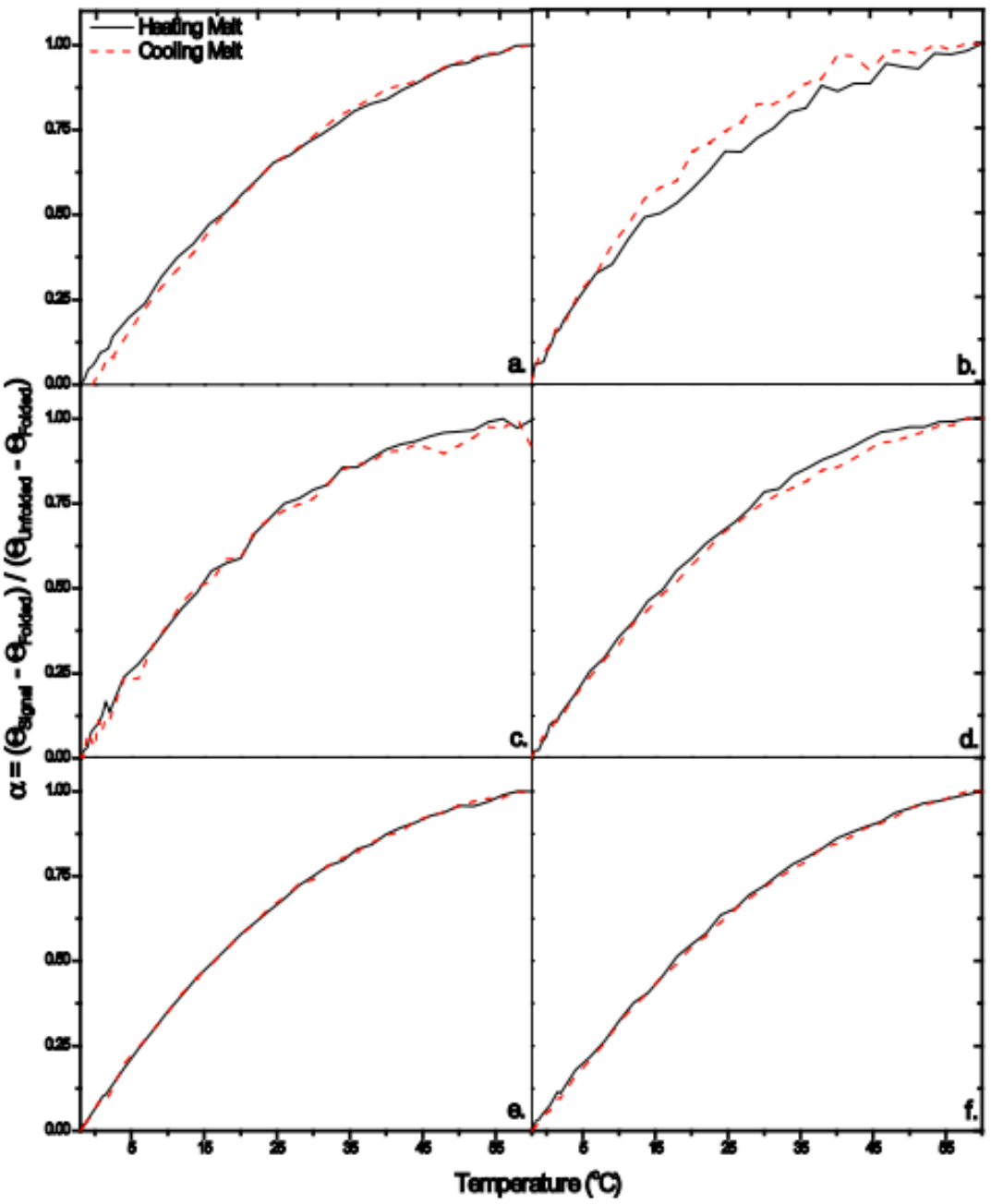

Figure 2.10 Overlaid heating and cooling melt curves for FM, FM^{Ox}, FA, AM, AM^{Ox} , and AA peptides. Raw Elliptical signal (mdeg) at 222nm was normalized from 0-1 for each peptide construct. Heating curves are represented by a black solid line, and cooling curves are represented by a red dashed line. Ellipticity displayed as a fraction of unfolded peptide. FM heating and cooling melt (a), FMOx heating and cooling melt (b), FA heating and cooling melt (c), AM heating and cooling melt (d), AMOx heating and cooling melt (e), and AA heating and cooling melt (f).

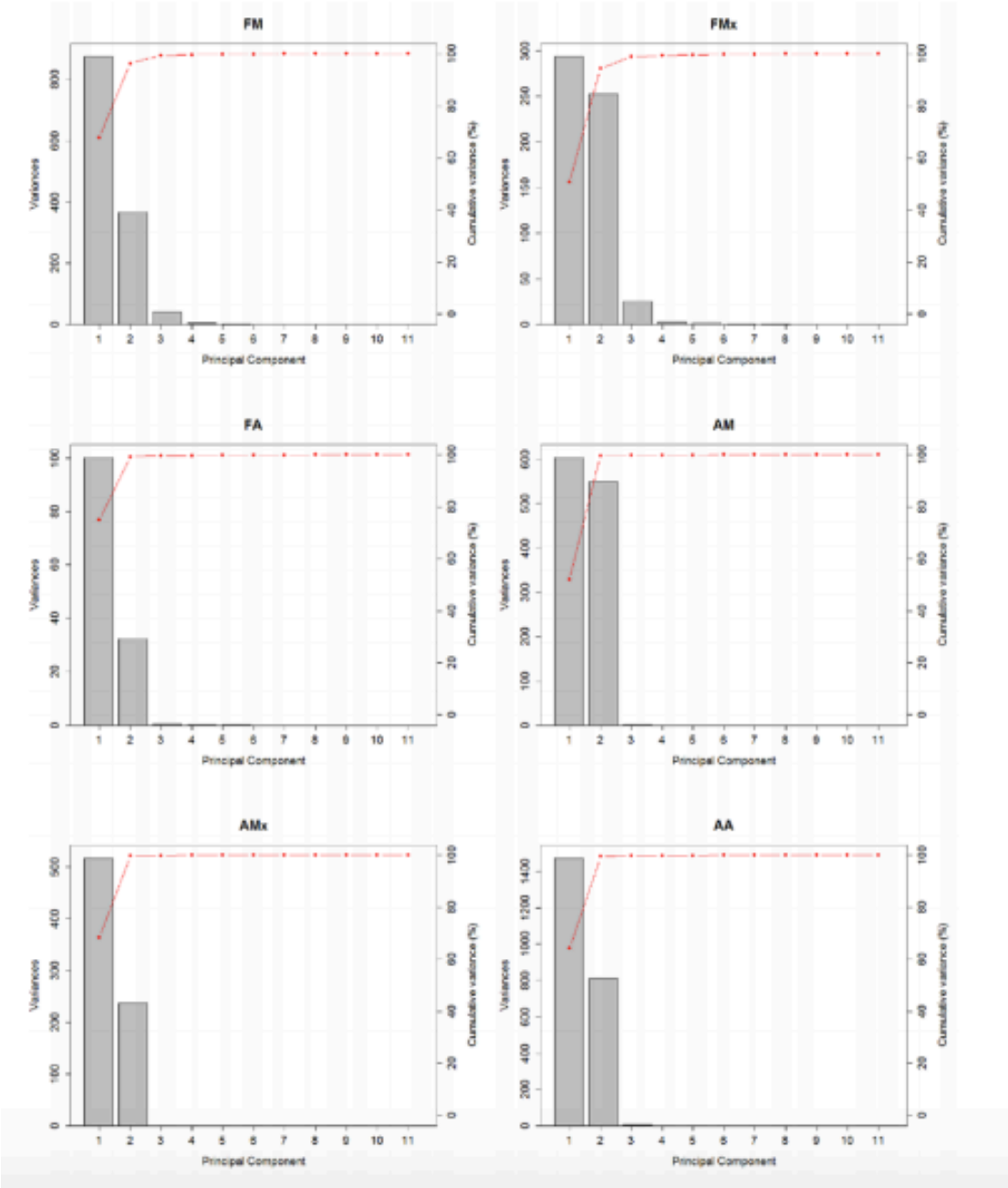

Figure 2.11 Principal Component Analysis. The variance for all principal components is shown as gray bars, and the cumulative percent variance is shown as red lines for all peptides.

Table 2.6 Principal Component Analysis. The details of PCA for each peptide are shown as standard deviations, proportion of variance, and cumulative proportion of variance.

FM	PC1	PC2	PC3	PC4	PC5	PC6	PC7	PC8	PC9	PC10	PC11
σ	29.55	19.16	6.30	1.99	1.40	0.85	0.62	0.59	0.37	0.27	0.00
Var Prop.	0.68	0.29	0.03	0.00	0.00	0.00	0.00	0.00	0.00	0.00	0.00
Cum. Prop.	0.68	0.96	0.99	1.00	1.00	1.00	1.00	1.00	1.00	1.00	1.00
FMx	PC1	PC2	PC3	PC4	PC5	PC6	PC7	PC8	PC9	PC10	PC11
σ	17.12	15.89	5.03	1.62	1.46	0.93	0.67	0.55	0.36	0.32	0.00
Var Prop.	0.51	0.44	0.04	0.00	0.00	0.00	0.00	0.00	0.00	0.00	0.00
Cum. Prop.	0.51	0.94	0.99	0.99	1.00	1.00	1.00	1.00	1.00	1.00	1.00
FA	PC1	PC2	PC3	PC4	PC5	PC6	PC7	PC8	PC9	PC10	PC11
σ	10.00	5.69	0.66	0.46	0.36	0.29	0.23	0.21	0.18	0.14	0.00
Var Prop.	0.75	0.24	0.00	0.00	0.00	0.00	0.00	0.00	0.00	0.00	0.00
Cum. Prop.	0.75	0.99	1.00	1.00	1.00	1.00	1.00	1.00	1.00	1.00	1.00
AM	PC1	PC2	PC3	PC4	PC5	PC6	PC7	PC8	PC9	PC10	PC11
σ	24.56	23.44	1.30	0.87	0.59	0.52	0.42	0.31	0.23	0.16	0.00
Var Prop.	0.52	0.48	0.00	0.00	0.00	0.00	0.00	0.00	0.00	0.00	0.00
Cum. Prop.	0.52	1.00	1.00	1.00	1.00	1.00	1.00	1.00	1.00	1.00	1.00
AMx	PC1	PC2	PC3	PC4	PC5	PC6	PC7	PC8	PC9	PC10	PC11
σ	22.72	15.39	0.65	0.39	0.36	0.25	0.21	0.20	0.12	0.12	0.00
Var Prop.	0.68	0.31	0.00	0.00	0.00	0.00	0.00	0.00	0.00	0.00	0.00
Cum. Prop.	0.68	1.00	1.00	1.00	1.00	1.00	1.00	1.00	1.00	1.00	1.00
AA	PC1	PC2	PC3	PC4	PC5	PC6	PC7	PC8	PC9	PC10	PC11
σ	38.38	28.45	2.60	1.19	1.07	0.80	0.47	0.42	0.27	0.19	0.00
Var Prop.	0.64	0.35	0.00	0.00	0.00	0.00	0.00	0.00	0.00	0.00	0.00
Cum. Prop.	0.64	1.00	1.00	1.00	1.00	1.00	1.00	1.00	1.00	1.00	1.00

2.7 **Oxidation rearranges Met-aromatic contacts in calmodulin**

To test the impact of the increased strength of the S^{Ox}-Ar motif in proteins, we first investigated the effects of methionine oxidation in an already well-characterized protein, CaM. The C-terminal helix of CaM has high methionine content and is sensitive to oxidative stress in vivo, which alters the protein's structure and function.[132–137] In the

crystal structures of CaM, both in its calcium-bound (halo, 3CLN)[138] and unbound (apo, 1CFD)[139] forms, a C-terminal methionine forms an S-Ar interaction with Phe141 (Met144 in apo (**Figure 2.12A**) and Met145 in halo). It has been speculated previously that oxidation at Met144 and Met145 might destabilize the protein by altering an important, nearby hydrogen bond between Tyr138 and Glu82 that connects the short C-terminal helix to the central linker.[135,140] No specific molecular mechanism for this effect has been proposed or tested.

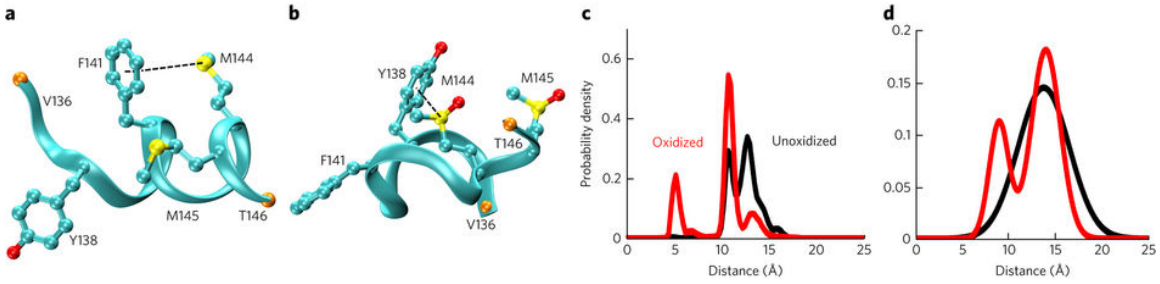

Figure 2.12 REMD simulations and EPR spectroscopy measurements of CaM. (a,b) Structure of unoxidized apo-CaM fragment (residues 136−146; PDB: 1CFD) where Phe141 interacts with Met144 (a) compared to a representative structure of the Tyr138 aromatic interacting with oxidized Met144 (b) from REMD simulations. (c,d) Distance distribution calculated between Cα atoms of Thr136 and Val146 from REMD simulations (c) and best-fit models of the distance distribution from dipolar EPR spectroscopy at submicromolar [Ca^{2+}] with maleimide spin labels at Cys residues 136 and 146 (d).

Based on our results above, one possibility is that oxidation of Met144 anMet145 increases the likelihood of an S^{Ox}-Ar interaction with Tyr138, which would be manifest in a spatial rearrangement within the C-terminal domain that should be observable by EPR spectroscopy. As Met144-Met145 and Tyr138 are on opposite ends of a short helix, such an interaction would require helical unwinding, an effect that has been observed using NMR spectroscopy.[141] We ran REMD simulations of the isolated, Ca^{2+}-free (apo) C-terminal peptide fragment (residues 136−146) of CaM to guide the design and

interpretation of experimental EPR spectroscopy measurements on full-length protein. We simulated both the unoxidized and doubly oxidized (at Met144 and Met145) forms. Because of the expectation of helical unwinding, a computational investigation of full-length CaM is hampered by limitations in sampling efficiency. Thus, although the peptide fragment is an abstraction of the real system, it is nevertheless a useful tool because it accelerates the sampling of relevant conformational space. Furthermore, the simulations were useful in (i) establishing Val136 and Thr146 as appropriate sites for spin labels to test the impact of oxidation on the full-length protein; and (ii) providing molecular-scale details unavailable from EPR spectroscopy experiments that correlate distance changes to the potential presence of an S^{Ox}-Ar motif.

In the simulation of the unoxidized peptide, an S-Ar interaction formed between Tyr138 and Met144 or Tyr138 and Met145 only 3.3% of the time. On the other hand, an S^{Ox}-Ar interaction formed 22.7% of the time when both Met144 and Met145 were oxidized (**Figure 2.12B** and Error! Reference source not found.). In only 1.2% of these interactions id a hydrogen bond form (**Figure 2.14**). The S^{Ox}-Ar interaction with Tyr138 led to a spatial rearrangement that brought together Val136 and Thr146 (**Figure 2.12B**), and the distribution of the distance between the Cα atoms of those two residues is shown in **Figure 2.12C**. Likewise, the frequency of the native interaction between Met144 and Phe141 also increased upon oxidation (49% versus 12% of frames; **Figure 2.12**). Thus, oxidation increased the total percentage of simulated frames in which an S-Ar interaction occurred by 3.7-fold (72% versus 15%). Based on Boltzmann's law, this change reflects a roughly 1.6 kcal/mol increase in the free energy of the interaction upon oxidation. This value

compares well to the results of our peptide experiment (0.62 kcal/mol) and supports the underlying conclusion of increased interaction strength upon oxidation of the S-Ar motif, even in the absence of hydrogen bonds. It is important to note that the simulations of the short, unoxidized peptide fragment sampled unfolded conformational states that were not represented by the crystal structure (where residues 138−146 are helical) and may not be accessible in a simulation of the full-length protein. Nonetheless, the emergence of a second population of states containing the S^{Ox}-Ar motif (with Tyr138), only in the oxidized simulation, motivated experiments to explore whether this subpopulation exists in the full-length protein when oxidized.

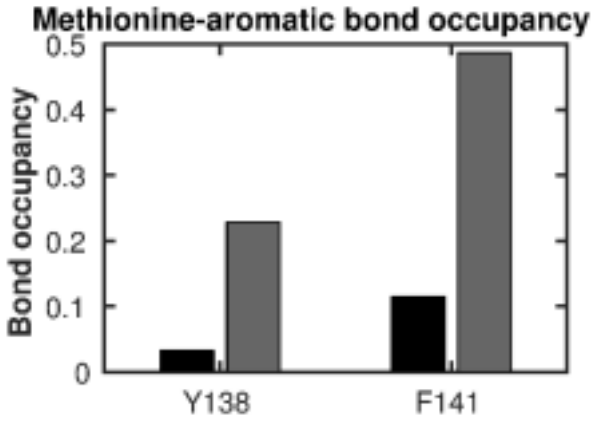

Figure 2.13 S/Ar interactions in CaM simulations. The fractional occupancy of the unoxidized (black) and oxidized (gray) methionine aromatic interaction involving either M144 or M145 from the REMD simulation.

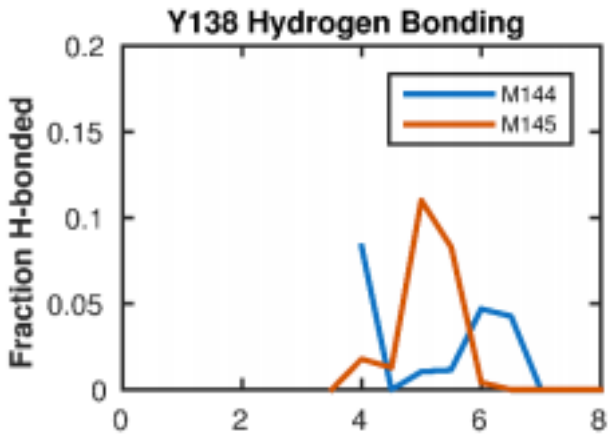

Figure 2.14 Hydrogen bonding of MOx144 and MOx145 with Y138 in the calmodulin simulations. The histogram shows that only a small fraction of Met-aromatic interactions involve a hydrogen bond. The methionine-aromatic distances were binned, and then the fraction of structures that were hydrogen bonded in each bin was plotted.

To test the effects of oxidation of CaM's C-terminal helix in the full-length protein, we used dipolar EPR spectroscopy to detect intramolecular structural perturbations at submicromolar [Ca^{2+}] (**Figure 2.12D**). The EPR spectrum of the unoxidized protein was best fit to a single broad Gaussian distance distribution, centered at 13.7 Å. After methionine oxidation, the data were best fit to a two-population model in which one population was centered at a similar distance to that observed in the absence of oxidation (14.0 Å), and there was a new population at shorter distance (8.9 Å). These experimental EPR spectroscopy results confirmed key predictions from MD simulations (**Figure 2.12C**): the long-distance population became narrower, and a new well-ordered short distance emerged. It is not surprising that the EPR spectroscopy distance distributions did not match precisely those predicted by MD simulation, as the MD simulations report distances

between Cα atoms, whereas EPR spectroscopy distances are between nitroxide groups at the ends of flexible side chains. EPR spectra do not directly detect Cα-Cα distances, but changes in such distances have been shown to correlate well with EPR data.[142] The convergence of the simulated and experimental results strongly suggests that upon oxidation of CaM, a new S^{Ox}-Ar interaction forms between either Met144 and Tyr138 or Met145 and Tyr138. Additional work is needed to definitively show that this minor component in the overall accessible conformational space (**Figure 2.12C, D**) is responsible for disruption of the Tyr138-Glu82 hydrogen bond and alters the protein's function.

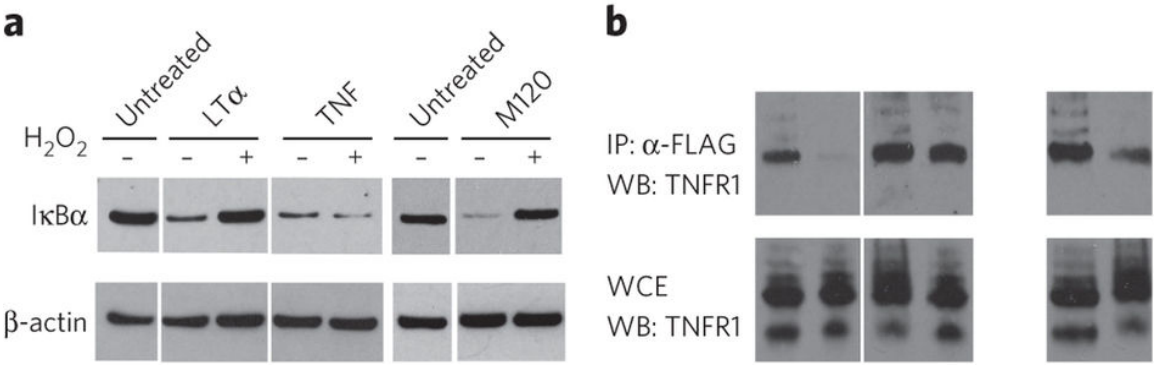

Figure 2.15 Oxidation of LTα, but not TNF ablated its interaction with TNFR1.(a) Western blot analysis of IκBα degradation in response to treatment with oxidized (+) and unoxidized (−) LTα and TNF. (b) Immunoprecipitation (IP) of TNFR1 with oxidized (+) and unoxidized (−) ligands. Western blots (WB) are representative of at least two independent experiments. Full gels are shown in **Figure 2.21**.

2.8 **Oxidation of LTα prevented ligand-receptor binding**

We investigated the effects of oxidation on the bioactivity and binding of LTα and TNF in live cells. We have previously shown that the interaction between LTα and TNFR1 is stabilized by a methionine-aromatic interaction via Met120 of LTα and Trp107 of TNFR1. Substitution of Met120 to alanine interrupts ligand binding, resulting in a more than tenfold loss in ligand function.[115] Thus, we hypothesized that the increased strength

of the S-Ar interaction upon oxidation should stabilize binding via the Met120-Trp107 interaction. Tumor necrosis factor (TNF) is structurally homologous to LTα and similarly activates TNFR1, but notably lacks methionine residues. Therefore, we expected its action to be unaffected by oxidative stress. Western blot analysis (**Figure 2.15A**) showed that untreated LTα and TNF efficiently induced downstream signaling, as has been definitively established. To our surprise, LTα pretreated with H_2O_2 did not induce IκBα degradation.

To isolate the impact of oxidation of Met120 on LTα function and binding, we substituted Met20 and Met133 to remove their susceptibility to oxidization. This mutant ligand, denoted here as Met120 or $Met^{Ox}120$ when oxidized, triggered IκBα degradation in the unoxidized form to the same extent as wild-type (indicating that two other substituted methionine residues, Met20 and Met133, were not important for activity). Site-specific oxidation ($Met^{Ox}120$) rendered LTα inactive (**Figure 2.15A**). Co-immunoprecipitation experiments explained this loss in function as a result of lost binding of the $Met^{Ox}120$ ligand to TNFR1 (Figure 2.15B). Thus, we concluded that oxidation of LTα inhibited its activity by disrupting the critical Met120-Trp107 methionine-aromatic interaction, thereby preventing binding to TNFR1.

To explore the molecular basis for this loss in binding, and to explain this apparent contradiction (decreased binding despite increased S-Ar interaction strength), we used molecular dynamics simulations and quantum calculations. Analysis of the ligand-receptor

crystal structure (1TNR) revealed aromatic residues in the ligand (Tyr96 and Tyr122) that are near to and on the same chain as Met120 (**Figure 2.16A**).

Given their spatial proximity, it is likely that Met120 forms S-Ar contacts with either or both of these tyrosines. MD simulations of the unbound ligand showed this to be the case in approximately 70% of the simulated frames (the Met120-Tyr122 interaction was approximately twice as frequent as the Met120-Tyr96 interaction (**Figure 2.16A**)). Oxidation of Met120 increased the interaction strength of Met120 with Tyr96; again, using the Boltzmann equation we calculated an increased affinity of 0.35 kcal/mol. This value is lower than that described above for CaM, but once again is consistent with our general conclusion that oxidation strengthens S-Ar interactions. There was no oxidation-induced change in the frequency of Met120-Tyr122 contacts. These data raise the possibility that Tyr122 and Tyr96 interact differently with Met120 under oxidative conditions. We confirmed that hydrogen bonding was not a major factor in the interaction (**Figure 2.17**). We again used the simulations to generate an ensemble of configurations for quantum energy calculations. As was the case with our calculations on the non-hydrogen-bonded

ensemble of DMS-phenol or DMSO-phenol configurations, oxidation increased the strength of the S-Ar interaction by 1−2 kcal/mol (**Figure 2.16**C).

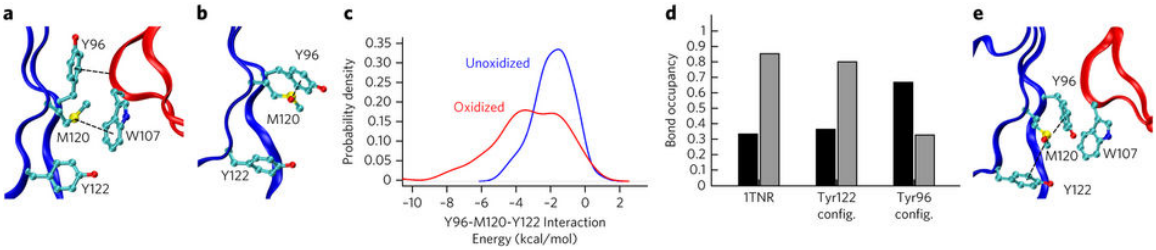

Figure 2.16 Molecular dynamics simulations of LTα with Met120 oxidized showed that competitive interaction of Met120 with Tyr96 prevented its interaction with Trp107. (a) In the receptor bound state, Tyr96 is folded upward so that it interacts with the backbone of the receptor, allowing Met120 to form a stable methionine-aromatic interaction with Trp107. (b) When Met120 is oxidized, it draws Tyr96 downward where it interferes with assembly of the ligand-receptor complex. (c) Interaction energy between Met120 and Tyr96 or Tyr122 calculated from 128 structures taken from the MD simulations. The histogram was smoothed with the Gaussian kernel smoothing function 'density' of the program R. (d) Bond occupancy of Met120 and Tyr96 or Tyr122 (black) and Met120-Trp107 (gray) interactions for the unmodified crystal structure (1TNR), the Met120-Tyr122 interacting configuration (Tyr122 config.), and the Met120-Tyr96 interacting configuration (Tyr96). (e) Snapshot of the Tyr96 interacting system with Tyr96 blocking the Met120-Trp107 interaction.

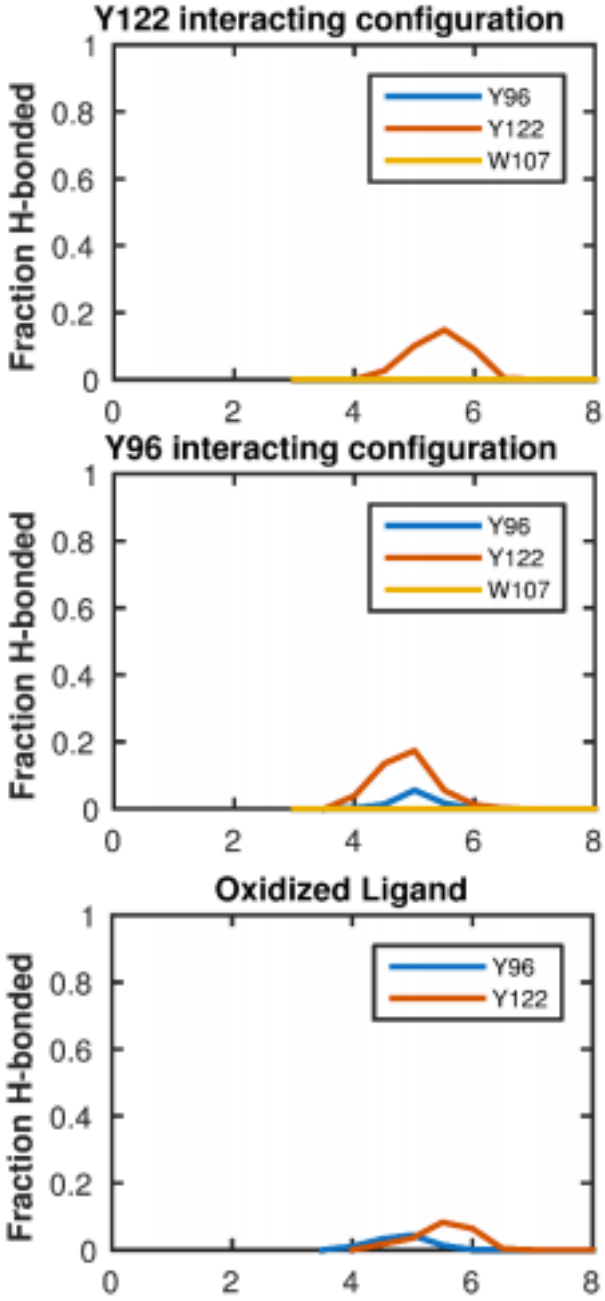

Figure 2.17 Hydrogen bonding in the molecular dynamics simulations of LTα. The fraction of frames in which hydrogen bonding occurs for the range of methioninearomatic distances. The methionine-aromatic distances were binned, then the fraction of structures that were hydrogen bonded in each bin were plotted. In all three simulations, the fraction of structures that are hydrogen bonded is small.

We hypothesized that the strengthened Met^{Ox}120-Tyr96 interaction could lock the ligand in a configuration that prevents Met^{Ox}120-Trp107 interaction, thereby interrupting binding. To test this, we first needed to test whether the addition of a sulfonyl oxygen to Met120 in the crystal structure binding configuration does not itself destabilize the binding pocket by steric overlap or electrostatic repulsion. We first simulated the unoxidized crystal structure of the ligand-receptor complex. In **Figure 2.16D** we highlight the stability of the Met120-Trp107 interaction, and show the infrequent instances of Met120 interaction with either Tyr122 or Tyr96. We then started a simulation of the ligand-receptor complex in a configuration in which the Met^{Ox}120-Tyr122 pair was pre-formed (using a configuration generated from the unbound ligand simulation). Tyr96 was allowed to remain in its receptor backbone binding position. The binding cavity organization reverted to that of the crystal structure configuration after 50 ns (**Figure 2.16D**) and was stable throughout the remainder of the simulation (**Figure 2.18**). Therefore, we concluded that loss of ligand-receptor binding was not caused by intrinsic steric clashes with Met^{Ox}120 that disrupt the binding pocket. We also concluded that Met^{Ox}120-Tyr122 interactions did not prevent Met^{Ox}120-Trp107 interactions and ligand binding.

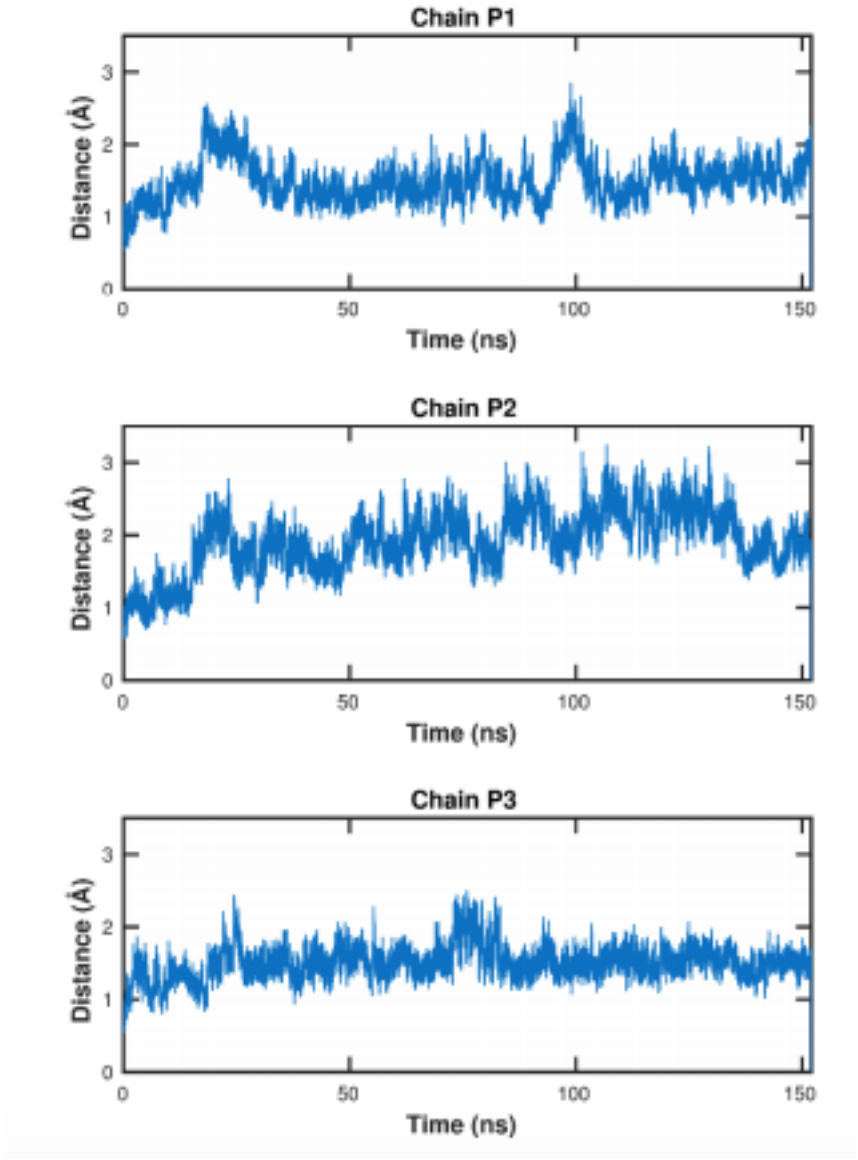

Figure 2.18 RMSD of the binding pocket for the MOx120-Y122 interacting configuration. The RMSD is shown for the binding pocket (all ligand and receptor residues within 15 Å of MOx120) for the 3 ligand chains. All three binding pockets are stable.

We then started a second oxidized ligand-receptor simulation, this time with a pre-formed Met^{Ox}120-Tyr96 pair. We observed two distinct effects of oxidation, both of which are consistent with loss of receptor binding. In two of the three chains (of the symmetric

ligand trimer), $Met^{Ox}120$ remained stably bound to Tyr96, preventing it from forming the critical S-Ar motif with Trp107 (**Figure 2.16D**) as well as preventing Tyr96 from binding the receptor backbone. In these cases, the $Met^{Ox}120$-Tyr96 pairing (**Figure 2.16E**), along with the surrounding binding pocket, remained stable throughout the simulation. In the remaining chain, Tyr96 released from $Met^{Ox}120$, and in this process disrupted the binding pocket while ejecting the receptor. Collectively, the results suggest that increased stability of the $Met^{Ox}120$-Tyr96 pair prevented the critical Met120-Trp107 interaction and destabilized the bound state.

2.9 **Discussion**

Oxidative stress has a prominent role in a number of normal and pathological biological functions. However, the precise chemical and physical mechanism through which oxidative modification of proteins influences their structures and functions is largely unknown. We showed that oxidation of methionine strengthened the methionine-aromatic interaction motif, independent of hydrogen bonding, by at least 0.5 kcal/mol and up to 1.5 kcal/mol. In the vast majority of instances in the PDB and CSD as well as the two proteins studied here in detail, the aromatic group did not form a stable hydrogen bond with the sulfoxide owing to solvation of both the donor and acceptor by water. Hydrogen bonding may enhance the interaction in hydrophobic and aprotic environments, but we did not observe that in our two test cases where the motif was solvent-exposed. In LTα-TNFR1 and CaM, we showed that competing interactions between methionine sulfoxide and nearby aromatic residues contributed to the modulation of protein structure and function.

To conclude, noncovalent interactions are the cornerstone of biological molecular recognition events. For bioactive small-molecule development, which exploits these interactions, sulfur is the third most commonly incorporated heteroatom in pharmaceuticals after nitrogen and oxygen.[143] The sulfoxide-aromatic interaction provides a new handle for tuning affinities of small molecules for chemical probe and therapeutic development as well as altering protein function. Moreover, the dynamic nature of methionine oxidation provides a reversible switch that can be used for introducing responsive molecules to changes in redox environment. The energy range of these altered interactions corresponded to a twofold to a tenfold change in the equilibrium constant, which together with the ambivalent character of sulfoxide functional groups, the dynamic nature of their formation, and their prevalence in biology and pharmaceutics, offers medicinal chemists and chemical biologists a useful tool to probe biological systems.

2.10 **Experimental**

2.11 **Structural bioinformatics analysis of the Protein Data Bank.**

We analyzed a nonredundant subset of the PDB, comprised of all structures containing at least one DMSO molecule using the Biopython toolset and a custom Python script adapted from our previous study.[115] Structures sharing >90% sequence identity were represented by a single structure with the highest score as ranked according to RCSB PDB quality factor algorithm. Redundant structures were excluded, as they do not represent truly independent data points for the purposes of our informatics study. Distances were defined between the DMSO sulfur and the center of the aromatic ring. Distance data were collected up to a cutoff of 20 Å. Hydrogen bonds were defined as having a heavy-atom donor to

sulfonyl oxygen distance of < 3.5 Å. For the radial density function (RDF), the distances from each DMSO to aromatic groups were binned, and the histogram was normalized by shell volume. Each RDF was normalized by the relative population of amino acids in the analyzed PDB files (divided by 9.25% for Phe, Tyr and Trp, by 22.47% for Leu, Ile, and Val, and by 100% for all standard amino acids). The resulting plots were normalized by the mean value at the long distance, non-interacting region of the 'all amino acids' RDF to shift the bulk density to 1 and to cast the *y* axis as an enrichment factor.

2.12 **Structural bioinformatics analysis of the Cambridge Structural Database.**

Searches were executed in the Conquest program of the CSD (version 5.35, 2014 release), and structural analyses were performed using the Mercury program (v 1.5). The distance was defined as in the PDB. C-CH_2-C was used as a noninteracting analog to C-S-C, following a previous CSD analysis.[115] The sulfur (or carbon in control) atom to aromatic distance was constrained to 0−10 Å. For the radial density function (RDF), the distances from each DMSO (or C-CH_2-C) to all aromatic groups were binned and divided by shell volume, then normalized by the total number of contacts. The resulting RDFs were shifted to 1 as in the PDB analysis, by normalizing to the value at the flat region of the C-CH_2-C RDF. A total of 20,630 DMSO-aromatic pairs were found in 840 structures, and 3,093,875 C-CH_2-C-aromatic pairs were found in 72,745 structures.

2.13 **Adaptive biasing force simulations of DMSO and aromatic groups in three solvents.**

Simulations were performed using the adaptive biasing force (ABF) module in NAMD 2.9 using the CHARMM 36 generalized force field. The ABF module was used so

that the system could overcome free-energy barriers and fully sample all conformational states. Parameters for DMS were adapted from those for ethylmethylsulfide. The distance between the DMSO thioether and the center of mass of the six-membered ring of phenol, or indole was used as the reaction coordinate of the mean force calculation. The system potential along the reaction coordinate was negated by the adaptive biasing force to simulate a flat free energy landscape. Each system was solvated in a ~45 $Å^3$ periodic box of TIP3P water, hexane or ethyl acetate, for a total of 18 systems. The adaptive biasing potential was applied between 2.5 Å and 14 Å with a bin width of 0.1 Å, and simulations were carried out for at least 7.5×10^6 steps. All other simulation parameters were set as in our traditional MD (see molecular dynamics simulations of LTα and TNFR1 methods). **Table 2.7** shows the effects of solvation on the calculated interaction energy between DMS or DMSO and each aromatic compound. The calculated PMF was not used in our analysis. **Figure 2.19** shows the distance between the aromatic ring and each heavy atom of the DMSO molecule and demonstrates no strong bias for the methyl groups to interact with the aromatic ring.

Table 2.7 Effects of solvation on quantum mechanical interaction energy. The effect of solvation on quantum mechanical interaction energies has been tested for the complex of benzene with DMS and DMSO. The interaction energy in kcal/mol for the complexes optimized in gas phase at the M06-2X level was calculated in the gas phase and with single point PCM calculations to describe the effect of solvation in EtOAc and water. The basis set employed was 6-311+G(d,p). The ΔEint entry shows that the effect of solvation is less than 0.4 kcal/mol.

	Gas	EtOAc	Water
DMS	-4.7	-3.9	-3.6
DMSO	-6.2	-5.1	-4.7
ΔE_{int}	-1.5	-1.2	-1.1

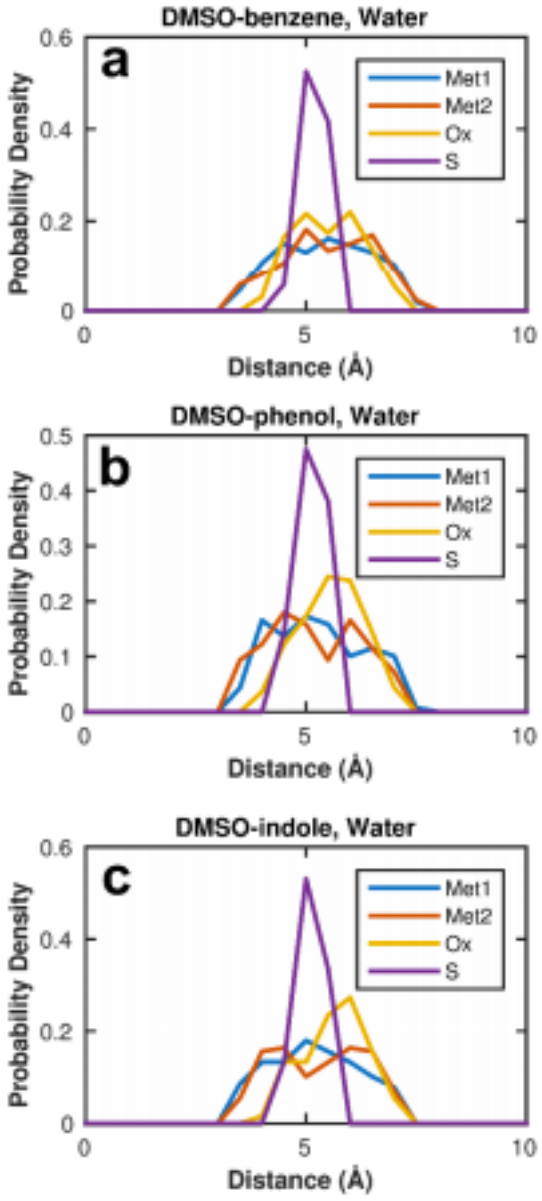

Figure 2.19 Histogram of distances from each DMSO atom to the center of the aromatic ring. Non-hydrogen-bonded DMSO-aromatic pairs from the ABF simulations were analyzed and show no strong bias for the methyl groups to interact with the aromatic ring. Benzene (a), phenol (b), and indole (c).

2.14 **Peptide synthesis.**

To study the appropriate pair sequences in a peptide chain, the unoxidized amino acid Met or oxidized Met was inserted into the designed sequence framework, producing:

(i)-Tyr-Gly-Gly-Ser-Ala-Ala-Glu-Ala-aromatic-Ala-Lys-Ala-Met-Ala-Arg-NH_2, (ii)-Tyr-Gly-Gly-Ser-Ala- Ala-Glu-Ala-aromatic-Ala-Lys-Ala-Met^{ox}-Ala-Arg-NH_2. The peptides were assembled on Fmoc-PAL-PEG-PS resin by Fmoc chemistry using a PE Biosystems Pioneer protein synthesis system. Single Met oxidation was accomplished by incorporation of Fmoc-Met^{ox}-OH during synthesis. Standard *N*-[(dimethylamino)-1*H*-1,2,3-triazolo[4,5-*b*]pyridin-1-ylmethylene]-*N*-methylmethanaminium hexafluorophosphate N-oxide (HA TU)/*N,N*- diisopropylethylamine (DIEA) (1/2.4 eq.) activation, in 1-methyl-2-pyrrolidinone (NMP), was applied. Fmoc deprotection was achieved with 20% piperidine in NMP. The final release of the peptides, with removal of the side-chain protecting groups, were accomplished by exposure of the peptide resin to 82.5% trifluoroacetic acid (TFA), 5% phenol, 5% thioanisol, 2.5% 1,2-ethanedithiol, 5% water (Reagent K). The peptides were precipitated with cold methyl-*t*-butyl ether, vortexed, centrifuged, decanted and dried over argon. The dried peptides were dissolved in degassed water and purified by high-performance liquid chromatography (HPLC) using a reversed-phase C8 HPLC column. Peptide elution was achieved with a linear gradient from 0 to 34% B (95% acetonitrile, 5% water and 0.1% TFA) in 40 min at a flow rate of 2.5 mL/min with detection at 280 nm using a System Gold Beckman Coulter system. The HPLC fractions were collected and analyzed by mass spectrometry (MS).

2.15 **Peptide scaffold design.**

The peptide scaffold used for defining the energetic impact of oxidation on Met-aromatic interaction had a number of specific design elements. The helical content was optimized to reside within a range that enabled sensitive detection of its change by CD.

The capping box motif at the N terminus is the sequence Ser/Thr-X-X-Glu/Gln and is a helix stop signal. This stop signal has Ser or Thr as the N-cap and a Glu or Gln residue at position $I + 3$, specifically; the sequence Ser-Ala-Ala-Glu is the capping motif in each of the peptides of the double mutant cycle. The N terminus had a tyrosine added for concentration determination. The C terminus was blocked by changing the COO^- to a $CONH_2$ to mediate this effect of dipole destabilization and to increase helical propensity.[144]

2.16 **Electrospray Ionization (ESI)-MS.**

The peptides were analyzed on a LC-MSD ion trap (Agilent). ESI-MS spectra were acquired in positive ion mode. The solvent contained 40% acetonitrile and 0.1% formic acid. 10 to 30 µL sample were directly injected at a flow rate of 10 µL/min with a source temperature of 300 °C. The applied spray voltage was 3,500 V, and the skimmer voltage, 40 V. MS scans were acquired over an *m/z* range of 200 to 2,000. The scan for the native mass 1,499.69 Da of the sequence Tyr-Gly-Gly-Ser-Ala-Ala-Glu-Ala-Phe-Ala-Lys-Ala-Met-Ala-Arg, showed the single charged ion with *m/z*1,500.0 and the double charged ion *m/z* 750.7. The scan for the Met^{Ox}-Phe sequence pair (1,515.69 Da) showed the singly charged ion with *m/z* of 1,515.7, the double charged ion *m/z* of 758.4, and the triple charged ion *m/z* of 505.9. The observed masses for the respective molecular ions agreed with the theoretical peptide scaffold design.

2.17 **Circular dichroism spectroscopy.**

All peptides were stored in tetrafluoroethylene (TFE) after synthesis, which was removed by evaporation using nitrogen gas before use. To ensure complete removal of the TFE, the sample was then put under vacuum for one hour. The dried peptide was

reconstituted in 10 mM KH_2PO_4, 100 mM KCl at pH 7.5, and prepared for CD data collection. All CD experiments were performed on a Jasco J-815 CD Spectrometer using a 0.1 cm quartz cuvette at ~150 μM peptide concentration. Concentrations of the peptide samples were determined using a Nanodrop spectrometer. To display helical content and the presence of an isodichroic point ellipticity was measured between 200 nm to 260 nm in 1-nm increments from −2 °C to 60 °C for the Phe-Met, Phe-Met^{Ox}, Phe-Ala, Ala-Met, Ala-Met^{Ox} and Ala-Ala peptides. Once these characteristics were established for each construct, one data point was collected at 222 nm at each 0.5 °C or 2 °C change as temperature increased from −2 °C to 60 °C. Cooling melts were also collected, recording the signal at 222 nm, on all peptides as temperature decreased from 60 °C to −2 °C. All collected data points were averaged from three acquisitions of the recorded ellipticity.

2.18 **Analysis of CD data.**

To extract the free energy of interaction from the temperature dependence of the CD, spectra were collected from the lowest experimentally accessible temperature (−2 °C) to a temperature beyond which there were no observable changes in spectral shape for all peptides (60 °C). The spectra are given in **Figure 2.9.** Following Greenfield et al.,[145] we used the signal, Θ, at 222 nm to report on changes in peptide structure. This wavelength was chosen because it reflects helical content and is also the wavelength at which the overall change in ellipticity is greatest across the temperature ramp. Following the same rationale we used previously,[146] the CD signal is given by:

$$\Theta=(\Theta_{\text{initial}}+K\Theta_{\text{final}})/(1+K) \qquad (3)$$

where $\Theta_{initial}$ is the value at 222 nm recorded at −2 °C, and Θ_{final} is the value at 222 nm recorded at 60 °C. Because $K = e^{-\delta G/RT}$, we rewrote this equation as:

$$\Theta_T = (\Theta_{initial} + e^{-\frac{\Delta G}{RT}}\Theta_{final})/(1 + e^{-\frac{\Delta G}{RT}}), \quad (4)$$

We then fit the temperature dependent data, Θ_T, by substituting the Gibbs-Helmholtz equation into equation (4),

$$\Delta G = \Delta H_{Tm}\left(1 - \frac{T}{T_m}\right) + \Delta C_p\left(T - T_m - T\left(\ln\left(\frac{T}{T_m}\right)\right)\right) \quad (5)$$

and varying the three parameters: enthalpy (ΔH_{Tm}), heat capacity change (ΔC_p), and transition temperature (T_m). Data for Phe-Met and Phe-Met^{ox} are given for each replica in **Figure 2.7**. By varying the concentrations of the peptide in each of its three replicates, the measured signal varies for each replica. The three replicates are globally fit simultaneously, an approach that improves the stringency of the parameter fits for each peptide. The free energy is then extracted from the fit at the desired temperature (T = 0 °C in this case). The change in free energy for each leg of the double mutant cycle is reported in **Figure 2.8**.

2.19 **Double mutant cycle.**

To construct a double mutant cycle, peptides were synthesized in which the aromatic residue and Met (or Met^{Ox}) was replaced first individually, then concurrently by the neutral residue, Ala. The difference in ΔG between the Met-aromatic (oxidized or unoxidized) and its respective singly substituted construct, or between the singly

substituted construct and the doubly mutated construct gives a $\Delta\Delta G$. The difference of the respective $\Delta\Delta G$ values produces a $\Delta\Delta\Delta G$, which indicates whether the specific interaction is contributing to the stabilization of structure. $\Delta\Delta\Delta G$ is simplified here as ΔG_{int} to match the free energy of interaction reported (the two expressions are thermodynamically equivalent, although the cited study did not use a double mutant cycle).[120] If ΔG_{int} equals zero, the interaction observed is not contributing to the structural stability; if greater than zero, the interaction is stabilizing; and if less than zero, destabilizing.[147–149]

2.20 **Principal component analysis.**

Principal component analysis for each of the Phe-Met, Phe-Met^{Ox}, Phe-Ala, Ala-Met, Ala-Met^{Ox}, and Ala-Ala peptides data sets was carried out with the 'prcomp' function of the program R (v. 3.2.1). For each data set only one of the three replicates was used. To increase the sensitivity of the analysis, we focused on the isodichroic point region by analyzing only the wavelengths between 200 nm and 210 nm (11 data points), while the entire temperature range was included in the analysis. The correlation matrix was calculated between the mean-centered vectors of wavelengths:

$$C_{ij} = T_i(\lambda_1, \lambda_2, \ldots, \lambda_N) \cdot T_j(\lambda_1, \lambda_2, \ldots, \lambda_N)$$

where C_{ij} is the covariance between the temperatures i and j, and $T_i(\lambda_1,\lambda_2,...,\lambda_N)$is the vector of absorbances at the temperature i at the wavelengths $\lambda_1,\lambda_2,...,\lambda_N$.

The results reported in **Figure 2.11** and **Table 2.6** show that the first two principal components describe 94% or more of the total variance, which is consistent with the assumption that the change in molar ellipticity is dominated by only two sources of signal.

2.21 **NMR spectroscopy experiments.**

Concentrations of peptide samples were obtained using ultraviolet absorbance of tyrosine (ε = 1,450 L mol^{-1} cm^{-1}) in 8 M urea. Peptide Tyr-Met^{Ox} (YGGSAAEAFAKAM(ox)AR-NH_2) was dissolved in deuterated methanol (3 mM). Phe-Met^{Ox} (YGGSAAEAFAKAM(ox)AR-NH_2) was dissolved in acidic (pH 3.5) D_2O, taken at 4 °C. ^1H-^1H ROESY experiments (mixing time = 200 ms) were performed on a Bruker 700 MHz spectrometer with a CryoProbe: 5 mm TXI probe of *z*-axis gradient. ^1H experiments comparing control peptide, Ala-Met^{Ox} to Phe-Met^{Ox} in MeOD were performed on a Bruker Advance III HD 500 MHz instrument with a 5 mm Prodigy TCI cryoprobe with *z*-axis gradients. Data were processed and analyzed using Bruker Topspin 3.2.

2.22 **Dipolar EPR spectroscopy of spin-labeled calmodulin.**

A mutant, encoding mammalian CaM with Val136 and Thr146 both substituted to Cys, was prepared by site-directed mutagenesis (QuikChange II kit, Agilent), confirmed by DNA sequencing, expressed and purified as described previously,[150] and dialyzed overnight at 4 °C against 10 mM NaCl and 10 mM Tris (pH 7.0). Spin-labeling with maleimide spin label (MSL, N-(1-oxyl-2,2,5,5-tetramethyl pyrrolidinyl) maleimide, Toronto Research Chemicals) was carried out by incubating 120 μM CaM with 480 μM MSL in CaM buffer (10 mM NaCl, 10 mM Tris, 5 mM EGTA, pH 7.0) for two hours at 22 °C (followed by overnight dialysis against CaM buffer to remove unreacted label), resulting in complete labeling of the two Cys residues, as shown by MS. To oxidize methionine side chains, spin-labeled CaM was incubated in 500 mM hydrogen peroxide for 30 min, followed by dialysis into CaM buffer. As shown previously under similar

conditions,[150] MS was used to verify that all of the nine methionine residues of CaM were oxidized. X-band (9.5 GHz) EPR spectra of 200 μM CaM (in CaM buffer plus 10% glycerol) were acquired at 200K with a Bruker ER500 spectrometer, using 1 G modulation amplitude and subsaturating microwave power (0.63 mW). EPR spectra were analyzed to determine the distribution of distances between the two spin labels, as described previously.[151]

2.23 **Ligand preparation and treatment.**

Plasmids with sequence encoding human LTα and human TNF with an N-terminal FLAG tag, downstream from an inducible T7 promoter were subcloned using standard cloning techniques. Plasmids were transformed into chemically competent BL21 bacteria, plated on LB agar plates, and cultured in LB to an OD_{600} of ~0.5. Cultures were then cooled to 18 °C, induced with 0.5 mM isopropyl β-D-1-thiogalactopyranoside, and grown for 18 h. The bacteria suspension was centrifuged, and then lysed by sonication in ice-cold PBS. The lysate was column purified using anti-FLAG M2 Affinity Gel (Sigma) according to the manufacturer protocol, dialyzed exhaustively against MilliQ H_2O, and then lyophilized. FLAG-LTα, as prepared in our laboratory, contained four methionine residues, of which Met120 and Met133 potentially play structural and functional roles in the ligand-receptor complex. Met133 is buried between two folds of a β-sheet, and its precise functional role, if any, has not been established. For the LTα-Met120 variant, we substituted Met133 to valine and Met20 to alanine to match the homologous residues found in *Bos taurus*LTα, which shares 73% sequence identity and 81% sequence similarity (Sequence Manipulation

Suite), but lacks methionines except for its N terminus. TNF, which also binds to and activates TNFR1 with similar potency[152] was used as a control.

Oxidative stress was applied by dissolving 8 μg of ligand in buffer containing 10 mM HEPES, 100 mM KCl, 1 mM MgCl, 1 mM CaCl, then adding 100 mM H_2O_2 to a total volume of 100 μL. The oxidation reaction was allowed to proceed for 18 h at room temperature, then stopped by removing H_2O_2 in two sequential stages using Zeba 7 kDa molecular weight cutoff spin columns. Removal of H_2O_2 was confirmed by Amplex red assay, and the residual concentration of $H_2O_2$was determined as insufficient to induce autophagy. We measured tryptophan fluorescence to confirm that oxidation does not lead to gross unfolding of LTα, finding no shift in the emission spectrum when excited at 280 nm (**Figure 2.20**).

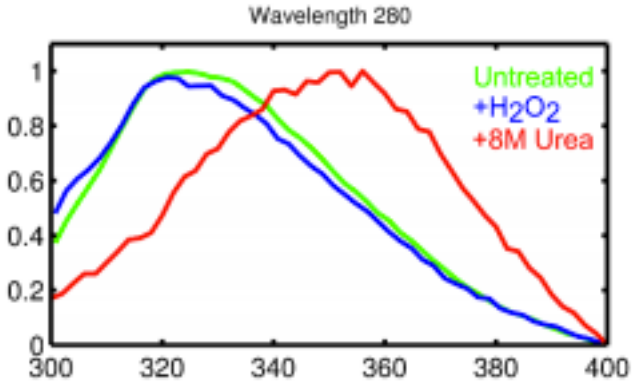

Figure 2.20 Tryptophan fluorescence of LTα after exposure to oxidative stress. LTα was left untreated or oxidized as in cell experiments, and its fluorescence emission spectrum was measured after ~18 hours. The unfolded control sample was dissolved in 8M urea for several hours before measuring its emission spectrum. Fluorescence emission wavelength scans from 300 – 400 nm were taken on a Varian Cary Eclipse Fluorescence spectrometer at an excitation wavelength of 280 nm and a scan rate of 30 nm/min. Excitation and emission slits were set to 5 nm. The emission spectra were normalized between 0 and 1. Total unfolding in 8M urea causes tryptophan residues to become exposed to polar solvent, resulting in a red-shifted emission spectrum (red). Exposure of LTα to oxidative stress does not result in red-shifting of the emission spectrum (blue) compared with the untreated LTα spectrum (green), indicating that the ligand is stably folded.

2.24 **Western blot analysis of IκBα.**

HEK 293 cells were maintained in DMEM supplemented with 10% FBS, penicillin/streptomycin, and 2 mM L-glutamine. Confluent cells were split at 1:12 into 6-well plates and used for experiments on day 3. Untreated and oxidized ligands were added to cells to final concentrations of 200 ng/mL and 20 ng/mL for LTα and TNF respectively, and incubated for 20 min at 37 °C. Cells were then washed once and gently sheared from the plate with ice-cold PBS, then centrifuged and resuspended in radioimmunoprecipitation assay (RIPA) lysis buffer. Cell lysates were normalized to equal protein concentrations, and 60 μg were loaded onto 4–12% Bis-Tris gradient gels for western blot analysis. IκBα was detected rabbit α-IκBα (Cell Signaling Technology, #9242, 1:1,000) and

horseradish peroxidase (HRP)-conjugated α-rabbit IgG (Amersham, 1:10,000). Full gels are shown in **Figure 2.21**.

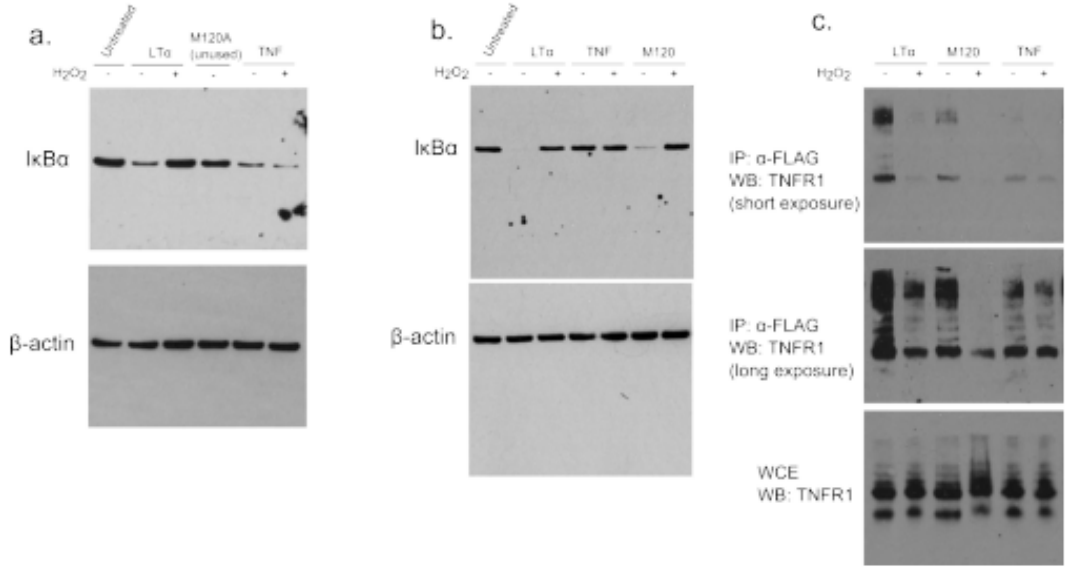

Figure 2.21 Full gels from Western Blots and immunoprecipitation. IκBα degradation is induced by unoxidized LTα and unoxidized or oxidized TNF. Oxidation of LTα prevents it from inducing IκBα degradation. M120A is a reduced-binding mutant negative control and was not the subject of this investigation (a). A second iteration of the same experiment is shown with the M120 control (b). The full immunoprecipitation blots are shown with short and long exposure times (c).

2.25 **Co-immunoprecipitation.**

Co-immunoprecipitation was performed using anti-FLAG M2 agarose beads (Invitrogen) according to the manufacturer instructions. Briefly, HEK 293 cells were split at 1:12 into 15-cm plates and transfected with 8 μg of plasmid encoding TNFR1 (pCMV6-XL5-TNFR1) on day 1 by calcium phosphate transfection. On day 3, cells were lifted by shearing, washed once, and resuspended in ice-cold PBS at ~10^6/mL. LTα and TNF were added at 12 ng/mL and 25 ng/mL respectively, and the cells were incubated for 30 min at

4 °C while rocking. Cells were then washed three times in ice-cold PBS and resuspended in RIPA lysis buffer, then analyzed by western blot. TNFR1 was detected using rabbit α-TNFR1 (Abcam, ab19139, 1:1,000) and α-rabbit secondary, as described above. Full gels are shown in Figure 2.21.

2.26 **Quantum calculations.**

The interaction energy between model compounds was investigated with quantum mechanical calculations performed in the gas phase. The reduced and oxidized states of methionine were modeled by DMS and DMSO, respectively; the side chains of phenylalanine, tyrosine and tryptophan were modeled by benzene, phenol and indole. The interaction energy between compounds *A* and *B* was defined as:

$$E(AB)_{\text{int}} = E(AB)_{\text{complex}} - E(A) - E(B) \qquad (1)$$

All energies were obtained from fully unrestrained structure optimizations carried out with Gaussian 09[153] using the Møller-Plesset perturbation theory at the second order (MP2) method with the 6-311+G(d,p) basis set and corrected for basis set superposition error.[154] Additional data computed using the M06-2X density functional theory[155] are reported in **Table 2.1**. These two levels of calculation were chosen because we previously showed that they bracket the interaction energy calculated at the couple-cluster truncated at single and double excitations with triple excitations added perturbatively (CCSD(T)) level[115] with the 6-311+G(d,p) basis set.[115] Notice that for each complex several minima were characterized, and the data are reported only for the lowest energy one.

The dispersion energy contribution to the complex formation was calculated by taking the difference between the interaction energy (equation (1)) computed at the MP2 and Hartree-Fock (HF) levels.[115] In both cases the same basis set was used, and the HF energies were calculated as single point on the MP2 optimized structures.

The effect that the variety of conformations adopted in solution has on the interaction energy was investigated by averaging the interaction energies of 128 structures randomly sampled from the minimum (sulfur-aromatic distance between 4 Å and 6 Å) of the ABF simulations in ethyl acetate described above. Hydrogen bonded structures were defined as having donor-acceptor distance of <2.5 Å and non-hydrogen-bonded structures had a donor-acceptor distance of >4 Å. Upon removal of the solvent, the instantaneous interaction energy was calculated at the MP2/aug-cc-pVDZ level using equation (1) without any additional structure optimization.

A similar procedure was used to investigate the interaction energy between the side chains of Met120, Tyr96 and Tyr122 in LTα. From the MD simulations described below, 128 structures were randomly selected and the average interaction energy calculated at the MP2/aug-cc-pVDZ level as:

$$E\left(Met120\ Tyr96\ Tyr122\right)_{\text{int}} = E\left(Met120\ Tyr96\ Tyr122\right)_{\text{complex}} - E(Met120) - E\left(Tyr96\right) - E(Tyr122) \quad (6)$$

The side chains were truncated at the C_β-C_γ bond and the missing valence was saturated with a hydrogen atom. Upon removal of the rest of the protein and the solvent and without any further optimization, the interaction energy was calculated at the MP2/aug-cc-pVDZ level and corrected for the basis set superposition error.

For the calculations on the ethyl acetate simulations described above, the NBO[156] charges were calculated and averaged over all 128 structures. The NBO localization scheme was tested along Mulliken[157] localization over a number of different basis sets of increasing size. Because the results showed a strong dependence of the Mulliken charges on the basis set size[158] whereas NBO charges did not, the NBO localization scheme was preferred.

2.27 **Replica-exchange molecular dynamics of calmodulin.**

The REMD simulation was performed in NAMD 2.9 using the CHARMM22 potential parameters.[159] Eleven residues of the last helix (136−146) of CaM (PDB ID: 3CLN)[138] were used in the all-atom point-charge force field *in vacuo* to match conditions of the quantum calculations. Eight replicas with temperatures exponentially spaced from 300K to 600K (300K, 331.23K, 365.7K, 403.77K, 445.8K, 492.2K, 543.43K, 600K) were used with the initial velocities of the atoms generated by the Maxwell-Boltzmann distribution and a timestep of 1 fs. The first 10^6 steps were performed without attempting exchanges to equilibrate, then exchanges were attempted every 1,000 steps (1 ps) with an acceptance rate ~20%. Coordinates were taken every 100,000 steps (100 ps). 78,810 frames were taken for the unoxidized peptide and 74,400 frames for the oxidized peptide, corresponding to a total simulation time per replica of 985 and 930 ns, respectively. Only

the replicas at 300 K were used in the analysis. Methionine-aromatic interactions were identified as having a distance of <7 Å and an angle less than 60°, consistent with previous definitions.[115,116] Hydrogen bonds were cutoff at <2.5 Å from hydrogen to acceptor.

2.28 **Molecular dynamics simulations of LTα and TNFR1.**

We carried out molecular dynamics simulations of oxidized or unoxidized LTα in its unbound state and unoxidized in complex with TNFR1 using the structure, 1TNR as the starting configuration.[160] Two additional systems, a Tyr122 interacting configuration and a Tyr96 interacting configuration, were constructed in which Met120 began bound to Tyr122 or Tyr96, respectively, whereas all other residues in the 1TNR crystal structure were left essentially unchanged (minor manipulation and steepest descent minimization was required to resolve overlap in the binding pocket). The starting configurations of Met120, Tyr96 and Tyr122 in these systems were taken from the oxidized ligand simulation. Each system was solvated in a box of at least 40,000 explicit water molecules modeled as TIP3P to fully capture solvation effects[161] and the charge was neutralized by adding K^+ and Cl^- ions. The isothermal-isobaric (NPT) ensemble was used along with the CHARMM36 force field[162–164] at a temperature of 303K and 1 atm pressure, which were maintained using the Langevin piston and Nosé-Hoover[165] algorithms. Parameters for Met^{Ox} were provided by K. Kuczera[166] and adapted for use in the CHARMM36 force field. Long-range electrostatics were calculated using the particle mesh Ewald method[167] with a 1.5 Å grid spacing and fourth order interpolation. Lennard-Jones interactions were switched off at a cutoff distance of 10 Å. Each system (except the Tyr96 and Tyr122 interacting configurations) was minimized using NAMD 2.8[159] for 1,000 steps, then

equilibrated with Cα harmonic constraints of 1, 0.1, and 0.01 kcal/mol Å^2 for 2 ns at each stage. Dynamic trajectories were propagated with the r-RESPA algorithm[168] with a 2 fs time step and the RATTLE algorithm[169] was applied to all covalent bonds involving hydrogen. The ligand-receptor system was simulated for ~35 ns and distance and angle analyses were averaged over the entire trajectory. The ligand-only systems were simulated for a total of ~430 ns. The first 150 ns (including relaxation) were excluded from structural analyses to allow re-equilibration of the ligand after removal of the receptor chains. The Tyr96 and Tyr122 interacting systems were equilibrated with great care before running unrestrained dynamics. Each was minimized to resolve steric clashes, then equilibrated according to the scheme shown in **Table 2.8**. Distances and angles were calculated from the thioether sulfur of Met120 to the centers and normal vectors of the aromatic groups of Tyr96, Tyr122 and Trp107. Methionine-aromatic interaction cutoffs were defined as in the CaM simulations.

Table 2.8 Relaxation schedule for the MOx120-receptor complex simulations. Restraint spring constants are given in kcal/mol/Å2.

Stage	Receptor		Ligand		Steps
	Backbone	Sidechain	Backbone	Sidechain	
1	1	1	1	1	10^6
2	0.1	1	1	1	10^6
3	0.01	1	1	1	10^6
4	0	1	1	1	10^6
5	0	0.1	1	1	10^6
6	0	0.01	1	1	10^6
7	0	0.005	1	1	10^6
8	0	0	1	1	10^6
9	0	0	0.1	1	10^6
10	0	0	0.01	1	10^6
11	0	0	0	1	10^6
12	0	0	0	0.1	10^6
13	0	0	0	0.01	10^6
14	0	0	0	0.005	10^6
15	0	0	0	0	10^6

Chapter 3. Thioether Cosslinked Macrocycles for Modulating Protein-Protein Interaction

Motivation:

Due to the prevalence as well as the increased stabilization energy of sulfoxide-π interactions we identified in Chapter 2, we were inspired to utilize sulfur oxidation states within thioether-bridged macrocycles to disrupt PPIs. Through the incorporation of two thio-ethers, we were able to modify the polarity of peptides with sulfoxide and sulfone functional groups. The thioether-bridged macrocycle mimics the active site of MLL, to disrupt the KIX:MLL interacting site.

3.1 **Introduction**

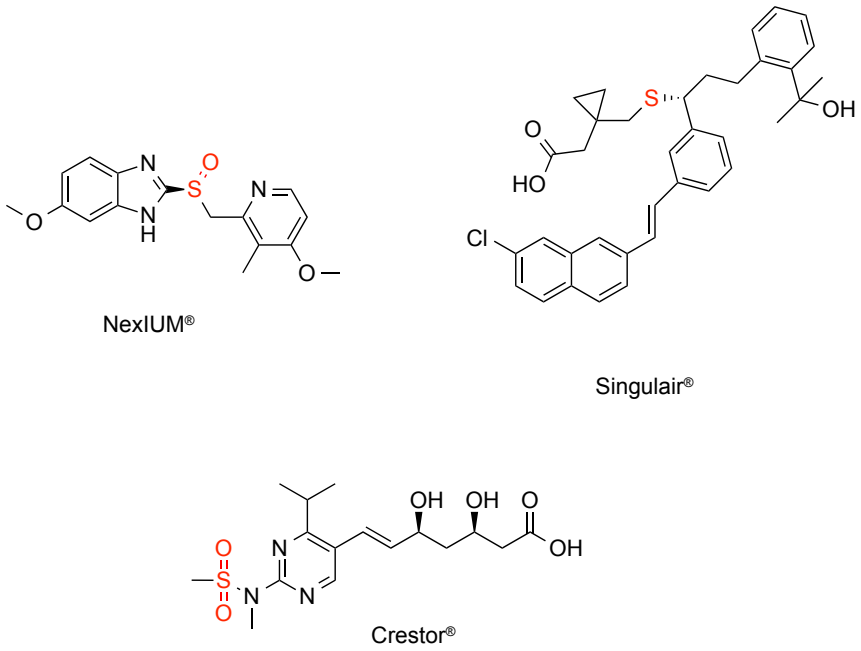

Figure 3.1 Suflur-containing drugs on the market including Crestor®, NexIUM®, and Singulair®.

The role of sulfur within biological systems has been identified to be useful with respect to drug discovery. Sulfur has been prominently used in small-molecule drugs, with 24.8% of drugs containing a sulfur atom, **Figure 3.1**.[143] One important contribution to this prevalence of sulfur-containing functional groups in drugs is the range of non-covalent interactions involving the various oxidation states of sulfur. These interactions range from ionic in character, to dipolar, and dispersive. For example, the sulfur atom of cysteine and methionine are found with increasing frequency near aromatic side-chains of proteins.[106,115] Computationally, the methionine-aromatic interaction has an interaction energy of ~1–1.5 kcal/mol greater than the alkyl-aromatic-equivalent interaction.[115] The sulfur-aromatic interaction has been experimentally investigated to have a stabilization

effect of 2 kcal/mol[120] for phenylalanine and cysteine. For phenylalanine-methionine and tryptophan-methionine interactions, stabilization energies have been measured to be 0.3 kcal/mol.[106] Oxidation of methionine to a sulfoxide further enhances the phenylalanine-methionine interaction by 0.5 - 0.6 kcal/mol (See Chapter 2).[170] Dougherty and co-workers have also shown sulfonium ions to engage in cation-π interactions.[110] Sulfur's ability to access a variety of oxidation states including, thioethers, sulfoxides, sulfones, and sulfonium ions gives rise to sulfur's chemical plasticity for molecular recognition. A systematic analysis of these functional groups, which can be accessed under mild and chemoselective conditions, can inform how varied polarity states can affect the binding, stability, and physicochemical properties of sulfur-containing medicinal agents.

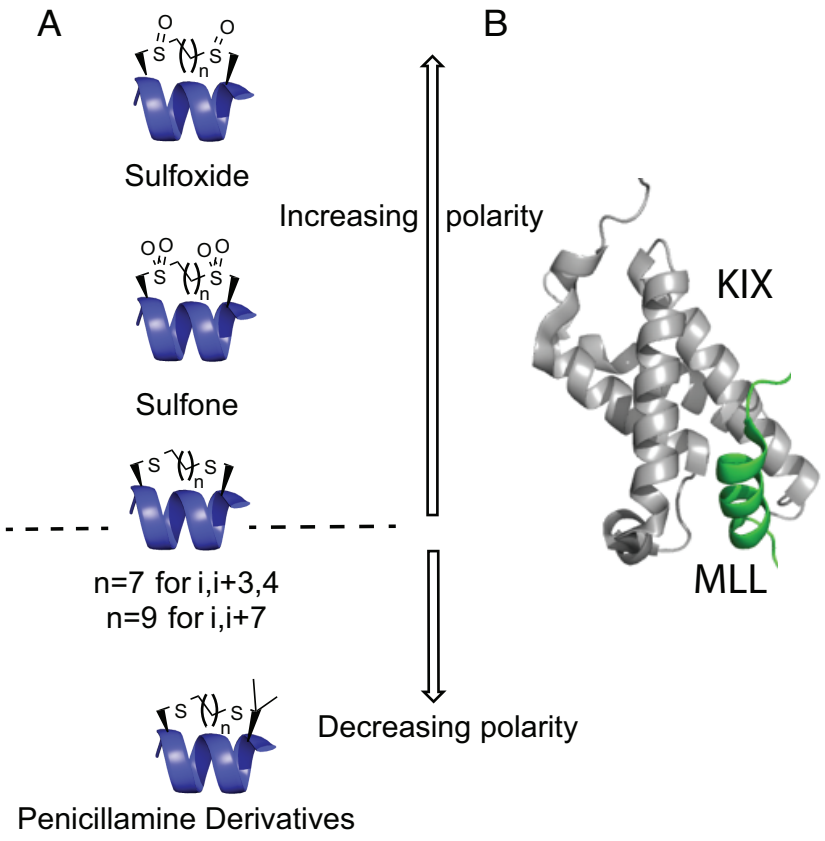

Figure 3.2 A. Sulfur-containing α-helical macrocycles in various oxidation states and polarities. B. NMR solution structure of KIX (grey) binding to the α-helical peptide MLL (green), PDB ID: 2AGH.

One emerging area of research in medicinal chemistry is the exploration of sulfur-bridged-peptide macrocycles as protein-protein interaction (PPI) inhibitors. Protein-protein interactions are vital in all biological processes,[30] and have been shown to be critical points for which manipulation may be possible.[171] All-hydrocarbon 'stapling'[12,172,173] and lactam formation[35,36,174] have received wide-spread use for stabilizing α-helices and increasing cellular uptake. Cysteine-mediated macrocycle formation has also been an effective conformational constraint due to the sulfhydryl reactivity profile and the encodability of this natural amino acid.[63,175] Various methods have been employed for macrocyclization including *S*-alkylation with bis-electrophiles,[68,176] S_NAr,[69] and thiol-ene[64]

reactions to form thioethers. Determining what factors affect cell penetration of crosslinked peptides has recently been assessed by Walensky et al. where they determine hydrophobicity, α-helicity, and pI are the driving factors of cellular uptake.[177] Despite the increased approaches for macrocycle formation in both synthetic and genetically encodable libraries of stabilized α-helices, a systematic evaluation of the use of sulfur oxidation states of the nascent thioethers for tuning the physicochemical, biological, and molecular recognition properties of these peptides has yet to be explored. Here we use the α-helical region of the transcriptional activation domain of the mixed lineage leukemia protein (MLL), as a model system to evaluate how thioether oxidized states would affect secondary structure, stability, and affinity of stabilized α-helical peptides for future development of PPI inhibitors (**Figure 3.2**).

The KIX domain of the coactivator CBP (cAMP-response element binding protein (CREB)-binding protein, **Figure 3.2B**) plays a versatile scaffolding role through interactions with over a dozen transcription factors, which engage two distinct binding sites. Three notable transcription factors include the kinase inducible domain of CREB, and the transcriptional activation domains of c-Myb and MLL. While MLL is a necessary component of the transcriptional machinery that regulates normal blood cell growth, aberrant levels of MLL-mediated transcription leads to cancer cell growth.[178] Recruitment of E2A to KIX –which binds to the same site as MLL—has been shown to induce acute lymphoblastic leukemia.[100] MLL binding to KIX has also been shown to potentiate binding of c-Myb and CREB with KIX through an allosteric mechanism.[179]

The MLL transcriptional activation domain folds into an α-helical secondary structure upon binding to KIX, which leads to formation of the activator-coactivator complex within the transcriptional machinery. This interaction is dictated by a dynamic, large hydrophobic region that has been difficult to target. Few small molecule inhibitors have been discovered and none with sub-micromolar affinities.[83,92] The difficult nature of this PPI motivated our study by using MLL as a model to explore KIX PPIs.

3.2 **Results and Discussion**

3.2.1 Polarity Assessment of Sulfur Oxidation at the Side-Chain, Amino Acid, and Peptide Level.

Prior to evaluating effects of thioether oxidation on molecular recognition sites in proteins, we first sought to evaluate how modulations of the structure and oxidation state of the sulfur-bridged side chains can affect the physiochemical properties of peptides. By incorporating a bis-thioether constraint to enforce α-helicity in a sequence defined manner, helicity and polarity are evaluated (**Figure 3.1A**).[63] Oxidation of thioether groups into sulfones and sulfoxides provides a facile method of increasing polarity of otherwise hydrophobic peptides.[180,181] Whereas lactam bridging is one method for increasing the polarity of the all-hydrocarbon-based cross-links, oxidized sulfur atoms may be less energetically costly for desolvation for eventual cellular uptake.

To characterize the energy of solvation for the amide, thioether, sulfoxide, and sulfone moieties, we used the four model compounds shown in **Figure 3.3A**. Solvation free energies in water were determined with density functional calculations using the SM12 solvation model. The results in **Figure 3.3** show that N-methylacetamide has the largest

solvation energy (-9.1 kcal/mol) of the series, within 1 kcal/mol of the -10.0 kcal/mol experimental value.[182] The large solvation energy is to be attributed to the hydrogen bonds formed both by the carbonyl oxygen and the amide hydrogen with water, accompanied by polarization of the wavefunction (the dipole moment increased from 3.6 D to 4.6 D in going from the gas phase to water). Much less favorable interactions with water were shown by the ethyl methyl thioether, which displayed a solvation energy of -0.7 kcal/mol, because of the inability of the thioether to form strong hydrogen bonds, and of its modest polarization by water (i.e., the dipole moments changed from 1.8 D in the gas phase to 2.0 D in water).

Oxidation of sulfur from a thioether to either a sulfoxide or sulfone greatly increased the magnitude of the calculated solvation energy to -5.7 and -6.8 kcal/mol for the sulfoxide and sulfone containing molecules, respectively. Although the calculations showed that the free energy of solvation of the sulfone is 1.1 kcal/mol more negative than the sulfoxide, it is to be noted that only three oxidized sulfur compounds with available experimental data were included in the SM12 training set. Given the greater computational uncertainty associated with these moieties, the difference between solvation energies cannot be distinguished. Both sulfoxides and sulfones can form hydrogen bonds with water, but density functional calculations showed that the sulfoxide forms a hydrogen bond that is approximately 3 kcal/mol stronger than the sulfone (see experimental for details). Such a capacity to hydrogen bond may in part explain the differences in partition coefficients and HPLC retention times described below.

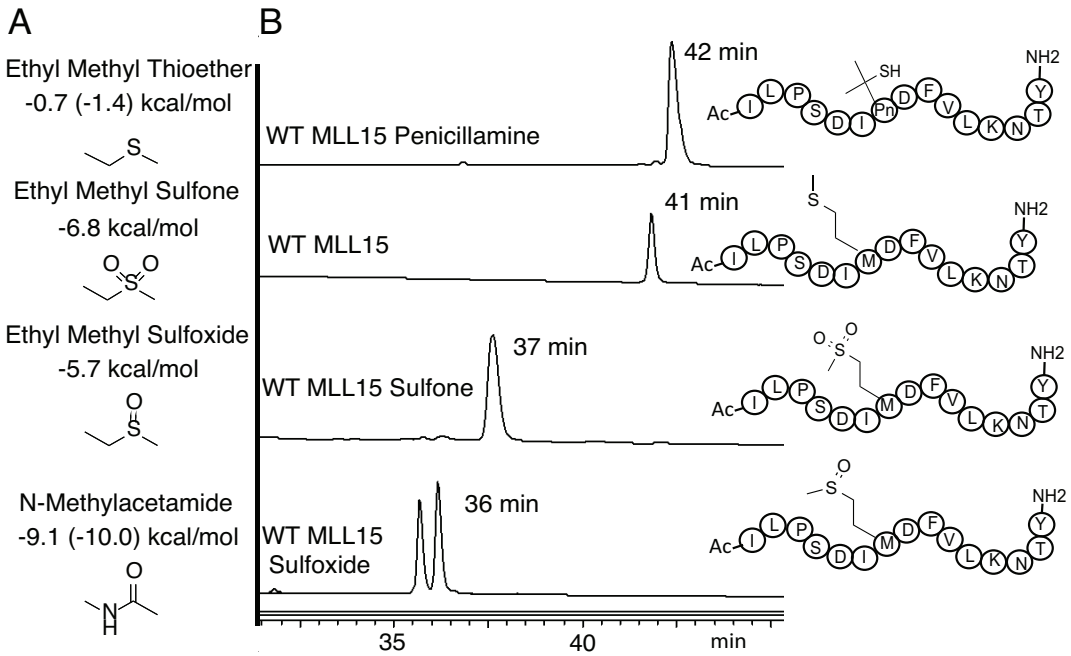

Figure 3.3 A. Computational analysis of the solvation energies in water in kcal/mol. Literature values from experimental measurements are in parentheses. B. HPLC retention time analysis of various MLL15 peptides with sulfur containing side-chains. A one percent per minute gradient of elution solvent acetonitrile was used in all cases.

We next compared our computational results of sulfur-containing side chains to experimental data from Schenck et al., where they evaluated the relative hydrophobicity of the amino acids glutamine, norleucine, methionine, methionine sulfoxide, and methionine sulfone via examination of partitioning coefficients between water and methylene chloride (P_m).[181] Consistent with our solvation energy studies, significant differences in hydrophobicity were observed between methionine sulfoxide (P_m = 11± 3) and methionine (P_m = 0.046 ± 0.002). Both sulfur-containing amino acids have increased hydrophilicity compared to the all-hydrocarbon norleucine, (P_m = 0.018 ± 0.002). Methionine sulfone, while still hydrophilic, is somewhat less polar than the sulfoxide (P_m = 1.9 ± 0.2) which can form stronger hydrogen bonds with water as described above, and substantially less polar than glutamine (P_m = 78 ± 3) in this solvent system.[181]

Based on the results at the amino acid and side-chain level, and the discrepancy in partition coefficient and desolvation energy between sulfoxide- and sulfone-containing amino acid side chains, we next measured the ability of an individual amino acid for altering the polarity of a peptide in the context of a 15-residue peptide of MLL (WT MLL15), **Figure 3.3B**. We based our analysis on the retention times through a C18 HPLC column as a relative comparative value for polarity. WT MLL15 contains one methionine residue and elutes at 41 minutes (51% acetonitrile). Chemical oxidation using H_2O_2 leads to a diastereomic mixture of two sulfoxides within the peptide and yields an average retention time of 36 minutes (46% acetonitrile). When WT MLL15 is oxidized to a sulfone using H_2O_2 and performic acid, the less polar sulfone increases the retention time by 1 minute relative to the sulfoxide (37% acetonitrile). Finally, when a regioisomer of methionine is used, penicillamine (Pn), the most hydrophobic peptide is produced eluting at 42 minutes (52% acetonitrile). We conclude from these findings that through the structural manipulation and/or oxidation of a single sulfur-containing amino acid within a short peptide, we can alter the retention time of the peptide by over six minutes leading to a large window of polarity and desolvation energy differences. Bis-thioether linkages discussed below, allow for an even greater range of tunability of the peptide polarity by chemical manipulation.

3.3 **Secondary Structure Evaluation of Cross-linked Peptides**

Incorporation of a side-chain crosslinking motif has been shown to increase the stability of α-helical peptides towards proteases, cellular uptake, and bioactivity.[173] Furthermore, crosslinking pre-organizes the peptide into the active secondary structure, thus reducing the entropic cost for folding which leads to significant increases in affinity towards a given target.[22] More recently, the macrocycle hydrocarbon crosslinks or "staples" have also been shown to engage in favorable binding with hydrophobic sites on the protein surface.[183] While this can increase affinity in some cases, such as the ATSP-7041-HDMX[49] and $SAHB_D$-MCL-1,[44] the hydrophobic nature can induce altered geometries, as seen in the ERα-SP6 interaction.[184,185] Thus, perturbations of PPIs by the hydrophobic linker can affect affinity and be potentially detrimental to binding near polar residues on the protein surface.

To investigate the effect of sulfur-containing side-chain macrocycles on α-helicity and subsequent binding affinity, we established a set of reaction conditions for peptide macrocyclization and subsequent oxidations at various positions within the helical region of the transcriptional activation domain of MLL. Evaluation of the NMR solution structure of a complex of the KIX domain with MLL (PDB ID: 2AGH, **Figure 3.2**)[85] shows MLL embedded on two faces of the α-helix which encompasses 11 amino acids. Therefore, we chose a 12-residue sequence of this peptide including a C-terminal tyrosine for a spectroscopic concentration determination handle. We used this peptide sequence initial evaluation of helical propensity effects mediated by sulfur-containing cross-links referred to herein as MLL12. A single aspartate to lysine mutation at position 2848 of the native

sequence (which is equivalent to the second residue in our sequence), was made to increase solubility of this peptide construct. We further studied 15-residue peptides keeping the native aspartic acid and extending the sequence towards the N-terminus, as a leucine residue outside the α-helix has been shown to be important for binding to KIX.[186] Of the available synthetic methods for peptide macrocyclization, we chose bis-thiol alkylation using dibromoalkanes of varying chain length using modified conditions from Hyunil et al.[176] We increased the reaction temperature to 80 °C in a microwave reactor for 20 min to afford crosslinked peptides, which were subsequently purified by RP-HPLC.

MLL15:

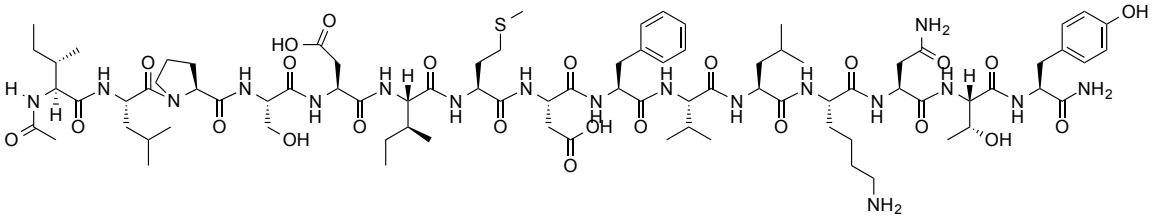

Ac-ILPSDIMDFVLKNTY

MLL12:

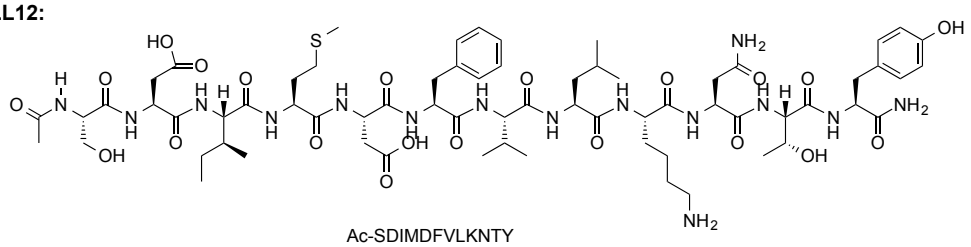

Ac-SDIMDFVLKNTY

Figure 3.4 MLL Sequences either 12 or 15 residues of the helical portion of the protein that interacts with KIX.

We conformationally constrained the MLL peptides (12-15 residues) with alkyl crosslinkers, **Figure 3.4**. In an α-helix, there are 3.6 amino acids per turn, which makes amino acids that are 3, 4, or 7 residues apart ideal targets for crosslinking. We therefore

incorporated two cysteine residues at an initial site (*i)* and at either position 3, 4, or 7 (**Table 3.1**). Incorporation of D-cysteine at the *i+3* position was used when an *i,i+3* crosslink is synthesized. Previous reports have shown the most stereochemically favorable crosslink incorporates L- amino acids at the *i* site and D-amino acids at the *i+3* position.[187] For *i, i+4* or *7,* L-stereochemistry is used at both positions.[16] We utilized a 10-carbon alkyl chain for the *i,i+7* crosslink, and an 8-carbon chain for the *i,i+3* or *4* crosslink, as this optimal length of the crosslinker has been reported.[64]

Table 3.1 MLL peptide constructs showing primary sequence, incorporated linkage length and oxidation state (Sox) with corresponding % helicity. Amino acids with sulfhydryl groups indicated in bold, and crosslinked sequences indicated via X.

No.	Sequences*	Linker site	Linker Length, S_{ox}	% Helicity
WT MLL15	ILPSDIMDFVLKNTY	--	--	24
1	SKICDFC$_d$LKNTY	i,i+3	--	21
1X	SKICDFC$_d$LKNTY	i,i+3	8	25
2	SKIMDFCLKNCY	i,i+4	--	34
2X	SKIMDFCLKNCY	i,i+4	8	32
3	SKICDFVLKNCY	i,i+7	--	26
3X	SKICDFVLKNCY	i,i+7	10	43,44**
3Xa	SKICDFVLKNCY	i,i+7	10, sulfone	33,34**
3Xb	SKICDFVLKNCY	i,i+7	10, sulfoxide	39
4	ILPCDIMDWICKNTY	i,i+7	--	9
4X	ILPCDIMDWICKNTY	i,i+7	10	16
5	ILPSDICDWILKNCY	i,i+7	--	53
5X	ILPSDICDWILKNCY	i,i+7	10	43
5Xa	ILPSDICDWILKNCY	i,i+7	10, sulfone	11
5Xb	ILPSDICDWILKNCY	i,i+7	10, sulfoxide	8
6	ILPCDIC$_d$DWILKNTY	i,i+3	--	7
6X	ILPCDIC$_d$DWILKNTY	i,i+3	8	12
7	SKICDFVLKNPnY	i,i+7	--	45
7X	SKICDFVLKNPnY	i,i+7	10	10
8	SKICDFVPnKNTY	i,i+4	8	35
8X	SKICDFVPnKNTY	i,i+4	8	21

C_d abbreviated for D-Cysteiene; Pn abbreviated for Penicillamine
*All peptides acetylated at N-terminus
**CD experiment run at two concentrations (100 μM, and 25 μM, respectively)

Helical stabilization has been shown to be beneficial for binding, cellular uptake, and proteolytic stability. Therefore, we used circular dichroism in the far UV region to identify specific sequences that have increased helicity with the incorporation of a crosslinking constraint and for evaluating changes in sulfur oxidation to the overall peptide helicity. We first investigated the effect of bis-thioether macrocylcization on α-helicity at

various peptide positions within the MLL sequence. The uncrosslinked MLL12 peptides containing two cysteine mutants show moderate helical propensity without stabilization (21-34%, Peptides **1**,**2**,**3**,**Table 3.1**). For the cross-linked peptides we chose the eight and ten carbon alkyl cross-linker used by Wang et al. as they observed a slight increase in helicity in their crosslinked *i,i+4* and *i,i+7* peptides, respectively.[64] We also investigated how the eight carbon alkyl crosslink at the *i, i+3* position affects helicity as this linkage site was not evaluated previously. In the case of the *i,i+4* crosslinked MLL12 peptide, **2X**, we observed a small decrease in helicity (0.9 fold to 32%, **Figure 3.7**) whereas in peptide **1X**, containing the *i, i+3* crosslink, a slight increase in helicity was observed (1.2 fold to 25%, **Figure 3.7**). In the case of the *i,i+7* crosslink we were able to observe a larger 1.7 fold increase in helicity from 26% to 43% for the MLL12 peptide **3X.** This latter crosslinking position is our most favorable site for macrocyclization.

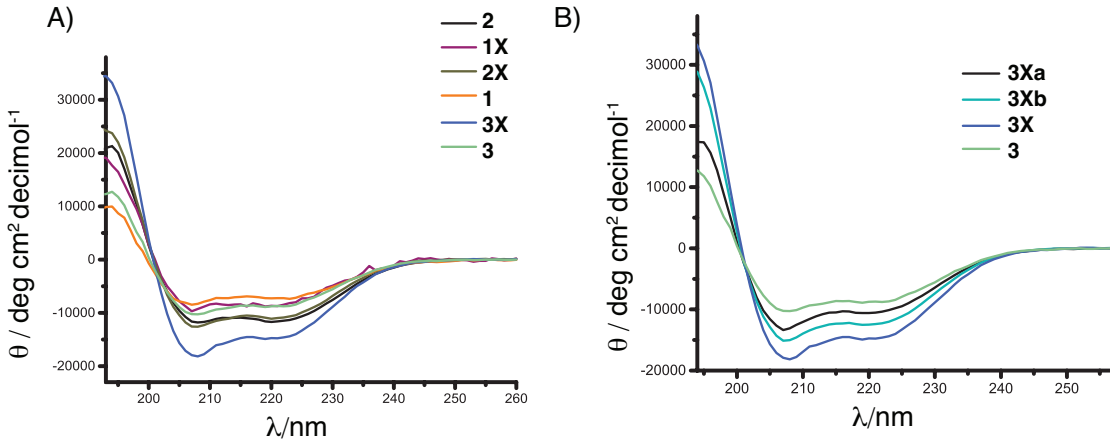

Figure 3.5 Far-UV CD spectra used to evaluate helicity of MLL constructs, taken in a 10 mM phosphate buffer, pH 7.4 with 30% TFE at 100 μM. A. **3X** shows the highest helicity within the *i,i+3,4,7* MLL12 series. B. Oxidation of the *i, i+7* MLL12 to the sulfoxide **3Xb** and sulfone **3Xa**.

Helicity can also be affected by peptide aggregation. This was recently observed in a report using an all-hydrocarbon stapled peptide.[188] We tested if the α-helicity of **3X** was affected by aggregation by carrying out the experiment for **3X** at two different concentrations 25 μM and 100 μM. In this case the helicity remained similar, arguing against an artificially high CD concentration-dependent signature from aggregation (43% vs 44%, **Figure 3.6**). The more polar thioether may also be beneficial in this case for promoting solvation.

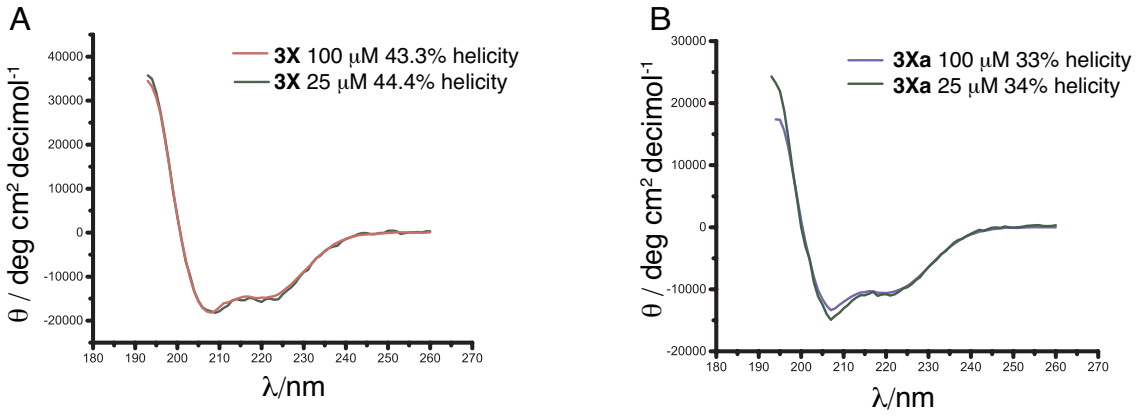

Figure 3.6. CD experiments showing the α-helical traces of MLL12 bisthioether **3X** at 25 and 100 μM concentrations yield the similar % helicity (44.4% and 43.3%, respectively), indicating the helicity is concentration independent. B. α-helical traces of MLL12 bisthioether sulfone **3Xa** at different concentrations also yields similar % helicities (34% and 33%). bisthioether sulfone **3Xa** at different concentrations also yields similar % helicities (34% and 33%).

We extended our investigation to look at longer peptides including a mutant of MLL which exchanges a phenylalanine and valine (residues 9 and 10) to tryptophan and isoleucine for increasing the potency of MLL15 against KIX. In this case, we assessed both the *i,i+7* and *i,i+3* crosslinks. Peptides **4X** and **5X** contain an unstructured N-terminal ILP sequence, to include the a hotspot leucine residue for binding KIX[75] and an *i, i+7*

crosslink at two different positions. These peptides show a similar increase in helicity as **3X** upon macrocyclization (1.8- and 1.7-fold respectively) although the total helicity was lower for **4X** (16%, **Table 3.1**). Peptide **6X** with the *i, i+3,* crosslink also showed a 1.7-fold enhancement of helicity to 12% from the uncrosslinked analog **6**, **Figure 3.7**. Together, these results identify suitable sites for crosslinking to enhance structure within the thioether macrocycles, but indicate a significant sequence-dependent effect on helicity, consistent with prior studies.[17]

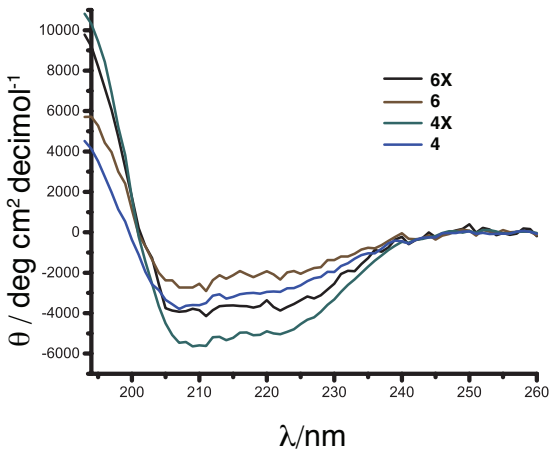

Figure 3.7. CD traces of α-helical signatures show **6X** with increased helicity, but low compared to **6** (7%-12%). Peptide **4X** also has enhanced helicity compared to the uncrosslinked analog (9%-16%).

Once a favorable crosslink was identified for peptide **3X,** sulfur oxidation was investigated for additional structural perturbation from this side-chain modification. First, peptide **3X** was oxidized to contain two sulfones (**3Xa**) leading to a drop in helicity (1.3 fold drop to 34%, **Table 3.1**), although the overall helicity is higher than the uncrosslinked peptide **3**. This value was also concentration independent (**Table 3.1, Figure 3.6B**). Alternatively, when peptide **3X** was oxidized to contain the sulfoxides in **3Xb**, a smaller drop of helicity was observed (1.1-fold drop to 39%, **Table 3.1**). Although in two of the three cases oxidation resulted in a % helicity change of 10% or less, the peptide **5Xa** containing two sulfones showed a more drastic loss in helicity (43% to 11%, **Table 3.1**), with respect to its reduced counterpart, **5X**. The sulfoxide variant, **5Xb** also had decreased helicity to 8%, **Figure 3.8**.

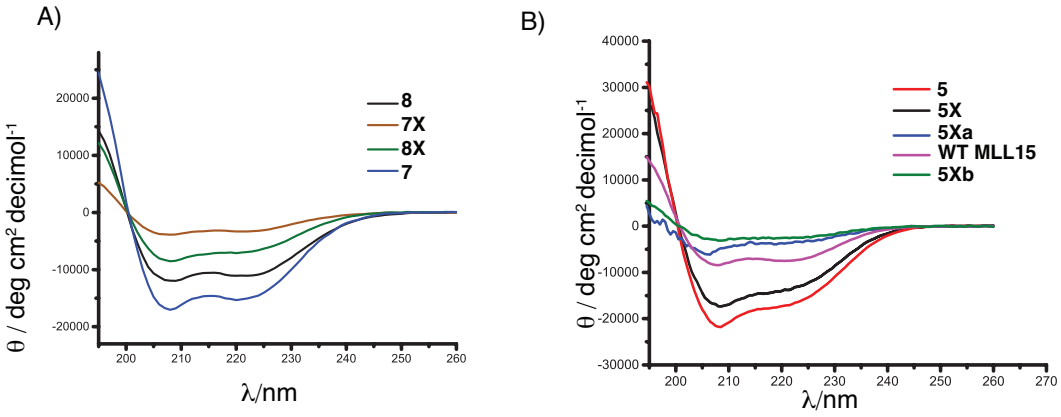

Figure 3.8 A. Penicillamine series with MLL12 i,i+4 and 7 compared to uncrosslinked analogs. B. Full length **5** compared with the crosslinked peptide, **5X**, oxidized variant, **5Xa** and the WT MLL 15.

Our findings on potential detrimental effects upon thioether oxidation from cysteine precursor amino acids, are consistent with a recent report by Zhang et al. using short single turn helical macrocycles. Using shorter hydrocarbon linkers, they also observe a reduction in helicity for singly oxidized thioether-crosslinked peptides to both a sulfoxide and a sulfone.[189] Furthermore, it was observed that only one sulfoxide epimer enhances the helicity, whereas the other disrupts helicity. When the sulfoxide points away from the helix in the *R*-configuration, Zhang et al. calculated an N-C-C-S dihedral angle of approximately -66°, whereas in the *S*-configuration the sulfoxide oxygen points towards the peptide causing a steric clash leading to an increase of the dihedral angle to -81°.[189] As we are unable to separate the diasteromeric sulfoxide species, we may have enhanced helicity from only one diastereomer. These results support that although oxidation within the peptide macrocycle was tolerated in several cases, modest perturbation towards the α-helical conformation can occur and should be considered in future studies.

In some cases, an increased hydrophobic crosslink may be important. Replacement of cysteine with penicillamine leads to a more hydrophobic side-chain modification and serves as a potential valine mimic. We evaluated how the conformationally constrained hydrophobic amino acid affected helicity. Surprisingly, the *i,i+7* series of the uncrosslinked peptide containing a single penicillamine near the C-terminus **7,** led to a high level of helicity 45%, versus 26% for having a cysteine at the same position in peptide **3**. However, the α-helicity was substantially reduced 4.6-fold to 9.8% upon macrocylization to **7X** (**Table 3.1, Figure 3.8**). Crosslinking at *i,i+4* positions is also destabilizing but led to a less substantial loss in helicity upon macrocylization from 0.6 fold to 21% (**8** to **8X**, **Table 3.1, Figure 3.8**).

We conclude for our initial studies of thioether macrocyclization that alkyl crosslinkers of appropriate length are both tolerated within the α-helix at positions *i,i+3, i +4* and *i+7*, and can enhance α-helicity in certain peptide sequences. Sulfoxidation and sulfonation can be installed within the peptide side-chain macrocycles but at the expense of some degree of helicity. Oxidation can also dramatically affect the relative polarity of these peptides. In the case of peptide **5X**, oxidation to a sulfone **5Xa**, or sulfoxide, **5Xb**, leads to over a fourteen minute difference in HPLC retention time (**Figure 3.9**). Due to the potential for thioether oxidation of cysteine-macrocyclized peptides in cellular settings, intracellular functional effects should be interpreted with care.

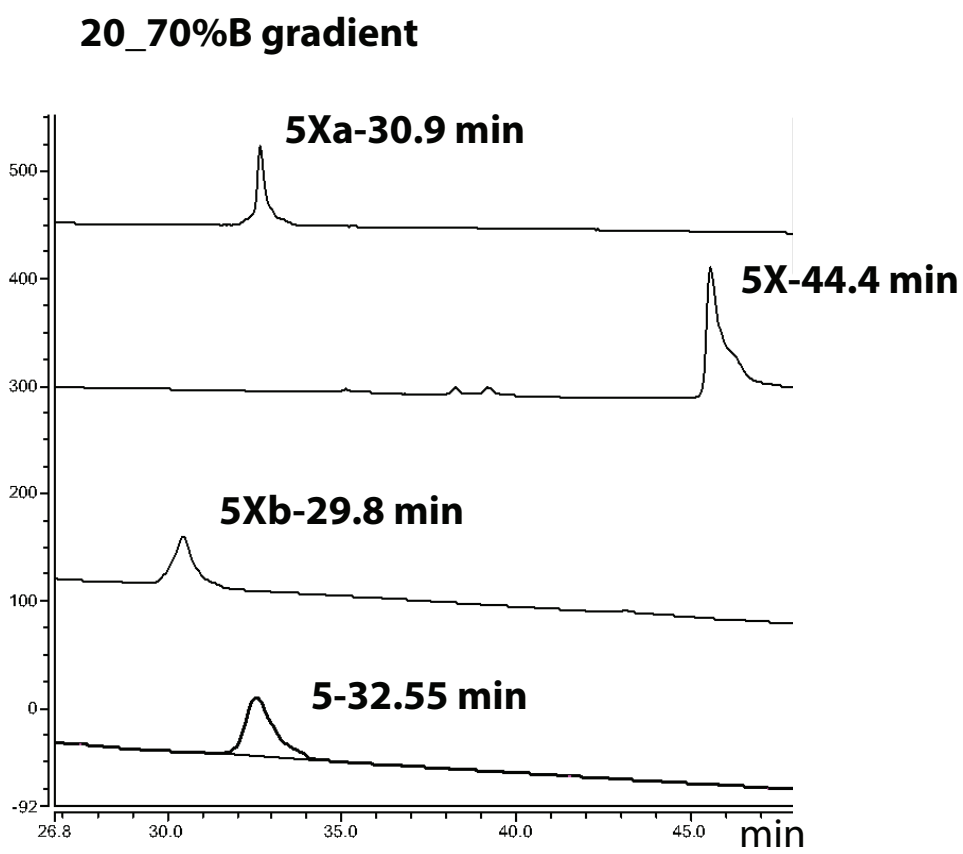

Figure 3.9 Stacked HPLC traces of **5, 5X, 5Xa, and 5Xb** with a 20_70 %B gradient run on the same C18 RP-Column. The sulfoxide shows the most polar retention time (29.8 min), followed by the sulfone (30.9 min), the uncrosslinked (32.55 min) and the crosslinked variant (44.4 min). Chromeleon Software v. 7.2 Peak Pick analysis tool was used in determining retention times.

3.3.1 Proteolytic Stability Upon Macrocylization and Oxidation

An additional advantage of crosslinking peptides is the enhanced stability towards proteases due to reduced populations of the extended conformation necessary for protease-mediated hydrolysis. As an initial evaluation of the effects of conformational crosslinks and oxidation within the crosslinks, we tested four peptides containing the i+7 crosslink. We used the 15 residue MLL peptide, **5X**, two oxidized versions: the dual sulfone, **5Xa,** and the dual sulfoxide, **5Xb**, as well as the uncrosslinked analog **5**, and the native peptide sequence for MLL (**WT MLL15**).

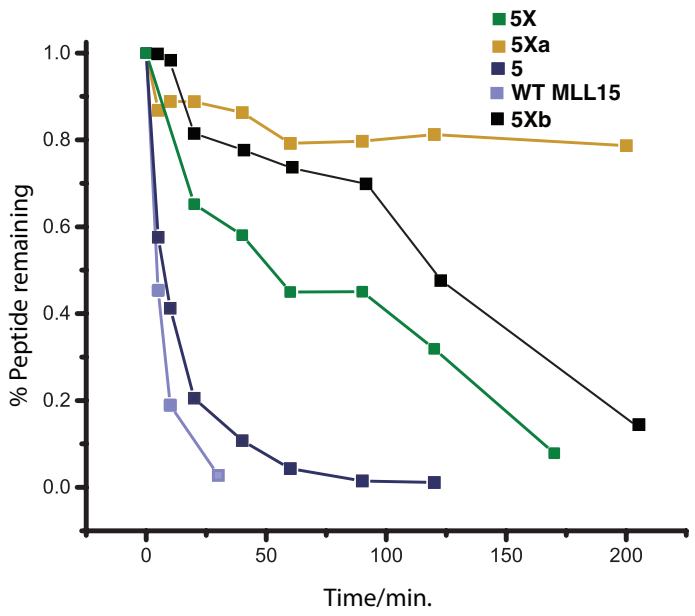

Figure 3.10 Proteolytic stability assessesment of MLL and MLL-derived peptide macrocycles during a tryptic digest. WT MLL15 (pale purple) and acyclic peptide **5** (mauve) proteolyze rapidly compared to the crosslinked **5X** (green $T_{1/2}$ = 50 min), **5Xb** (black $T_{1/2}$ = 100 min) and **5Xa** (gold, 21% degraded at 200 min). Remaining peptide was quantified via RP-HPLC integration.

We chose trypsin as a model protease to measure relative stability as there was a single lysine recognition site within all peptide sequences. A significant stability for the crosslinked peptide **5X** was seen ($t_{1/2}$ = 50 min) whereas **5** ($t_{1/2}$ = 10 min) had a similar degradation rate to the WT MLL15 ($t_{1/2}$ = 5 min, **Figure 3.10**). These results are consistent with previous reports on stabilized α-helices. Surprisingly, despite the low helicity, oxidation of **5X** to the sulfoxide variant, **5Xb** showed enhanced proteolytic stability ($T_{1/2}$ = 100 min). The peptide **5Xa**, showed an even stronger resistance towards proteases (21% degraded at 200 min, **Figure 3.10**). The origin of these stabilizing effects upon oxidation are unknown. From our studies above, we could not attribute this increase in stability to helix stabilization. The dual sulfone- and dual sulfoxide-containing peptides in this case may afford additional resistance towards proteases caused by an inability to fit into the

enzyme active site due to the increase in size of the side-chain, or non-productive molecular recognition effects. This stabilization will be further studied in future investigations.

3.3.2 Molecular Recognition with KIX

Having demonstrated a moderate increase in peptide helicity from *i* to *i*+7 crosslinks, a modest perturbation to structure upon oxidation, and an increase in proteolytic stability with both the constrained and oxidized peptides, we evaluated the effects of crosslinking and oxidation upon PPIs with KIX. We turned our attention to a protein-observed fluorine NMR method (PrOF NMR), which has recently been used to characterize binding of small molecules[190] and the binding footprints of peptides to the KIX protein differentiating the MLL site from the CREB site.[191] This method uses a protein that is sequence-selectively labeled with 3-fluorotyrosine (3FY). Y631 is a diagnostic amino acid found within the MLL binding site. Titration of 3FY-labeled KIX with WT MLL15 shows a concentration-dependent decrease in the intensity of the Y631 resonance. Between one and two equivalents of WT MLL15 (i.e., 50 and 100 μM peptide), the resonance completely broadens into baseline, consistent with the intermediate chemical exchange regime, **Figure 3.11**. Although potency cannot directly be obtained for high affinity peptides in a straightforward manner by this method, chemical exchange in the intermediate to slow exchange regimes are consistent with the expected mid to low micromolar affinity of MLL peptides for KIX.[192]

MLL engages KIX through more than a single helical face and through N-terminal residues outside of the α-helix in WT MLL15.[75] Therefore, appropriate crosslinking sites can be challenging to identify at positions that do not disrupt binding. To evaluate the

relative effects on binding affinity from various crosslinking motifs within the MLL sequence, we compared each binding titration to an uncrosslinked analog containing the two cysteine residues. In an attempt to increase affinity, we also mutated residues in position 9 and 10 from phenylalanine and valine to tryptophan and isoleucine respectively based on published data[92] and frequency of tryptophan at protein hotspots[9]. In the case of uncrosslinked peptide **5,** Y631 has already broadened into baseline at one equivalent peptide. When the peptide **5** was crosslinked to **5X** (*i,i+7)***,** binding was slightly attenuated at 1 eq, giving rise to resonance broadening of Y631 of KIX similar to WT MLL15 (**Figure 3.12A, B**). The resonance further broadens into baseline with two equivalents of peptide (100 μM **5X**, **Figure 3.12C**). However, oxidation of **5X** to the dual sulfone **5Xa** abolished binding (**Figure 3.12C**), indicating the thioether was the proper oxidation state in this case. More studies on the effect of oxidation will be necessary to harness its potential utility within crosslinked peptide inhibitors for affecting protein interactions.

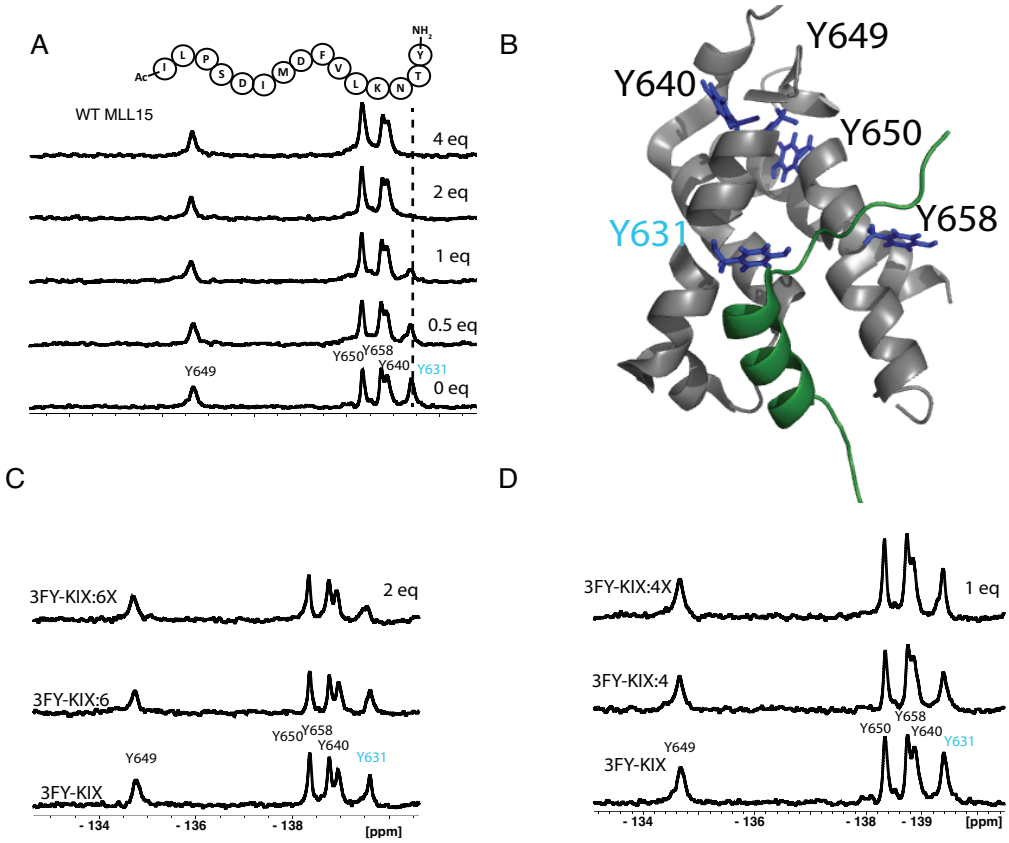

Figure 3.11. ^{19}F-NMR experiments were carried out with 3FY-labeled KIX protein (50 μM 3FY-KIX, 50 mM HEPES and 100 mM NaCl, pH 7.2). A. Titration of WT MLL15 into 3FY-KIX shows perturbation of Y631 with significant broadening into baseline between 1 and 2 equivalents of WT MLL15. B. NMR solution structure of KIX (grey) binding to MLL (green) with the five tyrosine residues (blue) with side chains labeled (PDB ID: 2AGH, MLL-interacting residue Y631 shown in blue) C. ^{19}F-NMR spectra with **6**/**6X** are overlaid with 3FY-KIX at 2 equivalents of peptide. D. ^{19}F-NMR spectra of **4**/**4X** overlaid with 3FY-KIX at 1 equivalents of peptide. NMR spectra from full titrations can be found in the supporting information.

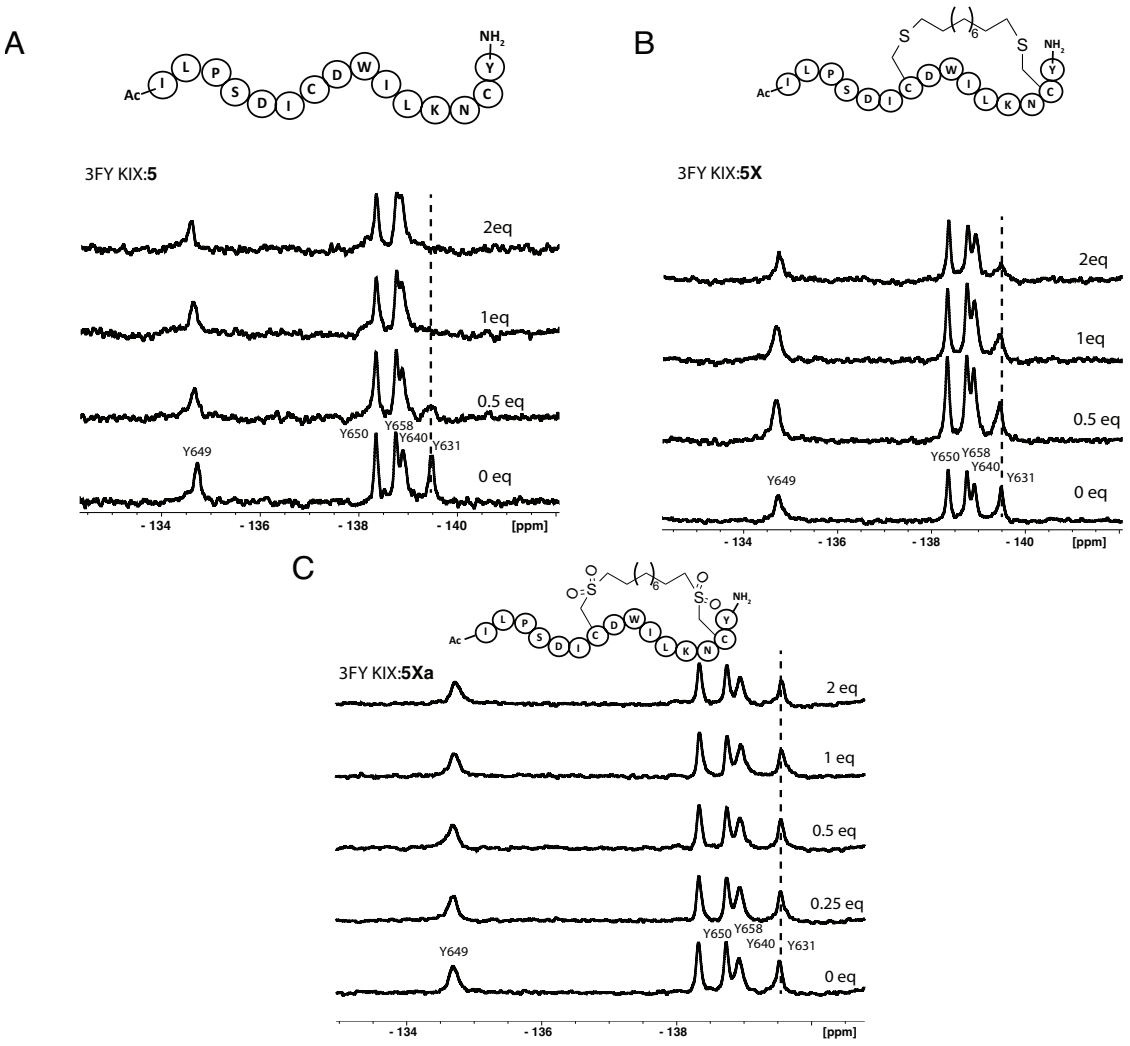

Figure 3.12 ^{19}F-NMR experiments were carried out with 3FY-labeled KIX protein (50 μM 3FY-KIX, 50 mM HEPES and 100 mM NaCl, pH 7.2). A-C. Overlaid NMR plots of A. Complete loss of signal at 1 equivalent of **5**. B. Less binding is observed for the crosslinked analog, **5X**. C. Oxidized macrocycle **5Xa** disrupts binding relative to the uncrosslinked and crosslinked analog.

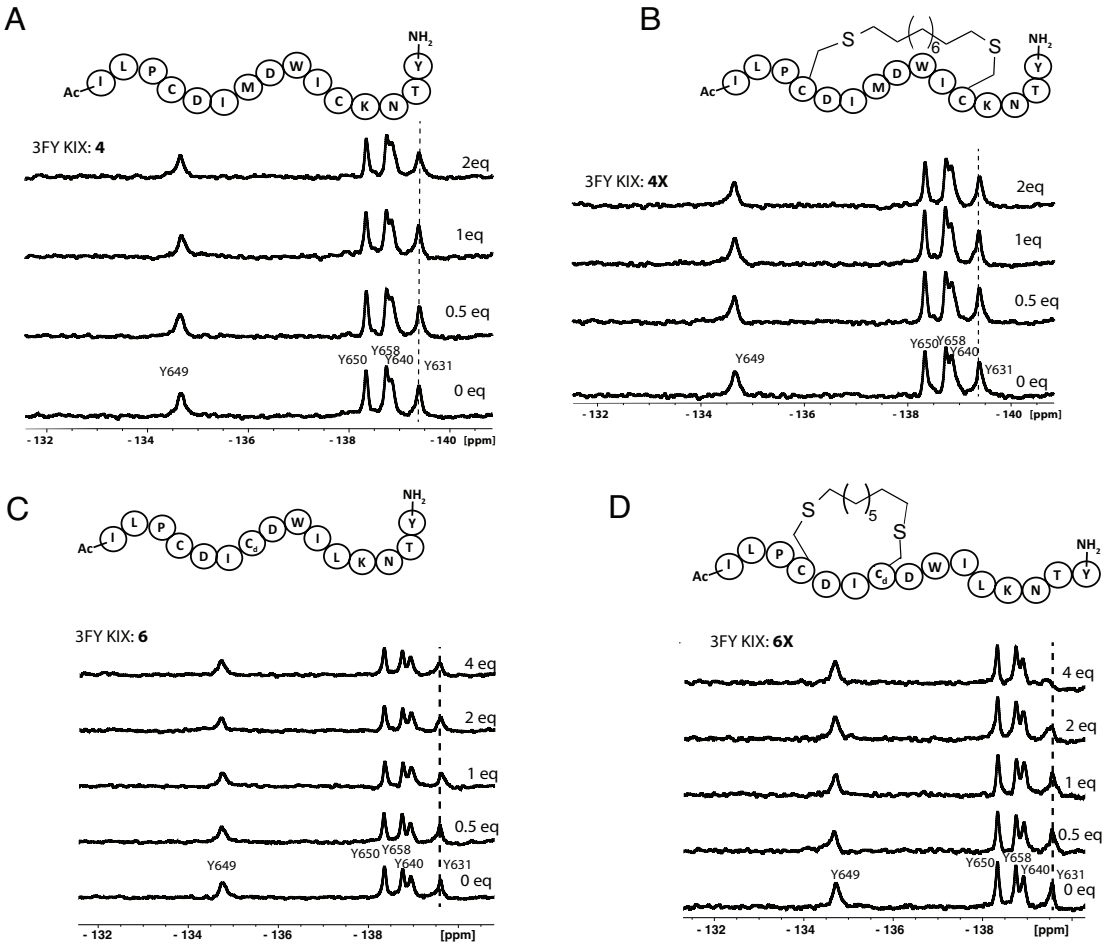

Figure 3.13 ^{19}F-NMR experiments were carried out with 3FY-labeled KIX protein (50 μM 3FY-KIX, 50 mM HEPES and 100 mM NaCl, pH 7.2). A-D. Overlaid NMR plots of A) MLL derivative **4** with slight perturbations of Y631 at 2 equivalents of ligand. B. Crosslinked **4X** shows little change in tyrosine resonances, indicating it does not bind well to KIX. C. *i, i+3* cysteine incorporated peptide **6** shows small perturbations. D. Peptide **6X** has increased perturbations of Y631 relative to the uncrosslinked analog, with significant broadening at 4 equivalents of ligand.

To evaluate a second cross-linking position, we tested a different MLL15 peptide, **4X**, with an *i,i+7* crosslink replacing an important leucine residue at the binding interface. We compared the binding to uncrosslinked 4. In these two cases, both peptides do not perturb Y631 resonance indicating no binding, **Figure 3.13 A,B**. As a final series of peptides, we chose a shorter cross-linker with an *i,i+3* relationship which are oriented away from the KIX interface in the NMR structure of KIX (PDB ID: 2AGH). In this case, the side-chain crosslink is beneficial as peptide **6** in the *i,i+3* series showed no appreciable binding interactions with KIX up to 200 μM peptide (**Figure 3.13 D**), whereas the crosslinked variant **6X** broadened Y631 with four equivalents of ligand (**Figure 3.13 C**, **D**). We interpret the lower degree of broadening at high concentrations to indicate overall weaker binding than **5X**, **Figure 3.12**. Although none of the peptides surpasses the apparent affinity of MLL15, peptide **5X** is an encouraging starting point based on its increased proteolytic stability and moderate binding to KIX for future designs targeting this challenging PPI.

3.4 **Conclusions**

In summary, we have evaluated the effects of modulating the polarity of sulfur-containing peptide macrocycles by varying sulfur oxidation states through chemoselective reactions from thioethers to sulfoxides and sulfones. We first evaluated the relative effects of desolvation of sulfur containing side-chains relative to amide groups computationally and evaluated the polarity differences of short peptides containing either penicillamine, methionine, methionine sulfoxide, or methionine sulfone. These peptides access a range of polarities, but all are less polar than an amide, but more polar than an all-hydrocarbon

side-chain. Such polarity tuning possibilities from a single sidechain may be a consideration for altering peptide aqueous solubility and modifying propensities for cellular uptake. For sulfur-containing peptide macrocycles, in some cases we were able to both enhance α-helicity as well as proteolytic stability. For the case of *i* to *i* +*7* crosslinkers, dual sulfoxidation and sulfonation are also tolerated within the peptide macrocycle such as in **3X**, **3Xa** and **3Xb**. Finally, as a first step towards evaluating peptides as future PPI inhibitors of the MLL-KIX interactions, macrocycle **5X** is able to maintain binding to KIX, and may serve as a starting point for developing cell permeable inhibitors of KIX function. In the future, additional sulfur-containing amino acids and helix promoting side-chain linkers such as bibenzyl[193] and perfluorobiphenyl groups[69] may be useful for studying the effects of sulfur oxidation on polarity tuning, conformation, and molecular recognition at PPI interfaces.

3.5 **Future Works**

3.5.1 Fluorescence Microscopy for Evaluating Cellular Uptake

Constrained helical peptide constructs have large utility as pharmaceutical drug candidates for intracellular proteins due to their ability to penetrate through the cellular membrane. To evaluate the penetration capabilities of our thioether cross-linked peptides, we incubated fluorescently-labeled peptides, **Fluor-5**, and **Fluor-5X** with HeLa cells, washed the cells thoroughly, fixed on a plate, and used Hoescht nuclear dye for fluorescence microscope imagery. A known cell penetrating peptide with eight arginine residues is known to penetrate cells through an active cellular uptake process**, Figure 3.14A**.[194] The typical punctate pattern of fluorescence is observed throughout the cytosol for the octa-arginine peptide.[194] An unalkylated MLL peptide **Fluor-5** image surprisingly shows diffusion throughout the cytosol **Figure 3.14B**, whereas the crosslinked variant **Fluor-5X**, which should have increased permeability localizes around the outside of the

cellular membrane, but does not penetrate through, **Figure 3.14D**. With such a large amount of penetration observed for **Fluor-5**, we re-evaluated the peptide mass after it was dissolved in DMSO, and observed disulfide formation. The disulfide constrained peptide may allow the construct to penetrate cells. We are still investigating why the thioether cross-linked peptide does not penetrate the membrane. Other constrained peptides should be investigated in future studies to confirm if impermeability is due to a specific cross-linked sequence, or if the thioether crosslink has a detrimental effect to cellular permeability. Further studies are necessary to evaluate optimal thio-ether crosslinked peptides, and their ability to be taken up into cells.

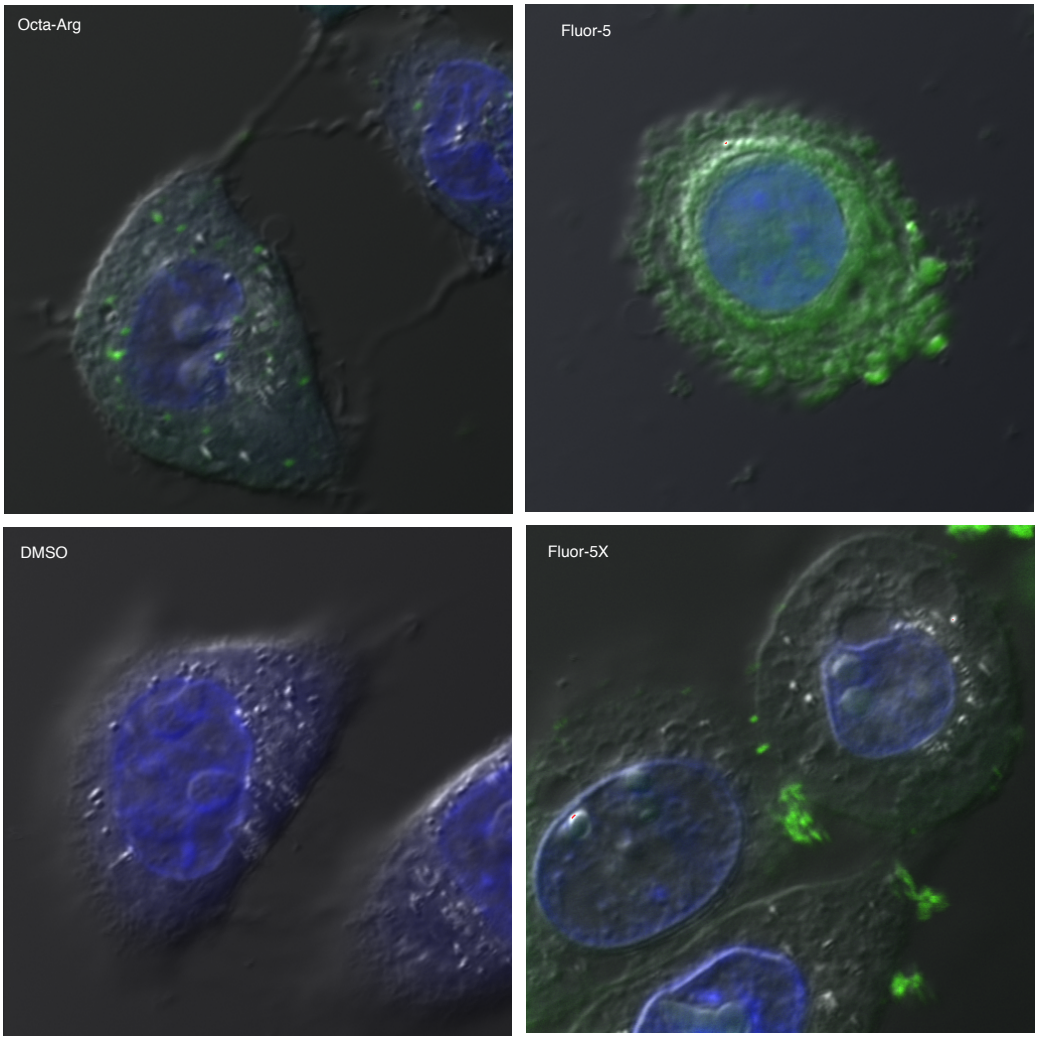

Figure 3.14 Merged fluorescence microscopy image of HeLa cells with Hoescht nuclear stain (blue) incubated with A) fluorescenated Octa-Arg (green), a control peptide known to penetrate through cellular membranes B) **Fluor-5** (disulfide, green) **5** C) DMSO control, and D) **Fluor-5X** (green).

3.5.2 Extended MLL peptide sequences may enhance affinity and solubility (Mentored project with Rachel Staebell)

Extending the MLL peptide at the C-terminus may add binding affinity. This region is a flexible tail, but may provide ionic salt bridges or other non-covalent interactions that allow this 20-residue peptide to bind with higher affinity than the 15-residue peptide. There is an arginine (R145) at the C-terminus of KIX which potentially could interact with aromatic rings, **Figure 3.15**. By mutating residues within the extended region to either alanine or aromatic residues, we can identify which residues contribute to the binding affinity, and where potential crosslinking motifs will be amenable. Fluorescence polarization was used to monitor these interactions. When alanine replaced proline (peptide **B**), a there is a slight decrease in affinity (constrained K_i = 4.14 vs. 2.13 μM), indicating proline is a necessary residue. However, for the other alanine mutated residues, higher affinity was observed (peptides **C,D,E**, **Table 3.2**, **Figure 3.16**) with the greatest affinity for the serine mutation to alanine (peptide **C,** constrained K_i = 0.77 μM). To identify possible non-covalent interactions with R145, we replaced Q86 with a glutamic acid (**F**), a phenylalanine (**G**), tryptophan (**H**), and tyrosine (**I**). The tryptophan mutation (**H**) showed the highest affinity, with a constrained K_i = 0.94 μM, **Figure 3.17**. This research is ongoing, and may prove to be higher affinity sequences to evaluate with thio-ether bridged crosslinking motifs to disrupt PPIs.

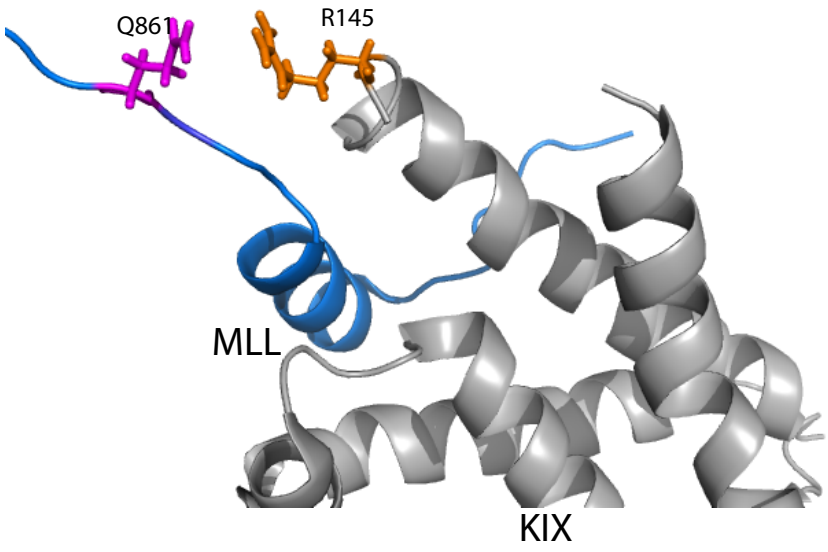

Figure 3.15 Solution structure of MLL interacting with KIX (PDB ID: 1KDX). Glutamine 86 on MLL (pink) is replaced with aromatic residues including tryptophan, which may lead to a cation-π interaction with arginine 145 on KIX (orange).

Table 3.2 Fluorescence polarization IC_{50} and K_i values, constrained and unconstrained for extended MLL peptides

Letter	Sequence	IC_{50} (μM)	Constrained IC_{50} (μM)	K_i (μM)	K_i Constrained (μM)
MLL15 WT	ILPSDIMDFVLKNTY	11.3 ± 0.85	15.7 ± 0.96	1.42	1.97
A	ILPSDIMDFVLKNTPSMQAY	12.7 ± 2.18	17.0 ± 1.40	1.59	2.13
B	ILPSDIMDFVLKNT**A**SMQAY	11.5 ± 1.47	33.1 ± 1.20	1.44	4.14
C	ILPSDIMDFVLKNTP**A**MQAY	5.73 ± 0.57	6.13 ± 0.42	0.72	0.77
D	ILPSDIMDFVLKNTPS**A**QAY	8.88 ± 0.93	12.3 ± 1.02	1.11	1.54
E	ILPSDIMDFVLKNTPSM**A**AY	12.7 ± 1.15	15.1 ± 0.85	1.59	1.89
F	ILPSDIMDFVLKNTPSM**E**AY	14.8 ± 1.06	18.9 ± 0 .81	1.85	2.36
G	ILPSDIMDFVLKNTPSM**F**AY	10.6 ± 0.48	10.7 ± 0.32	1.32	1.34
H	ILPSDIMDFVLKNTPSM**W**AY	3.29 ± 0.29	7.53 ± 0.42	0.41	0.94
I	ILPSDIMDFVLKNTPSM**Y**AY	9.52 ± 0.63	8.50 ± 0.40	1.19	1.06

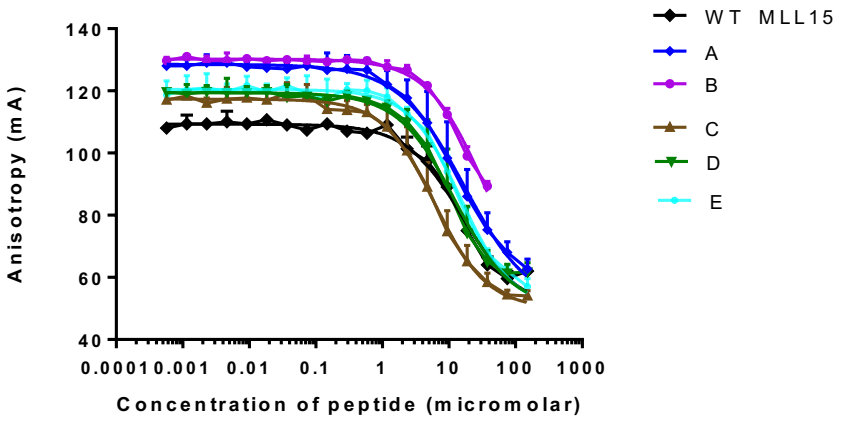

Figure 3.16 Fluorescence polarization curves with 20-residue MLL peptides with a alanine mutations. Peptide **A** is the native 20-residue MLL sequence, (**B**) replaces proline, (**C**) replaces serine, (**D**) replaces methionine, (**E**) replaces glutamine with alanine.

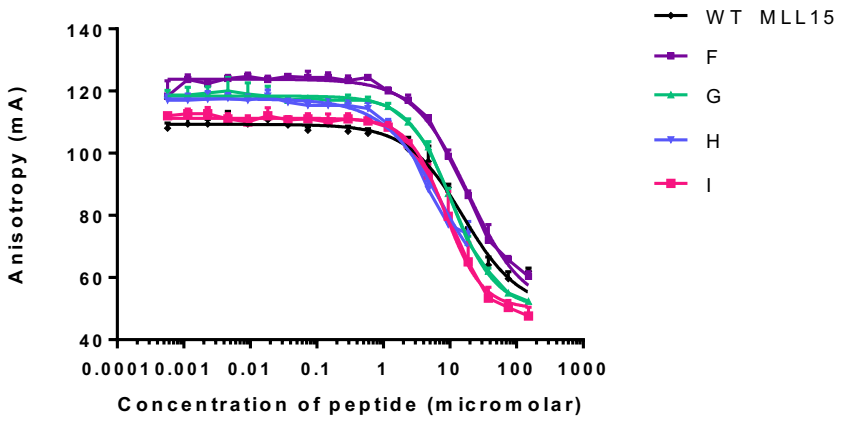

Figure 3.17 Fluorescence polarization curves with 20-residue MLL peptides with a mutation of Q86 with glutamic acid (**F**), phenylalanine(**G**), tryptophan (**H**), and tyrosine (**I**).

3.5.3 β-hairpin motif examining the Met-Ox interactions with tyrosine and phenylalanine (NMR taken by Laura Hawk)

To evaluate the interactions between the sulfoxide of methionine and aromatic residues, a β-hairpin motif, as previously described by Waters and colleagues[106] was utilized with the sequence, RM^{OX}VTVNGKTI**X**Q with **X** being either alanine, phenylalanine, tryptophan, or tyrosine. The hairpin motif allows one to evaluate interactions between discrete residues at positions two and 11. ^{1}H NMR analysis shows the incorporation of the residue of interest at position 11 shifts the diastereomeric methyls next to the sulfoxide upfield with increasing electron-rich aromatic residues, **Figure 3.18**. When alanine is incorporated, the methyls resonances are at 2.695 and 2.687 ppm. Phenylalanine incorporation at position 11 shifts both methyl resonances upfield, 0.07-0.08 ppm, respectively. Tyrosine further shifts resonances to 2.601 and 2.593 ppm. Tryptophan shifts the resonances significantly upfield compared to the alanine control as well as the other aromatic residues, with resonances at 2.544 and 2.529, respectively. Each amino acid has a propensity to fold the β-sheet slightly differently, which potentially can affect the shift in the methyl resonances. If amino acid propensity is the driving factor, then tyrosine would shift the resonances furthest upfield (propensity 1.29), followed by phenylalanine (1.28), tryptophan (1.19), and alanine (0.97); However, since we see tryptophan with the furthest

upfield methyl shift, β-sheet propensity is not the reason for the upfield shifts. The upfield shift is consistent with idea of a more electron-rich ring current within tryptophan shielding the methyl groups stronger than the other aromatic substituents, of which we previously evaluated in Chapter 2.

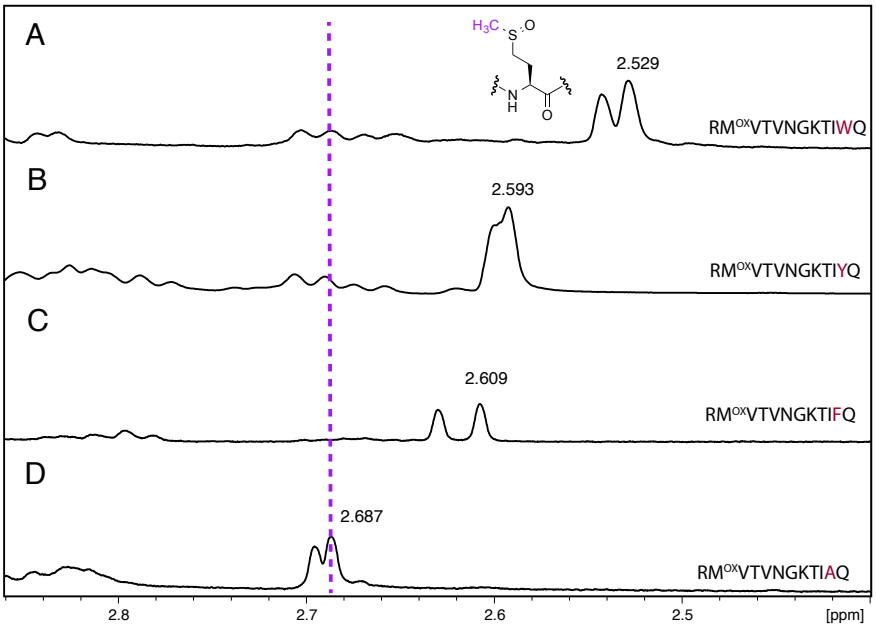

Figure 3.18 ^{1}H NMR overlay of four peptides in a hairpin motif. A. tryptophan incorporated within position 11 of the peptide shifts the resonances significantly upfield. B. tyrosine incorporated at postion 11 C. Phenylalanine methyls shifted upfield compared to the alanine control, D.

3.6 **Efforts Towards a Perfluorinated Aryl-Thioether-Bridged Macrocycle Monitored with ^{19}F-NMR in Collaboration with Professor Ratmir Derda**

3.6.1 Introduction

A novel macrocyclization strategy utilizing cysteine side chains in a nucleophilic aromatic substitution (SnAr) reaction has proven to be a suitable method to constrain helical peptides, **Figure 3.19**. Derda and colleagues have used a highly reactive (up to 180 $M^{-1}s^{-1}$) S_NAr electrophile, decafluoro diphenylsulphone (DFS) to efficiently form a stable

macrocycle.[175] The reaction is completed within two hours by first adding a disulfide reducing agent, TCEP (1mM), diluting the reactants 10-fold with 0.5 mM Tris, pH 8.5, 5% DMF, and DFS to afford the final product.[175] Two peptides were identified to bind to Human Serum Albumin (HSA) to improve their serum half-life through phage display, but specific affinity values had not been ascertained. Molecules that are able to bind to the plasma have a dramatic effect on the transport and distribution of the drug, and allows for a prolonged half-life.[195] A major component within plasma that is frequently responsible for the binding of drugs is HSA.[196] HSA has two subdomains that bind the majority of its ligands: Site IIa and Site IIIa.[197] We evaluated two peptides for their affinity and site specificity towards HSA.

The peptides evaluated are identical except for the last three residues being either –KKK or –SSS (**Figure 3.19**), hence the naming scheme**, DFS-KKK** or **DFS-SSS**, respectively. To evaluate how the stabilized macrocycles affect affinity, we used a peptide observed fluorine NMR technique, analogous to prior PrOF NMR studies.[192] The utility of ^{19}F-NMR to analyze binding affinity of fluorinated protein to ligand has been validated in the Pomerantz lab.[190,198] A reverse experiment where the fluorine label on the ligand with increasing equivalents of protein titrated has been evaluated by others and shown to be an effective method to quantify peptide binding affinity.[199]

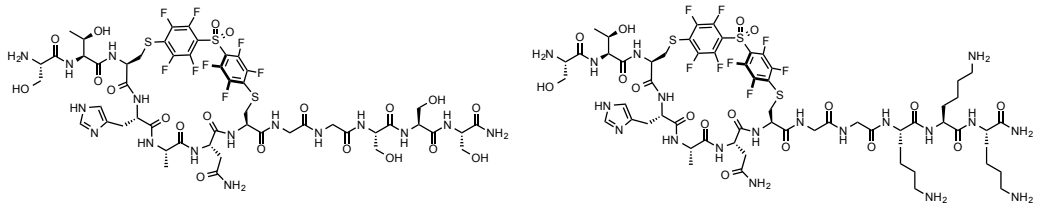

STCHANCGGSSS-DFS
DFS-SSS

STCHANCGGKKK-DFS
DFS-KKK

Figure 3.19 Decafluoro-diphenyl sulfone crosslinked peptide sequences shown for both **DFS-SSS** and **DFS-KKK**.

3.6.2 Results and Discussion

To assess conditions to monitor the fluorinated small molecule resonance shifts with increasing protein concentration, we used a known ligand of bovine serum albumin, Dexamethasone, which has one fluorine atom, a doublet at -165.4 ppm, **Figure 3.22**. It has been previously shown that dexamethasone binds to bovine serum albumin with ~ 30 μM affinity.[200] Using bovine serum albumin at increasing concentrations, a shift in the dexamethasone fluorine doublet upfield was observed (**Figure 3.22**). The resonance shift was fit to a binding isotherm, and a dissociation constant of ~ 30 μM was estimated. Due to the broadening of the peaks at higher BSA concentrations, and the high standard deviation of the binding fit, we could only conclude an estimation of K_d, **Figure 3.20**.

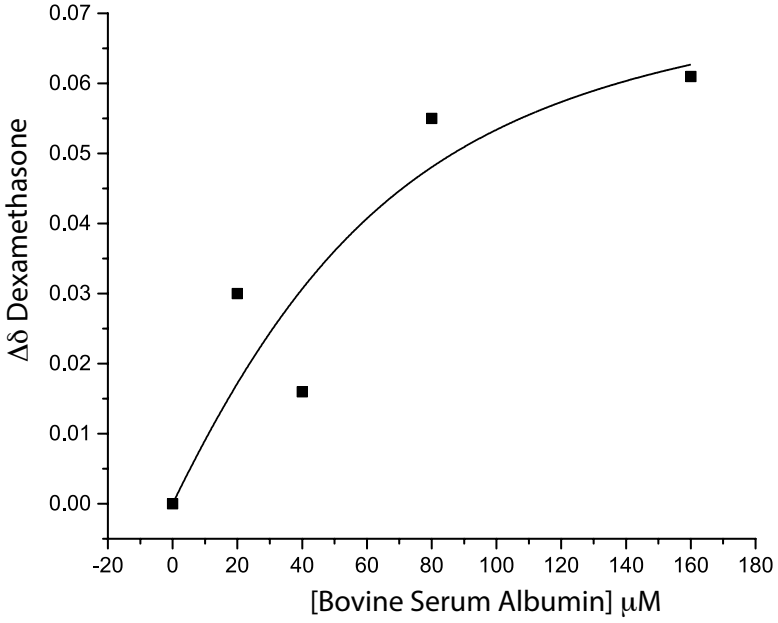

Figure 3.20 Binding Isotherm of Dexamethasone with Bovine Serum Albumin A K_d = 32 ± 59 μM was calculated from the binding fit. Due to such large error, this value should be only taken as an estimate.

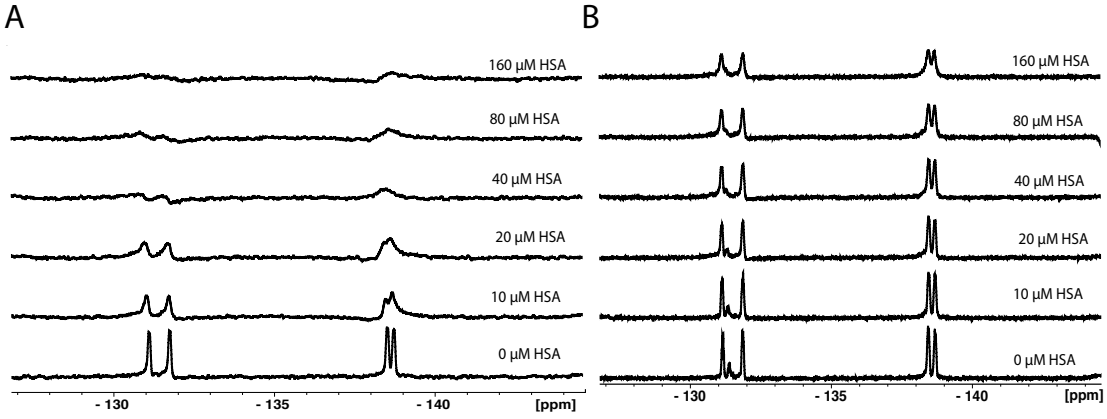

Figure 3.21 Increasing concentrations of HSA was added to a 20 μM DFS-KKK peptide solution. B. Added HSA was titrated into a constant 20 μM solution of DFS-SSS.

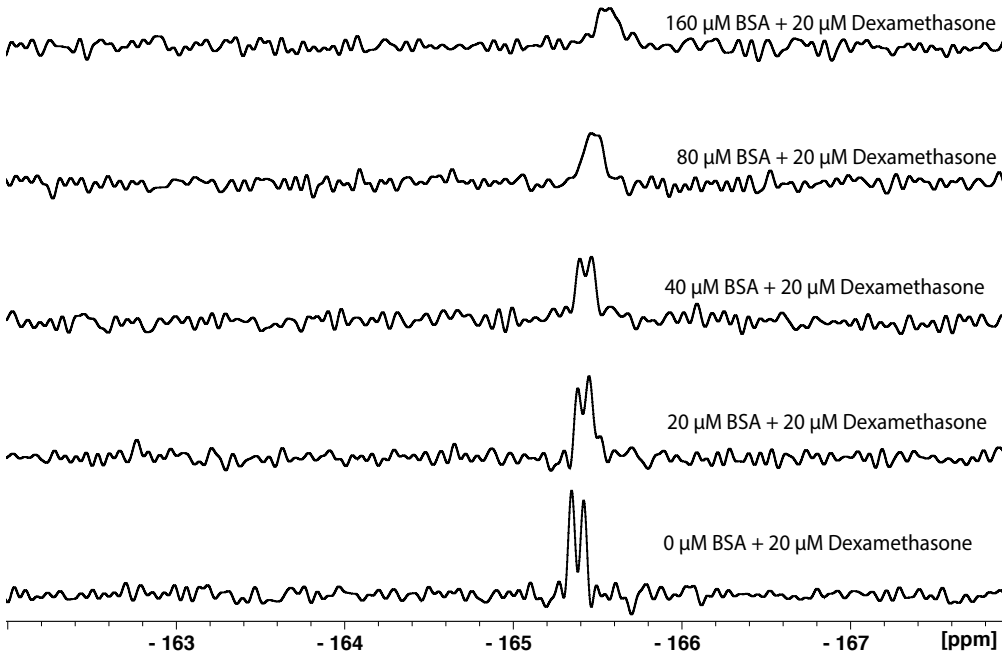

Figure 3.22. ^{19}F-NMR spectrum overlay with increasing concentrations of BSA titrated into Dexamethasone. The single fluorine doublet in dexamethasone shifts upfield and broadens into baseline. A binding isotherm fit to the resonance shift estimates the K_d to be around 30 µM.

After determining the proper experimental conditions, an evaluation of HSA with DFS cross-linked peptides were carried out, **Figure 3.21**. At a fixed concentration of DFS-peptide at 20 μM, HSA was titrated from 0-1.6 mM. No substantial change was observed for the aromatic fluorine residues of the DFS-SSS peptide, but with DFS-KKK peptide, a broadening of the fluorine resonances into baseline was seen. The broadening effect would be characterized as intermediate chemical exchange kinetics. Due to the broadening, a binding isotherm cannot be fit to a resonance shift; however, intermediate chemical exchange binding behavior is consistent with ligands binding with low to mid-micromolar affinity.

To parse out the binding site on HSA, competition NMR assays were used with previously reported HSA ligands: L-Tryptophan and Ibuprofen. Both L-Tryptophan and Ibuprofen bind the IIIa site of HSA, albeit with varying affinity. [196]

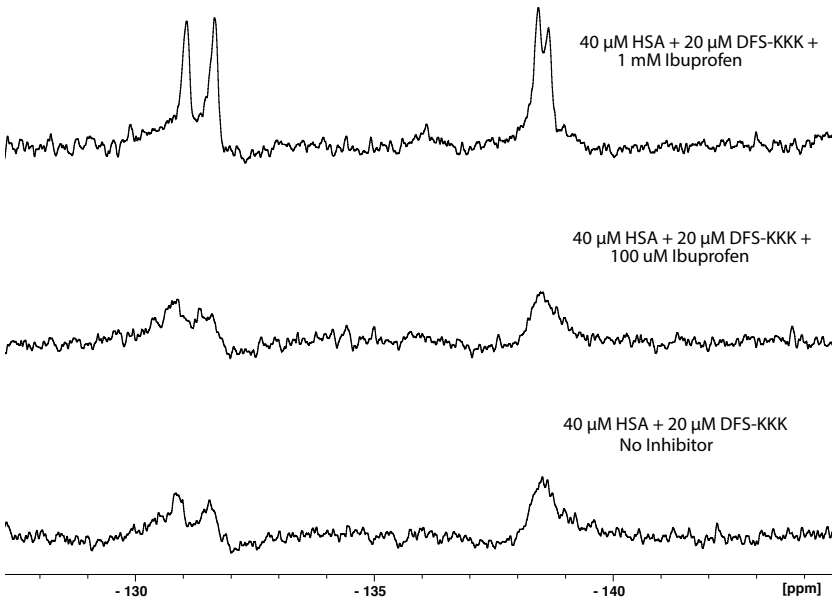

Figure 3.23 Competition with Ibuprofen at 0, 100 uM, and 1 mM. Resonances come back out of baseline at 1 mM competitor, indicating binding at the same site. Ibuprofen has previously been observed to bind site IIIa.

Ibuprofen is a tight binder of the site, with 370 nM, **Figure 3.23**. L-Tryptophan however has a lower affinity towards the same site, K_d = 100 µM.[196] To better understand the binding site of the DFS-KKK ligand, we competed it off with both the high and low affinity competitors. By adding 20 µM of DFS-KKK to 40 µM HSA, a broadening of resonances is observed. If the competitor binds at the same site with higher affinity than the peptide, the resonances will return. Such a result could also be due to an allosteric effect. We were unable to compete off 20 µM DFS-KKK with either 100 µM or 1 mM of L-Tryptophan, most likely due to the weaker affinity. With Ibuprofen, however, we did see competition with 1 mM, where the resonances were able to return fully.

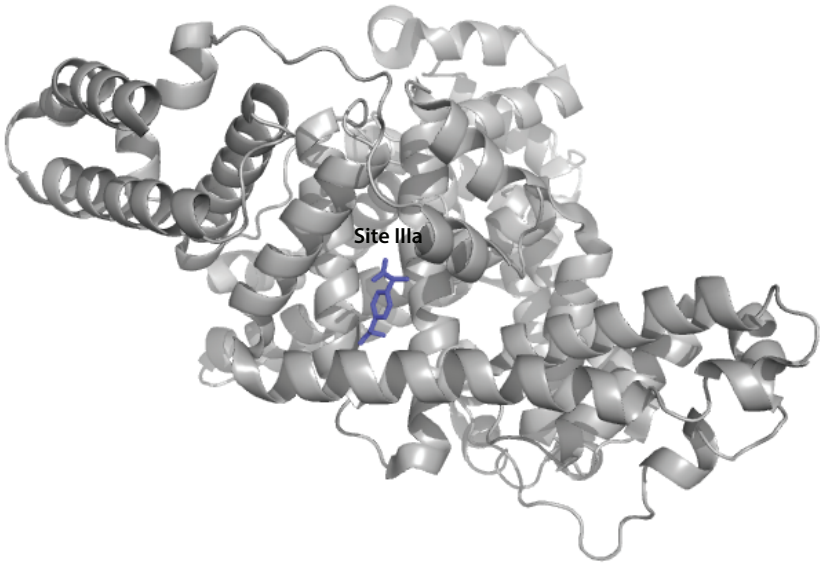

Figure 3.24 Solution structure of Human Serum Albumin (gray) binding to Ibuprofen (blue) in the IIIa binding site with 370 nM affinity (PDB ID: 2BXG)[201]

3.6.3 Conclusion

Two peptides with a DFS-crosslink were evaluated for affinity towards the HSA protein. The peptide, **DFS-KKK** showed a significant enhancement of affinity towards HSA, with broadening of the resonances seen at 20-40 μM. This type of broadening of the fluorine resonances is due to intermediate exchange, consistent with a mid-micromolar affinity. HSA displays specificity towards **DFS-KKK**; however, the **DFS-SSS** peptide displays only modest broadening of fluorinated aryl resonances near 80-160 μM HSA. The charged lysine residues may fit within the binding site more readily. The binding site IIIa may be less amenable to the serine residues, **Figure 3.24**. More structural and binding studies may elucidate the specificity seen towards **DFS-KKK**. Crystal structures of HSA with DFS-peptides are currently being explored. This is a first step in identifying DFS-

peptide interactions with proteins such as HSA. Furthermore, the utility of using fluorinated ligands to identify protein interactions is far reaching due to the ubiquitous use of fluorine within drug candidates (20% in 2014).[143] This work highlights the utility of ^{19}F-NMR to monitor fluorinated ligands binding to the protein of interest.

3.7 **Experimental Section**

3.7.1 Computational Methods

Geometry optimizations of the compounds listed in **Figure 3.3A** were carried out in the gas phase with Q-Chem 4.1[202] at the B3LYP/6-31G(d) level by Alessandro Cembran.[203–206] Free energies of solvation in water were then carried out as single point calculations on the gas phase minima with the same functional, basis set, and program using the continuum solvation model SM12.[182] Charge analysis was performed using the CM5 model.[207]

3.7.2 Density Functional Theory Calculations of Hydrogen Bond Interactions

We investigated the strength of hydrogen bonds with water of both sulfone and sulfoxide using density functional theory calculations on dimethyl sulfoxide (DMSO) and methylsulfonylmethane (MSM). The smaller models with respect the main text were chosen in order to rule out any possibility of different energy values arising from different conformational states of the ethyl moiety with respect to the water molecule. By using this approach, any energy difference between the sulfoxide and sulfone is to be attributed only to the different hydrogen bonding strength.

We employed the same level of theory and program as for the calculations described in the main text. Calculations were performed with Q-Chem 4.1 at the B3LYP/6-31G(d) level, and solvation effects were taken into account using the SM12 continuum solvation model. In one set of calculations, the difference in the hydrogen bond energy of the complex $DMSO \cdot Water$ and the complex $MSM \cdot Water$ was calculated from the gas-phase optimized geometries (see **Figure 3.25**) using the following scheme:

$$\Delta(\Delta E_{interaction}) = [E(DMSO \cdot Water) - E(DMSO)] - [E(MSM \cdot Water) - E(MSM)] \quad (1)$$

To take into account the solvation effects on the calculated energies, single point energy calculations on all the gas-phase optimized geometries were performed using the SM12 continuum solvation models in water solution. Using the same scheme, in a second set of calculations we investigated the effects of adding a second water molecule to the complex. As shown in **Figure 3.25**, for MSM each oxygen is hydrogen bonded to one water. The results in **Table 3.3** show that in the gas phase the hydrogen bond formed by DMSO is 2.6 kcal/mol stronger than for MSM. Inclusion of solvation effects further increases the strength of the interaction difference to 3.3 kcal/mol. Addition of a second water molecule confirms this trend, showing a stronger interaction energy for DMSO both in the gas phase (3.1 kcal/mol) and including solvation effects (5.6 kcal/mol).

Table 3.3 Interaction energy differences from Eq. 1 calculated at the B3LYP/6-31G(d) in the gas phase and using the SM12 solvation model. Results are reported in kcal/mol for the complexes with one water and two water molecules.

Molecule	Gas Phase	Water Solution
1 Water Complex	-2.6	-3.3
2 Waters Complex	-3.1	-5.6

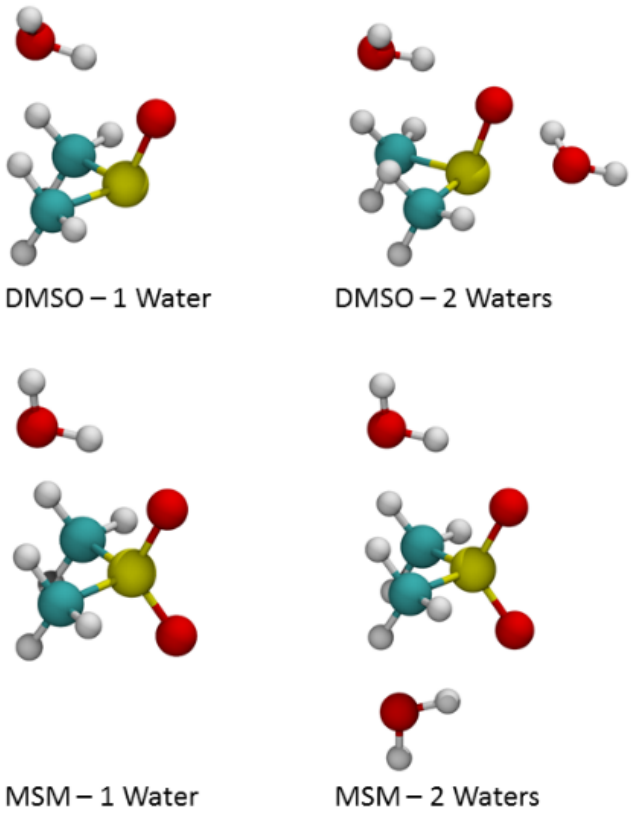

Figure 3.25 Gas-phase optimized geometries of the water complexes of DMSO and MSM.

3.7.3 Alkylation of peptides

Prior to purification of the acyclic peptide, the peptide was dissolved (~5 mg/mL) in 1:5 CH_3CN:NH_4HCO_3 (20 mM, pH 8.3) to which 1.5 eq TCEP was added and stirred at RT for ~ 1h.[193] The solution pH is maintained at pH 8 with 1N NaOH. Dibromoalkane (10 eq) is added, and heated in a microwave reactor for 25 min at 80 ºC. The crude mixture is diluted 2X with a 60:40 0.1% TFA water: CH_3CN solution followed by RP-HPLC purification.

3.7.4 Oxidation of thioether crosslinked peptides

3.7.4.1 Sulfone formation

A solution of 30% (v/v) hydrogen peroxide (49 μL) was added to a chilled formic acid solution (1.95 μL) and stirred on ice for 2 h to form performic acid. The MLL peptide (~1 mg) was separately dissolved into 80 μL formic acid, 20 μL methanol; solution and chilled to 4 ºC. Performic acid (50 eq) was added and stirred for 1.5 h. The reaction was quenched with β-mercaptoethanol and purified on HPLC.[181]

3.7.4.2 Sulfoxide formation

The MLL peptide (~1 mg) was dissolved in 600 μL methanol and 20 μL of 30% (v/v) hydrogen peroxide solution (450 eq). The reaction was stirred for 2 h, and then quenched with β-mercaptoethanol and purified by RP-HPLC.[208]

3.7.5 Circular Dichroism Methods

Peptides were run on a Jasco J-815 Spectropolarimeter at room temperature using standard measurement parameters: wavelength, 190-260 nm; step resolution, 1.0 nm; accumulations, 4; path length, 0.1 cm; bandwidth, 1 nm; scanning speed, 50 nm/min. Compounds were dissolved in 10 mM phosphate buffer, pH 7.4 with 30% TFE to concentrations of 100 μM. A baseline of 30% TFE in buffer was subtracted from each run. Data was converted from mdeg into ellipticity ([θ], deg cm^2 $dmol^{-1}$) using equation 1. below:

$$[\theta] = \frac{\psi}{1000nlc} \quad \text{(Eq. 1)}$$

where ψ is the signal in degrees, *n* is the number of amides, *l* is the path length in cm, and *c* is the concentration in $dmol/cm^3$. The percent helicity is the ratio of $[\theta]_{222}/^{max}[\theta]_{222}$ where

$^{max}[\theta]_{222} = (-40\ 000\ X\ [1 - k/n])$, k = 2.5, n = number of residues.[18]

3.7.6 Proteolysis

Peptides were dissolved in 100 mM NH_4HCO_3, pH 8.1 to a final concentration of 200 μM. A 1 mg/mL stock concentration of trypsin was prepared, and using a 100: 1 substrate: enzyme ratio, trypsin was added to a stirring peptide solution. Time points were quenched with 10 μL of trifluoroacetic acid, and injected onto a Dionex 3000 RP-HPLC. Peak area degradation was analyzed and plotted against time.

3.7.7 Protein Observed Fluorine NMR (PrOF)

Protein observed 1D ^{19}F NMR samples were obtained as previously described[192] using a frequency window of -131 to -141 ppm, a D1 of 0.6 sec and an acquisition time of 0.1 sec. Peptide stock solutions were prepared in DMSO at 1-10 mM. Peptides were titrated into KIX (protein solutions at 55 μM in 50 mM HEPES, 100 mM NaCl, 5% D_2O, pH 7.4) at 0, 0.5, 1.0, and 2.0 equivalents of protein with a final concentration of 0.5% (v/v) DMSO.

3.7.8 Protein Expression Experimental

3FY-labeled KIX was expressed using *E. coli*/Bl21(DE3) co-transformed with the pRARE plasmid expressing tRNAs for rare codons. 3FY-labeled protein was expressed with LB media grown until an O.D. at 600 nm of 0.7 was reached, as verified on a Varian Cary 50 Bio UV/Vis spectrophotometer. Cells were harvested and resuspended in defined media of Muchmore et al.[209] which contained 3-fluorotyrosine (60 mg/L) in place of tyrosine. Resuspended bacteria were incubated at 37 ^{o}C while shaking for 1.5 h. The bacterial culture was cooled to 20 ^{o}C for 30 min. then induced with 1 mM IPTG for 18-20 h at 20 °C. Cells were pelleted and stored at -20 °C. Pellets were thawed to room temperature, and lysis buffer (50 mM Phsophate pH 7.4, 300 mM NaCl), PMSF (5 mM), and Egg White Lysozyme (1 mg/mL) were added followed by sonication and purified via FPLC using NTA-resin (Qiagen) and an imidazole gradient (0 to 400 mM). Concentration of KIX was evaluated via absorbance at 280 nm.[210]

3.7.9 Solid Phase Peptide Synthesis

Peptides were made on a 25 μmol scale on NovaSyn TGR® resin in a CEM MARS microwave reactor. The resin was weighed into a fritted 6 mL syringe, swelled in methylene chloride (DCM) for 5 min, and washed with *N,N'*-dimethylformamide (DMF) three times. In a separate vial containing 25 μmols of Fmoc-amino acid, 1000 μL of DMF, 1-hydroxybenzotriazole monohydrate (HOBT, 200 μL, 0.5 M solution in DMF), *O*-benzotriazol-1-yl-*N, N, N', N'*-tetramethyluronium hexafluorophosphate (HBTU 200 μL, 0.5 M solution in DMF), and diisopropylethylamine (DIEA 200 μL, 1.0 M solution in DMF) activated the amino acid. The mixture stirred at 70 °C (400 W power, ramp 2 min, hold 4 min) for the coupling reaction. The resin was washed 3 x with DMF, DCM, and 3X with DMF). To remove the Fmoc group, 2 mL of 20% piperidine in DMF (solution v/v) was added to the resin and the solution was irradiated at 80 °C (400 W power, ramp 2 min, hold 2 min). The resin was subsequently washed and the coupling/deprotection reactions were repeated until the complete peptide was synthesized and the final residue deprotected. Acetylation of the N-terminus was accomplished by adding 500 μL acetic anhydride, 100 μL triethylamine (TEA), and 1.4 mL DCM to the resin and stirring for 1.5 h. For fluorescent peptides, a β-alanine spacer was added to the N-terminus. With the final Fmoc-deprotected from β-alanine, NHS-fluorescein ester (2 eq) was stirred with the peptide on resin (12.5 μmols) in 1000 μL DMF and 200 μL DIEA, stirred at R.T. overnight. Cleavage from the resin was carried out by stirring the resing for 2 h in a mixture 95:3:2 TFA: thioanisole: ethanedithiol at room temperature. The cleavage solution was separated from the resin, and concentrated under a stream of N_2. The peptide was precipitated out in ether, cooled to -20 °C for at least 15 min, and pelleted out by centrifugation at 3000 x *g* for 5

min at 4 °C. The pellet was dissolved into a 60:40 0.1% TFA in H_2O: acetonitrile mixture with added DMF to ensure dissolution. Dissolved peptides were injected into a Dionex Ultimate 3000 RP-HPLC using a C-18 column on a 10-60% acetonitrile gradient over 60 min. Purified peptides were analyzed via Ab-Sciex 5800 MALDI-TOF/TOF Mass Spectrometer. Peptides theoretical and actual masses are shown in **Table 3.5**.

3.7.10 Fluorescence Microscopy

HeLa cells were seeded 100,000 on 35 mM glass-bottomed plates and incubated in 2 mL media (DMEM with 1% penicillin-streptomycin cocktail) supplemented with 10% FBS for 24 h at 37 °C. Checked for confluency (~ 40%), aspirated the media, rinsed 2x2 mL PBS. We added 1.5 mL PBS and incubated with 2.7 μM fluorescently-labeled peptide for 60 min at 37 °C. The cells were aspirated and washed 2X 2 mL PBS. 1 mL of paraformaldehyde was added, agitated on shaker for 10 min., aspirated, and rinsed 2X 2 mL PBS. 1 mL of Hoescht stain 34560 (1 μg/mL in H_2O) was added to stain nucleus. Shake for 10 min., and were aspirated and washed 2X 2 mL PBS. A final 2 mL of PBS was added and images were taken on a were taken on an Olympus FV1000 IX2 Inverted Confocal Microscope. Images were analyzed with Olympus Fluoview, v. 4.0 software. [Hoescht: λ(ex) = 358 nm, fluorescein: λ(ex) = 492 nm].

3.7.11 DFS-peptide titrations with serum albumin

Peptide observed 1D ^{19}F NMR samples were obtained as previously described using a frequency window of -160 to -170 ppm, a D1 of 0.7 sec and an acquisition time of 0.05 sec. Dexamethasone and BSA stock solutions were prepared at 2 mM. BSA was titrated into DexMeth (20 μM), or HSA was titrated into DFS-SSS or DFS-KKK at 0, 10,

20, 40, 80, and 160 μM. Competition studies were done with 0, 100 μM, or 1 mM of L-Trp or Ibuprofen, 40 μM of HSA, and 20 μM of DFS-KKK peptide. A frequency window of -125-145 ppm was used. See **Table 3.4** below for competition experimental conditions.

Table 3.4 Competitive ^{19}F-NMR experiments with added Ibuprofen or L-Tryptophan

Competition Expt	Inhibitor Ibuprofen (100 mM) μL	Inhibitor L-Tryptophan (5 mM) uL	DMSO	Protein (40 μM) Volume	KKK-DFS (20 μM) Volume	TFE (μL)	D2O (μL)	Water (μL)
No Inhibitor L-Trp Blank	0	0	0	10	15.4	2	25	447.6
No Inhibitor Ibuprofen Blank	0	0	5	10	15.4	2	25	442.6
100 uM Ibuprofen	0.5	0	4.5	10	15.4	2	25	442.6
100 uM L=Trp	0	10	0	10	15.4	2	25	437.6
1 mM Ibuprofen	5	0	0	10	15.4	2	25	442.6
1 mM L-Trp	0	100	0	10	15.4	2	25	347.6

Table 3.5 Peptide sequences with corresponding theoretical mass, and observed mass, taken on a MALDI-TOF/TOF mass spectrometer.

Name	Peptide sequences	Theoretical [M + Na]	Observed [M + Na]
WT MLL15	Ac-ILPSDIMDFVLKNTY	1831.94	1832.3
MLL15-Sulfone	Ac-ILPSDIMDFVLKNTY + 2Oxygen	1863.93	1864.1
MLL15-Suloxide	Ac-ILPSDIMDFVLKNTY + Oxygen	1825.9*	1825.8**
1X	Ac-SKICDFCdLKNTY + 8 Carbon Chain	1607.8	1607.7
1	Ac-SKICDFCdLKNTY	1497.69	1497.5
2X	Ac-SKIMDFCLKNCY + 8 Carbon Chain	1637.8	1637.5
2	Ac-SKIMDFCLKNCY	1483.7	1483.45
3X	Ac-SKICDFVLKNCY + 10 Carbon Chain	1633.86	1634.06
3	Ac-SKICDFVLKNCY	1472.7*	1473.5**
3Xa	Ac- SKICDFVLKNCY + 10C + 4Oxygen (sulfone)	1697.84	1697.75
3Xb	Ac- SKICDFVLKNCY + 10C + 2Oxygen (sulfoxide)	1665.85	1665.76
4X	Ac-ILPCDIMDWICKNTY+ 10 Carbon Chain	2030.0	2029.2
4	Ac-ILPCDIMDWICKNTY	1890.8	1891.0
5	Ac-ILPSDICDWILKNCY	1835.9*	1836.97**
5X	Ac-ILPSDICDWILKNCY + 10 Carbon Chain	1998.04	1997.39
5Xa	Ac-ILPSDICDWILKNCY+ 10 Carbon Chain + 4 Oxygen	2062.02	2063.11
5Xb	Ac-ILPSDICDWILKNCY+ 10 Carbon Chain + 2 Oxygen	2008.03*	2007.95**
6X	ILPCDICdDWILKNTY+ 8 Carbon Chain	1984.0	1983.2
6	ILPCDICdDWILKNTY	1872.9	1873.0
7X	Ac-SKICDFVLKNPnY + 10 Carbon Chain	1661.89	1662.2
7	Ac-SKICDFVLKNPnY	1523.75	1524.1
8X	Ac-SKICDFVPnKNTY + 8 Carbon Chain	1621.82	1622.1
8	Ac-SKICDFVPnKNTY	1511.71	1511.9
Fluor-5X	K_{fluor}-βAILPSDICDWILKNCY +10 Carbon Chain	2513.95	2513.2
Fluor-5	K_{fluor}-$^{\beta}$AILPSDICDWILKNCY	2373.06	2373.3
Octa-Arg-Fluor	Fluor-$^{\beta}$ARRRRRRRR	1695.94*	1696.26**
GP4097A	Ac-SKIMDCILKCTY + *m*-xylene	1582.78*	1582.88**
GP4097B	Ac-SKICDWICKNTY + *m*-xylene	1638.77	1638.63

** Denotes [M+H] observed mass
* Denotes [M+H] theoretical mass

Table 3.6 Peptide sequences with corresponding %B elution from HPLC trace

No.	Sequences	Linker site	HPLC %B Elution
WT MLL15	ILPSDIMDFVLKNTY	n/a	51
1	SKICDFC$_d$LKNTY	i,i+3	33
1X	SKICDFC$_d$LKNTY	i,i+3	44
2	SKIMDFCLKNCY	i,i+4	33
2X	SKIMDFCLKNCY	i,i+4	47
3	SKICDFVLKNCY	i,i+7	39
3X	SKICDFVLKNCY	i,i+7	51
3Xa	SKICDFVLKNCY	i,i+7	37
3Xb	SKICDFVLKNCY	i,i+7	36
4	ILPCDIMDWICKNTY	i,i+7	54
4X	ILPCDIMDWICKNTY	i,i+7	66
5	ILPSDICDWILKNCY	i,i+7	55
5X	ILPSDICDWILKNCY	i,i+7	66
5Xa	ILPSDICDWILKNCY	i,i+7	51
5Xb	ILPSDICDWILKNCY	i,i+7	50
6	ILPCDICdDWILKNTY	i,i+3	54
6X	ILPCDICdDWILKNTY	i,i+3	68
7	SKICDFVLKNPnY	i,i+7	41
7X	SKICDFVLKNPnY	i,i+7	56
8	SKICDFVPnKNTY	i,i+4	32

*Pn stands for Penicillamine

Table 3.7 Extended MLL peptides sequences with corresponding mass spectrometry data, , taken on a MALDI-TOF/TOF mass spectrometer.

Peptide Name	Sequence	Theoretical [M + Na]	Observed [M + Na]
MLL15 WT	ILPSDIMDFVLKNTY	1831.94	1833.06
A	ILPSDIMDFVLKNTPSMQAY	2347.16	2347.59
B	ILPSDIMDFVLKNT**A**SMQAY	2321.70	2321.47
C	ILPSDIMDFVLKNTP**A**MQAY	2331.17	2331.40
D	ILPSDIMDFVLKNTPS**A**QAY	2286.16	2286.51
E	ILPSDIMDFVLKNTPSM**A**AY	2290.14	2290.42
F	ILPSDIMDFVLKNTPSM**E**AY	2348.15	2348.49
G	ILPSDIMDFVLKNTPSM**F**AY	2366.17	2366.29
H	ILPSDIMDFVLKNTPSM**W**AY	2405.18	2405.49
I	ILPSDIMDFVLKNTPSM**Y**AY	2382.17	2382.43

3.7.12 HPLC Quality Control

Quality control HPLC traces below were run on two Dionex-3000 HPLC instruments with three different C-18 columns, which lead to slight deviations of retention times. Varied gradients of acetonitrile: 0.1%TFA water were run based on the hydrophobicity of peptide. The gradient used as well as the %acetonitrile (B solvent) at which the peptide elutes is shown on each Quality Control trace.

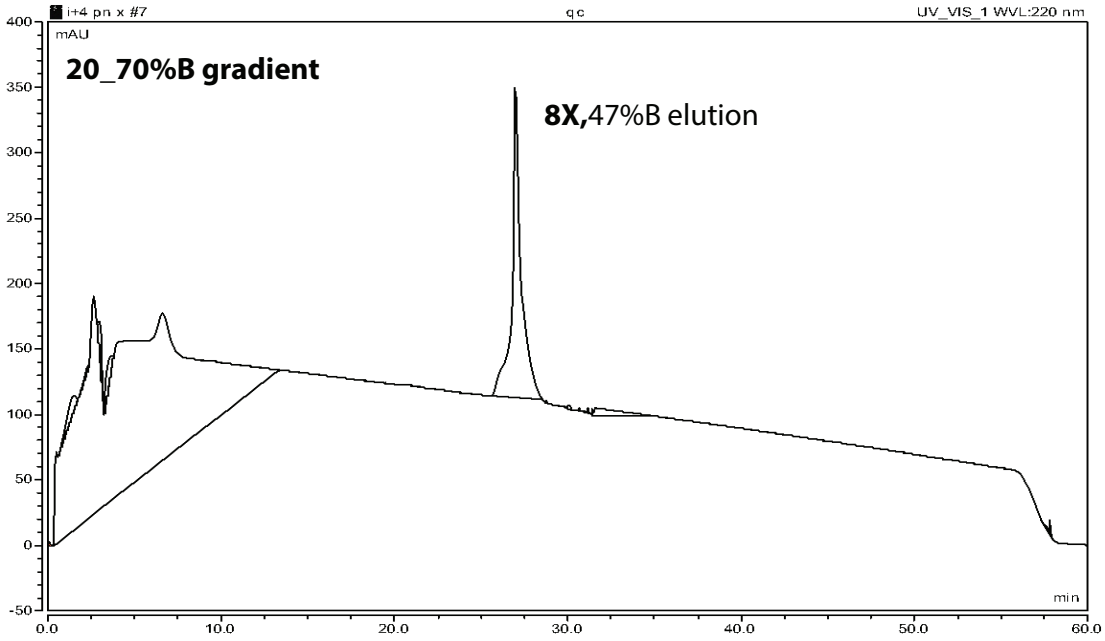
i+4 pn x #7
qc
UV_VIS_1 WVL:220 nm
mAU
20_70%B gradient
8X,47%B elution
min

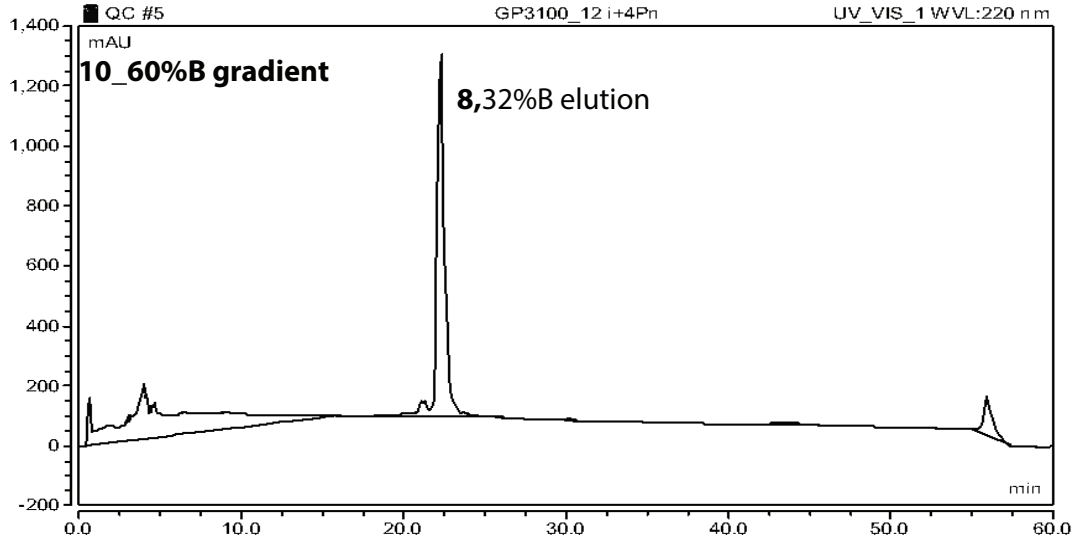
QC #5
GP3100_12 i+4Pn
UV_VIS_1 WVL:220 nm
mAU
10_60%B gradient
8,32%B elution
min

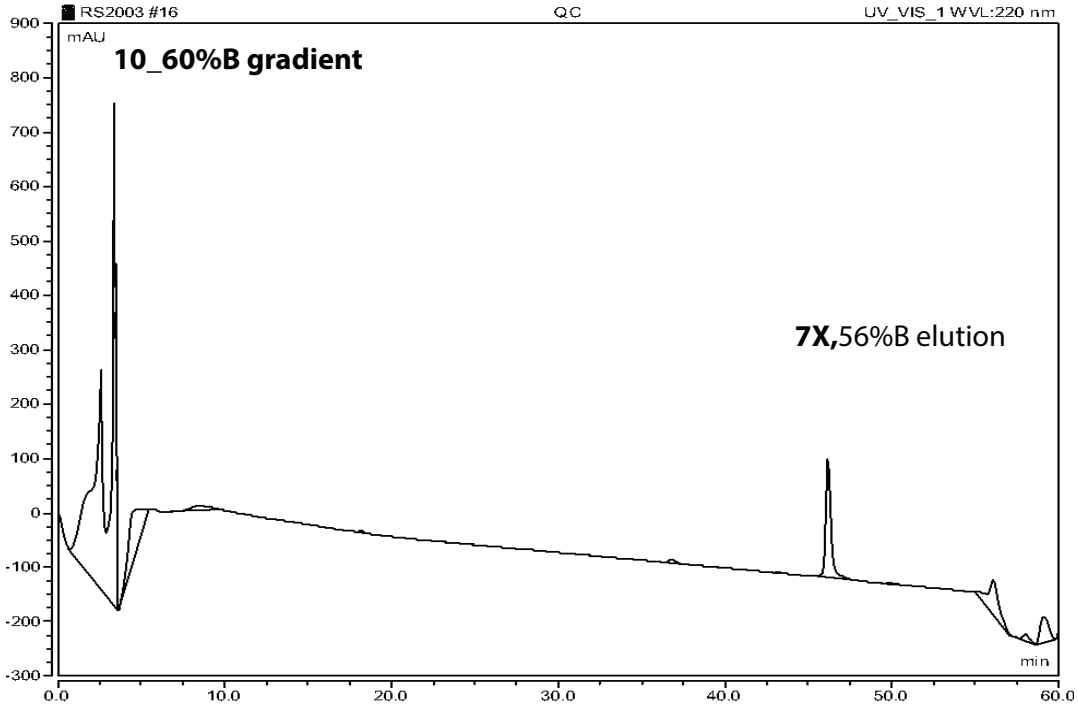
RS2003 #16
QC
UV_VIS_1 WVL:220 nm
mAU
10_60%B gradient
7X,56%B elution
min

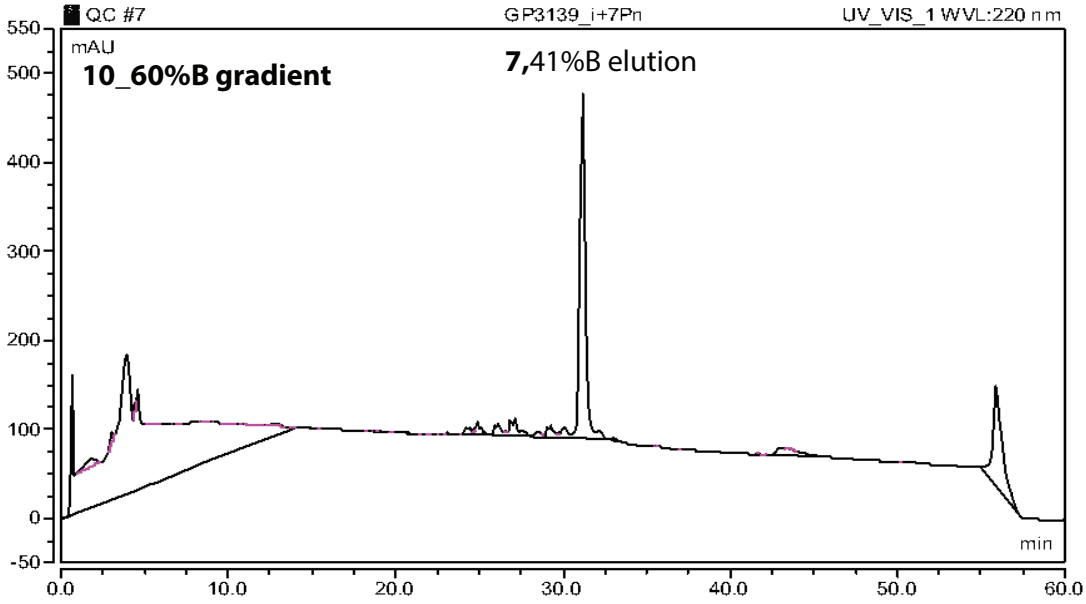
QC #7
GP3139_i+7Pn
UV_VIS_1 WVL:220 nm
mAU
10_60%B gradient
7,41%B elution
min

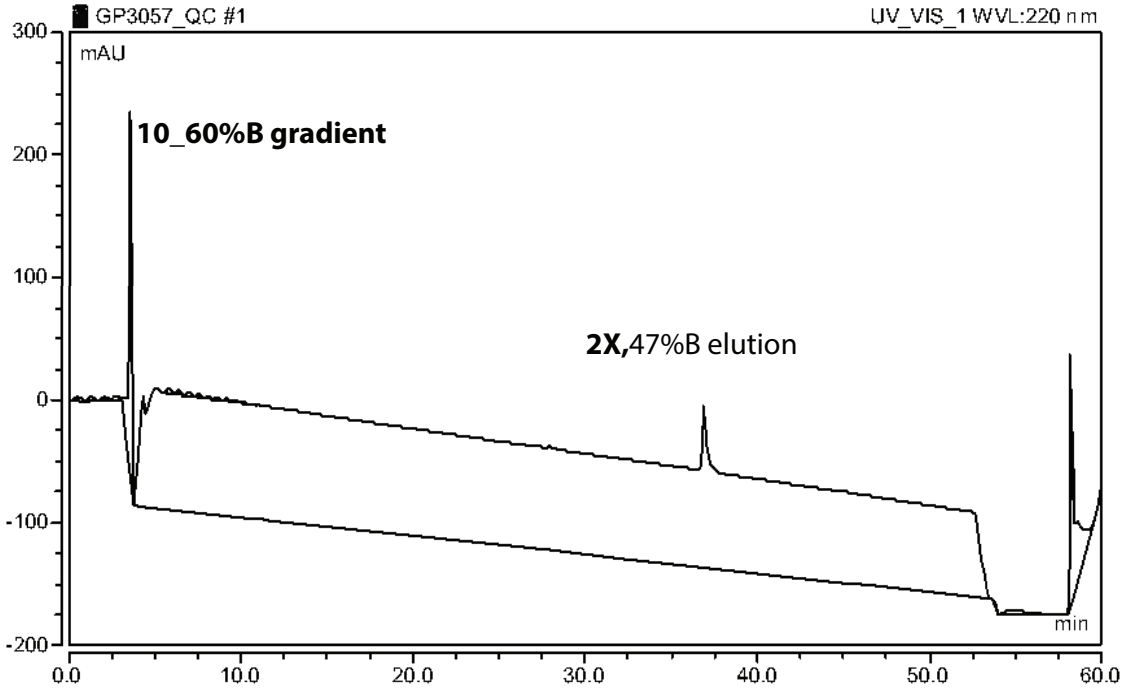
GP3057_QC #1
UV_VIS_1 WVL:220 nm
mAU
10_60%B gradient
2X,47%B elution
min
300
200
100
0
-100
-200
0.0
10.0
20.0
30.0
40.0
50.0
60.0

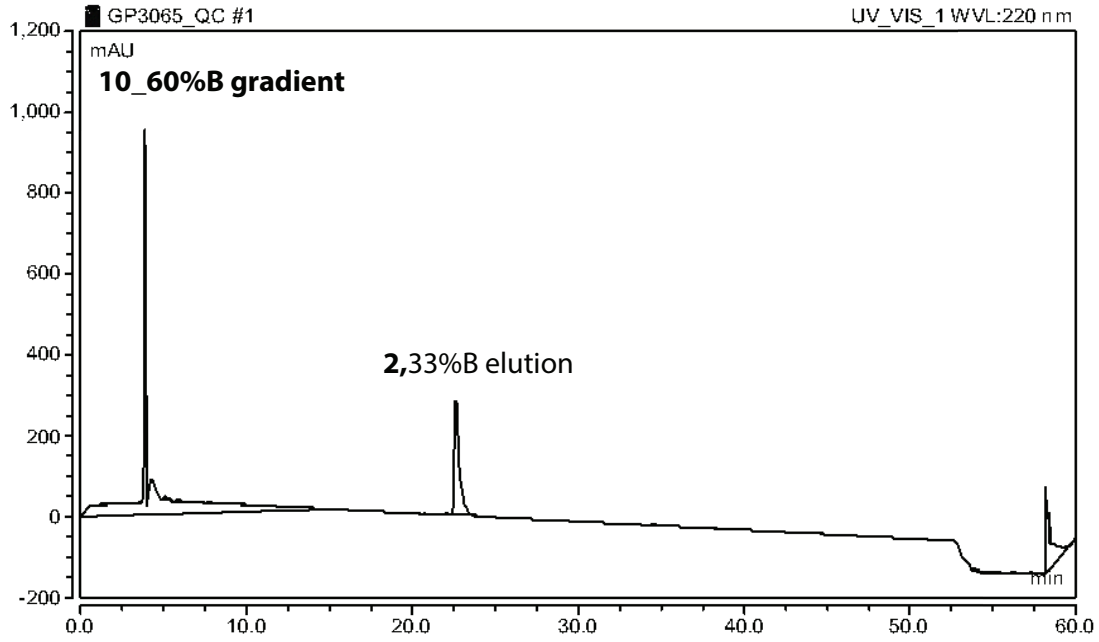
GP3065_QC #1
UV_VIS_1 WVL:220 nm
mAU
10_60%B gradient
2,33%B elution
min
1,200
1,000
800
600
400
200
0
-200
0.0
10.0
20.0
30.0
40.0
50.0
60.0

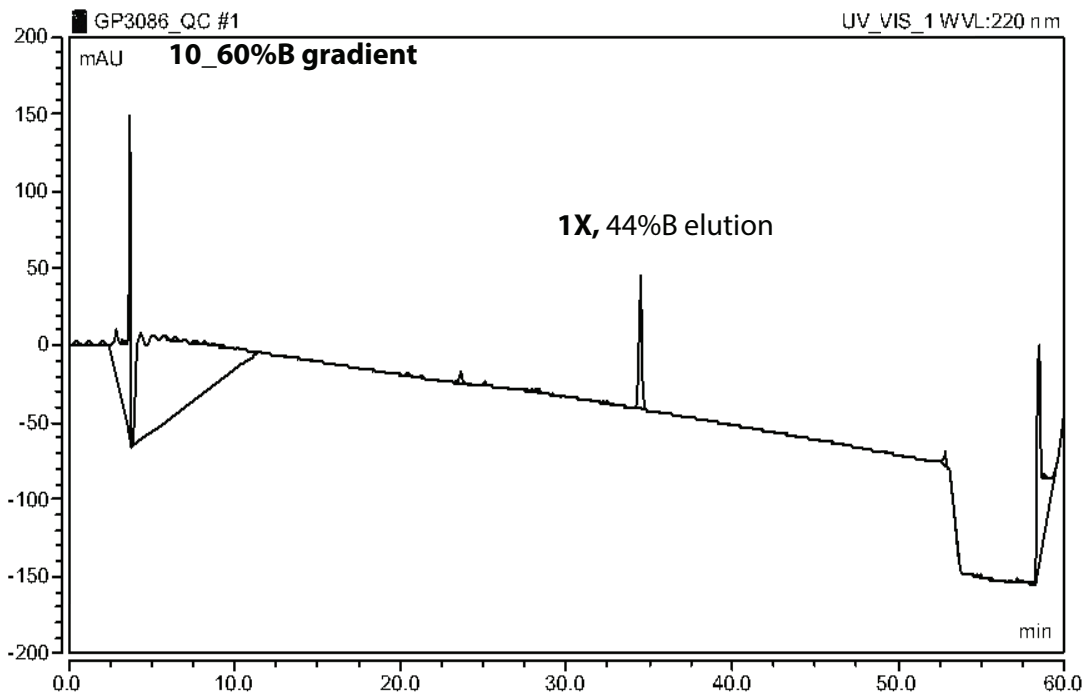
GP3086_QC #1
UV_VIS_1 WVL:220 nm
mAU
10_60%B gradient
1X, 44%B elution
min
200
150
100
50
0
-50
-100
-150
-200
0.0
10.0
20.0
30.0
40.0
50.0
60.0

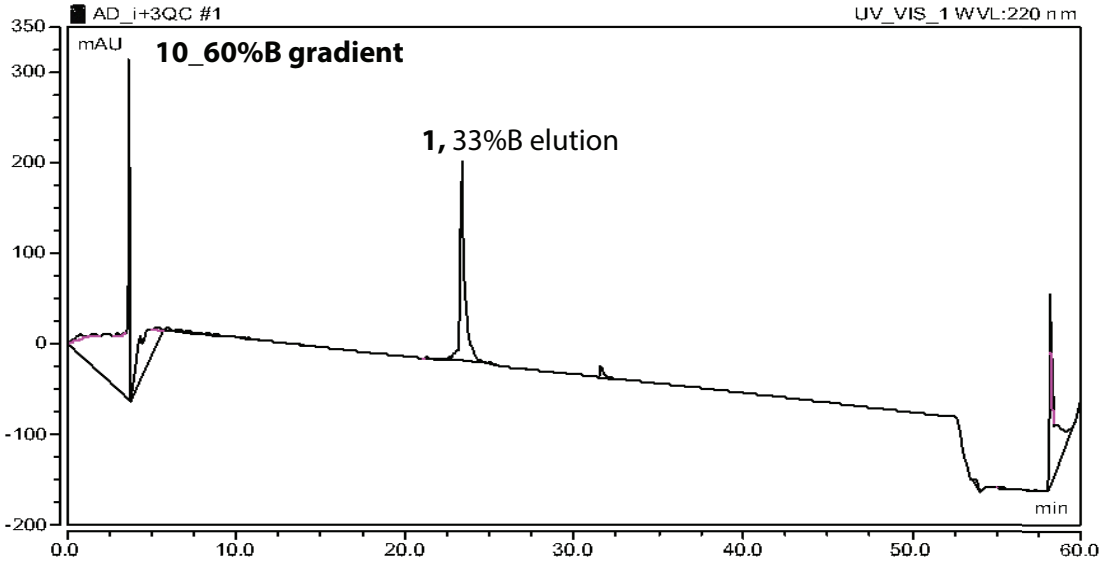
AD_i+3QC #1
UV_VIS_1 WVL:220 nm
mAU
10_60%B gradient
1, 33%B elution
min
350
300
200
100
0
-100
-200
0.0
10.0
20.0
30.0
40.0
50.0
60.0

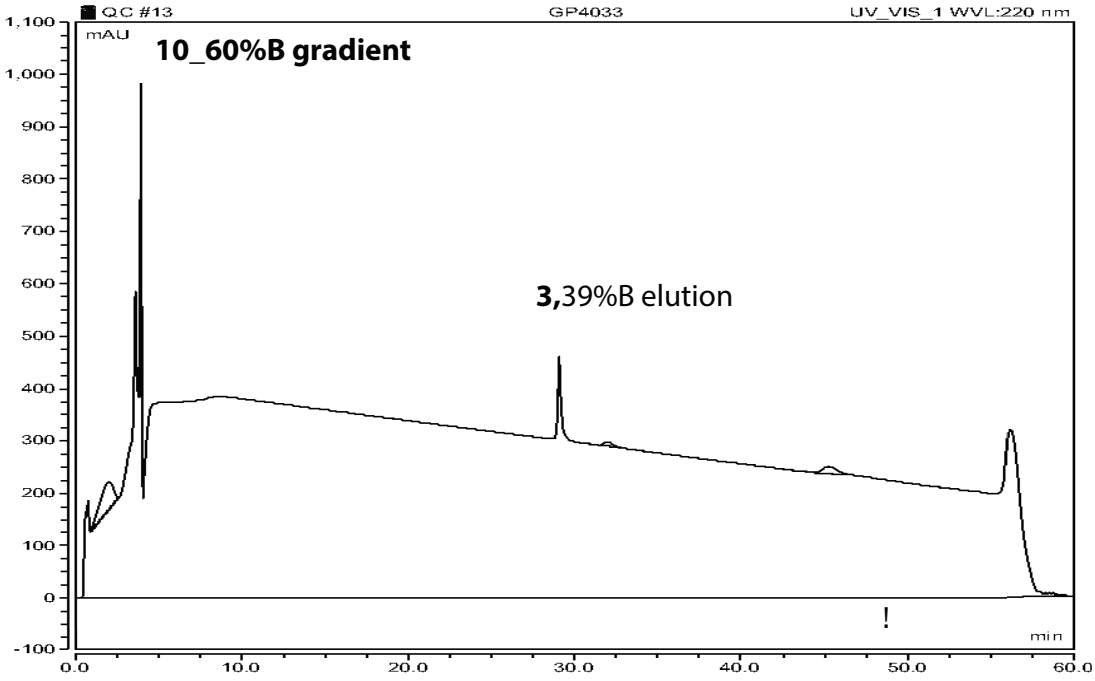
QC #13
GP4033
UV_VIS_1 WVL:220 nm
mAU
10_60%B gradient
3,39%B elution
!
min
1,100
1,000
900
800
700
600
500
400
300
200
100
0
-100
0.0
10.0
20.0
30.0
40.0
50.0
60.0

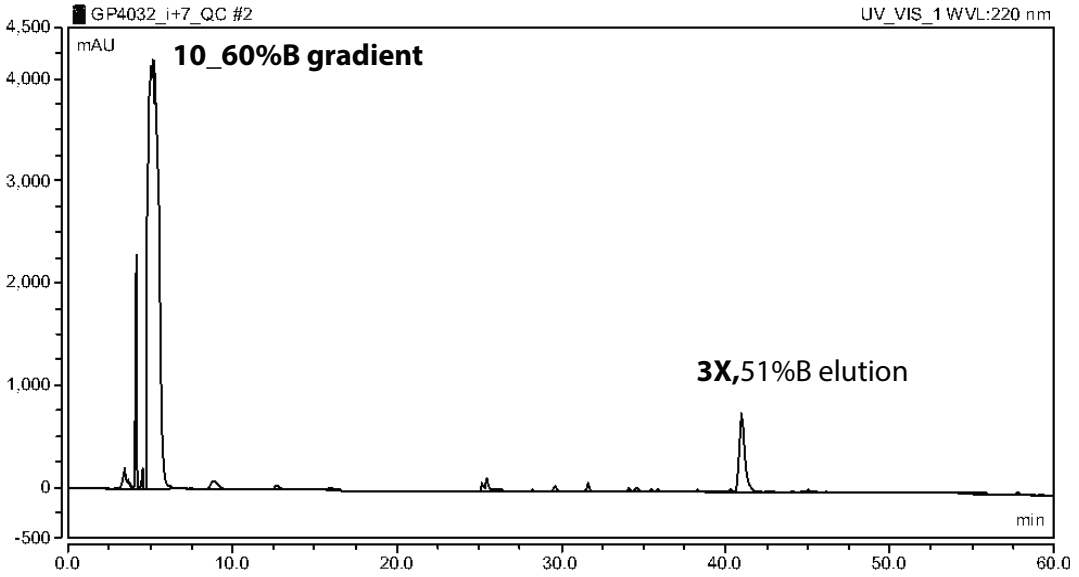
GP4032_i+7_QC #2
UV_VIS_1 WVL:220 nm
mAU
10_60%B gradient
3X,51%B elution
min
4,500
4,000
3,000
2,000
1,000
0
-500
0.0
10.0
20.0
30.0
40.0
50.0
60.0

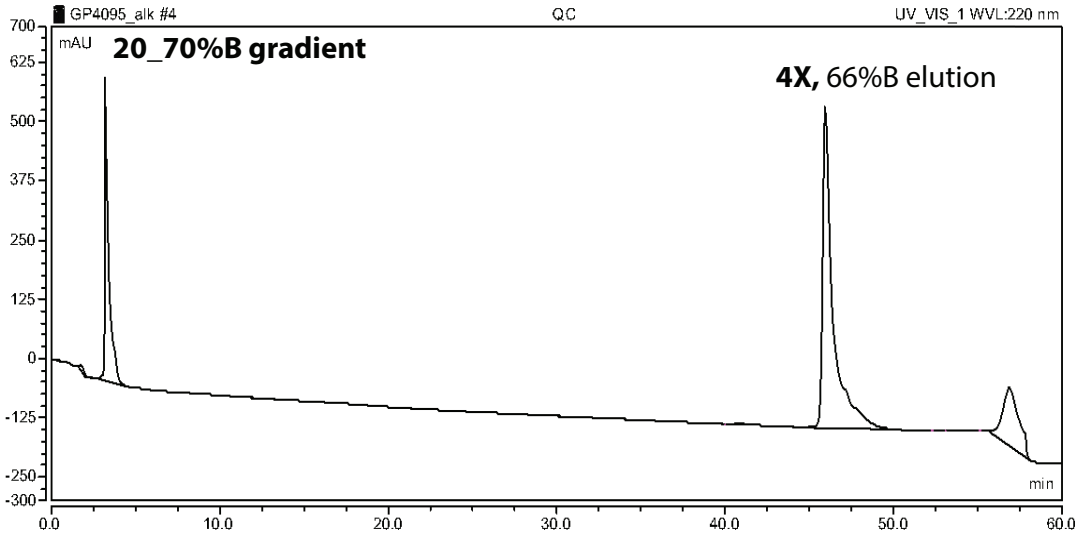
GP4095_alk #4
QC
UV_VIS_1 WVL:220 nm
mAU
20_70%B gradient
4X, 66%B elution
min

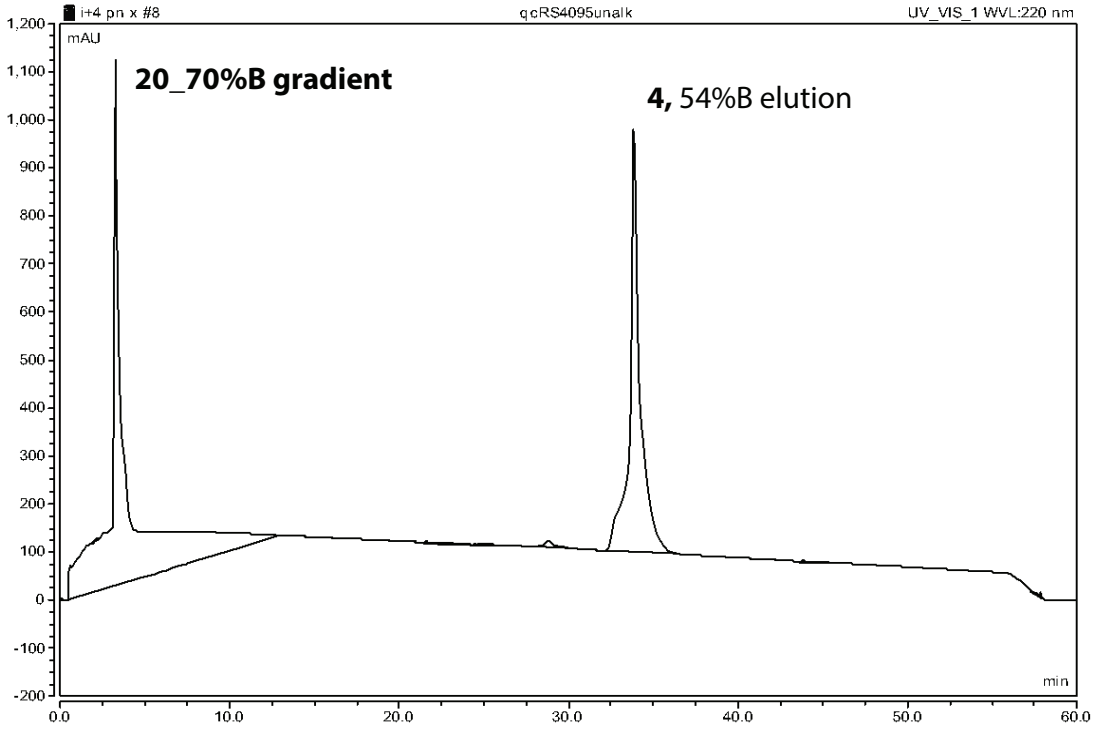
i+4 pn x #8
qcRS4095unalk
UV_VIS_1 WVL:220 nm
mAU
20_70%B gradient
4, 54%B elution
min

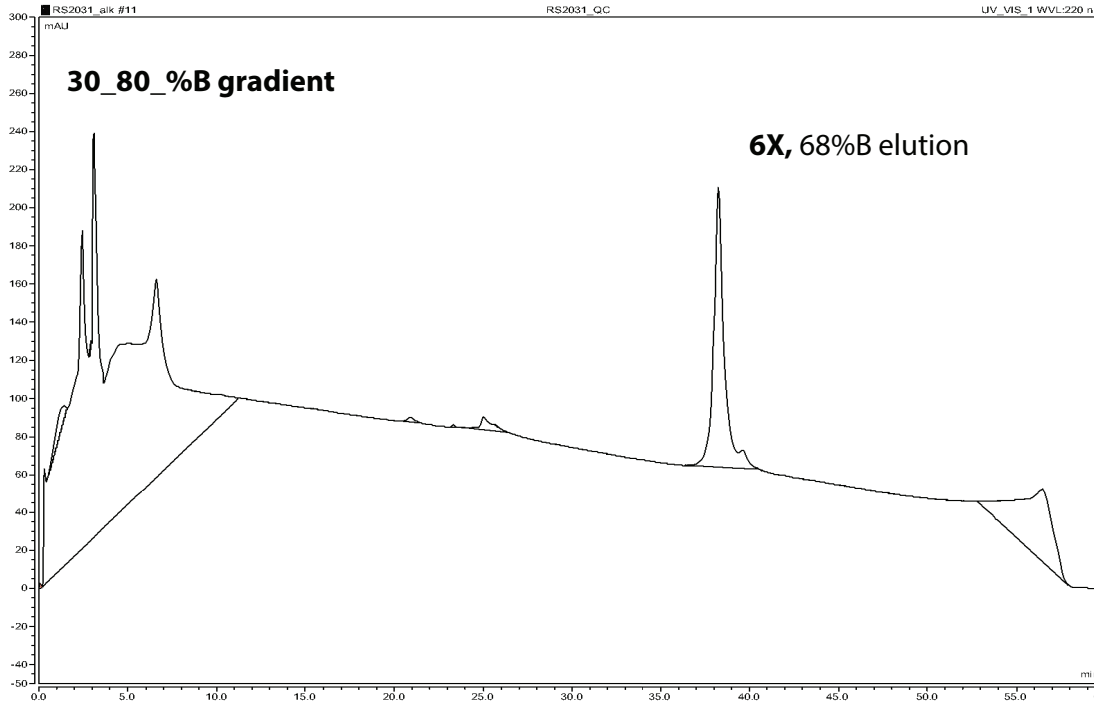
RS2031_alk #11
RS2031_QC
UV_VIS_1 WVL:220 n
mAU
30_80_%B gradient
6X, 68%B elution
min

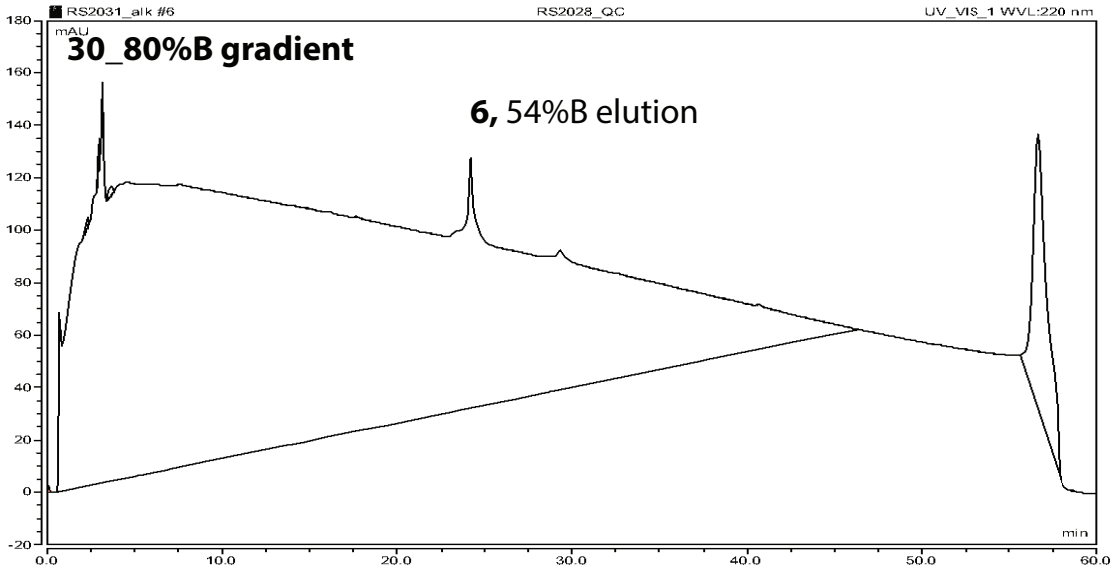
RS2031_alk #6
RS2028_QC
UV_VIS_1 WVL:220 nm
mAU
30_80%B gradient
6, 54%B elution
min

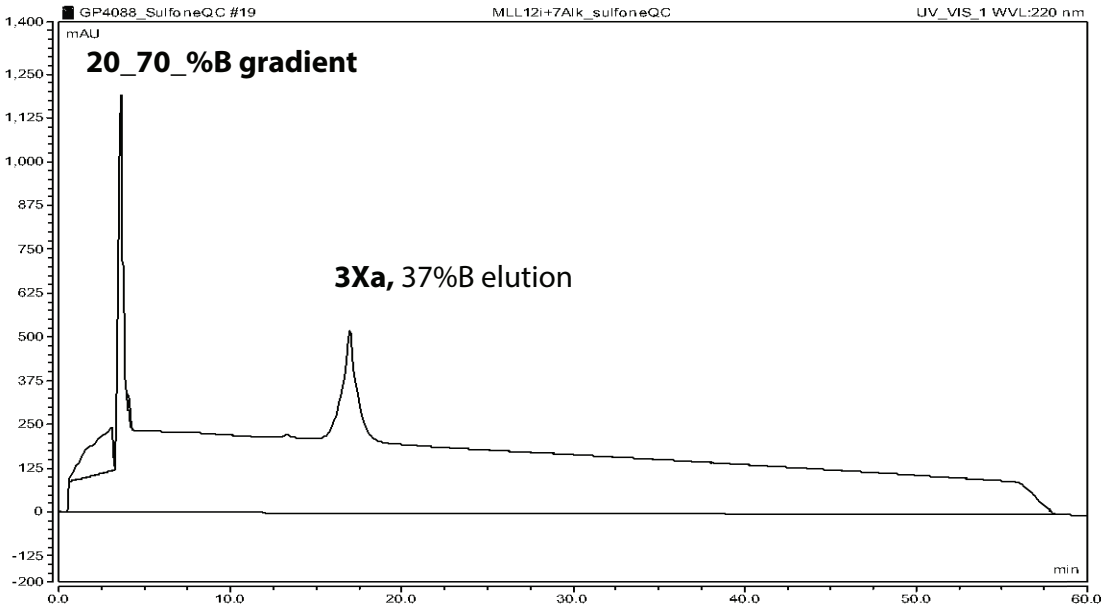
GP4088_SulfoneQC #19
MLL12i+7Alk_sulfoneQC
UV_VIS_1 WVL:220 nm
mAU
20_70_%B gradient
3Xa, 37%B elution
min

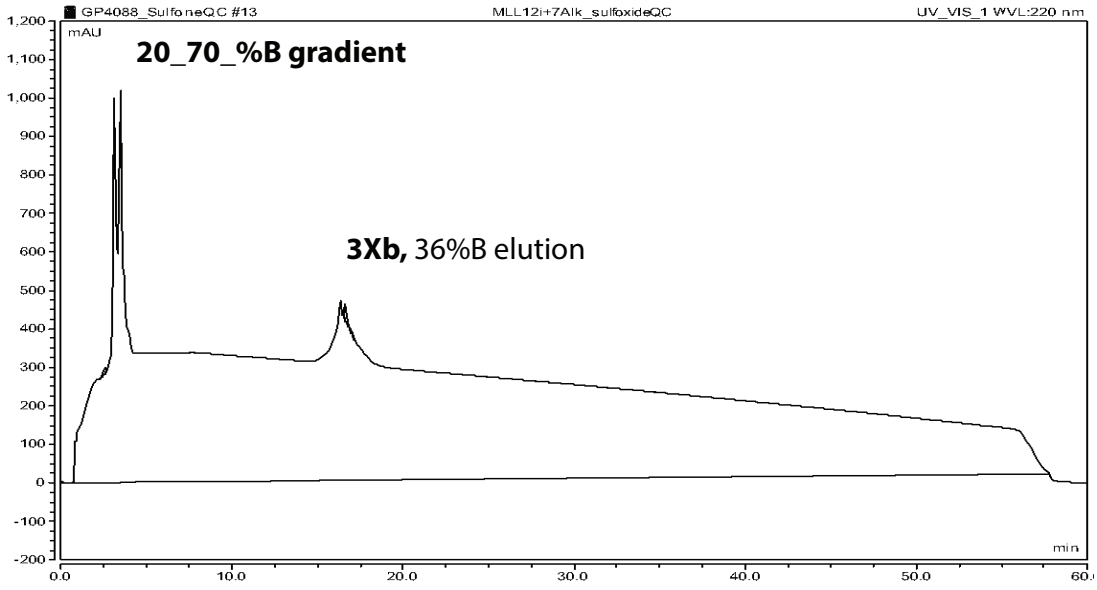
GP4088_SulfoneQC #13
MLL12i+7Alk_sulfoxideQC
UV_VIS_1 WVL:220 nm
mAU
20_70_%B gradient
3Xb, 36%B elution
min

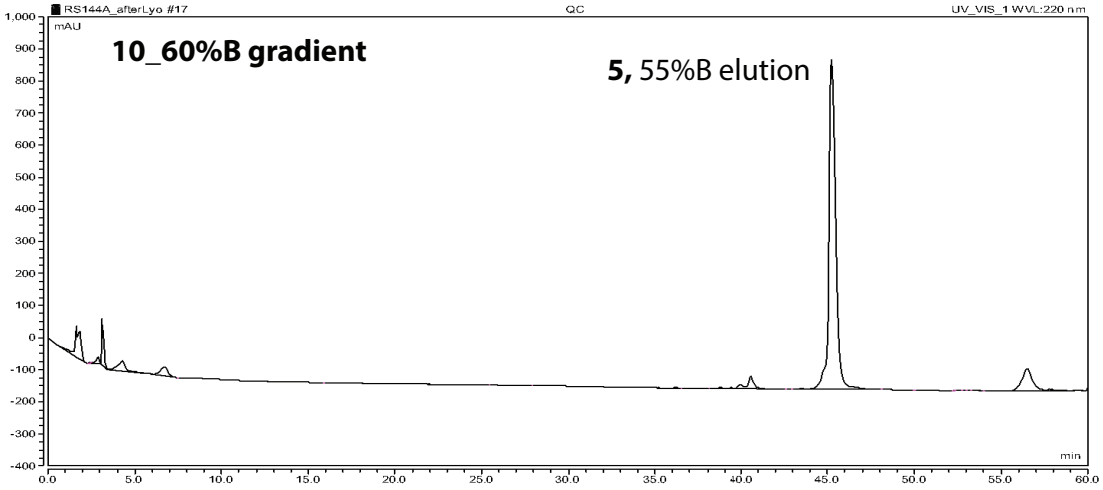
RS144A_afterLyo #17
QC
UV_VIS_1 WVL:220 nm
mAU
10_60%B gradient
5, 55%B elution
min

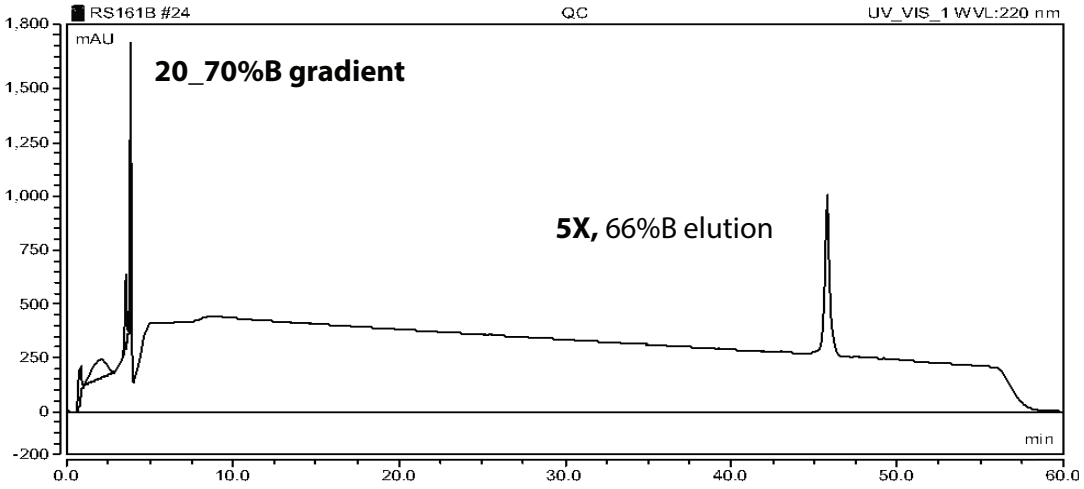
RS161B #24
QC
UV_VIS_1 WVL:220 nm
mAU
20_70%B gradient
5X, 66%B elution
min

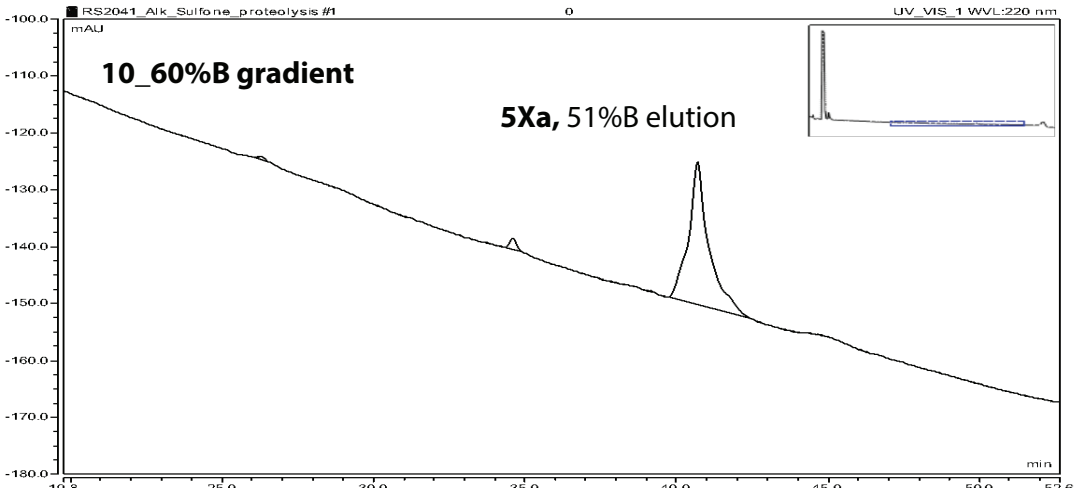
RS2041_Alk_Sulfone_proteolysis #1
UV_VIS_1 WVL:220 nm
mAU
10_60%B gradient
5Xa, 51%B elution
min

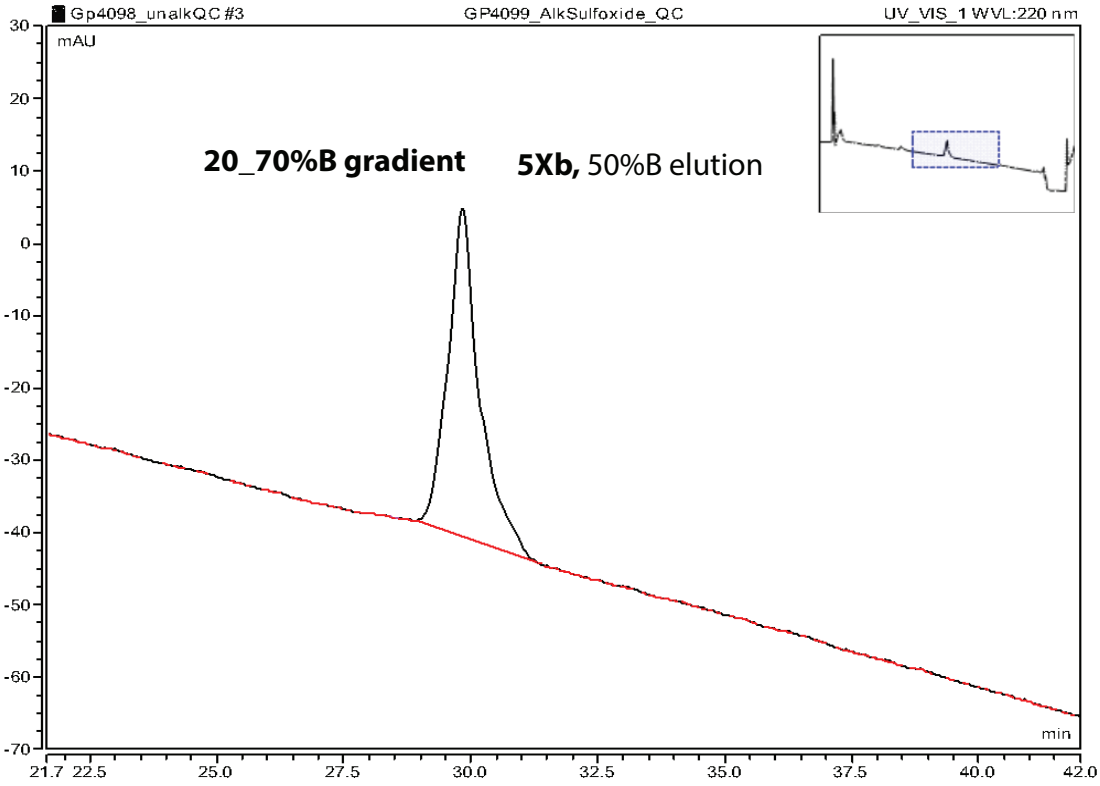
Gp4098_unalkQC #3
GP4099_AlkSulfoxide_QC
UV_VIS_1 WVL:220 nm
mAU
20_70%B gradient
5Xb, 50%B elution
min

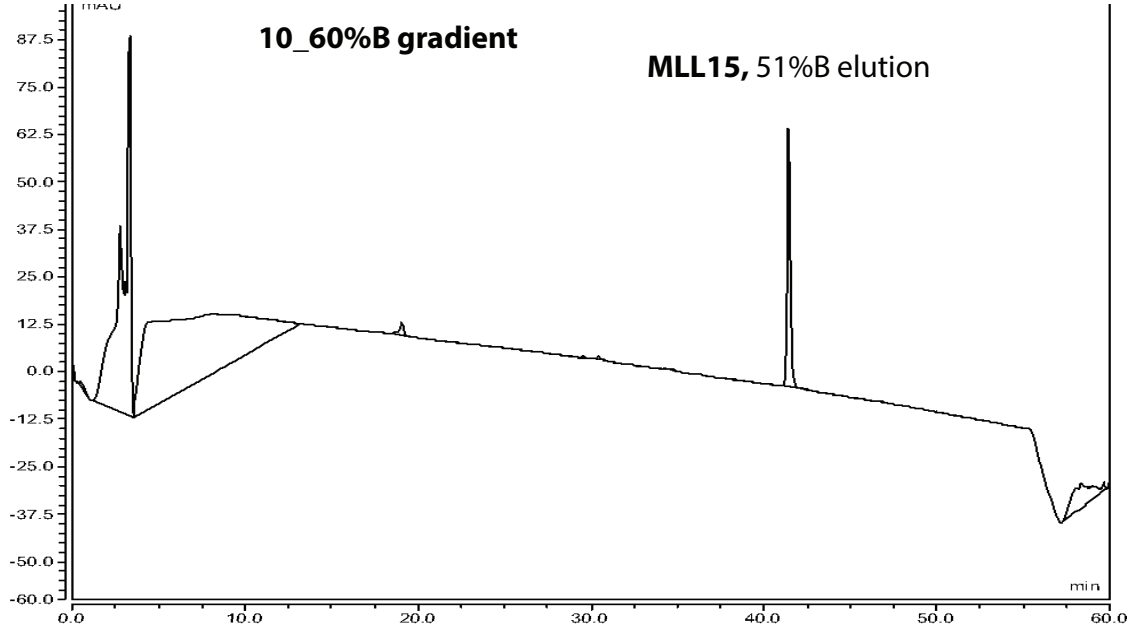
mAU
10_60%B gradient
MLL15, 51%B elution
87.5
75.0
62.5
50.0
37.5
25.0
12.5
0.0
-12.5
-25.0
-37.5
-50.0
-60.0
min
0.0
10.0
20.0
30.0
40.0
50.0
60.0

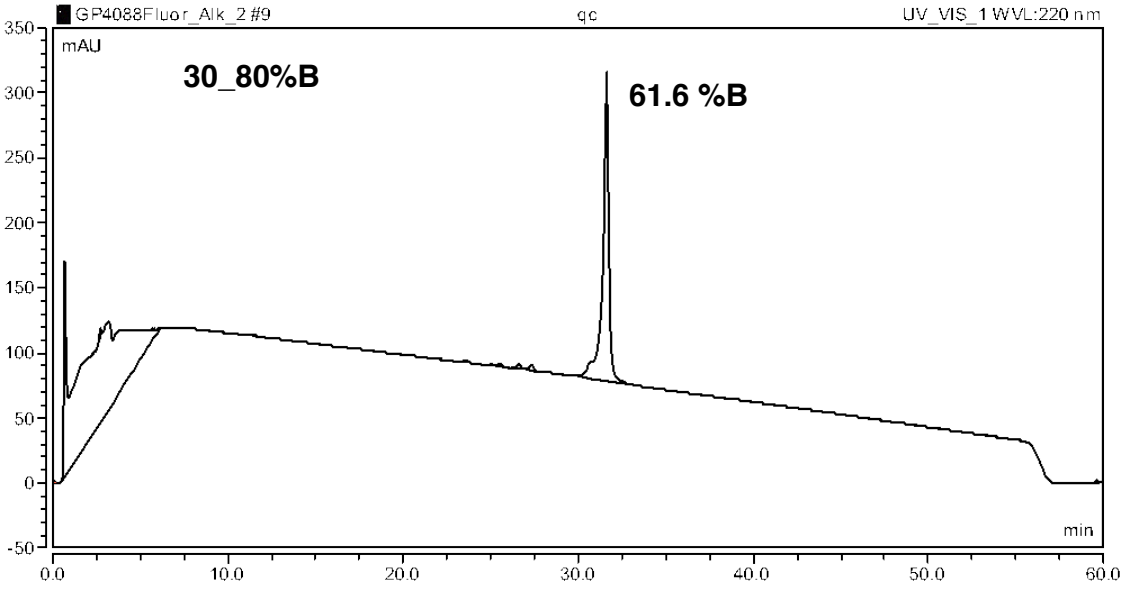
GP4088Fluor_Alk_2 #9
qc
UV_VIS_1 WVL:220 nm
mAU
30_80%B
61.6 %B
350
300
250
200
150
100
50
0
-50
min
0.0
10.0
20.0
30.0
40.0
50.0
60.0

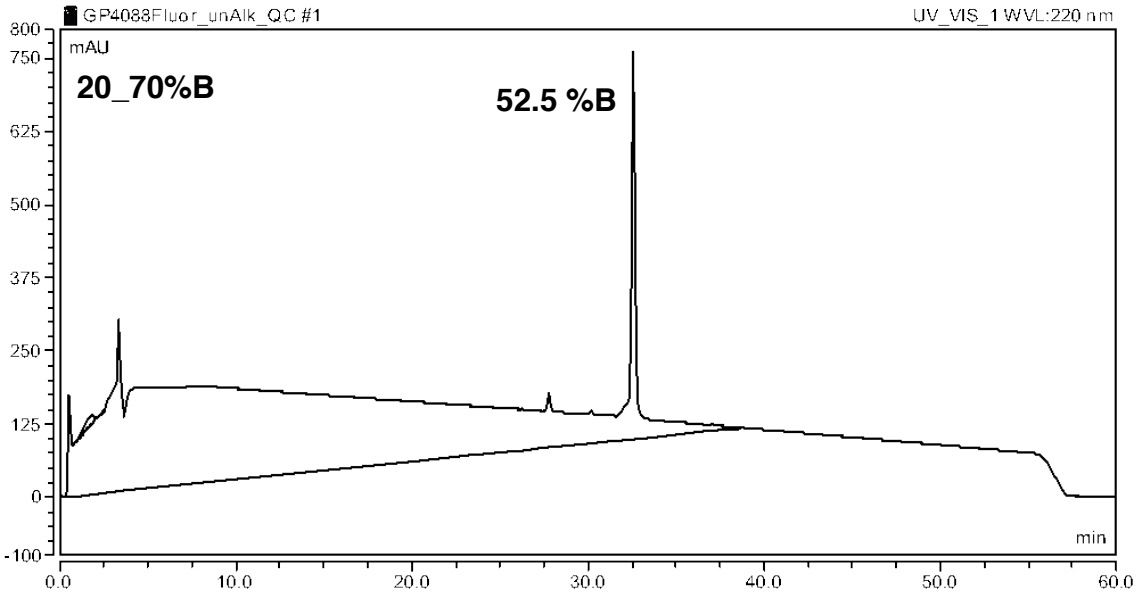
GP4088Fluor_unAlk_QC #1
UV_VIS_1 WVL:220 nm
mAU
20_70%B
52.5 %B
min

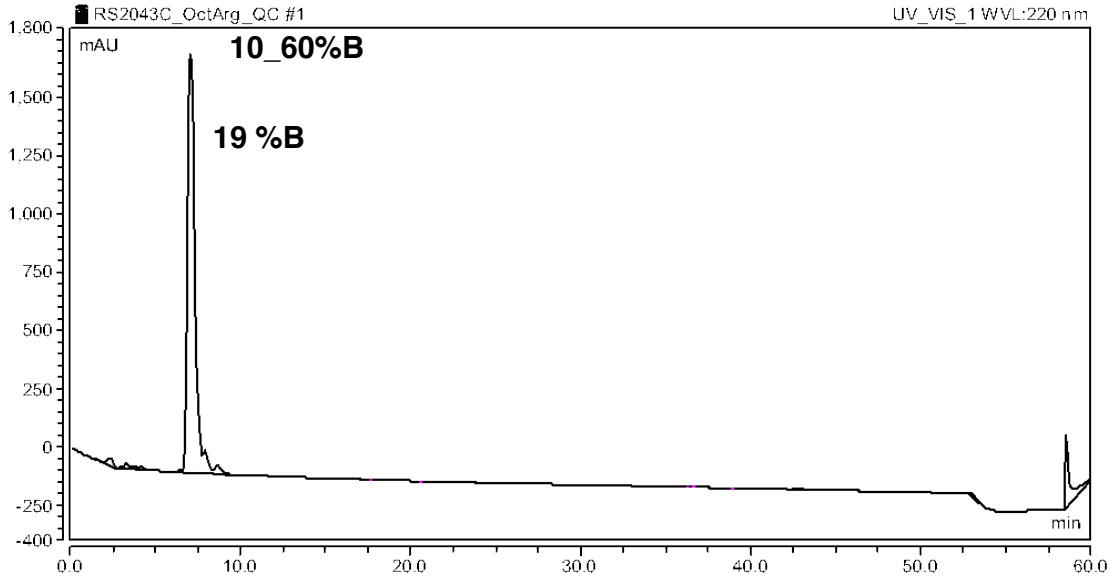
RS2043C_OctArg_QC #1
UV_VIS_1 WVL:220 nm
mAU
10_60%B
19 %B
min

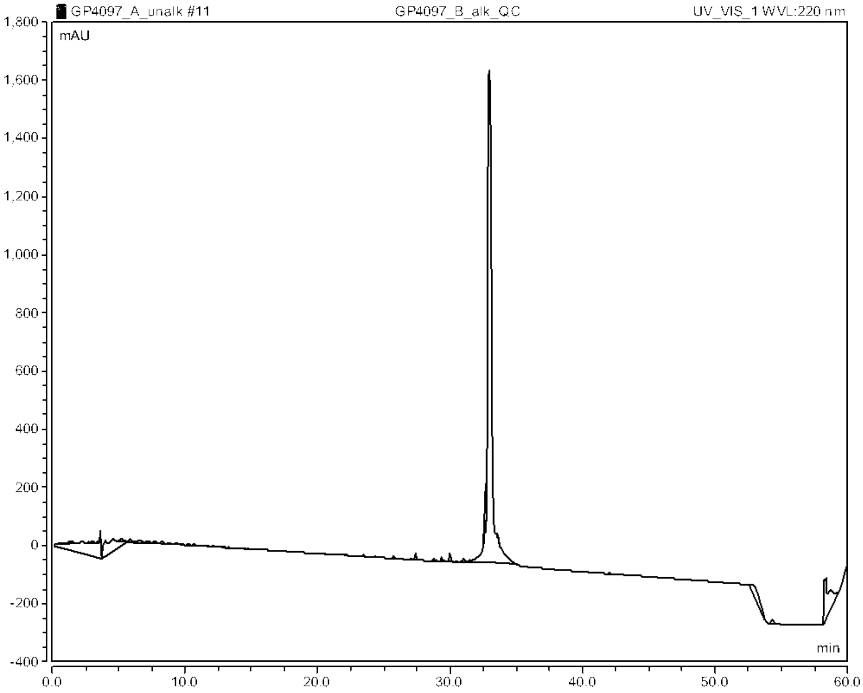
GP4097_A_unalk #11
GP4097_B_alk_QC
UV_VIS_1 WVL:220 nm
mAU
1,800
1,600
1,400
1,200
1,000
800
600
400
200
0
-200
-400
min
0.0
10.0
20.0
30.0
40.0
50.0
60.0

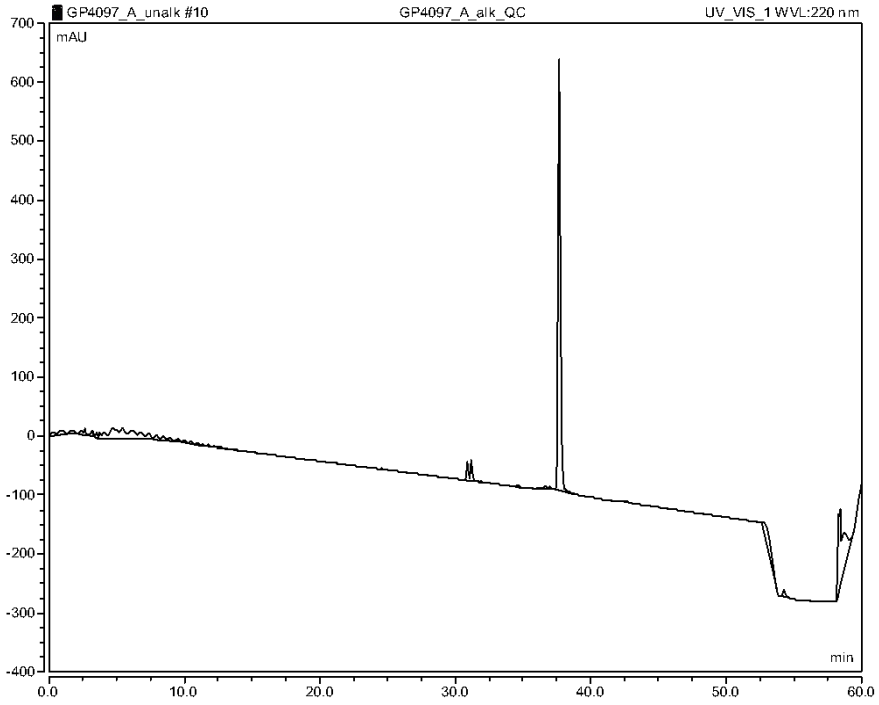
GP4097_A_unalk #10
GP4097_A_alk_QC
UV_VIS_1 WVL:220 nm
mAU
700
600
500
400
300
200
100
0
-100
-200
-300
-400
min
0.0
10.0
20.0
30.0
40.0
50.0
60.0

Extended MLL peptides

A

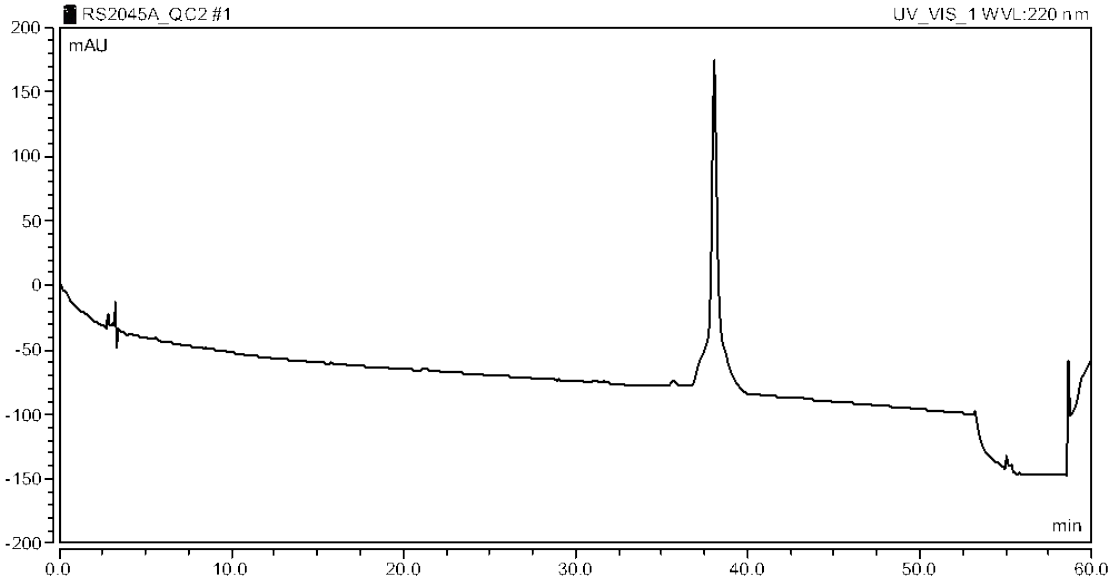

B

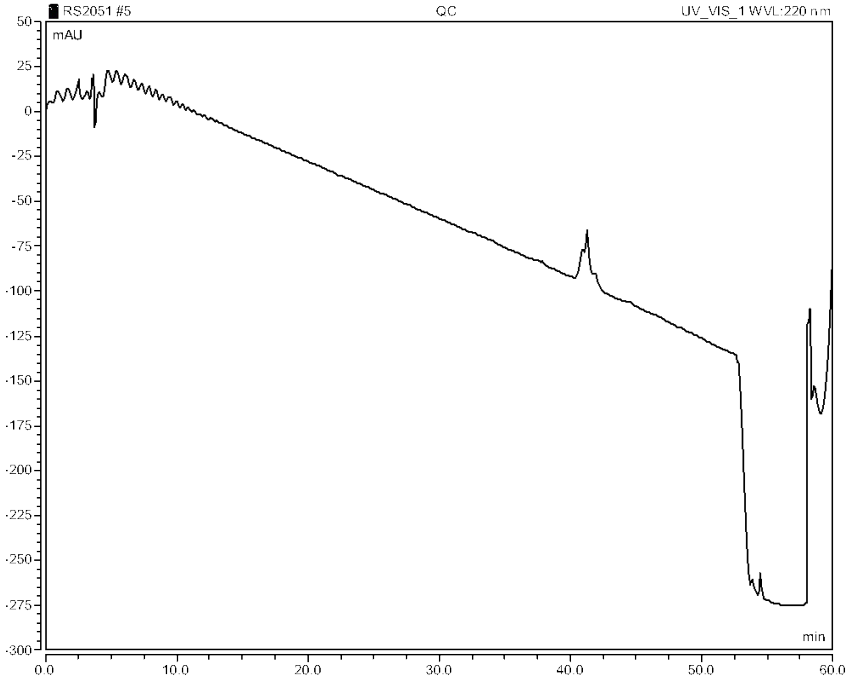

C

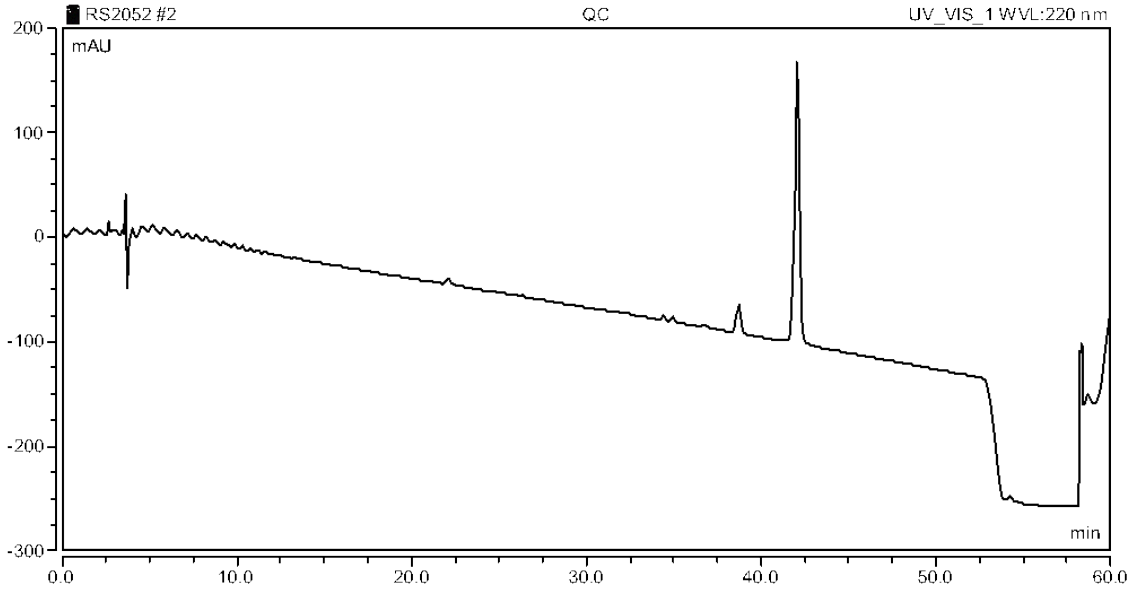
RS2052 #2
QC
UV_VIS_1 WVL:220 nm
mAU
200
100
0
-100
-200
-300
min
0.0
10.0
20.0
30.0
40.0
50.0
60.0

D

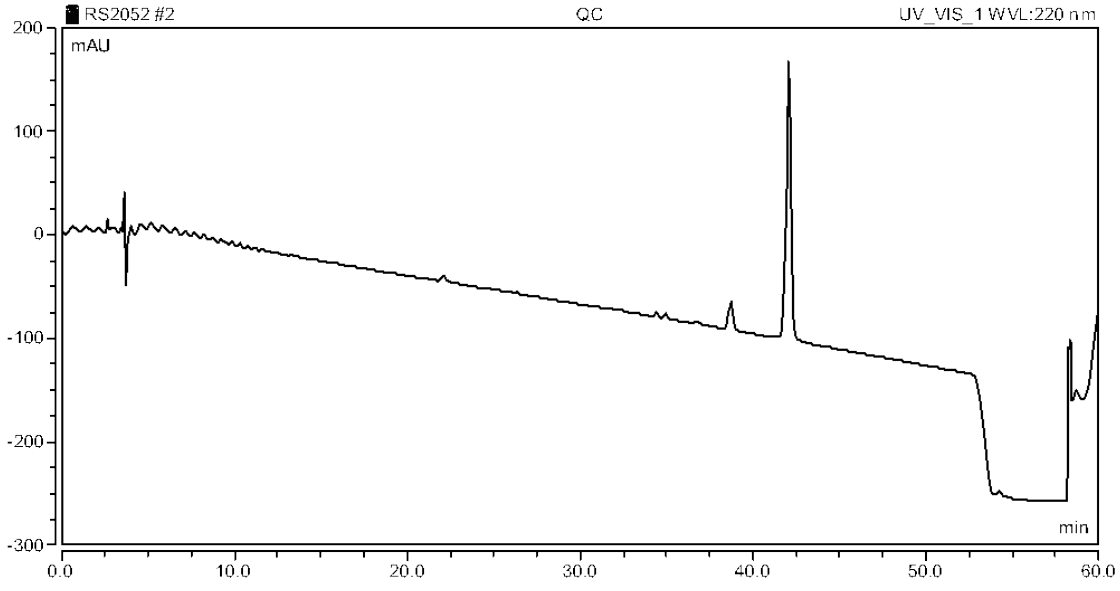
RS2052 #2
QC
UV_VIS_1 WVL:220 nm
mAU
200
100
0
-100
-200
-300
min
0.0
10.0
20.0
30.0
40.0
50.0
60.0

E

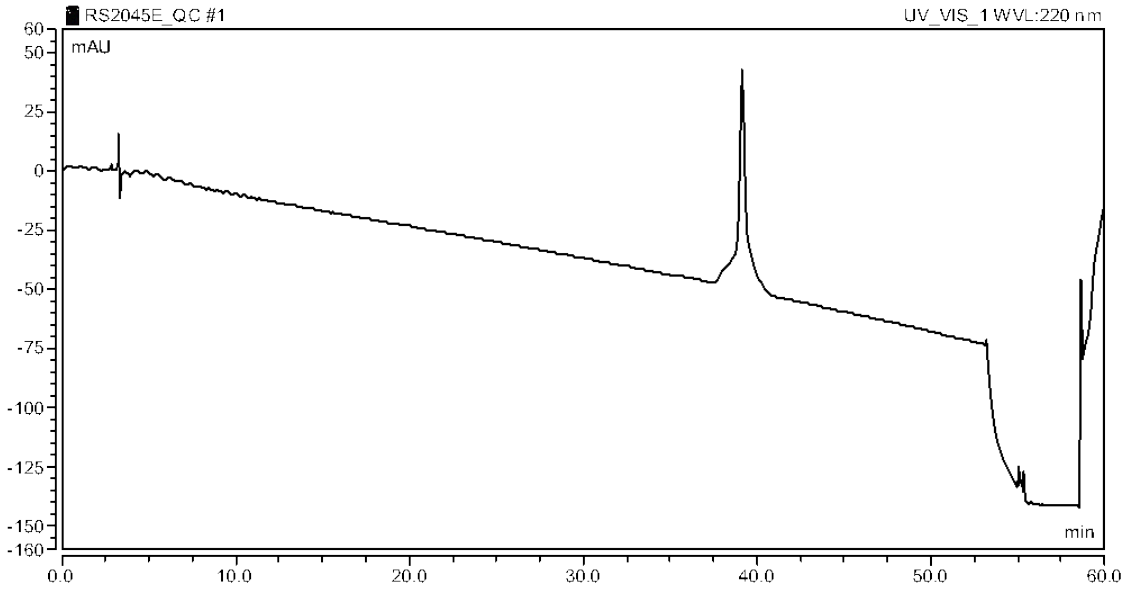
RS2045E_QC #1
UV_VIS_1 WVL:220 nm
mAU
60
50
25
0
-25
-50
-75
-100
-125
-150
-160
min
0.0
10.0
20.0
30.0
40.0
50.0
60.0

F

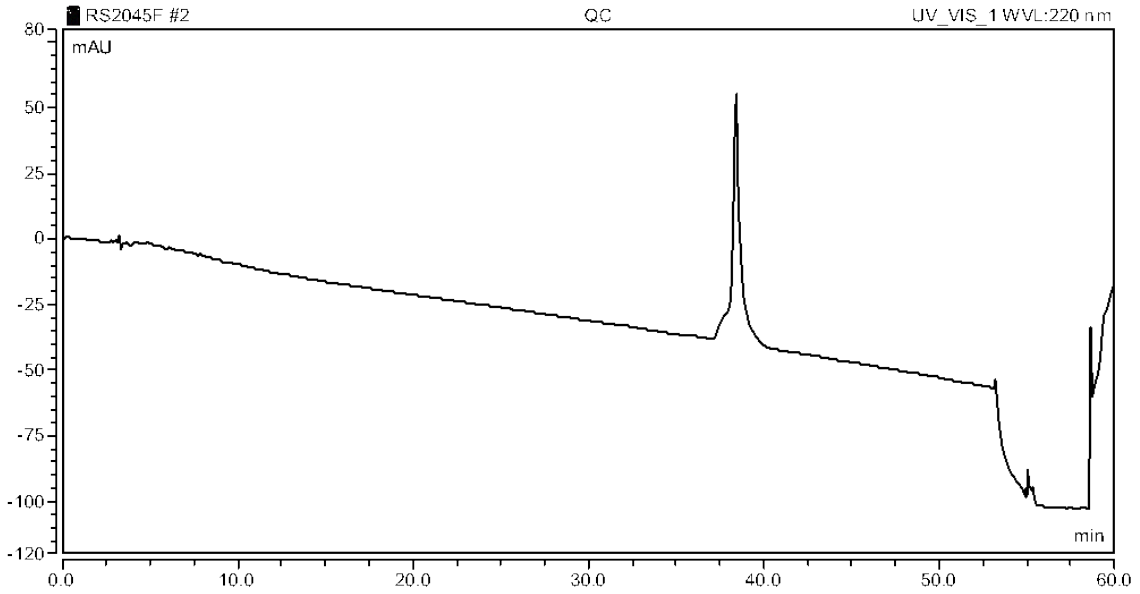
RS2045F #2
QC
UV_VIS_1 WVL:220 nm
mAU
80
50
25
0
-25
-50
-75
-100
-120
min
0.0
10.0
20.0
30.0
40.0
50.0
60.0

G

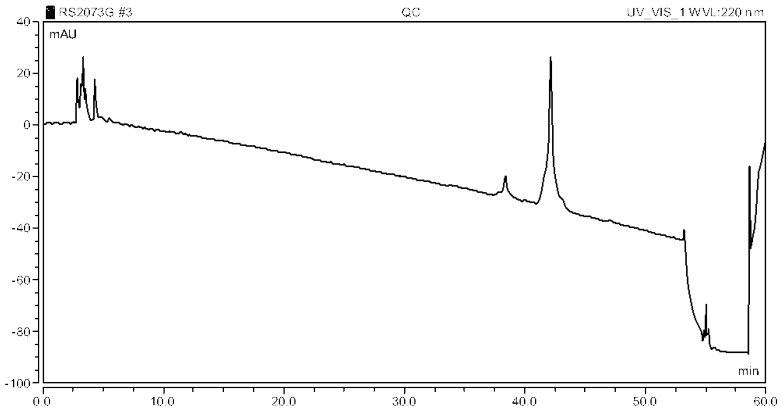
RS2073G #3
QC
UV_VIS_1 WVL:220 nm
mAU
min

H

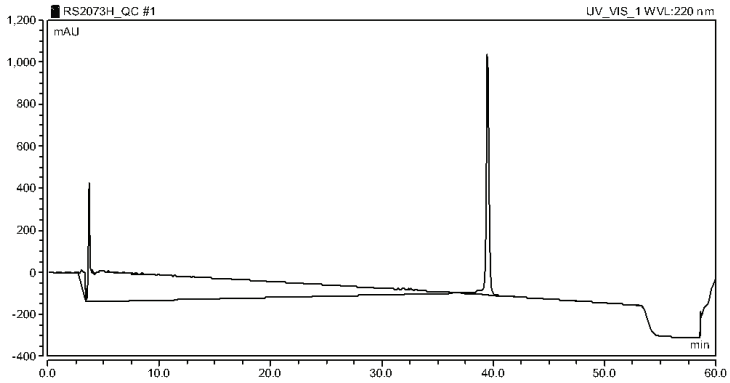
RS2073H_QC #1
UV_VIS_1 WVL:220 nm
mAU
min

I

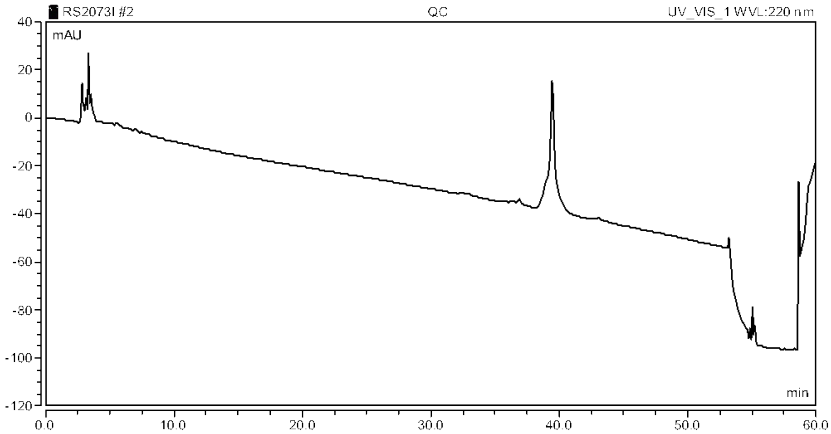
RS2073I #2
QC
UV_VIS_1 WVL:220 nm
mAU
min

3.7.13 NMR Spectra

RM^{OX}VTVNGKTIAQ

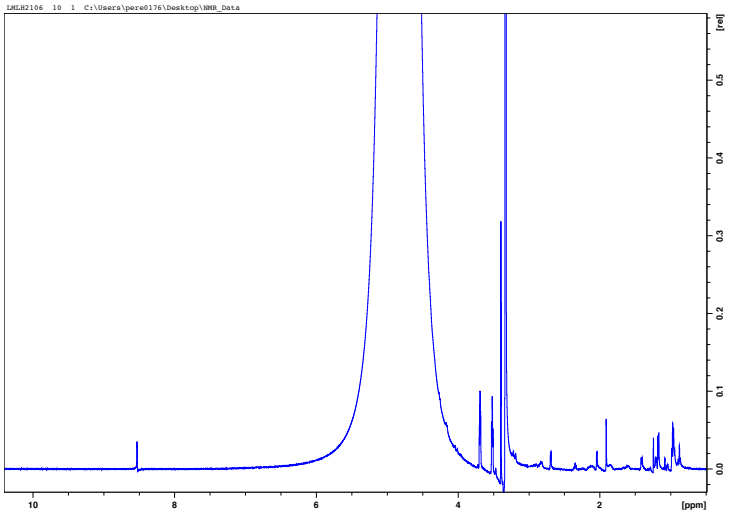

RM^{OX}VTVNGKTIFQ

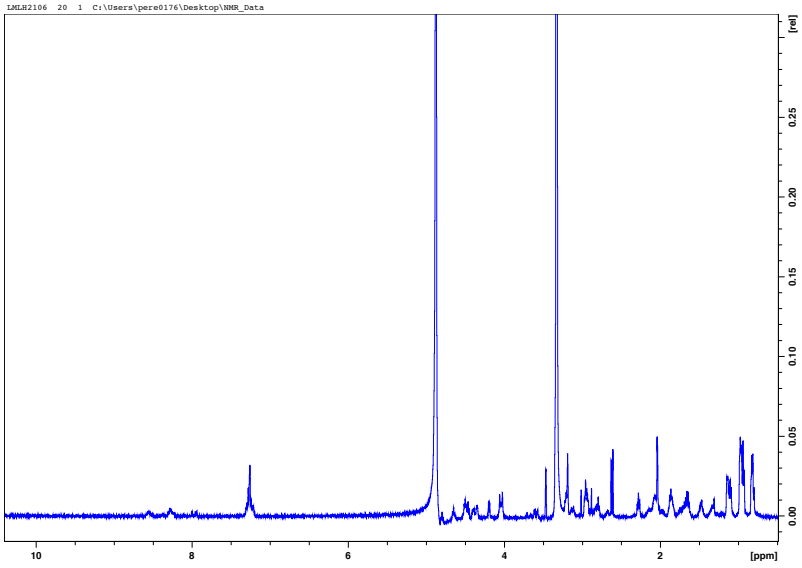

RM^{OX}VTVNGKTIWQ

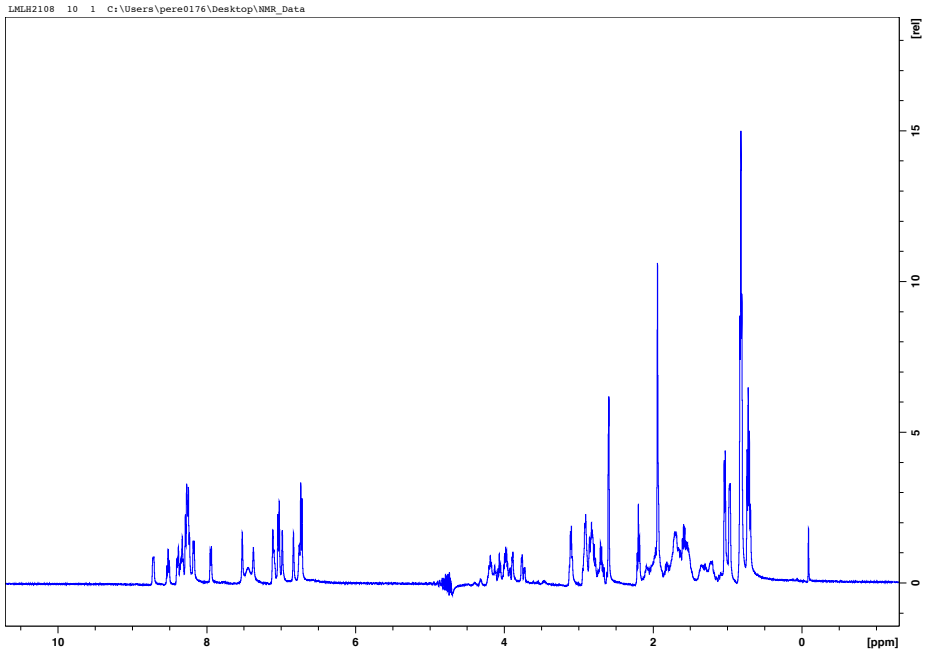

RM^{OX}VTVNGKTIYQ

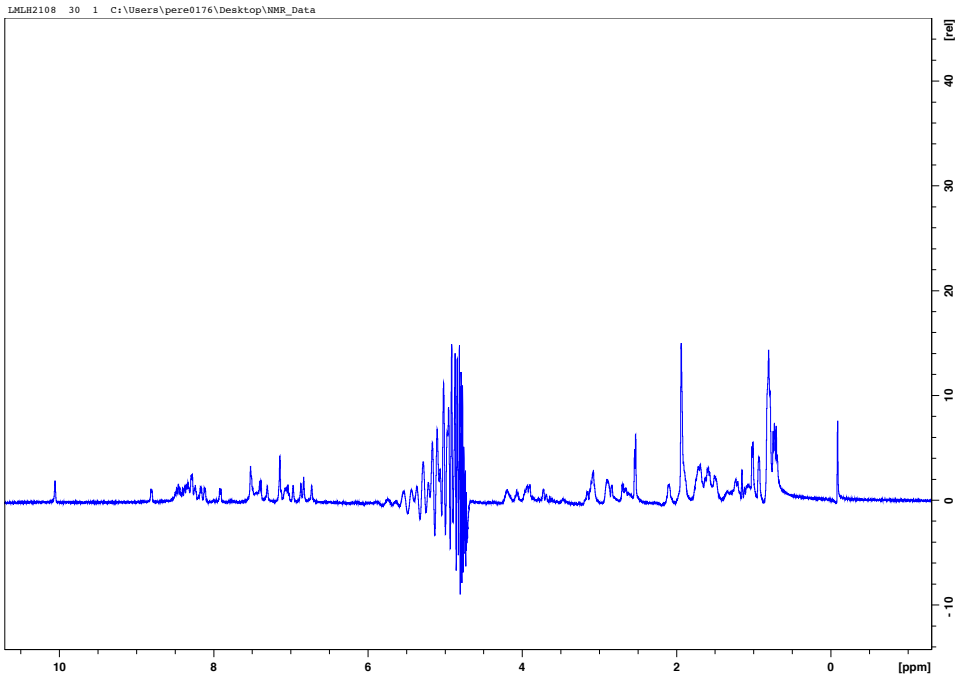

Chapter 4. Efforts Towards Intramolecular Thiol-Ene Reaction

Motivation

Researchers have utilized a variety of novel methods for the synthesis of macrocyclized peptides, including S_N2 reactions, ring closing metathesis reactions, and S_NAr, as discussed in Chapter 1. One reaction that we were particularly interested in was the thiol-ene reaction.[64,68] Unlike our previous method which oxidizes both thioethers, this strategy allows for specific tunable oxidation states at specific cysteines in the peptide backbone.

4.1.1 Introduction

The thiol-ene reaction has garnered much interest recently to cyclize peptides. A few labs have used a variety of thiol-ene reactions to afford thio-ether bridged peptides. Chou and colleagues have utilized a di-alkene to make the bis-thioether bond and have identified carbon linkages of 8-9 having robust yields (90-91%).[64] A recent study by Li and co-workers invoked a thiol-ene reaction to afford an intramolecular crosslink between a free thiol on cysteine seven residues away from a non-natural alkenyl glycine residue.[211] A tether of 10-11 atoms proved to be the most efficient, where longer tethers (12-13 atoms) lead to a lower percent conversion. Furthermore, they were able to oxidize the one sulfur atom within the tether to a sulfoxide using hydrogen peroxide. Analysis of the secondary structure using CD revealed that differing epimers of the sulfoxide influence helical content. One epimer led to a random coil whereas the other induced helicity.[189,211] This highlights the modular capability sulfoxides can have on secondary structure and the potential to further utilize specific sulfoxide epimers in distinct regions of the peptide.

Our research efforts were motivated by the lack of peptidomimetics which can incorporate a range polar functional groups. It has been observed that the hydrophobic linkage found in most macrocycles, i.e. stapled peptides can direct interactions with the binding site.[173,185] While some binding sites are more amenable to hydrophobic crosslinks, other sites have a more hydrophilic nature. We worked to develop a strategy that adds a range of potential polarities to identify optimal peptidomimetics for specific PPIs. Our interest with the thiol-ene reaction was due to the capability of incorporating various oxidation states to a specific thioether within the peptide macrocycle, of which we are unable to achieve with our previously reported strategy utilizing dibromoalkanes (Chapter 3). Tuning one or two thio-ethers into a variety of oxidation states would further add opportunities for optimized macrocyclic ligands that have not been previously utilized.

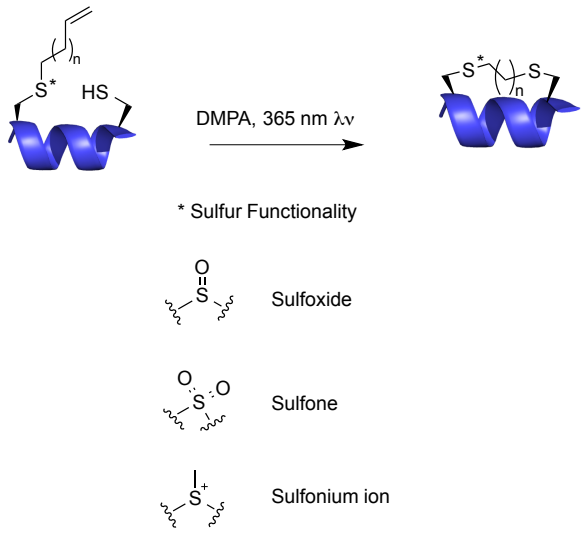

Figure 4.1 Thiol-ene approach to incorporating one oxidizable thiol into thioether crosslinked peptides. Thiol-ene reaction initiated with 2,2-dimethoxy-2-phenylacetephenone (DMPA) and 365 nm light to form a bisthioether linkage.

4.2 **Results and Discussion**

Using 365 nm light to initiate an –ene radical reaction, thiols could selectively react to form a thioether-bridged macrocycle, **Figure 4.1**.[212] This reaction could potentially be done either on resin or in solution, and can be monitored through HPLC. A number of applications of the thiol-ene reaction has been employed, including glycopolypeptides[213,214] and polymerization reactions.[215] While the reaction proceeds robustly with excess –ene, our method will not allow for more than a 1:1 ratio of thiol to –ene, as the reaction will proceed intramolecularly, **Figure 4.1**.

In order to incorporate the non-natural alkenyl substituent for crosslinked peptides, we developed a three step synthetic route for the synthesis of Fmoc-*S*-alkenyl cysteine (**Figure 4.2**). An initial esterification reaction with chlorotrimethylsilane in methanol generates a methyl ester **1** in a 78% yield.[216] Alkylation driven by the base, cesium carbonate, affords the *N*-Fmoc-*S*-butenyl-L-cysteine methyl ester **2** in 87% yield using the modified protocol of Salvatore *et al*.[217] The final product, *N*-Fmoc-*S*-butenyl-L-cysteine **3,** is obtained in 40% yield after a carboxylated displacement reaction with lithium iodide in refluxing ethyl acetate.[218,219] This amino acid can be incorporated into solid phase peptide synthesis in preparation for the thiol-ene reaction, and varying alkenyl linker lengths can be utilized to identify optimal lengths for the helical construct. This synthesis simplifies the on-resin chemistry by removing the multiple steps of incorporating orthogonal cysteine protecting groups resulting in subsequent deprotection of one group, alkylation, and deprotection of the second cysteine. Furthermore, the synthesis of the non-natural cysteine

amino acid allows for oxidation before incorporation into the peptide. This allows for two different oxidation states to be incorporated at two different sites.

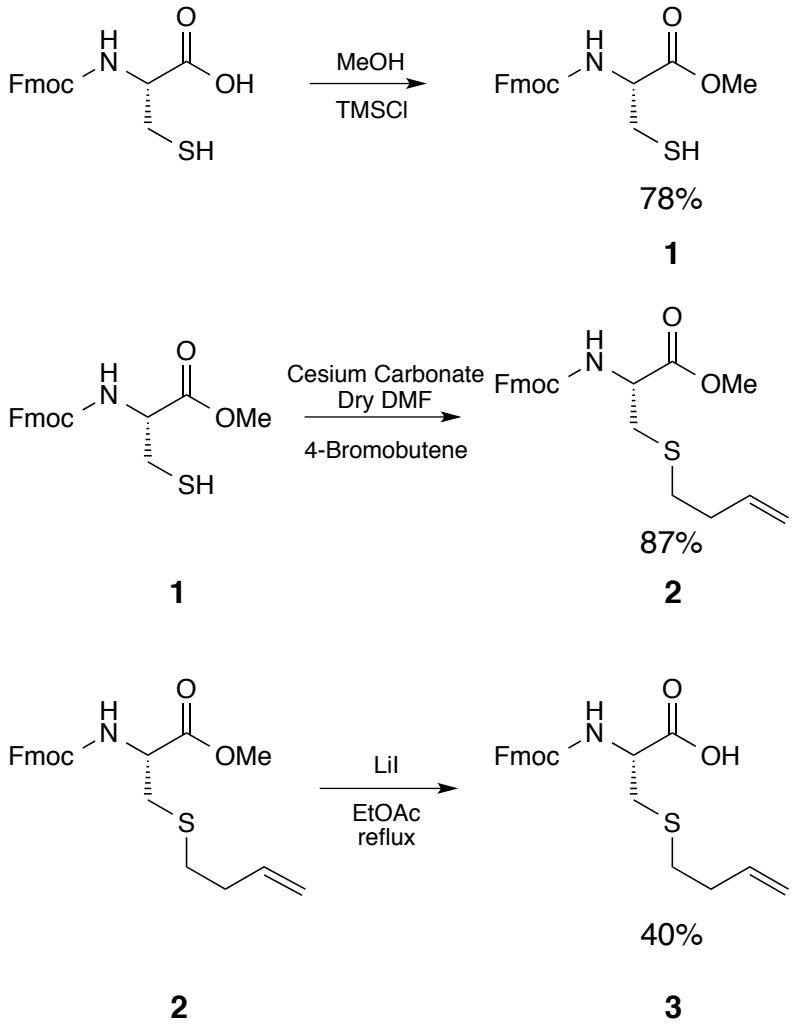

Figure 4.2 Three step synthetic Scheme for Fmoc-S-butenyl Cysteine with initial methyl-ester formation, alkylation of the thiolate, and final deprotection to afford the acid.

To test the reactivity of the Fmoc-*S*-alkenyl-cysteine, we first investigated how the Fmoc-*S*-butenyl-cysteine, **3,** could react with an exogenous thiol, β-mercaptoethanol,

Figure 4.3. Over one hour with 10 mol% DMPA photoinitiator, and 3 equivalents of thiol, the reaction afforded product, as observed through the diminishing alkene protons at 5.05 ppm, **Figure 4.4**. Alkene protons were compared to the Fmoc aryl proton 2H doublet resonance at 7.75 ppm. Due to Fmoc-protecting group susceptibility to weak bases, only 1.75 eq. of the alkenyl protons are observed. After one hour, a substantial reduction (83%) of the alkenyl protons was observed, indicating product, **4,** has formed. ESI-MS confirmed the final product mass, [M+H] = 442.4.

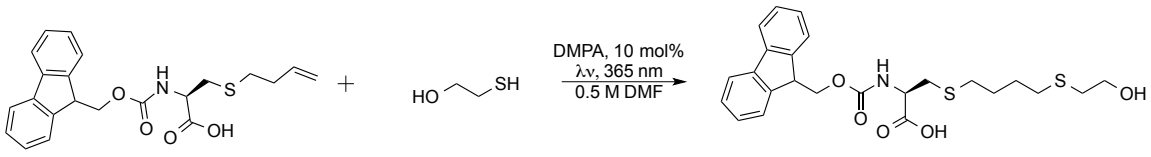

Figure 4.3 Synthetic Scheme thiol-ene reaction with exogenous thiol on Fmoc-*S*-butenyl-Cysteine.

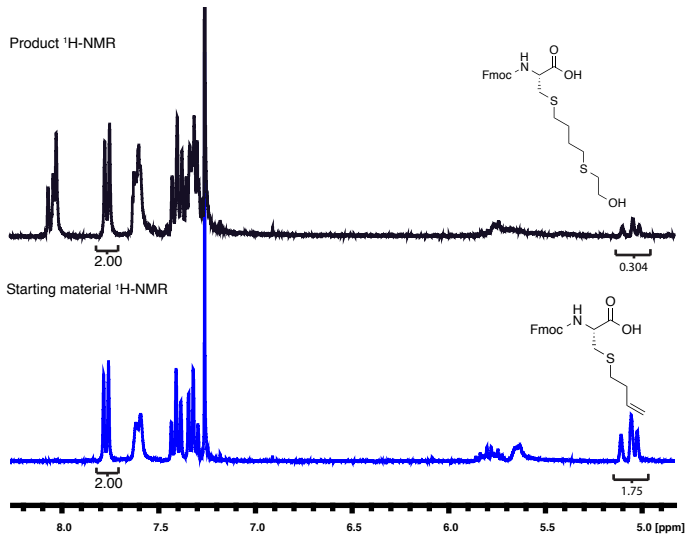

Figure 4.4 Thiol-ene reaction monitored with ^{1}H-NMR.

To evaluate racemization of the α-carbon on cysteine, we synthesized a tripeptide (Gly-Cys$_{butenyl}$-Phe). Monitoring racemization using RP-HPLC, we identified 95% of peptide stays in the L-configuration, with 5% conversion to the D-Cysteine, **Figure 4.5**. We compared the retention times of a Gly-Cys-Phe peptide with either L-Cys or D-Cys incorporated. We again see the retention time to be about 2 minutes different with the Gly-Cys(L)-Phe eluting earlier than Gly-Cys(D)-Phe, **Figure 4.5**.

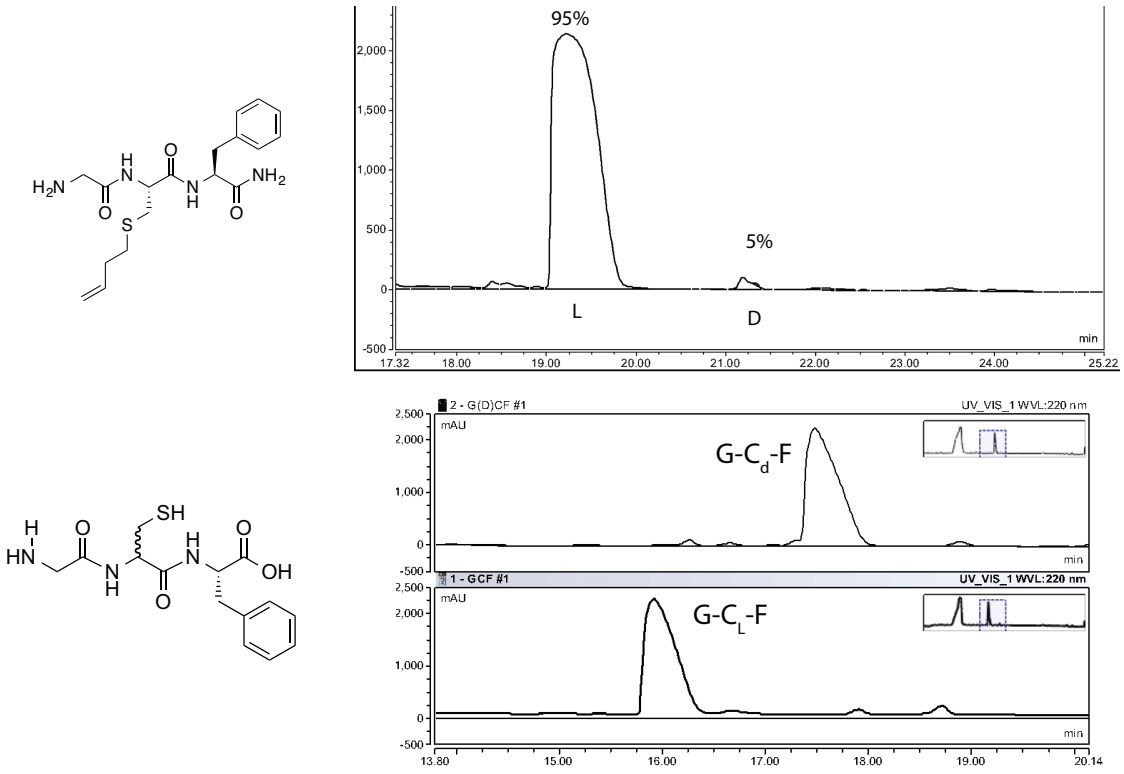

Figure 4.5 Racemization of tripeptide with 5% racemization to D-Cysteine.

Since we observed the thiol-ene reaction to proceed with exogenous thiol, we then evaluated the reactivity of an intramolecular thiol-ene reaction between residues on the same face of an α-helical peptide. We tested our method on a short 12-residue peptide, MLL, which binds to the KIX protein. Replacement of the methionine residue for Fmoc-*S*-butenyl-Cysteine or Fmoc-*S*-pentenyl-Cysteine using solid phase peptide synthesis. A cysteine residue was placed 7 residues away, which could then react with the alkene. The thiol-ene reaction was carried out off-resin using 365 nm UV light and a catalytic photo-initiator.[17,18] The reaction was tested with a number of variables, including the linker length, the distance between the linkage (3,4, or 7 residues), the photoinitiator, the amount

of photoinitiator, the solvent, and the light source, **Table 4.1**. Even with all these varied methods, we were still unable to achieve product. A competing product, where the thiols form intermolecular disulfide bonds was observed. If this side-reaction can be prevented, we may be able to obtain product; therefore, further investigation into reducing disulfide formation is on-going.

Table 4.1 Thiol-ene reaction variables evaluated

Sample	Solvent	Conc. (mM)	DMPA mol%	DMPA addition (min)	Time (min)	Light Source
Ac-SKICDFVC(S-butenyl)KNTY-NH2	DMSO + DTT	6.5	10%	0, 20	60	UV Lamp
Ac-SKICDFVC(S-butenyl)KNTY-NH2	DSMO	6.5	10%	0, 20	60	
Ac-SKIC(S-butenyl)DFVCKNTY-NH2	1:1 DMF:DMSO	3.2	90%	0	120	
Ac-SKIC(S-butenyl)DFVCKNTY-NH2	DMSO	3.2	45%	0, 30, 60 90	120	
Ac-SKIC(S-butenyl)DFVCKNTY-NH2	DMSO	6.4	45%	0, 30, 60 90	120	
Ac-SKIC(S-butenyl)DFVCKNTY-NH2	1:1 DMF:DMSO	3.2	45%	0	10	Rayonett
Ac-SKIC(S-butenyl)DFVCKNTY-NH2	1:1 DMF:DMSO	3.2	10%	0, 20, 40, 60, 80, 100	120	
Ac-SKIC(S-butenyl)DFVCKNTY-NH2	DMSO	3.725	45%	0, 20	30	
Ac-SKIC(S-butenyl)DFVCKNTY-NH2	1:1 DMF:DMSO	3.725	45%	0, 20	30	
Ac-SKIC(S-butenyl)DFVCKNTY-NH2	DMSO	7.45	45%	0	10	
Ac-SKICDFVC(S-pentenyl)KNTY-NH2	DMSO + DTT	6.5	10%	0, 20	60	UV Lamp
Ac-SKICDFVC(S-pentenyl))KNTY-NH2	DSMO	6.5	10%	0, 20	60	
Ac-SKIC(S-pentenyl))DFVCKNTY-NH2	1:1 DMF:DMSO	3.2	90%	0	120	
Ac-SKIC(S-pentenyl)DFVCKNTY-NH2	DMSO	3.2	45%	0, 30, 60 90	120	
Ac-SKIC(S-pentenyl)DFVCKNTY-NH2	DMSO	6.4	45%	0, 30, 60 90	120	

4.3 **Conclusion**

The strategy to utilize a thiol-ene reaction may prove to be of benefit in identifying high affinity, cell permeable peptidomimetics. Incorporating non-natural *S*-alkenyl cysteine derivatives will allow for varying oxidation states at only one cysteine position within the peptide construct. We have observed reactivity with exogenous thiol and a non-natural cysteine, but have been unsuccessful towards an intramolecular reaction within a peptide. A few factors may be disrupting the formation of the macrocycle including disulfide formation, type of initiator, solvent, and UV source. The suppression of the disulfide formation by purging the vial with nitrogen prior to irradiation may prove to be

of benefit, and we are currently investigating this avenue, as well as an increase in UV power.

4.4 **Future Works**

4.4.1 Oxidation states used to tune polarity

The ability to modify cysteine residues (**Figure 4.6**) into sulfones **5** or sulfoxides **7** allows for various polarities to be analyzed. With hydrocarbon staples, the hydrophobic chain is well suited to interact with the hydrophobic binding surface and increase its affinity, as seen with Bim-SAHB stabled peptides.[22] In other cases, an increase in polarity of the linker allowed for greater affinity. This shows the importance and variability of polarity within the targeted binding interaction. Expanding the options with tunable oxidation states allows for optimization of an inhibitor. Researchers have noticed the difficulty of negatively charged peptides on cellular uptake.[51] By converting thiols into sulfonium ions **6**, the net charge of a peptide can be increased.[211] Exploiting oxidation states may allow researchers to find suitable macrocyclic peptides that can successfully target and inhibit a range of PPIs.

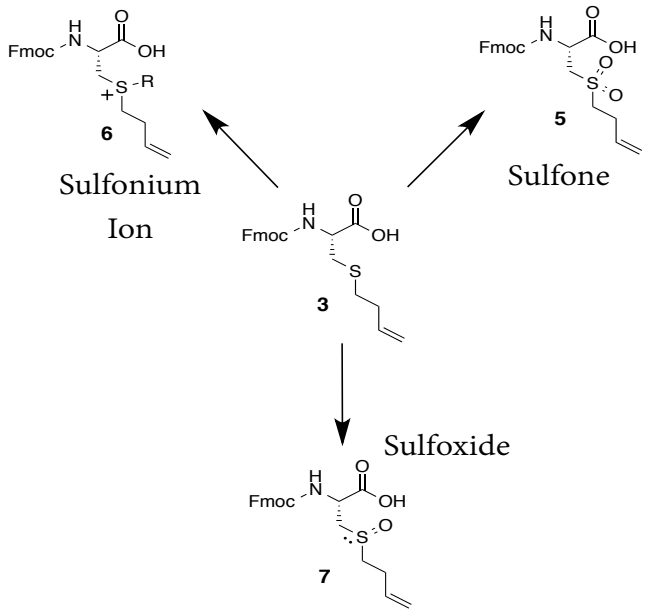

Figure 4.6 Oxidation of thiol groups for incorporation into solid phase peptide synthesis (SPPS) allowing for optimal polarity of stabilized peptides.

In determining the optimal polarity, synthesis of Fmoc-*S*-butenyl-L-cysteine amino acids that can be oxidized to sulfones (**5)**, sulfonium ions (**6),** or sulfoxides (**7**) prior to peptide synthesis would allow for a simplistic route to various oxidative peptide derivatives (**Figure 4.6**). Following a previously described protocol, we can use hydrogen peroxide and formic acid to form the sulfones or performic acid for sulfoxide formation.[181] Subsequent thioethers can further be alkylated at low pH to form sulfonium ions.[211] Additionally, the alkylation is orthogonal to all other amino acids under these acidic conditions.[220,221]

4.5 **Experimental**

4.5.1 Small molecule synthesis

_N_-Fmoc-L-cysteine methyl ester (1)

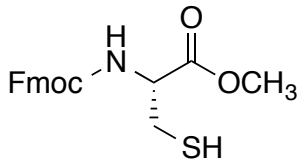

Chlorotrimethylsilane (0.55 mL, 3.645 mmol) was diluted to MeOH (5 mL) and stirred. *N*-Fmoc-L-cysteine (250 mg, 0.729 mmol) was then added, and the reaction mixture was stirred at ambient temperature for 2 h. The formed precipitate was then separated via vacuum filtration, washed with hexanes (2 × 3 mL), and dried under high vacuum yielding **1** as a white powder (203 mg, 0.568 mmols, 78% yield). Optical Rotation $[\alpha]_D^{23}$ + 8.813 (*c* 1.112, DCM), ^{1}H NMR (300 MHz, $CDCl_3$) δ 2.98-3.02 (dd, 2 H, J=2.4, 7.5), 3.81 (s, 3 H), 4.24-4.26 (t, 2 H, J=6.9), 4.45 (dd, 2 H, J=2.4, 7.2), 4.65-4.69 (dt, 1 H, J=4.2, 7.8), 5.68 (d, 1 H, J=7.5), 7.33-7.44 (cm, 4 H), 7.60-7.63 (d, 2 H, J=7.2), 7.76-7.79 (d, 2 H, J= 6.9).

_N_-Fmoc-_S_-butenyl-L-cysteine methyl ester (2)

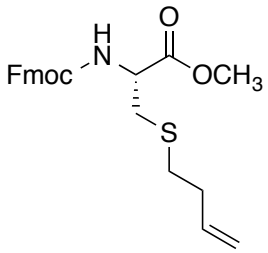

N-Fmoc-L-cysteine methyl ester (168.0 mg, 0.470 mmol) was diluted in 10 mL of anhydrous *N,N* dimethylformamide (DMF) and stirred. Cesium carbonate (270. mg, 0.564

mmol) and 4-bromo 1-butene (318. mg, 2.35 mmol) were added, and the reaction mixture was stirred at ambient temperature for 1.5 h. Reaction was quenched with ammonium chloride and extracted ethyl acetate (EtOAc, 3×). The organic layers were combined and washed with water (3×), brine (1×), dried over magnesium sulfate ($MgSO_4$), and concentrated under high vacuum. The residue was purified via flash column chromatography (4:1 hexanes: EtOAc) to yield a yellowish powder (167 mg, 0.406 mmols, 87% yield). ESI-MS confirmed the final product mass, [M+Na] = 434.138, theoretical [M+Na] = 434.14. Optical Rotation $[\alpha]_D^{23}$ + 7.22 (*c* 0.96, DCM). ^{1}H NMR (300 MHz, $CDCl_3$) δ 2.316 (dt, 2 H, J = 7.5, 14.4), 2.60 (t, 2 H, J = 7.2), 3.016 (d, 2 H, J = 5.1), 3.77 (s, 3 H), 4.243 (t, 1 H, J = 6.9), 4.392 (d, 2 H, J = 7.2), 4.615 (dt, 1 H, J=4.2, 7.8), 5.05 (dd, 1 H, J=1.2, 3), 5.110 (dd, 1 H, J=3, 4.5), 5.63 (d, 1 H, J = 7.5), 5.78 (ddt, 1 H, J=6.9, 10.2, 13.5), 7.33-7.44 (cm, 4 H), 7.60-7.63 (d, 2 H, J=7.2), 7.76-7.79 (d, 2 H, J= 6.9).

***N*-Fmoc-*S*-pentenyl-L-cysteine methyl ester**

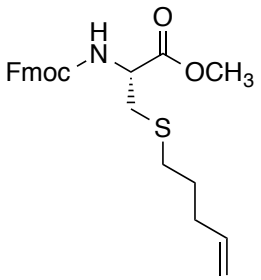

N-Fmoc-L-cysteine methyl ester (500 mg, 1.39 mmols) was dissolved in 10 mL of anhydrous *N,N* dimethylformamide (DMF) and stirred. Cesium carbonate (798 mg, 2.43 mmols) and 5- bromo 1-pentene (1.04 g, 0.825 mL) were added, and the reaction mixture was stirred at ambient temperature for 1.5 h. Reaction was quenched with ammonium

chloride and extracted ethyl acetate (EtOAc, 3×). The organic layers were combined and washed with water (3×), brine (1×), dried over magnesium sulfate ($MgSO_4$), and concentrated under high vacuum. The residue was purified via flash column chromatography (4:1 hexanes: EtOAc) to yield a yellowish powder (0.417 mmols, 0.177 g, 30% yield). ESI-MS confirmed the final product mass, [M+Na] = 448.155, theoretical [M+Na] = 448.16. Optical Rotation $[\alpha]_D^{23}$ + 6.568 (*c* 1.00, DCM). ^{1}H NMR (300 MHz, $CDCl_3$) δ 1.6927 (dt, 2H, J = 7.85, 14.49), 2.1645 (tt, 2H 8.19, 14.04), 2.5588 (t, 2H, J = 7.39), 3.029 (d, 2H, J = 3.08), 3.81 (s, 3 H), 4.268 (t, 1 H, J = 7.17), 4.433 (d, 2 H, J = 7.17), 4.615 (dt, 1 H, J=4.2, 7.8), 5.05 (dd, 1 H, J=1.2, 3), 5.110 (dd, 1 H, J=3, 4.5), 5.63 (d, 1 H, J = 7.5), 5.78 (ddt, 1 H, J=6.9, 10.2, 13.5), 7.33-7.44 (cm, 4 H), 7.60-7.63 (d, 2 H, J=7.2), 7.76-7.79 (d, 2 H, J= 6.9).

_N_-Fmoc-_S_-butenyl-L-cysteine (3)

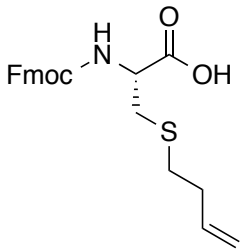

N-Fmoc-L-cysteine methyl ester (155 mg, 0.377 mmol) was dissolved in 1.9 mL ethyl acetate (0.2 M) and lithium iodide (252 mg, 5 eq), and stirred at reflux for 16 h. Upon completion, the reaction was acidified with 0.1 M HCl and extracted (1×) into EtOAc. The organic layers were combined and washed with water and brine, and extracted into 0.1 M NaOH (3×), washed with DCM (1×), acidified with 0.1 M HCl and extracted into EtOAc (3×). The organic layer was washed with sodium thiosulfate (1×), brine (1×), and dried

under high vacuum. The residue was purified via flash column chromatography (97:2:1 dichloromethane: isopropanol: acetic acid) to yield a white powder (39.0 mg, 40%). ESI theoretical [M+Na] = 420.12, observed [M+Na] = 420.4. Optical Rotation $[\alpha]_D^{23}$ - 1.81 (*c* 1.29, DCM), (10 replicate measurements in DCM). ^{1}H NMR (300 MHz, $CDCl_3$) δ 2.316 (dt, 2 H, J = 7.5, 14.4), 2.60 (t, 2 H, J = 7.2), 3.016 (d, 2 H, J = 5.1), 4.243 (t, 1 H, J = 6.9), 4.392 (d, 2 H, J = 7.2), 4.615 (dt, 1 H, J=4.2, 7.8), 5.05 (dd, 1 H, J=1.2, 3), 5.110 (dd, 1 H, J=3, 4.5), 5.63 (d, 1 H, J = 7.5), 5.78 (ddt, 1 H, J=6.9, 10.2, 13.5), 7.33-7.44 (cm, 4 H), 7.60-7.63 (d, 2 H, J=7.2), 7.76-7.79 (d, 2 H, J= 6.9).

***N*-Fmoc-*S*-pentenyl-L-cysteine**

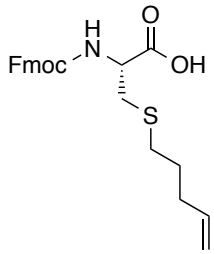

N-Fmoc-L-cysteine methyl ester (89 mg, 0.209 mmol) was dissolved in 1.9 mL ethyl acetate (0.2 M) and lithium iodide (139.9 mg, 5 eq), and stirred at reflux for 16 h. Upon completion, the reaction was acidified with 0.1 M HCl and extracted (1×) into EtOAc. The organic layers were combined and washed with water and brine, and extracted into 0.1 M NaOH (3×), washed with DCM (1×), acidified with 0.1 M HCl and extracted into EtOAc (3×). The organic layer was washed with sodium thiosulfate (1×), brine (1×), and dried under high vacuum. The residue was purified via flash column chromatography (97:2:1 dichloromethane: isopropanol: acetic acid) to yield a white powder (80.3% yield) ESI-MS confirmed the final product mass, [M+Na] = 448.155, theoretical [M+Na] =

448.16. Optical Rotation $[\alpha]_D^{23}$ = - 1.206 (*c* 0.995, DCM), (10 replicate measurements in DCM). ^{1}H NMR (300 MHz, $CDCl_3$) δ 1.6927 (dt, 2H, J = 7.85, 14.49), 2.1645 (tt, 2H 8.19, 14.04), 2.5588 (t, 2H, J = 7.39), 3.029 (d, 2H, J = 3.08), 4.268 (t, 1 H, J = 7.17), 4.433 (d, 2 H, J = 7.17), 4.615 (dt, 1 H, J=4.2, 7.8), 5.05 (dd, 1 H, J=1.2, 3), 5.110 (dd, 1 H, J=3, 4.5), 5.63 (d, 1 H, J = 7.5), 5.78 (ddt, 1 H, J=6.9, 10.2, 13.5), 7.33-7.44 (cm, 4 H), 7.60-7.63 (d, 2 H, J=7.2), 7.76-7.79 (d, 2 H, J= 6.9).

(4)

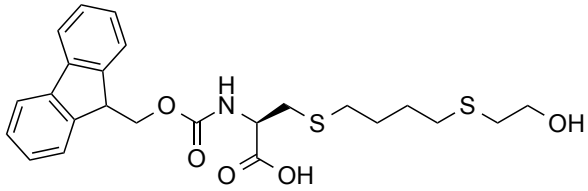

N-Fmoc-*S*-butenyl-L-cysteine (0.0378 mmols) was dissolved in DMF (0.5 M). β-mercaptoethanol (3 eq., 0.113 mmols) was added along with 10 mol % DMPA. A 365 nm UV lamp irradiated the sample for 1 h. A microscale pipette column was used to purify the sample. ESI-MS confirmed the final product mass, [M+H] = 442.4, theoretical [M+H] = 442.18.

***N*-Fmoc-L-cysteine methyl ester**

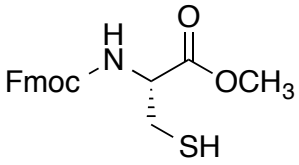

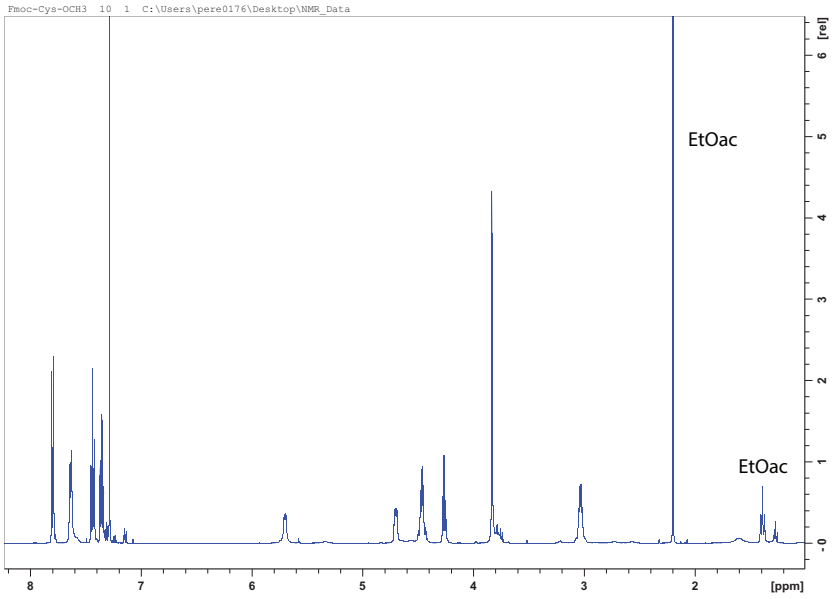

***N*-Fmoc-*S*-butenyl-L-cysteine methyl ester**

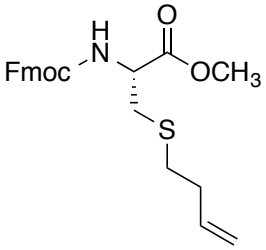

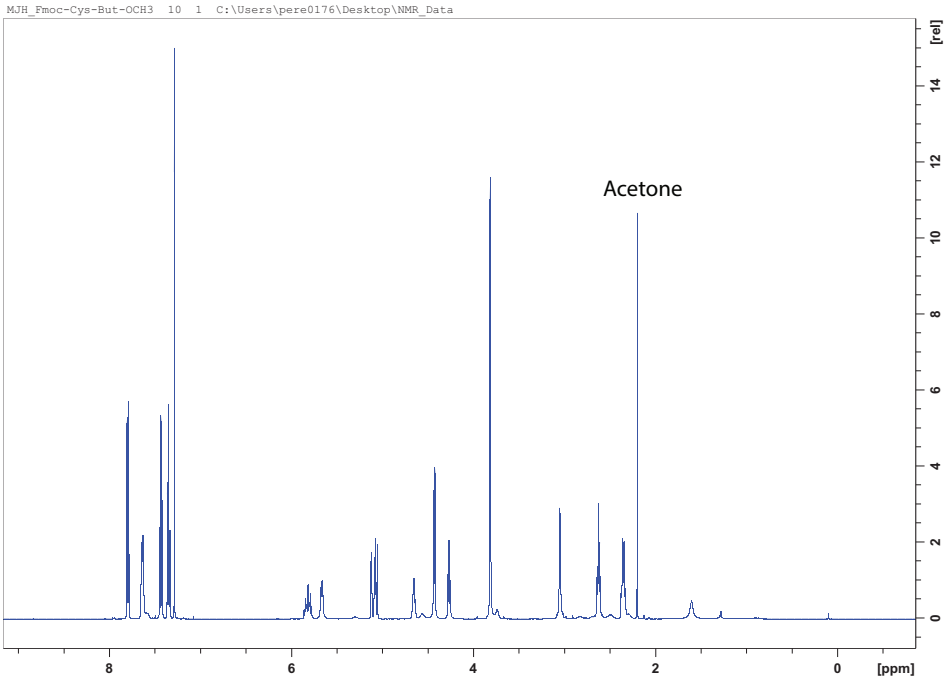

***N*-Fmoc-*S*-pentenyl-L-cysteine methyl ester**

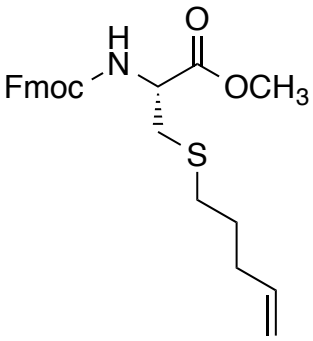

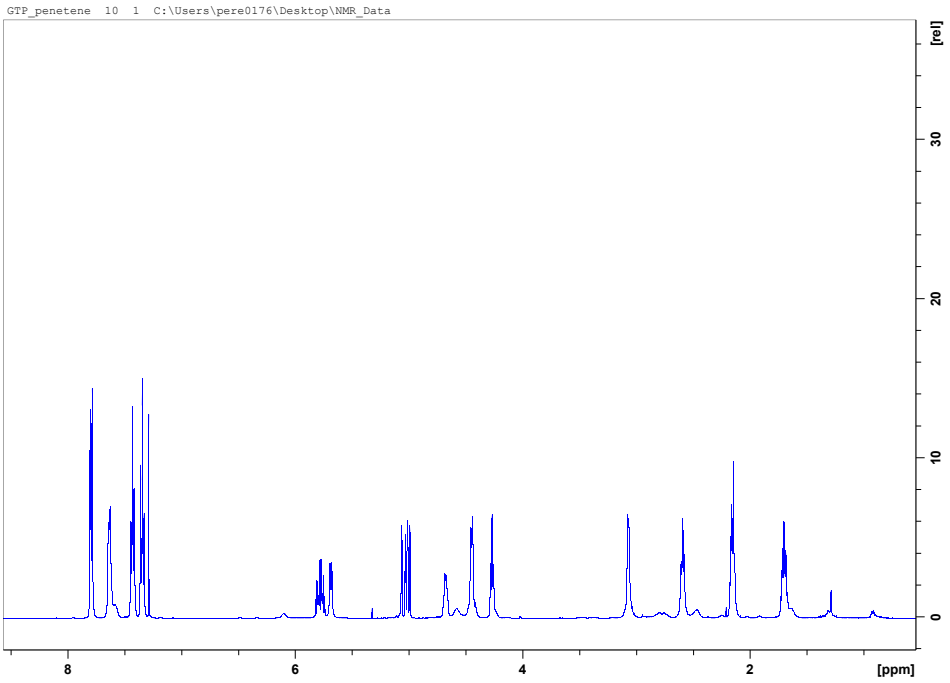

***N*-Fmoc-*S*-butenyl-L-cysteine**

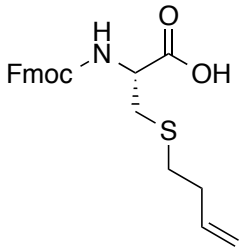

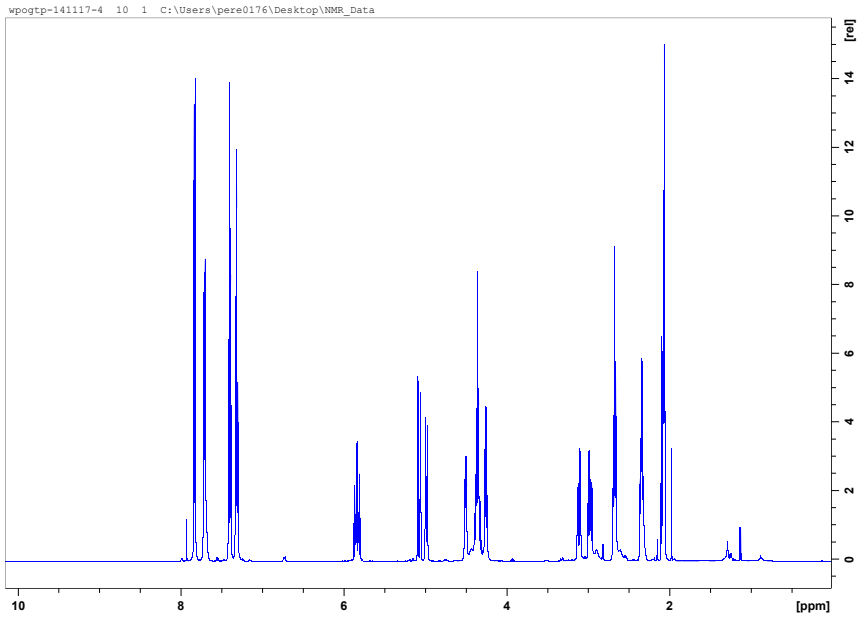

***N*-Fmoc-*S*-pentenyl-L-cysteine**

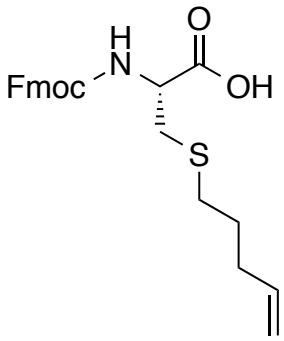

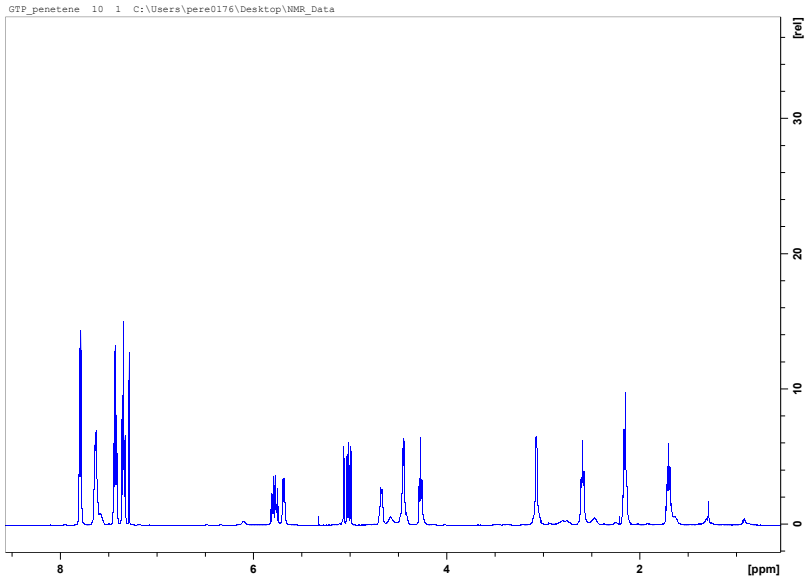
GTP_penetene 10 1 C:\Users\pere0176\Desktop\NMR_Data
[rel]
30
20
10
0
8
6
4
2
[ppm]

(4)

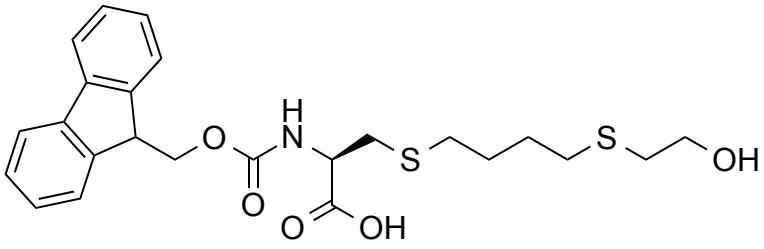
H
N
O
O
O
OH
S
S
OH

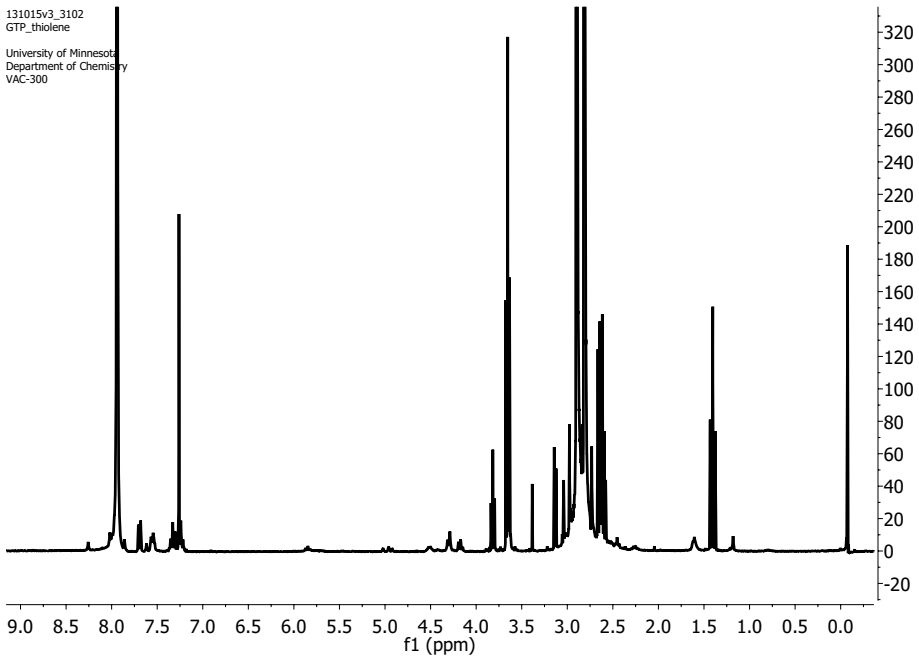
131015v3_3102
GTP_thiolene
University of Minnesota
Department of Chemistry
VAC-300
320
300
280
260
240
220
200
180
160
140
120
100
80
60
40
20
0
-20
9.0 8.5 8.0 7.5 7.0 6.5 6.0 5.5 5.0 4.5 4.0 3.5 3.0 2.5 2.0 1.5 1.0 0.5 0.0
f1 (ppm)

Chapter 5. Specific Acetylation Patterns of H2A.Z Form Transient Interactions with the BTPF Bromodomain & Small Molecule Inhibitors of the CBP Bromodomain Monitored with PrOF NMR

5.1 **Introduction**

5.1.1 Epigenetics

Epigenetics is the study of the alterations in phenotype due to a change in gene expression without modification of the genetic code. Much of the genome function is enoded by the DNA sequence and regulating transcriptional factors; however, depending on external stimuli, identical genomes can lead to varied levels and gene expressions. This variated interpretation is driven by the changes within packaged DNA. Epigenetics plays an important role in regulating gene transcription as well as the alterations within chromatin which lead to different patterns of expression. These chemical variations, termed post translational modifications (PTMs), can include lysine acetylation, methylation, ubiquitinylation, and serine or threonine phosphorylation can associate with DNA, or can occur on the DNA template itself, such as cytosine methylation. Researchers are discovering the scope and effect these dynamic, reversible processes can play within both healthy and diseased states.

PTMs occur within the chromatin, which is created through the packaging of DNA into tightly wound bundles. There are ~ 147 base pairs of DNA wrapped around eight of four highly conserved histone proteins (H3, H4, H2A, and H2B) that comprise chromatin. The organization of DNA into compact structures greatly influences the activation, or silencing of genes. When tightly bound, DNA is inaccessible, leading to the heterochromatin state,

Figure 5.1. When loosely packed with an appearance of 'beads on a string', the DNA is more accessible, which can lead to active transcription.[222] The histone proteins used to wrap DNA were initially thought to be static proteins acting as templates only necessary as a physical constraint on DNA. Researchers are now understanding the active role histone proteins play in gene expression, and recognizing the utility of these key regulators of cancer progression, previously thought to have been only implicated with genetic mutations.

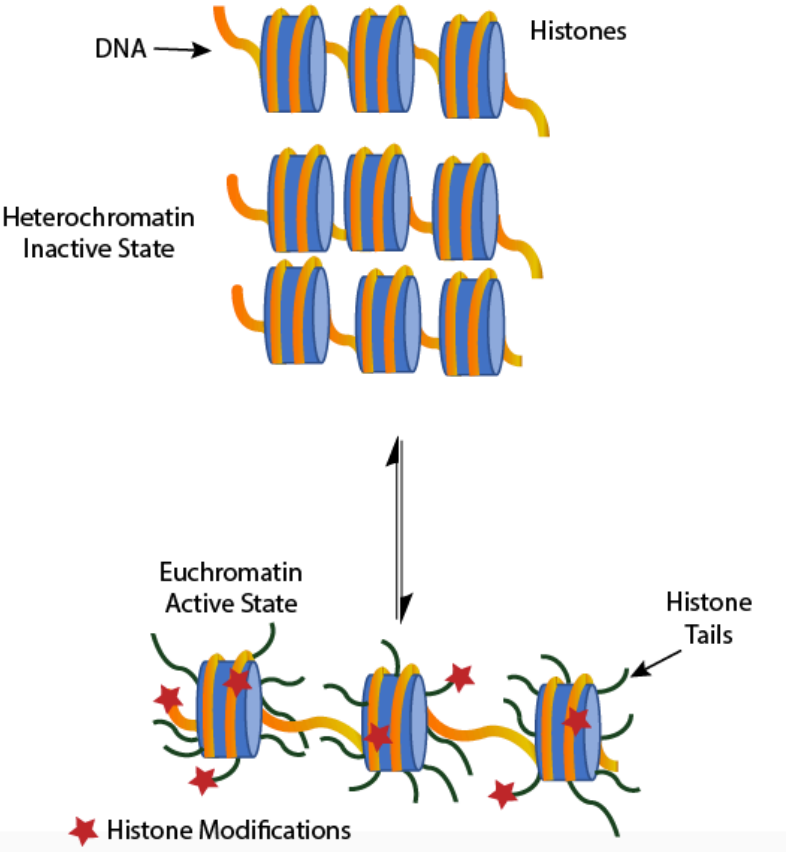

Figure 5.1 Varied states of DNA bundles wrapped around histone proteins. Tightly bundled histones lead to an inactive state, heterochomatin, whereas loosely wrapped DNA from an active state is termed the Euchromatin state.

Modifications of chromatin can directly change DNA through methylation, or chemical change histones that interact with DNA through covalent histone modifications.[223] This chapter will focus specifically on covalent histone modifications. Many histone alterations take place on the tail of the histone, the only unstructured portion of the protein that protrudes from the histone bundle (**Figure 5.1**). These extrusions can interact with other proteins, which leads to alterations of the tails through modifications such as acetylation, ubiquitination, and methylation. The vast influence histones have on biological diversity has led to the idea of a histone language where the encodability of histones are defined through the 'histone code'. There are three distinct roles that define the histone code: readers, writers, and erasers.

5.1.2 Histone Code Writers

Enzymes that add modifications are histone acetyltransferases and histone methyltransferases (HATs and HMTs)—the writers of the histone code that covalently crosslinks methyl or acetyl groups. Post-translational modifications of lysine residues on the histone tails has been extensively studied. Persuasive evidence has identified acetylation or methylation of specific lysine residues on the amino termini of a histone tail to regulate transcription.[224] One highly studied histone modification is on lysine 27 of H3 (H3K27). The histone methyltransferase, polycomb repressor complex 2 (PRC2) acts as a 'writer' of the histone code, where the catalytic subunit EZH2 of PRC2 methylates Lys27 of H3. Lysine methylation has a role in a variety of biological functions including heterochromatin formation, X-chromosome inactivation, and transcriptional regulation.[225] Interestingly, lysine has been found to be mutated to a methionine in disease states.[226] The

methionine mutation is able to diminish methylation of H3K27 through binding to PRC2, rendering it unable to methylate Lys27, which ultimately leads to detrimental downstream effects such as pediatric glioblastomas.[226] Researchers are realizing these modifications are central to vast changes in gene expression, and potential manipulation to these such sites may provide therapeutic strategies.

5.1.3 Bromodomains—Readers of the Histone Code

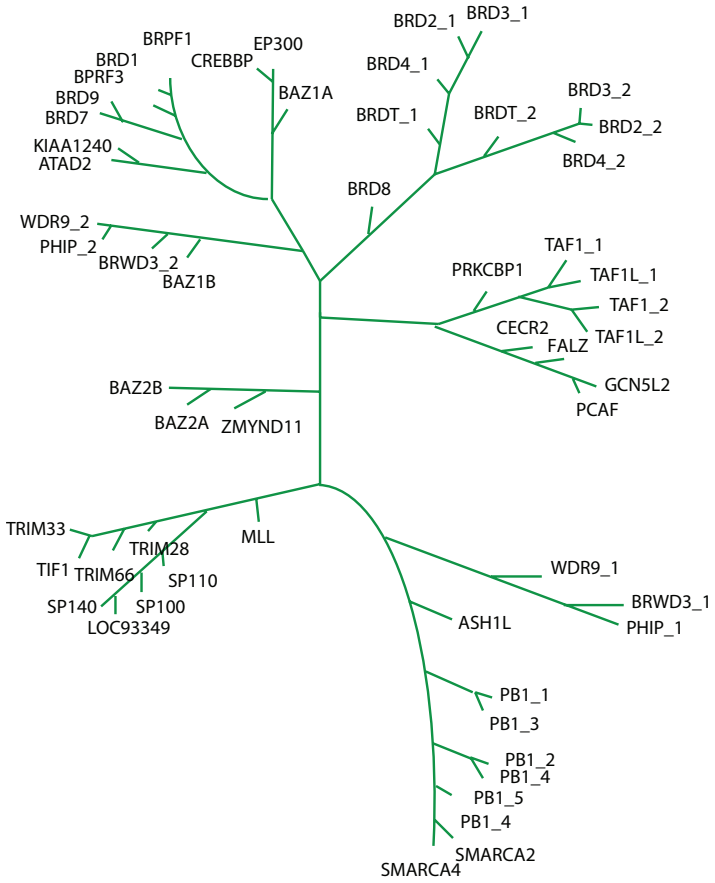

Figure 5.2 Homology Tree adapted from Prinjha et al.[227]

A class of 'reader' proteins that recognizes acetylated lysine residues on histone tails are termed bromodomains. The protein was first identified in 1992 by Tamkun et al. when studying the Brahma gene in drosophila.[228] They discovered it was necessary for activation of a variety of developmental genes, and without brahma function, developmental defects would arise. There are currently 61 human bromodomains identified, and categorized into 9 groups, based on sequence similarity (>35%) and sequence length, **Figure 5.2**.[227,229] The majority of bromodomains have a left-handed four-helix bundle (α_Z, α_A, α_B, α_C), called the 'BRD fold'.[230] Between the helices Z-A and B-C is a hydrophobic pocket that binds to acetylated lysine residues. While significant work had been done on both 'writers' and 'erasers', less was done on 'reader' proteins such as bromodomains. Not until 2010 was there a submicromolar inhibitor of the histone binding modules. Two groups published inhibitors of BRD4, within the bromodomain extra-terminal (BET) bromodomain family—Bradner and colleagues identified the small molecule inhibitor (JQ1),[231] and Tarakhovsky and colleagues determined I-BET to be a competitive inhibitor.[232] Since then, an emergence of research on BET bromodomains ensued, which led to the discovery of a variety of small molecule inhibitors.[233] Limited research has focused on the other 53 bromodomain proteins that do not fit into the BET class. The need to probe and understand other classes will be necessary for progression of novel bromodomain inhibitors within the field of epigenetics.

5.1.4 Histone Deacetylases

The erasers of the histone code, termed histone deacetylases (HDACs), are proteins which remove acetyl groups from the N-terminal tail of histones. By removing acetyl

groups, a positive lysine residue is revealed. This positive character is hypothesized to tighten the histone core into the heterochromatin state, thereby inactivating the histone, and down-regulating gene transcription.[234] The acetylation state of histones is a key component of active gene expression, and an elevated level of HDACs lead to diseased states, such as ovarian cancer, and T-cell lymphoma.[235] Since HDACs have been identified to associate with tumor-suppressor genes, they have been a key target in regards to cancer. [235] The first FDA approved HDAC inhibitor, vorinostat was approved for treatment in 2006.[236] Since then, a flurry of research on HDAC inhibitors has ensued, which may lead to more potent inhibitors of oncotargets.

5.1.5 Histone variants

Varied isoforms of all four main histone proteins have been identified.[237] These slight variations in amino acid sequence can lead to significant changes in expression.[237] An interesting variant of the H2A histone is the H2A.Z variant, which has 60% sequence similarity to H2A, and is highly conserved (90%) from yeast *S. cerevisiae* to humans.[238] H2A.Z has been involved in numerous biological processes including gene activation, chromosome segregation, heterochromatin silencing, and cell cycle progression.[239] One interesting regulatory effect involves the deletion of glycine at position 98 found within H2A.Z, which causes significant changes to the secondary structure. The mutation causes an extended α-helical structure on H2A.Z, which doubles the length of the helix.[240] The extension leads to an interaction with an H2A.Z chaperone, acidic nuclear phosphoprotein 32 kilodalton e(ANP32E). The chaperone preferentially interacts with the H2A.Z/H2B dimer, but not H2A/H2B dimer.[241] The extended α-helix is also incompatible with

nucleosome binding, and aids in the eviction of the H2A.Z histone.[240] This highlights the dramatic impact small changes in primary sequence can have on histone dynamics.

5.1.6 *Malarial H2A.Z*

Plasmodium falciparum is a deadly parasite to humans that causes malaria in more than 800,000 individuals per year.[242] This parasite has vast detrimental effects on both the economics and health of the human population. The parasitic virulence (*var*) gene expression dictates the pathogenicity by being turned on. There are 60 *var* genes within *P. falciparum* that have mutually exclusive expression to another, where only one gene will be active at a time, whereas the rest will be repressed. Epigenetics plays a key role in *var* expression by activating and silencing them based on the chromatin structure dictated through posttranslational modifications of the histones.

The lysine acetyltransferase domain of *Pf*GCN5 is known to acetylate H3K9 and H3K14.[243] Researchers have identified histone acetyltransferases as a potential target to turn off *var* gene expression levels, which leads to a decrease in the levels of parasitic growth.[244] Understanding the role histones play within epigenetic systems of *P. falciparum* may lead to anti-malarial therapeutics.

5.2 Specific Acetylation Patterns of H2A.Z Form Transient Interactions with the BPTF Bromodomain

Motivation:

While acetylation states have been shown to be necessary with the four canonical histones to be read by bromodomains, it has been less extensively evaluated with a highly conserved H2A variant, H2A.Z. We sought to understand which, if any, acetylation pattern on H2A.Z binds to specific bromodomains, since no direct interaction had been observed previously.

5.2.1 Introduction

Chromatin structure is dynamically regulated via post-translational modifications to both DNA and bound histone proteins. The nucleosome particle comprises approximately 147 base pairs of DNA surrounding an octameric bundle of four conserved histones: H2A, H2B, H3, and H4. This assembly provides a scaffold for recruiting transcription factors to accessible genomic regions for modulating transcription.[245] Histone acetylation is one such modification recognized by bromodomain effector modules and subsequently results in the recruitment of the transcriptional machinery. In addition to conserved histones, histone variants can be exchanged into nucleosomes dramatically affecting chromatin stability,[246] and provide an additional mechanism for transcriptional

control.[247] Here, we evaluate interactions of the histone variant H2A.Z with a select set of bromodomains.

H2A.Z is a non-conserved histone variant commonly found at transcription start sites,[248,249] leading to a destabilized nucleosome.[250] H2A.Z levels positively correlate with the activating histone mark, H3K4me3 and negatively correlate with the repressive modification, H3K27me3.[251–253] H2A.Z histones are spread throughout the promoter of inactive genes in the un-acetylated state, but they are acetylated near highly localized transcription start sites (TSS).[254] In yeast, the acetyltransferase, GCN5 acetylates N-terminal lysines of H2A.Z with a preference towards acetylation of K14.[255] Accumulation of hyperacetylated levels of H2A.Z at the TSS have been correlated with high levels of proliferative gene expression in bladder cancer,[256] melanoma,[257] and liver cancer.[258] However, the role and mechanisms employed by H2A.Z for regulating disease states are still being uncovered.

Histone chaperones also play a key role in the removal and addition of the H2A variant.[259,260] Recently, the histone chaperone ANP32e was identified to selectively remove H2A.Z from the nucleosome[240] and the SWR1 complex has been identified to catalyze the exchange of H2A with H2A.Z. The recruitment of SWR1 is partly directed through bromodomain subunit of SWR1, Bdf1, which identifies acetylated histone tails on H3 and H4.[261,262] While the acetylation state of H2A.Z correlates with disease states[254] and epigenetic control.[263] To date, direct bromodomain interactions with acetylated H2A.Z histones have not been systematically evaluated. An understanding as to which, if any, acetylation states on H2A.Z are necessary to bind bromodomains would further elucidate the role H2A.Z plays in gene regulation.

The bromodomain and PHD finger-containing transcription factor BPTF, has recently been described to serve an important regulatory role in cell cycle progression, proliferation, development, and the immune response;[264,265] furthermore, high levels of BPTF correlate with poor patient prognoses in various cancers.[266–268] One role of BPTF as a potential oncoprotein has been supported via identification of a c-Myc protein-protein interaction at low affinity interaction sites on chromatin, thus leading to BPTF's association with various Myc-dependent cancers.[269,270] Recently, it has been shown that BPTF selectively immunoprecipitated H2A.Z-containing nucleosomes over H2A-containing nucleosomes.[271,272] Further, knockdown of either BPTF or H2A.Z decreased the mRNA levels of ten elevated genes in bladder cancer that have H2A.Z enrichment near their TSS.[271] Based on these results, we sought to test if these effects were regulated via a direct interaction of the BPTF bromodomain with the acetylated H2A.Z histone as a potential mechanism for regulating transcription.

5.2.2 Results

5.2.2.1 Evaluation of Acetylation Patterns on H2A.Z with 5FW-BPTF Using PrOF NMR

Bromodomain-histone interactions are characteristically weak interactions with measured affinities at mid-micromolar to millimolar levels.[273] For example, the BPTF bromodomain has been characterized to recognize acetylated lysine 16 of histone H4 (H4acK16) with K_d = 99-210 μM affinity by ITC and fluorescence polarization, respectively, whereas the adjacent PHD domain of BPTF binds H3K4Me3 with a K_d = 1.6-2.7 μM, **Figure 5.3**.[274] Therefore, to characterize weak binding interactions with the BPTF

bromodomain, we turned to NMR spectroscopy which is capable of accurate quantitation of micromolar and millimolar dissociation constants.

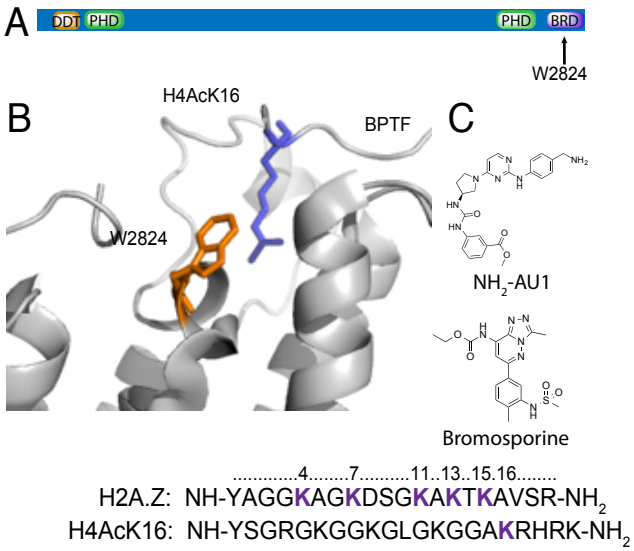

Figure 5.3 Proteins and ligands characterized in this study (A) BPTF sequence with varying domains including the DNA binding homeobox and Different Transcription factors (DDT), two plant homeodomain (PHD) fingers, and bromodomain (BRD). W2824 which is modified in this study is indicated for clarity. (B) BPTF bromodomain with W2824 highlighted (orange) in complex with H4AcK16 (purple) (PDB ID: 3QZS). (C) BPTF small molecule ligands NH_2-AU1 and bromosporine and peptide ligands H2A.Z and H4AcK16. Acetylatable lysines shown in purple.

Protein-observed ^{19}F NMR (PrOF NMR) has become a useful method for characterizing protein-ligand interaction binding sites and quantifying affinity, particularly for weakly binding ligands.[275,276] In the case of several bromodomains, there is a tryptophan that is part of a three-residue hydrophobic region called the WPF shelf. This tryptophan is near the histone binding site and has been used for detecting binding events by PrOF NMR, including with BPTF.[198] For studies presented here, a single fluorinated BPTF bromodomain was expressed with W2824 fluorine-labeled as 5-fluorotryptophan using previously reported methods, and defined as 5FW-BPTF for this report.[192] This protein construct was used to characterize the affinity of all peptides described in this report.

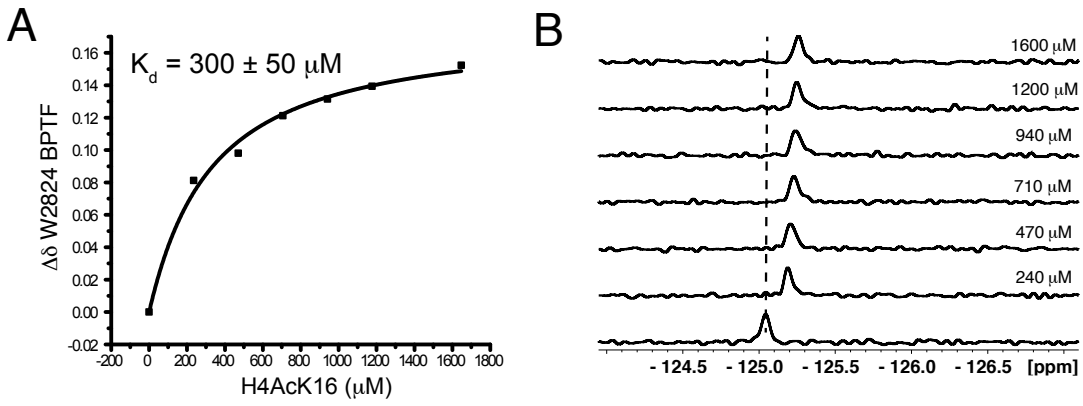

Figure 5.4 PrOF NMR experiments with H4AcK16 binding to 5FW-BPTF. (A) binding isotherm of H4AcK16 binding to 5FW-BPTF with K_d = 300 μM. (B) Overlaid ^{19}F NMR spectra with increasing concentration of H4AcK16 peptide with 47 μM BPTF.

To benchmark our method, we first characterized the interaction between the BPTF bromodomain and a 20-residue peptide of the N-terminal region of H4acK16. Titration of this peptide with the fluorinated bromodomain and measurement of the change in chemical shift of W2824 of BPTF yielded a K_d of 300 μM (**Figure 5.4A**), comparable to the reported affinity determined by fluorescence polarization of 210 μM.[274] The slight difference may correspond to experimental conditions, or a small perturbation from fluorine incorporation. We next turned our attention to H2A.Z. H2A.Z is found in two isoforms, I and II. We elected to study a 20-residue peptide of H2A.Z I with an N-terminal tyrosine residue as a chromophore for accurate concentration determination, as isoform I has been researched more extensively than isoform II. This peptide will be called H2A.Z for the rest of the manuscript. There are five lysine residues in the active portion of H2A.Z that can potentially be acetylated and 'read' by BPTF (K4, K7, K11, K13, and K15). To identify which, if any, acetylation state was necessary to bind BPTF, we acetylated the lysine residues in various mono-, di-, tri-, tetra-, and penta-acetylated patterns. Using ^{19}F

NMR we followed the shift of a single fluorine resonance from the 5-fluorotryptophan incorporated in BPTF (**Figure 5.5A**). An initial study of singly-acetylated lysine residues showed H2A.Z AcK4, -AcK7, and -AcK11 to have the greatest affinities (~ 1.2-1.3 mM, Figure 3B, C), whereas H2A.Z AcK15 and the un-acetylated histone displayed either non-saturating binding or no binding behavior.

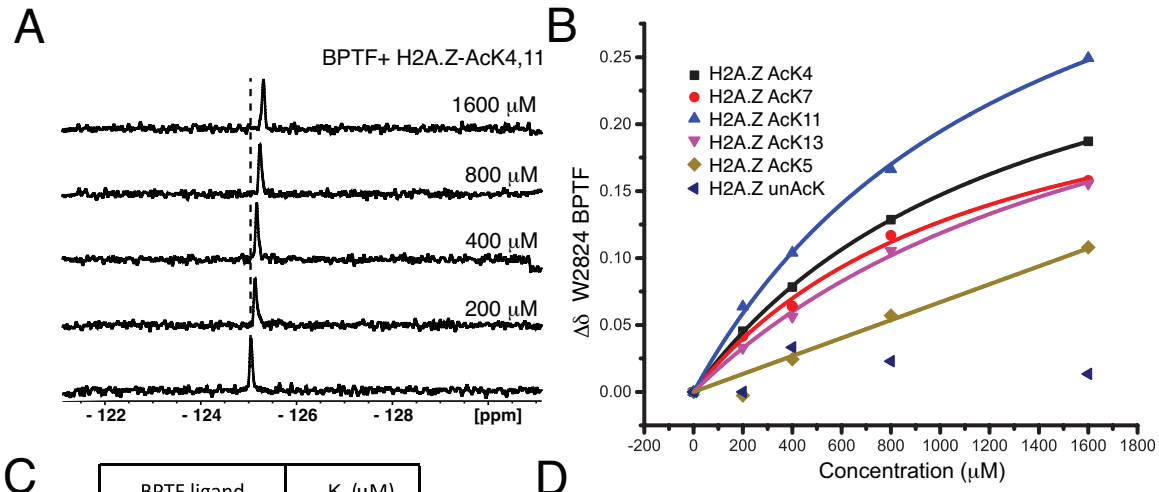

C

BPTF ligand	K_d (μM)
H2A.Z-AcK 7	1140±206
H2A.Z-AcK 4	1300±28
H2A.Z-AcK11	1300±130
H2A.Z-AcK 13	1810±261
H2A.Z-AcK 15	N.S.
H2A.Z-AcK 4,11	780±64
H2A.Z-AcK 4,7	990±46
H2A.Z-AcK 7,11	1200±48
H2A.Z-AcK4,7,11	1510±345
H2A.Z-AcK4,7,11,13	2100±290
H2A.Z-AcK 4,7,11,13,15	1410±328
H2A.Z-unAcK	N.B.

H2A.Z: YAGGKAGKDSGKAKTKAVSR-NH2

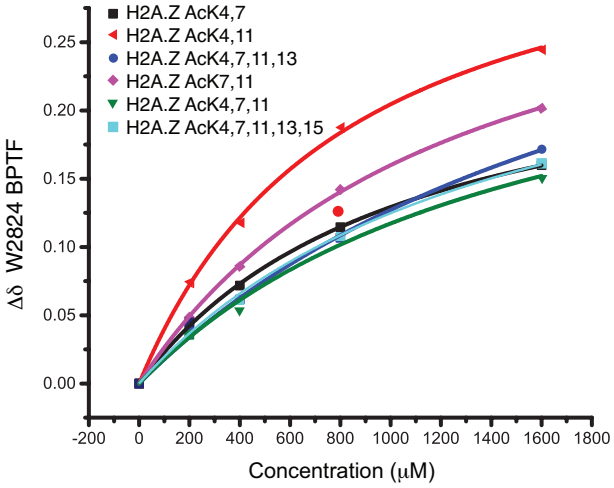

Figure 5.5 H2A.Z fluorine NMR binding experiments with BPTF. (A) PrOF NMR titration overlay with increasing concentrations of H2A.Z AcK4,11 shifting the 5-fluorotryptophan resonance on BPTF (50 μM protein). (B) H2A.Z histone peptide binding isotherms with various mono-acetylated states. (C) Dissociation constants determined using PrOF NMR on H2A.Z acetylated histone variants binding to 5FW-BPTF (N.B. = non-binding, N.S. = non-saturating). (D) An array of di-, tri-, tetra-, and penta-acetylated H2A.Z peptide PrOF NMR binding isotherms with BPTF. Dissociation constants are indicated with corresponding fitting error from nonlinear regression analysis.

Based on the singly-acetylated histone results and the known effects of hyperacetylated histones at TSS,[277] we then tested an array of di-, tri-, tetra-, and penta-acetylated histone peptides (**Figure 5.5D**). From these titrations, di-acetylated histone

H2A.Z AcK 4, 11 showed the highest affinity towards 5FW-BPTF with K_d = 780 μM and modest selectivity over the other acetylation patterns. H2A.Z AcK 4,7 also had increased affinity compared to other acetylation patterns, with a K_d = 990 μM. Higher acetylation states which included AcK4 and 11 led to attenuated binding, indicating avidity effects from hyperacetylation also do not promote this interaction. We conclude from these studies, that the BPTF bromodomain is capable of binding acetylated H2A.Z histones, albeit weaker than conserved histone H4AcK16.

5.2.2.2 Various Bromodomains Evaluated for Affinity Towards H2A.Z AcK4, 11

We selected four additional bromodomains as an initial evaluation if H2A.Z AcK4, 11 was a preferred acetylation pattern for BPTF over other bromodomains. Two bromodomains we selected from the bromodomain and extraterminal (BET) family, Brd4 and BrdT contain a WPF shelf similar to BPTF. We selected another bromodomain, GCN5 from *plasmodium falciparum* (*Pf*GCN5), which also contains a WPF shelf, and is predicted to be structurally related to BPTF based on the phylogenetic tree analysis with human GCN5L2 and BPTF. A fourth unrelated malarial bromodomain which does not contain a WPF shelf, PFA0510w was also evaluated. Malarial bromodomains were selected because within *P. falciparum,* the multi-gene *var* has shown to enrich both H2A.Z nucleosomes and H2B.Z, indicating these variants may have a specific functionality in regards to *P. falciparum* virulence.[242]

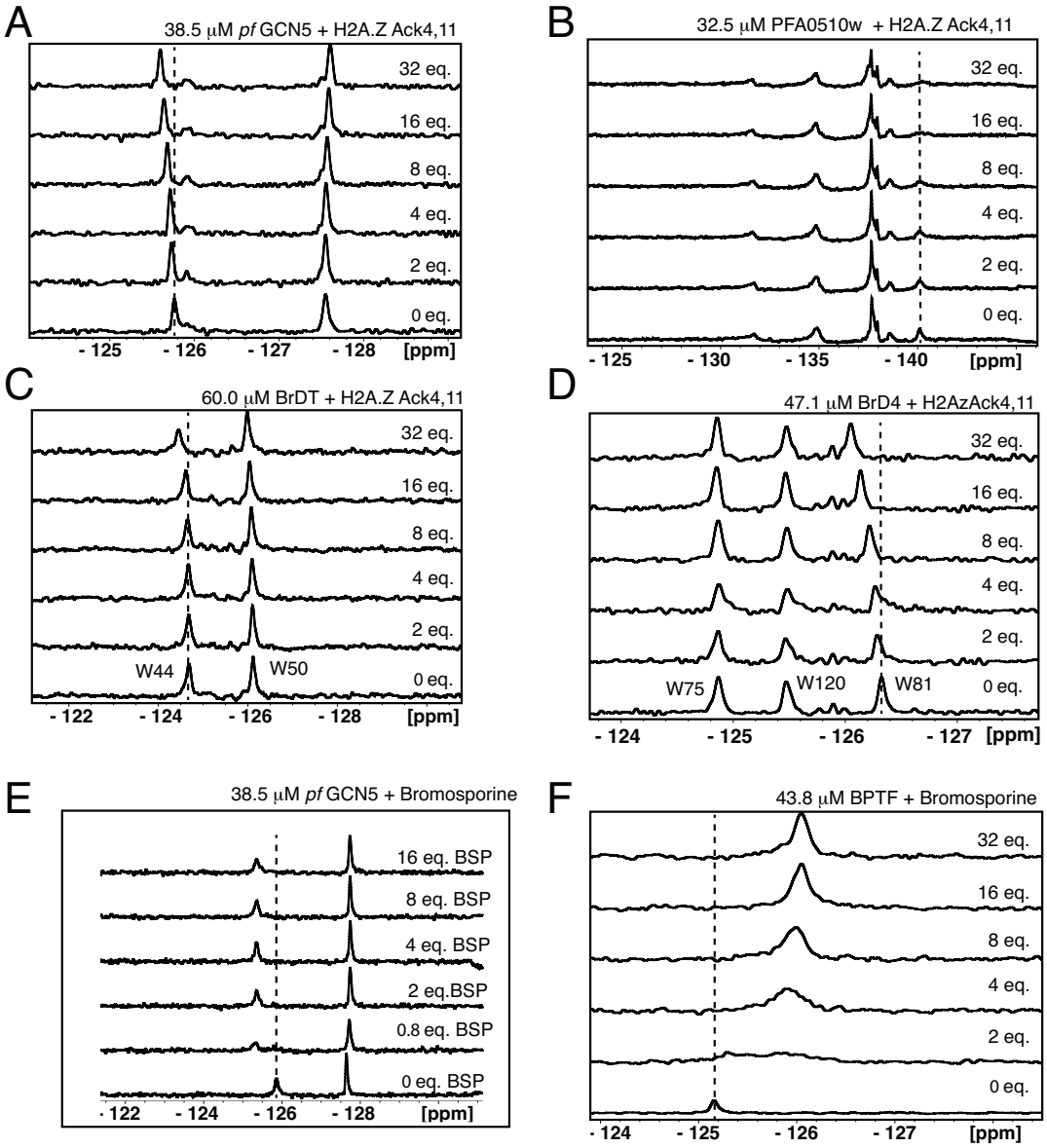

Figure 5.6 PrOF NMR titrations with various bromodomains and ligands. Stacked spectra with increasing concentration of H2A.Z AcK4,11 titrated into A. *Pf*GCN5 B. PFA0510w C. BrDT D. BrD4. In the case of BrdT, the only the non-WPF shelf resonance for W44 moves, consistent with binding somewhere outside the histone binding site. E. Bromosporine titrated into *Pf*GCN5 F. The Intermediate-slow exchange exhibited by bromosporine binding is consistent with a high affinity interaction. Based on this perturbation, the downfield resonance is tentatively assigned as the WPF-shelf tryptophan, W1379. F) Bromosporine titrated into BPTF exhibits intermediate to fast exchange binding kinetics, consistent with a weaker affinity interaction than with *Pf*GCN5.

A PrOF NMR titration indicated that H2A.Z AcK4, 11 exhibited weaker affinity towards the BET bromodomains (**Figure 5.7 A, B**) with K_d =1.5 and 4.2 mM for the N-terminal bromodomains of Brd4 and BrdT respectively. In the case of the Brd4 bromodomain, only the resonance for W81 was perturbed consistent with binding near the histone recognition site. However, in the case of BrdT, the WPF shelf resonance W50, was not affected, and only the resonance for W44 was perturbed. This latter interaction with BrdT may thus be a weak nonspecific binding event. Alternatively, *Pf*GCN5 showed a significant perturbation of the downfield fluorinated tryptophan resonance at -125.5 ppm resulting in an affinity of 0.65 mM, similar to our results with BPTF (**Figure 5.7 C, D**). We tentatively assign this resonance to the tryptophan in the WPF shelf, based on similar perturbations of this resonance from PrOF NMR experiments with pan-bromodomain inhibitor, bromosporine (**Figure 5.6A**, **Figure 5.8**). Finally, because the second PFA0510w bromodomain lacks a WPF shelf, we labeled this protein with 3-fluorotyrosine, due to the presence of a conserved tyrosine (Y1235) within the binding site, **Figure 5.8**. This final titration experiment with H2A.Z AcK4, 11 exhibited little chemical shift perturbation, with only slight broadening of the upfield resonance at high concentrations, which we attribute to a non-specific effect and did not pursue further (**Figure 5.6 B**). Although the affinity is modest, these studies with H2A.Z AcK4, 11 support a preference for the BPTF bromodomain and the structurally related *Pf*GCN5 bromodomain, although a larger panel of bromodomains would need to be evaluated to define a selectivity profile.

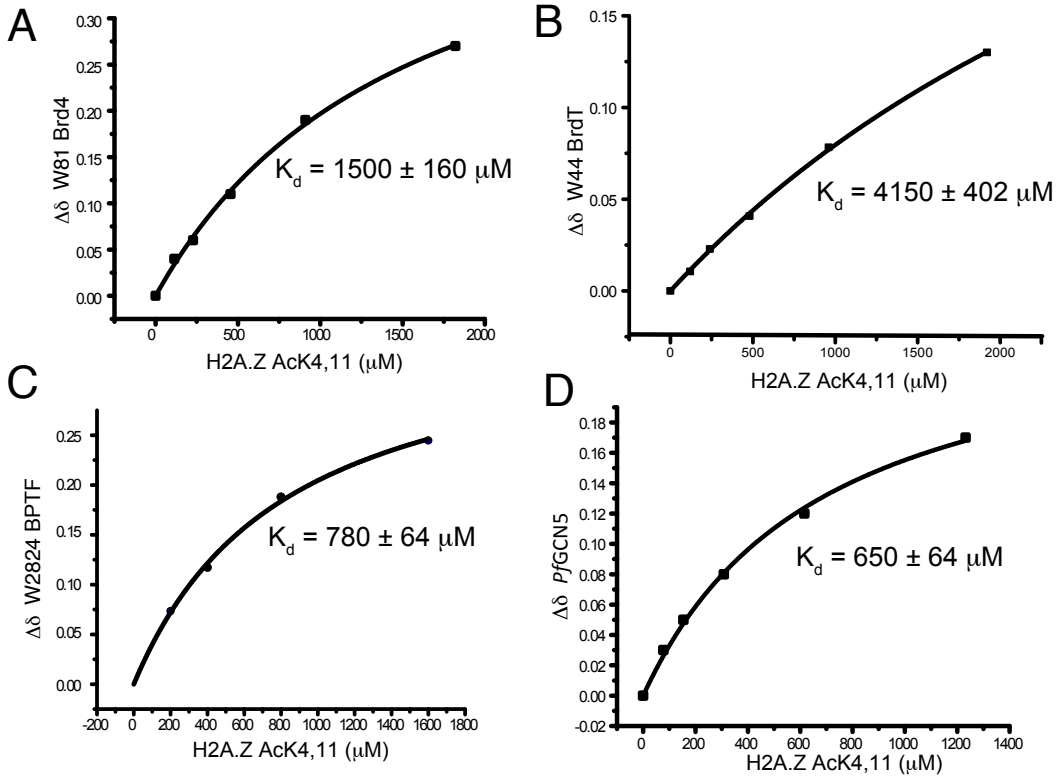

Figure 5.7 H2A.Z AcK4,11 histone peptide PrOF NMR binding isotherms with bromodomains (A) Brd4 (B) BrdT (C) BPTF and (D) malarial bromodomain *Pf*GCN5. Dissociation constants are indicated with corresponding fitting error from nonlinear regression analysis.

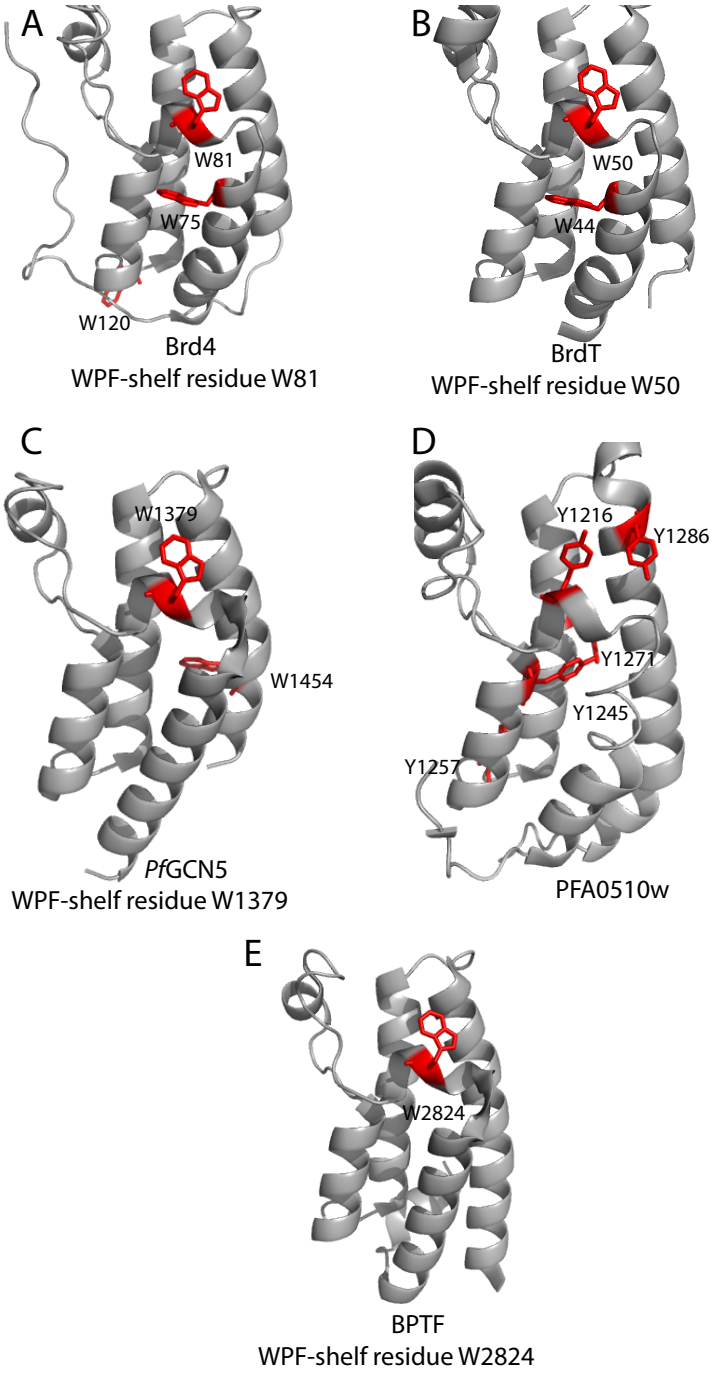

Figure 5.8 Five bromodomain-containing proteins shown in gray, with either tryptophan or tyrosine residues shown as sticks (red). (A) Brd4 with three tryptophan residues where W81 is part of the WPF-shelf (PDBID: 5HLS). (B) BrdT with two tryptophans, W50 part of the WPF-shelf (PDBID: 4FLP). (C) *Pf*GCN5 with two tryptophan residues, W1379 part of the WPF-shelf (PDBID: 4QNS). (D) PFA0510w with five tyrosine residues (PDBID: 4PY6). (E) BPTF with one tryptophan residue within the WPF-shelf (PDBID: 3UV2).

5.2.2.3 Ligand-Observed ^{1}H NMR Competition Experiments

Having established an acetylation pattern and preference for the *Pf*GCN5 and BPTF bromodomains, we further tested bromodomain binding site engagement versus a less specific binding mode using a ligand-observed ^{1}H NMR method, the Carr-Purcell-Meiboom-Gill (CPMG) competition experiment. The ^{1}H CPMG NMR experiment utilizes the transfer in the transverse relaxation time (T_2) of the protein to the ligand in the bound state which is subsequently filtered out. This transfer is observed as a drop in resonance signal intensity when a ligand binds to the protein of interest. Recovery of signal can be induced with addition of a high affinity competitor.[278] An initial experiment with only H2A.Z AcK4,11 shows the two acetyl singlet resonances near 1.88 ppm. When either *Pf*GCN5 or the BPTF bromodomain was added, a significant drop in the resonance intensity is observed, as expected if the ligand were binding to the bromodomain. In a separate experiment, we validated pan-bromodomain inhibitor bromosporine, binding to the *Pf*GCN5 bromodomain by PrOF NMR with high affinity (**Figure 5.6**). When we added bromosporine to *Pf*GCN5, a full recovery of resonance intensity was observed for *Pf*GCN5 with 400 μM bromosporine (**Figure 5.10A**). However, in the case of BPTF, only partial recovery (34%) was seen upon addition of 400 μM bromosporine. Titration of bromosporine with BPTF using PrOF NMR yielded a K_d of 37 μM (**Figure 5.9**) which may be too weak for full displacement of H2A.Z from BPTF, or the compound may become aggregated and not soluble at high concentrations. We recently reported on a BPTF bromodomain inhibitor AU1 with a K_d of 2.8 μM.[198] However, this compound is also not soluble at high concentrations. We therefore used an analog capable of binding to the BPTF bromodomain, but with a protonatable benzylic amine for solubility, NH_2-AU1. In

this case, addition of the inhibitor was able to dose dependently return the resonance intensity (75% at 800 μM). The CPMG experiment corroborates our initial assessment in that H2A.Z AcK4,11 binds to both BPTF and *Pf*GCN5 and can be competitively displaced with small molecule inhibitors which engage the histone binding pocket.

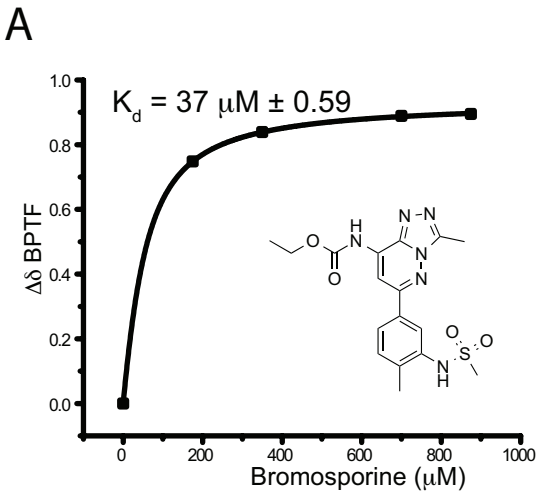

F**igure 5.9** PrOF NMR binding isotherm with bromosporine binding to BPTF. Data fit from spectra obtained in **Figure 5.6 F**.

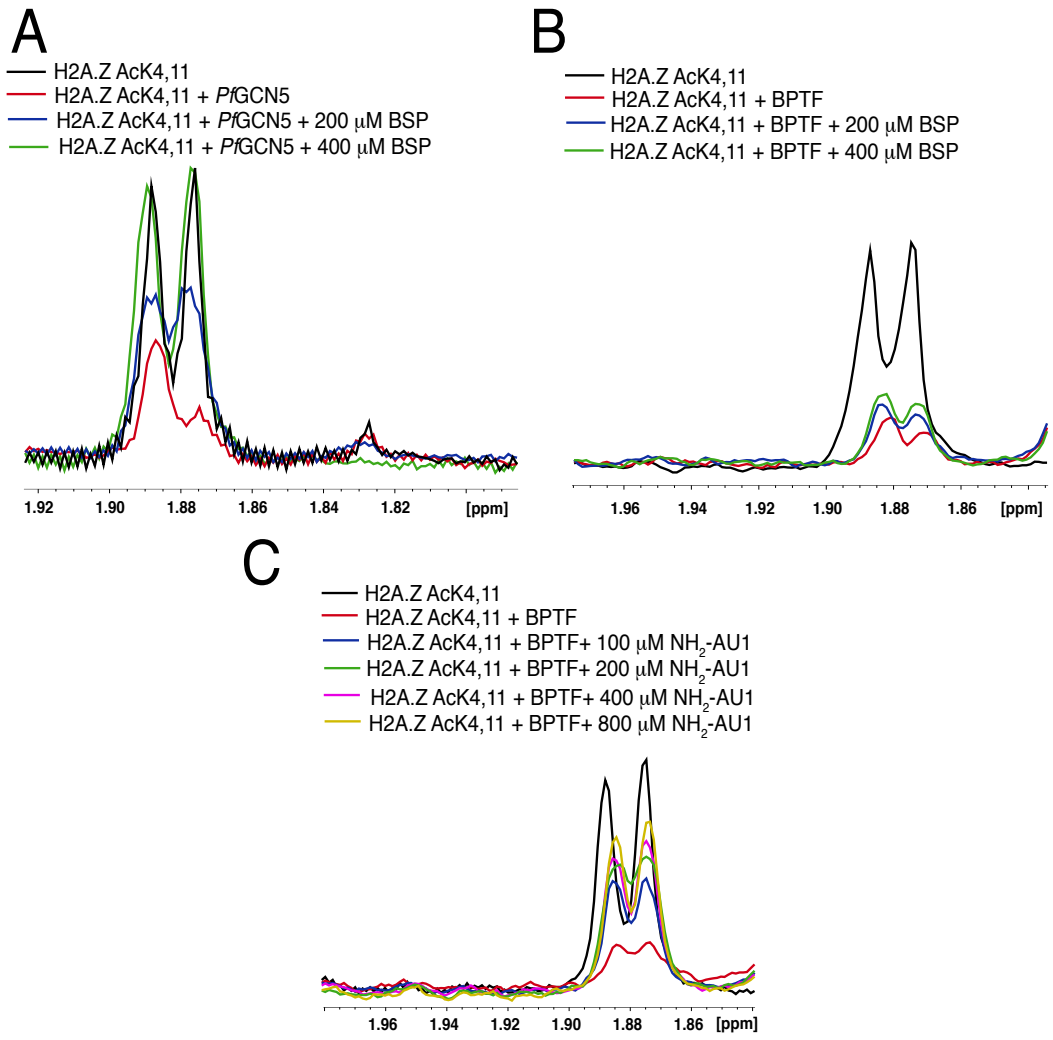

Figure 5.10 Ligand-observed ^{1}H NMR CPMG competition experiments for evaluating H2A.Z AcK4,11 histone binding site occupancy (A) *Pf* GCN5 and (B, C) BPTF. Experimental spectra are shown for the histone alone (black), the histone plus bromodomain (red), and the histone plus bromodomain and increasing concentration of inhibitor (blue, green in B) for bromosporine and (blue, green, magenta and gold in (C) for BPTF inhibitor NH_2-AU1.

5.2.2.4 Photo-crosslinking Captures a Transient Bromodomain Interaction

Sudhamalla et al. recently showed that photo-crosslinking experiments were capable of capturing transient bromodomain histone interactions using a BPTF bromodomain analog where the tryptophan in the WPF shelf was replaced with a para-azidophenylalanine (BPTF-*p*AzF).[279] Without higher resolution structural biology data,

we sought to capture the transient bromodomain histone interaction demonstrating bromodomain engagement near the WPF shelf. In this final set of experiments, we incubated three biotinylated H2A.Z peptide constructs with BPTF-*p*AzF—unacetylated H2A.Z, mono-acetylated AcK15, and di-acetylated AcK4, 11. Using 0.5 and 1.0 mM peptide, each solution with BPTF was irradiated with 365 nm light. Photo-crosslinked protein-peptide adducts were resolved via gel electrophoresis and detected via western blot with an anti-biotin antibody (**Figure 5.11**). In the case of the un-acetylated H2A.Z, no crosslinking was observed. For H2A.Z AcK15, low levels of crosslinking were observed consistent with the previously detected weak interactions from PrOF NMR titrations (**Figure 5.5 B, C**). However, for di-acetylated H2A.Z AcK 4, 11 increased crosslinking in a dose-dependent fashion was observed. Control experiments showed no crosslinking was detected in the absence of photo-irradiation in all cases. We conclude from these studies that di-acetylated H2A.Z AcK4, 11 engages the BPTF bromodomain in a manner consistent with previously characterized histone interactions.

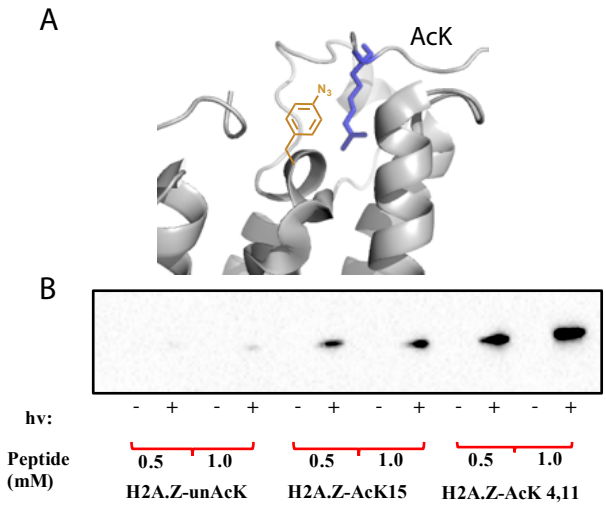

Figure 5.11 (A) *p*Azido-phenylalanine mutant replaces W2824 in BPTF for photo-crosslinking experiments. This residue is part of the acetylated lysine recognition site within the WPF Shelf of BPTF. (B) Photo-crosslinking anti-biotin western blot analysis of biotinylated H2A.Z variant peptides irradiated with BPTF-*p*AzF. Un-acetylated, mono-acetylated, and di-acetylated H2A.Z peptides: unAcK, AcK15, and AcK4,11, respectively were tested at 0.5 and 1.0 mM in the presence and absence of UV light.

5.2.3 Discussion

Nucleosomes with histone variant H2A.Z can alter chromatin accessibility, particularly near transcriptional start sites, leading to altered transcriptional programming.[280] Acetylation of H2A.Z was identified to play a fundamental role in changing chromatin states. The SWR-1-Com, NuA4, and GCN5 have been identified to acetylate H2A.Z,[260,281] and ANP32e is able to evict H2A.Z from the nucleosome.[240] However, to date no direct interaction of H2A.Z with a bromodomain had been characterized. Here, we identified specific acetylation states of the H2A.Z histone variant that can form transient interactions with the bromodomain of BPTF. All five lysine residues within the H2A.Z N-terminal tail were modified in a variety of mono- and multi-acetylated patterns. PrOF NMR identified H2A.Z AcK4,11 to have high micromolar affinity towards

BPTF (K_d = 780 μM). Acetylation of lysine 15 did not exhibit saturating binding behavior, arguing against a promiscuous acetyl-lysine recognition motif.

We compare our results with proteomics studies which have characterized abundant acetylation states of H2A.Z. In chicken erythrocytes, Dryhurst et al. found a tri-acetylated version of H2A.Z to be the most abundant where it was specifically acetylated at lysine 4, 7, and 11.[282] The second most abundant peptides found in their proteomic studies were di-acetylated histones acetylated at lysine 4, and 7, lysine 7 and 11, and lysine 4 and 11. Proteomic analysis of H2A.Z from mouse embryonic stem cells revealed the mono-acetylated lysine residues to be the most highly abundant with preference for lysine 4, 7, and 11, while di-acetylated lysines were the next highest in abundance. However, the di-acetylation pattern for lysine 4 and 11 was only detected at significant levels when H2A.Z was ubiquitinated.[253] These results demonstrate that di-acetylation patterns on H2A.Z can be found under physiological conditions and that additional acetylation patterns in addition to Lys 4 and 11 may be relevant.

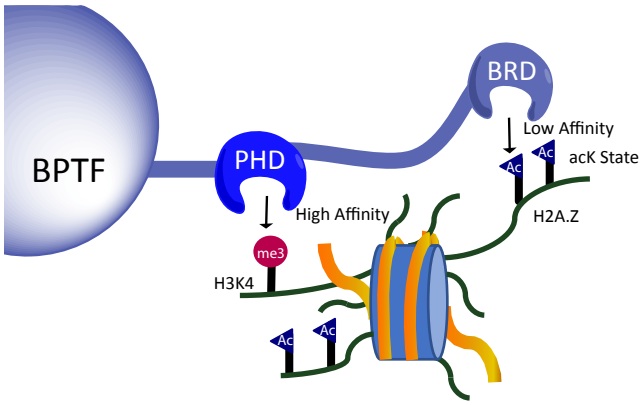

Figure 5.12 Cartoon depicting two domains on the BPTF PHD domain and bromodomain that bind post-translational modifications on histone tails. The PHD domain binds H3K4me3 with low micromolar affinity, while the bromodomain, BRD binds H2A.Z AcK 4, 11 with high-micromolar affinity. These two interactions may facilitate a bivalent intra-nucleosomal interaction as proposed by Ruthenburg et al.[274]

In our experiments, we attain only modest affinity for H2A.Z AcK4,11 towards BPTF. This affinity should not be sufficient to facilitate H2A.Z nucleosome enrichment on its own as observed by Kim et al.[271] However, enhancement of H2A.Z deposition near TSS correlates strongly with H3K4me3, a known recognition site for the BPTF PHD domain.[253] We believe the added affinity may strengthen a bivalent interaction (**Figure 5.12**), similar to how BPTF was demonstrated to interact with H4AcK16 and H3K4me3.[274] Ruthenburg et al. identified bivalent interactions of H4Ack16 interacting with the bromodomain, and H3K4me3 with the PHD domain of BPTF lead to a greater increase in total affinity than just one modification alone (2-3 fold enhancement of nucleosomal binding with both H4AcK16 and H3K4me3 over mononucleosomal binding with H3K4me3 alone).[274] While only modest increases were observed, the H3K4me3 interaction lead to specificity towards only H4AcK16, even though H4AcK12 has similar affinity alone. The interaction between H2A.Z AcK4,11 and BPTF may induce a similar bivalency with the PHD domain. This is a starting point in understanding the role acetylated H2A.Z plays in recognizing BPTF. Investigation into the bivalent interactions between the PHD and the bromodomain of BPTF with H2A.Z nucleosomes would be necessary to further understand their interactions in a more native-like environment.

Four other bromodomains were also evaluated for affinity towards H2A.Z AcK4,11—Brd4, BrdT, *Pf*GCN5, and PFA0510w. Of these proteins, only the *Pf*GCN5 bromodomain showed comparable affinity (K_d = 650 μM) to BPTF. The human GCN5L2 bromodomain is structurally similar to BPTF, and both proteins bind H4AcK16. In *Saccharomyces cerevisiae*, GCN5 promotes acetylation and binds acetylated nucleosomes via its bromodomain.[283,284] The human GCN5L2 bromodomain contains a deep

hydrophobic cavity that binds N^{ε}-acetylated lysines with modest affinity ($K_d \sim 900\ \mu M$), with no affinity towards unacetylated peptides.[285] The *Pf*GCN5 bromodomain binds to H2A.Z AcK4,11 with a similar level as the affinity of human GCN5L2 for H4AcK16. Although the human and *P. falciparum* H2A.Z sequences are not identical, these biochemical results for characterization of H2A.Z represent an interesting starting point for understanding the role of acetylated H2A.Z in regulating virulence of the parasite.

5.2.4 Conclusion

We have studied the effects of N-terminal acetylation of histone variant H2A.Z on the direct interaction with bromodomains. Of the peptides tested, we identified a di-acetylated lysine versus single or higher acetylation states of the H2A.Z histone that is responsible for recognition of the BPTF bromodomain. Both BPTF and H2A.Z play a significant role in cancer disease progression, and recent findings show a dependent functional activity of both proteins in bladder cancer. Our findings offer a potential link for modulating function through a direct interaction with H2A.Z in chromatin, but posit that a higher affinity multivalent interaction through a neighboring PHD domain may be necessary. Similar bromodomain interactions between H2A.Z and the *Pf*GCN5 protein may also be present in *P. falciparum*. Synthetic nucleosomes incorporating particular acetylation patterns have been useful for characterizing effector domain interactions using single and multi-domain protein constructs. These constructs will be useful for further testing this molecular recognition event.

5.2.5 Material and Methods

For E. coli growth, LB agar, LB media, defined media components including unlabeled amino acids, uracil, thiamine-HCl, nicotinic acid, biotin and buffer components were purchased from RPI corp. 3-Fluorotyrosine, thymine, cytosine, guanosine were purchased from Alfa Aesar. Magnesium chloride, manganese sulfate, succinic acid, calcium chloride and 5-fluoroindole were purchased from Sigma-Aldrich.

5.2.5.1 Peptide Synthesis

Solid-phase peptide synthesis was performed using the procedure outlined below. 1-hydroxybenzotriazole monohydrate (HOBT, Chem-Impex Int'l), *O*-benzotriazol-1-yl-*N*, *N*, *N*', *N*'-Tetramethyluronium hexafluorophosphate (HBTU, Novabiochem), and *N*,*N*-Diisopropylethylamine (DIEA, Sigma Aldrich) were used as received without further purification and dissolved into reagent-grade DMF (Fisher Scientific). N-α-Fmoc-N-ε-Boc-L-lysine and N-α-Fmoc-N-ε-trifluoroacetyllysine were received from Chem-Impex. N-α-Fmoc-O-tBu-tyrosine, N-α-Fmoc-glycine, and N-α-Fmoc-N-ε-Boc-D-lysine were received from Novabiochem. Piperidine, trifluoroacetic acid, dichloromethane (Sigma Aldrich), Triisopropylsilane (TCI America), acetic anhydride (Fisher Scientific), 3-maleimidopropionic acid NHS (Chem impex), and triethylamine (Mallinckrodt) were all used as received. Peptides were made on a 25 μmol scale on NovaSyn TGR® resin in a CEM MARS microwave reactor. All peptides were synthesized using HOBT and HBTU coupling reagents according to published methods.[286] Following Fmoc deprotection of the final residue, the peptides were cleaved from the resin using a mixture 95:2.5:2.5 TFA:TIPS:H_2O, and stirring for 2 h. The peptide cleavage solution was separated from

the resin, and the solution was concentrated under a stream of N_2. The crude peptide was precipitated with ether, cooled to -20 °C for at least 15 min, and pelleted out by centrifugation at 3000x*g* for 5 min at 4 °C. The pellet was dissolved into a 60:40 0.1% TFA in H_2O: acetonitrile mixture and sufficient DMF to aid solubility. Dissolved peptides were purified on a Dionex Ultimate 3000 RP-HPLC using a C-18 column on a 10-60% acetonitrile gradient over 60 min. Purified peptides were analyzed via Ab-Sciex 5800 MALDI- TOF/TOF Mass Spectrometer. Peptide theoretical and actual masses are shown in **Table 5.2**.

5.2.5.2 Protein Expression Conditions for Unlabeled or Fluorine-labeled Bromodomains Brd4(1), BrdT(1), BPTF, *Pf*GCN5 and PFA0510w

The pNIC28-BSA4 plasmid containing the Brd4(1) and BPTF genes were kind gifts from the laboratory of Stefan Knapp whereas plasmid containing gene of *Pf*GCN5 and PFA0510w were kind gifts from Raymond Hui lab at SGC Toranto.

5.2.5.3 Unlabeled Bromodomains

For unlabeled protein expression of BPTF and *pf*GCN5 bromodomains, the E. coli Rosetta (DE3) strain (Novagen) was first transformed with the pRARE (Novagen) plasmid. The transformed cells were selected using chloramphenicol. Calcium competent pRARE-containing E. coli cells were transformed with the respective plasmids. Co-transformed cells were selected by using 35 mg/L of chloramphenicol and 100 mg/L of kanamycin to select for the pRARE plasmid and bromodomain respectively. Following overnight incubation at 37 °C, a single colony was selected from the agar plate and inoculated in 50 mL of LB media containing kanamycin (100 mg/L) and chloramphenicol (35 mg/L). The

primary culture was grown overnight at 37 °C while shaking at 250 rpm. For secondary culture growth, 1 L of LB media containing kanamycin (100 mg/L) was inoculated with the primary culture and incubated at 37 °C while shaking at 250 rpm. When the O.D. of culture at 600 nm reached 0.6, the shaker temperature was reduced to 20 °C. After 30 minutes, the expression was induced with 1 mM IPTG overnight for 12-16 h. Cells were harvested by centrifugation and stored at -80 °C.

5.2.5.4 Fluorine-labeled Bromodomains

The expression of 3-fluorotyrosine and 5-fluoro-tryptophan labeled proteins were performed by using previously published methods[192,287] and briefly described here. To express the labeled protein, the secondary culture in LB media was grown until an O.D. at 600 nm of 0.6 was reached followed by harvesting the cells at 3000g for 10 minutes. Cells were resuspended in defined media of Muchmore et al.[209] containing 3F-tyrosine (10 mg/tyrosine residue in the respective protein/L defined medium) in place of tyrosine or 5-fluoroindole (60 mg/L) in place of tryptophan. The resuspended E. coli were incubated at 37 °C while shaking for 1 h followed by the cooling to 20 °C and media temperature equilibration for 30 min. Protein expression was induced by 1 mM IPTG overnight (14−16 h) at 20 °C. The cells were harvested and stored at −80 °C.

5.2.5.5 Protein-Observed Fluorine NMR

Protein-observed 1D ^{19}F NMR samples were obtained as previously described[192,198] using a frequency window of -120 to -130 ppm, a D1 of 0.7 sec and an acquisition time of 0.05 sec, SW of 30 ppm, NS = 1000, and a 90° pulse width. Peptide stock solutions were

prepared in MilliQ water at ~20 mM. Peptides were titrated into bromodomain protein (protein solutions at 40-50 μM in 50 mM TRIS, 100 mM NaCl, 5% D_2O, pH 7.4).

5.2.5.6 ^{1}H CPMG NMR Spectroscopy

^{1}H CPMG NMR experiments were carried out on a Bruker HD-500 NMR. A series of ^{1}H CPMG NMR spectra were recorded and carried out in a single NMR tube with the initial run of 100 μM peptide. 2) peptide plus 10 μM protein, and 3) peptide + protein + 100-800 μM competitor bromosporine or NH_2-AU1(with a filter length of 1.2 s, interpulse delay of 2.5 ms, and D_{20} of 25 ms, loop counter at 160).

5.2.5.7 Photo-crosslinking with H2A.Z (unAcK, AcK15, and AcK4, 11) Peptides

This work was done by our collaborators Babu Sudhamalla and Kabirul Islam from the University of Pittsburgh. The procedure for protein expression and phototo-crosslinking of BPTF-W2950AzF has been described previously.[279] W2950 reported previously, corresponds to W2824 used in this current study. In brief, for photo-crosslinking experiments, 0.5-1 mM biotin-labeled histone H2A.Z peptides (unAcK, AcK15, and AcK4, 11) were preincubated with 30 μM of BPTF-W2950AzF in a buffer containing 10 mM Tris-HCl pH 7.5, 150 mM NaCl, 0.05% Tween 20, and 0.5 mM TCEP. After 30 min of incubation at room temperature, samples were subjected to UV irradiation at 365 nm for 15 min at 4 °C. Negative controls were not subjected to UV irradiation. Samples were then bound to Ni-NTA agarose resin and incubated for 1 h at room temperature with gentle agitation. To remove uncrosslinked peptide, samples were washed 10 times each with 1 mL of washing buffer (50 mM Tris-HCl pH 8.0, 200 mM NaCl, 1% Triton X-100). Finally, cross-linked proteins were eluted with a buffer containing 50 mM

Tris-HCl pH 8.0, 150 mM NaCl, 5 mM β-mercaptoethanol, and 400 mM imidazole. The eluted proteins were separated on a 4-12% Criterion XT precast SDS-PAGE gel (Bio-Rad Laboratories) and analyzed by Western blotting as described below.

5.2.5.8 Western Blotting

This work was done by our collaborators Babu Sudhamalla and Kabirul Islam from the University of Pittsburgh. Equal volumes of the pulled-down samples (both UV irradiated and non-irradiated) were separated on SDS-PAGE and transferred onto a 0.2 μm supported nitrocellulose membrane (Bio-Rad Laboratories) at a constant current 67 mA for 16 h at 4 °C. Membranes were blocked with 20 mL of TBST buffer (50 mM Tris HCl pH 7.4, 150 mM NaCl, 0.01% Tween-20) with 5% nonfat dry milk for 1 h at room temperature with gentle shaking. The blocking buffer was then removed and membranes were washed with 20 mL of TBST buffer. Immunoblotting was performed with 1:500 diluted primary antibody (Biotin pAb, cat# PA1-26792, Invitrogen) for 16 h at 4 °C. The antibody solutions were removed and membranes were washed three times with TBST buffer at room temperature. The blots were then incubated with HRP-conjugated secondary antibody Donkey anti-Goat IgG (H+L) pAb (cat# NBP1-74815, Novus) with 5% nonfat dry milk (1:500 dilution) in TBST for 1 h at room temperature. After similar washing, protein bands were visualized by chemiluminescence using VISIGLO HRP Chemiluminescent substrates A and B (cat# N252-120ML and N253-120ML, aMReSCO) following manufacturer's protocol.

5.2.5.9 Synthesis of NH_2-AU1.

Synthesis and characterization of **AU1** analogs were done by Peter Ycas at the University of Minnesota, and will be reported in a subsequent thesis.

Materials. All solvents were commercial grade and used without further purification. Silica gel for flash chromatography was 60 Å, 70-230 mesh. TLC was performed using ALUGRAM® SIL G/UV_{254} aluminum backed plates. All reagents were commercially available and used as received. 4-(aminomethyl)aniline, 33% HBr in acetic acid, methyl 3-isocyanatobenzoate, and trifluoroacetic acid was purchased from Sigma Aldrich. Benzyl carbonochloridate was purchased from Acros Organics**,** (S)-3-(Boc-amino)pyrrolidine was purchased from Combi-Blocks

2,4-dichloropyrimidine was purchased from Chem Impex, Triethylamine was purchased from Mallinckrodt Chemicals

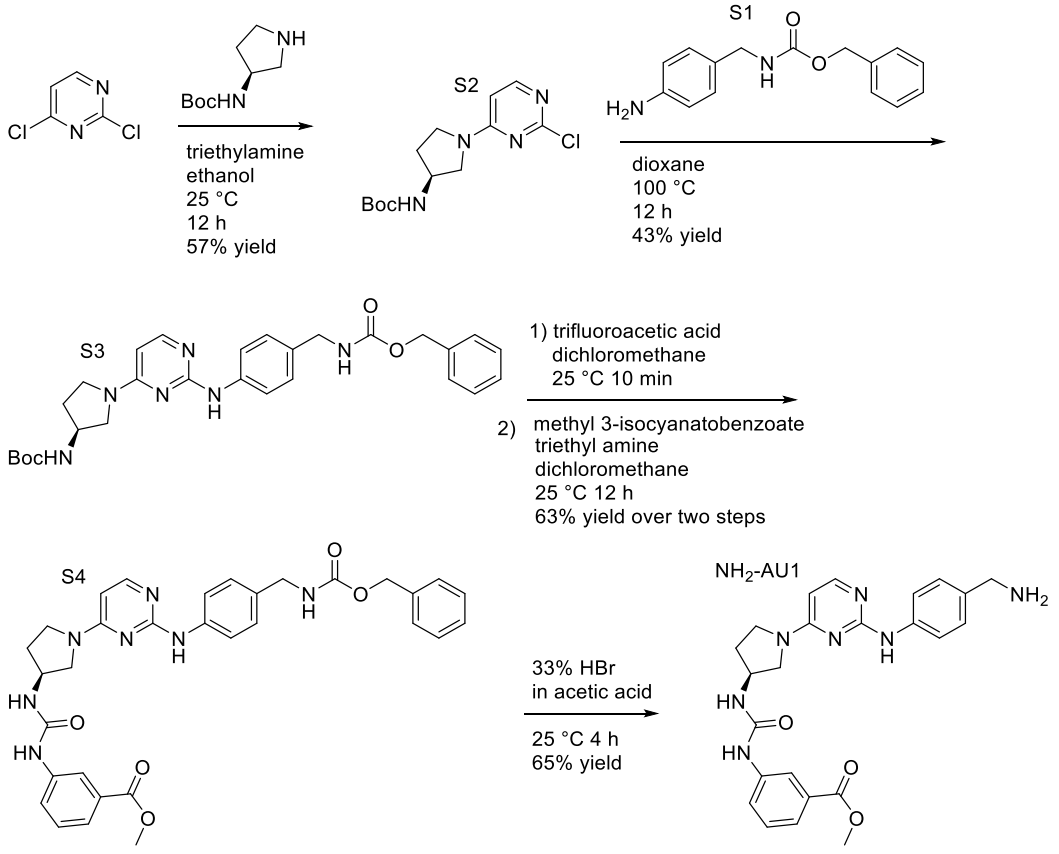

Figure 5.13 Reaction scheme for the synthesis of NH_2-AU1

Synthesis of S1

(S1) 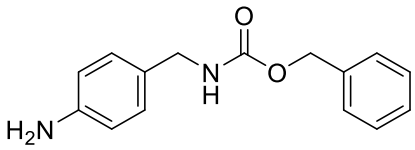

Compound **S1** was prepared according to published methods Angewandte Chemie, International Edition, 52(39), 10261-10264; 2013 ^{1}H NMR (500 MHz, Chloroform-*d*) δ 7.43 – 7.32 (m, 5H), 7.10 (d, *J* = 7.9 Hz, 2H), 6.66 (d, *J* = 8.4 Hz, 2H), 5.15 (s, 2H), 4.97 (s, 1H), 4.28 (d, *J* = 5.8 Hz, 2H).

Synthesis of S2

(**S2**) 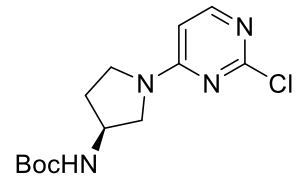

(S)-3-(Boc-amino)pyrrolidine (500 mg, 2.69 mmol)) was suspended in 5 mL of ethanol followed by dissolution upon stirring with triethylamine (370 µL, 5.04 mmol). 2,4-dichloropyrimidine (400 mg, 2.68 mmol) was then added to the solution and the mixture was stirred for 12 h at room temperature. Upon consumption of the starting material, the mixture was then treated with 5 mL of 1 M NaOH and extracted with 10 ml of ethyl acetate 3 times. The product was isolated by silica gel chromatography (2:1, hexanes ethyl acetate) and obtained as clear oil which solidified to a white solid upon resting at room temperature (57% yield, 578 mg). ^{1}H NMR (400 MHz, Chloroform-*d*) δ 8.01 (d, *J* = 6.0 Hz, 1H), 6.19 (d, *J* = 5.9 Hz, 1H), 4.70 (s, 1H), 4.33 (s, 1H), 3.93-3.18 (bm, 4H), 2.31 (s, 1H), 2.17 – 1.66 (bm, 1H), 1.44 (s, 9H). ^{13}C NMR (125 MHz, Chloroform-*d*) δ 161.12, 160.60, 156.46, 155.25, 102.09, 80.19, 52.91-51.93 (two resolved populations), 50.69-49.41 (two resolved populations), 44.74, 31.81-30.46 (two resolved populations), 28.35. ESI-MS Calculated mass: 298.12 Observed mass M+H: 299.13.

Synthesis of S3

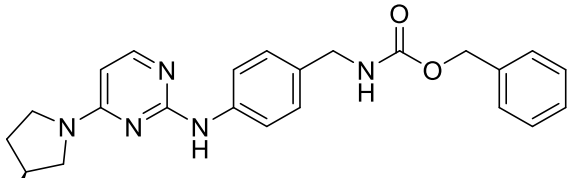

(**S3**) BocHN

Compound S2 (300 mg, 1.00 mmol) and (S1) (265 mg,1.03 mmol) were dissolved by stirring in 10 mL of dioxane at room temperature. The mixture was then heated to 100 °C for 12 h. The solvent was removed and the product was purified by silica gel chromatography (100% ethyl acetate) (43% yield, 198 mg). The product was obtained as a pale yellow solid. ^{1}H NMR (500 MHz, DMSO-d_6) δ 8.97 (s, 1H), 7.90 (d, J = 5.8 Hz, 1H), 7.72 (d, J = 7.7 Hz, 3H), 7.40 – 7.21 (m, 6H), 7.11 (d, J = 8.1 Hz, 2H), 5.91 (d, J = 6.0 Hz, 1H), 5.04 (s, 2H), 4.13 (d, J = 6.3 Hz, 2H), 3.76 – 3.08 (m, 5H), 2.13 (s, 1H), 1.89 (s, 1H), 1.40 (s, 9H) ^{13}C NMR (125 MHz, DMSO-d_6) δ 160.56, 159.86, 156.77, 156.05, 155.74, 140.63, 137.71, 131.96, 128.80 (2C), 128.22, 128.18(2C), 127.65 (2C), 118.67 (2C), 95.93, 78.37, 65.75, 52.05, 44.80, 43.99, 28.69 (3C), two resonances are not resolvable or obscured by the DMSO-d_6 resonance. ESI-MS Calculated mass: 518.26 Observed mass M+H: 519.27.

Synthesis of S4

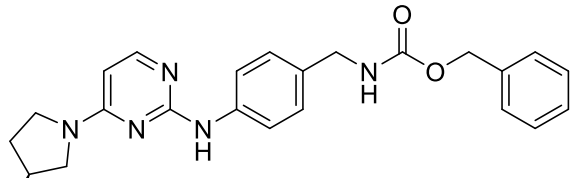

(**S4**) H_2N

Compound S3 (100 mg, 0.193 mmol) was dissolved in 2 mL of dichloromethane followed by room temperature dropwise addition of 0.5 mL of trifluoroacetic acid. After 10 min the reaction was complete as judged by ESI-MS. The mixture was quenched by addition of 2 mL of 6 N NaOH and the product was extracted with ethyl acetate. Solvent evaporation of the crude material yielded a reddish brown solid. The resulting crude product (S4) was used without further purification.

Synthesis of S5

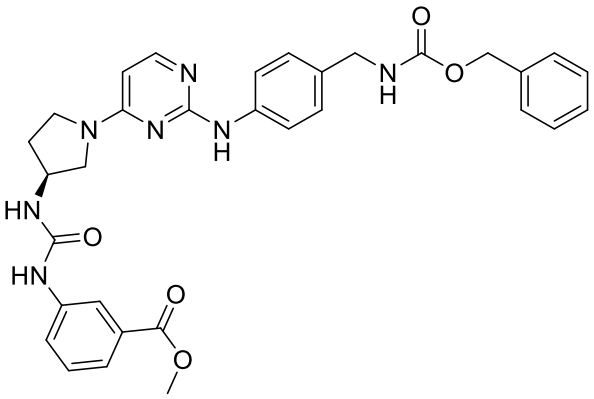

(**S5**)

(65 mg, 0.15 mmol) was dissolved by stirring in 2 mL of dichloromethane, methyl 3-isocyanatobenzoate (33 mg, 0.18 mmol) was dissolved in 1 mL of dichloromethane and added dropwise. The reaction was stirred at 25 °C for 12 h and purified by silica gel chromatography (0-10% dichloromethane-methanol). The final product was obtained as a tan solid (63% yield over two steps, 73 mg). ^{1}H NMR (400 MHz, DMSO-d_6) δ 9.04 (s, 1H), 8.62 (s, 1H), 8.15 (s, 1H), 7.93 (d, J = 5.9 Hz, 1H), 7.72 (d, J = 7.8 Hz, 3H), 7.56 (d, J = 8.1 Hz, 1H), 7.51 (d, J = 7.7 Hz, 1H), 7.42 – 7.24 (m, 6H), 7.13 (d, J = 8.2 Hz, 2H), 6.63 (d, J = 6.7 Hz, 1H), 5.99 (d, J = 5.9 Hz, 1H), 5.04 (s, 2H), 4.35 (s, 1H), 4.13 (d, J = 6.1 Hz, 2H), 3.84 (s, 3H), 3.56 (bm, 4H), 2.23 (s, 1H), 1.98 (s, 1H). ^{13}C NMR (125 MHz, DMSO-d_6) δ 166.75, 160.64, 159.52, 156.78, 155.61, 155.27, 141.14, 140.41, 137.70, 132.21, 130.54, 129.52, 128.85, 128.79 (2C), 128.22, 128.18 (2C), 127.70 (2C), 122.69, 122.35, 118.85 (2C), 118.59, 96.02, 65.76, 52.56, 52.44, 44.83, 43.99. One carbon is not resolvable or is obscured by the DMSO- d_6 resonance ESI-MS Calculated mass: 595.25 Observed mass M+1: 596.26

Synthesis of NH_2-AU1

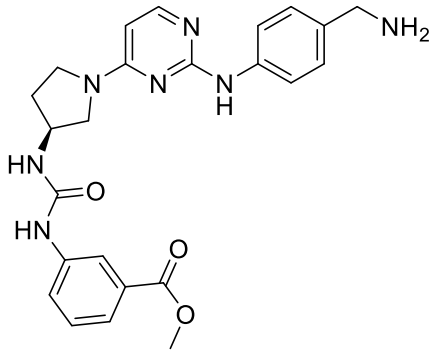

NH_2-AU1

Compound S4 (90 mg, 0.15 mmol) was dissolved in 1 mL of 33% HBr in acetic acid and the compound was stirred for 4 h at room temperature. The solvent was removed and the product was precipitated in diethyl ether followed by addition of 1 mL of 1 M NaOH and extraction with 1 mL of ethyl acetate 3 times. The product was isolated by silica gel chromatography (0-20% dicholoromethane-methanol). The product was obtained as a white-yellow powder (65%, 45 mg) The product used in this study was used as an HBr salt. ^{1}H NMR (400 MHz, DMSO-d_6) δ 11.81 (s, 1H), 10.26 (s, 1H), 8.92 (d, J = 10.6 Hz, 1H), 8.16 (d, J = 18.0 Hz, 3H), 8.00 (d, J = 11.0, 7.2 Hz, 1H), 7.72 – 7.63 (m, 2H), 7.57 (d, J = 6.4 Hz, 1H), 7.54 – 7.46 (m, 2H), 7.38 (t, J = 7.9 Hz, 1H), 6.97 (d, J = 5.8 Hz, 1H), 6.43 (d, J = 7.2 Hz, 1H), 4.02 (d, J = 6.2 Hz, 2H), 3.84 (s, 3H), 3.70 (d, J = 8.3 Hz, 1H), 3.58 – 3.34 (m, 4H), 2.36 – 2.20 (s, 1H), 2.12 – 1.95 (s, 1H). ^{13}C NMR (125 MHz, DMSO-d_6) δ 166.82, 160.62, 159.79, 156.12, 155.55, 141.73, 141.46, 130.47, 129.43, 129.27 (2C), 128.88, 128.56, 128.46, 127.92, 122.61, 122.12, 118.61 (2C), 118.47, 96.19, 52.54, 44.84, 43.07. ESI-MS Calculated mass: 461.22 Observed mass M+1: 462.22.

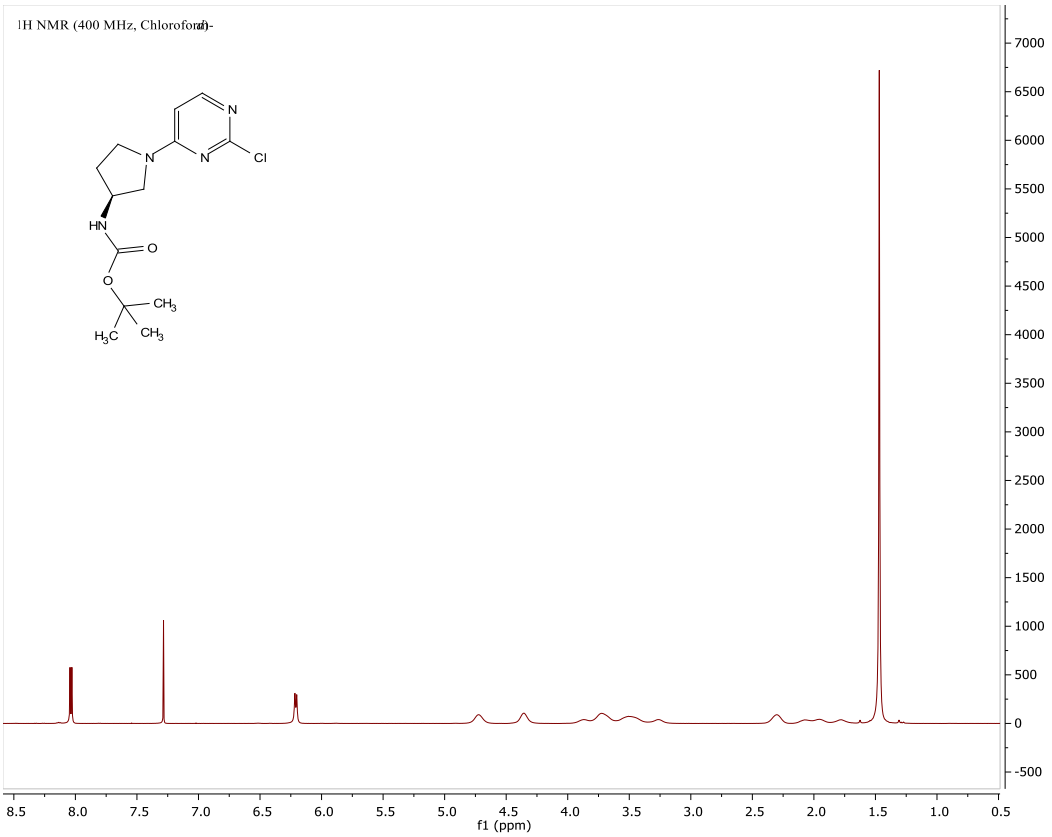

Figure 5.14 ^{1}H NMR of S2 acquired at 400 MHz in chloroform-d.

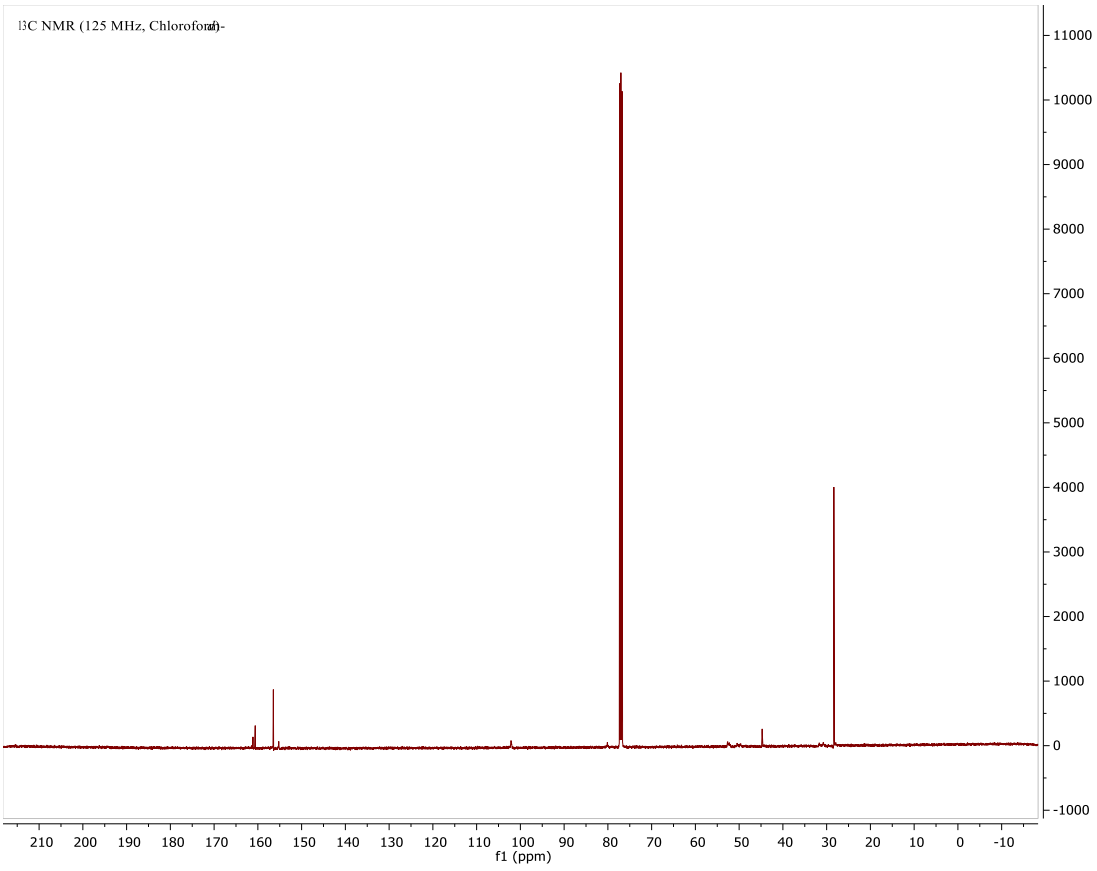

Figure 5.15 ^{13}C NMR spectra of S2 acquired at 125 MHz in chloroform-d.

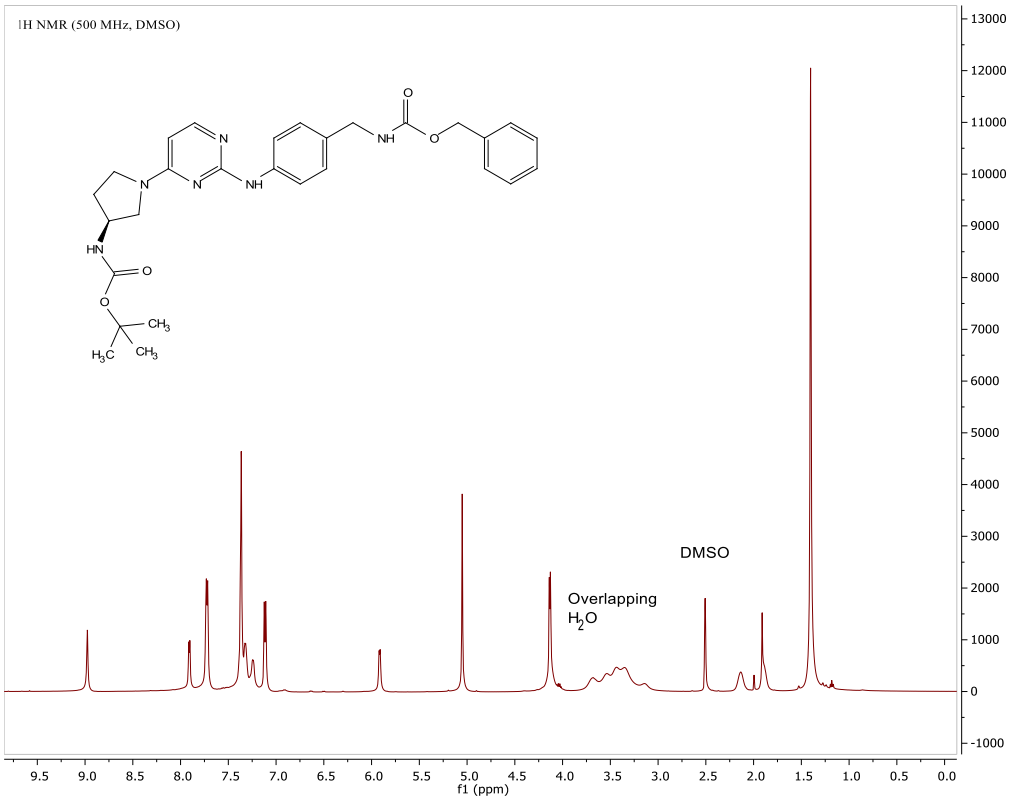

Figure 5.16 ^{1}H NMR of S3 acquired at 500 MHz in DMSO-d_6.

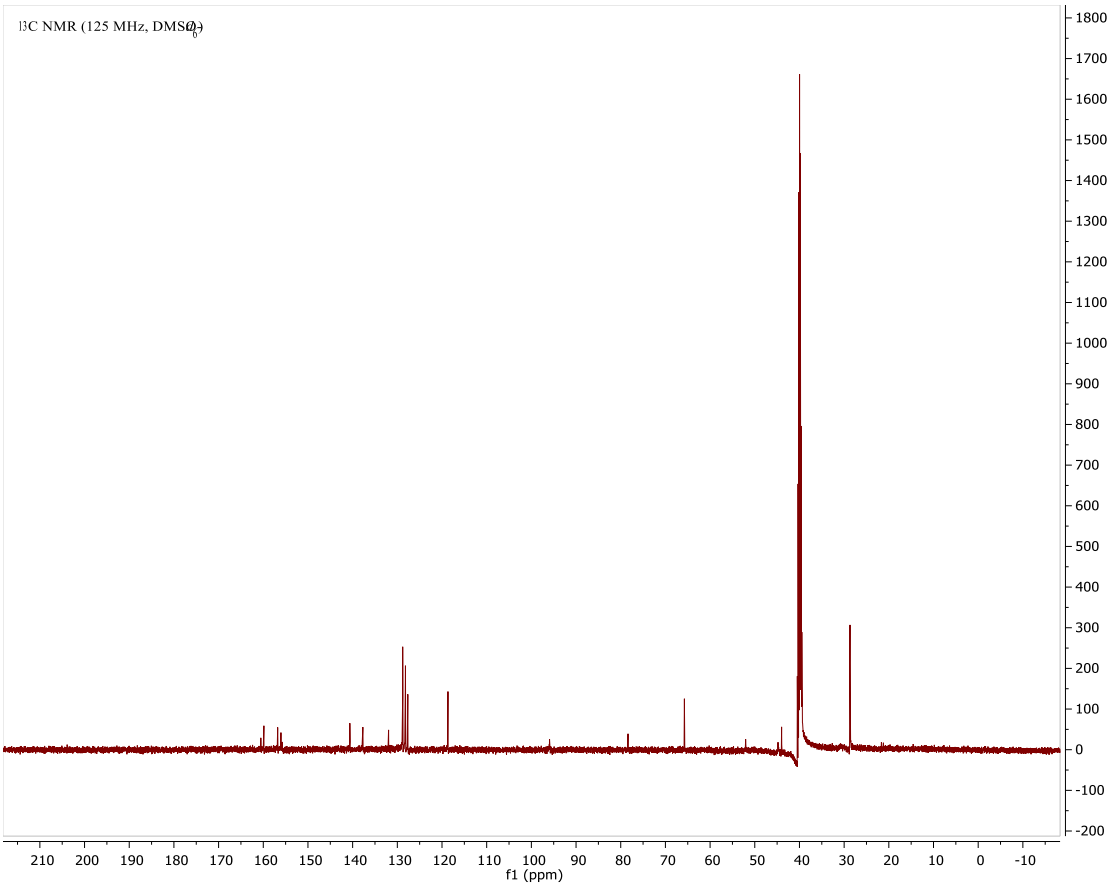

Figure 5.17 ^{13}C NMR spectra of S3 acquired at 125 MHz in DMSO-d_6.

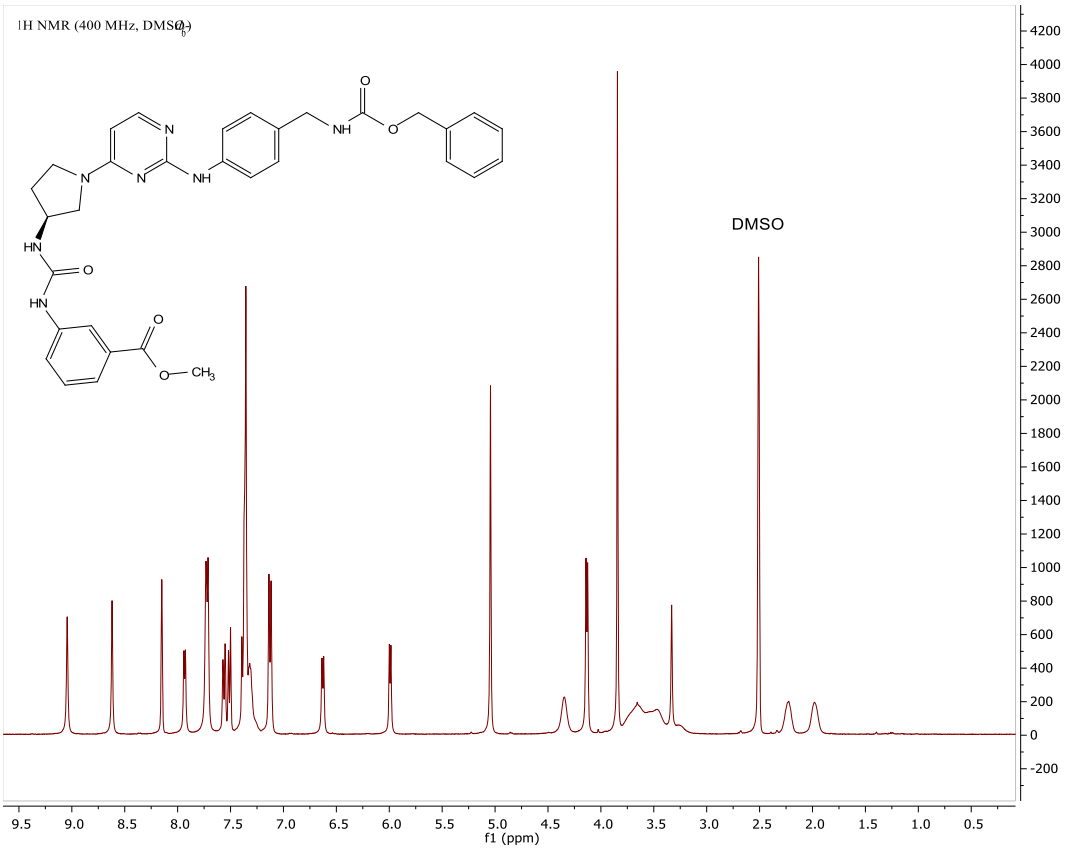

Figure 5.18 ^{1}H NMR of S5 acquired at 400 MHz in DMSO-d_6.

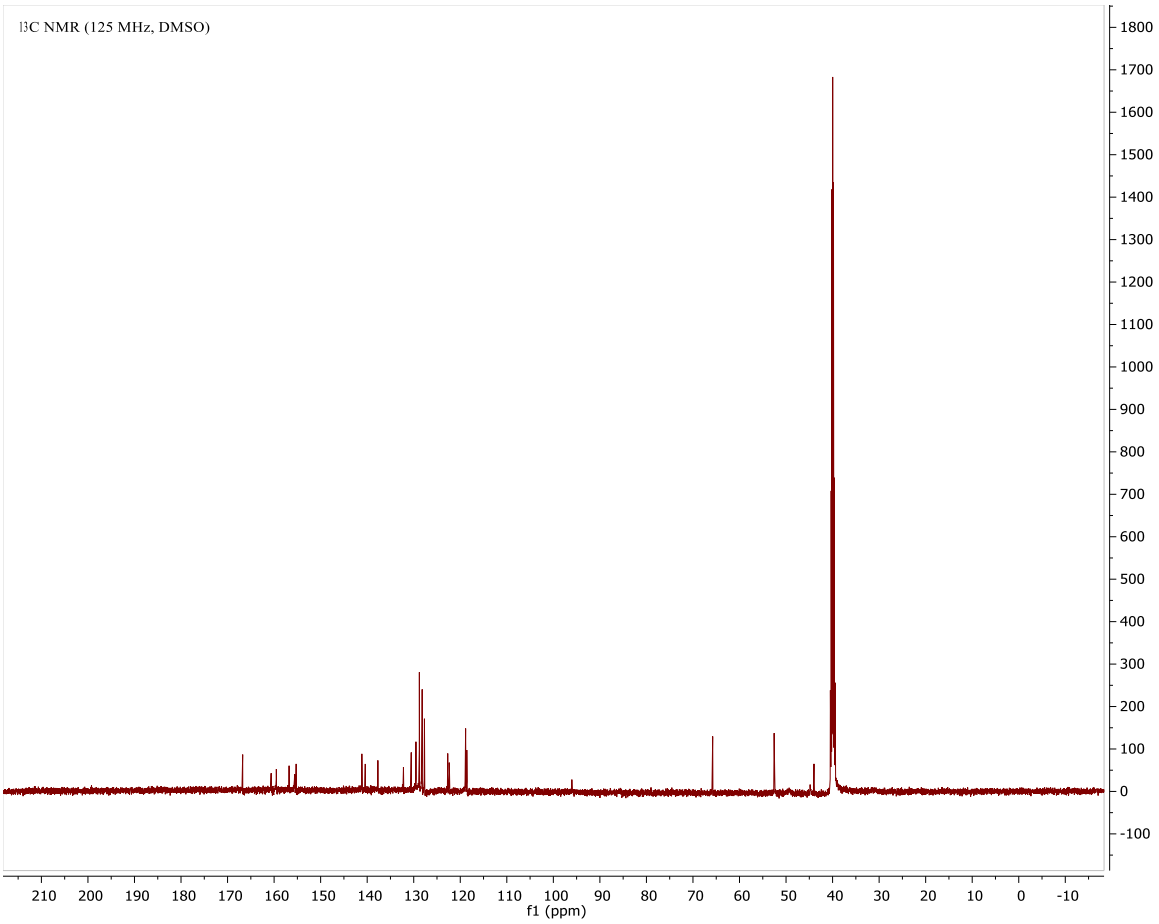

Figure 5.19 ^{13}C NMR spectra of S5 acquired at 125 MHz in DMSO-d_6.

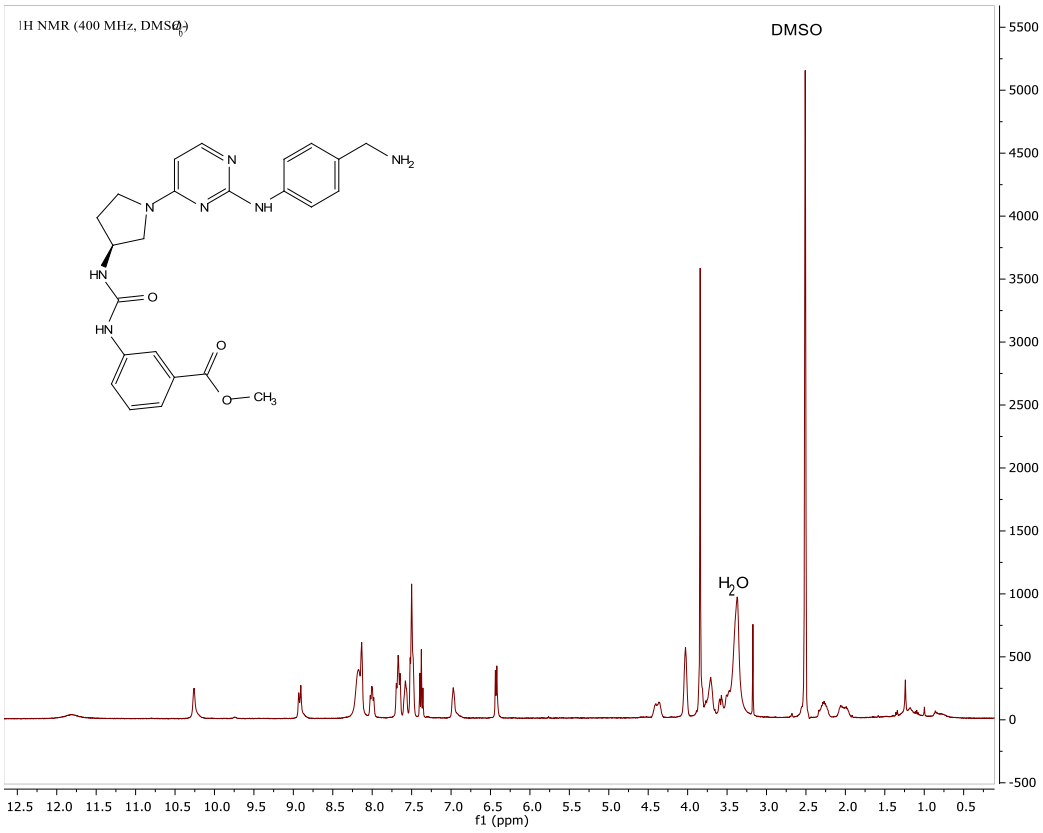

Figure 5.20 ^{1}H NMR of NH_2-AU1 acquired at 400 MHz in DMSO-d_6.

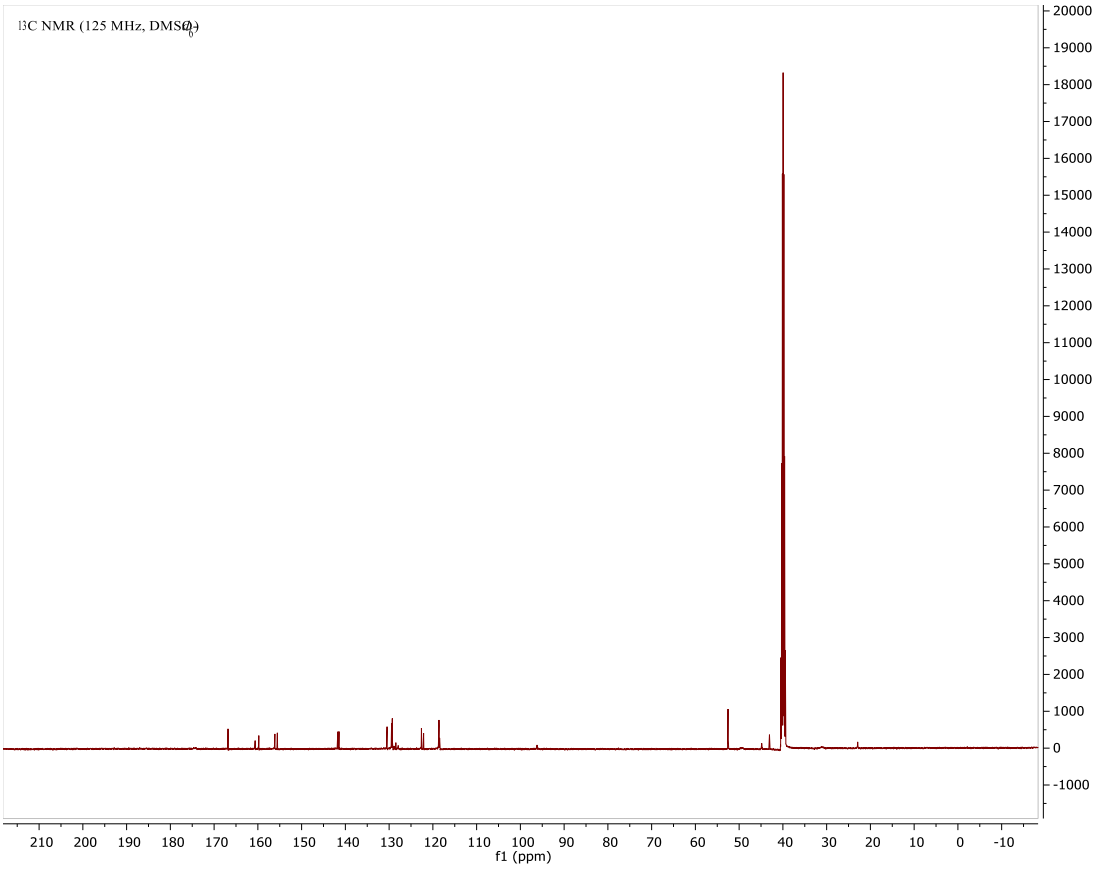

Figure 5.21 ^{13}C NMR spectra of NH_2-AU1 acquired at 125 MHz in DMSO-d_6.

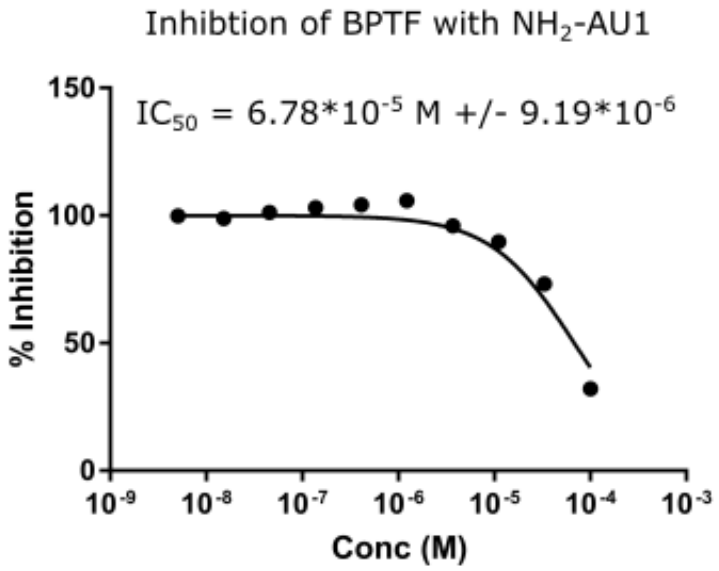

Figure 5.22 Inhibition curve of NH_2-AU1 with BPTF and a tetraacetylated histone determined by Alphascreen. The inhibitory constant was determined to be $6.78*10^{-5}$ M. The assay was performed by Reaction Biology Corp. The conditions of the experiment included 0.1% DMSO.

5.2.6 HPLC Quality Controls

Quality control HPLC traces below were run on Dionex-3000 HPLC instruments fit with a C-18 column. A gradient of 10-60% acetonitrile over 50 minutes was run, followed by a five min. flush (95% ACN) and five min. equilibration (10% ACN: 90% 0.1% TFA water).

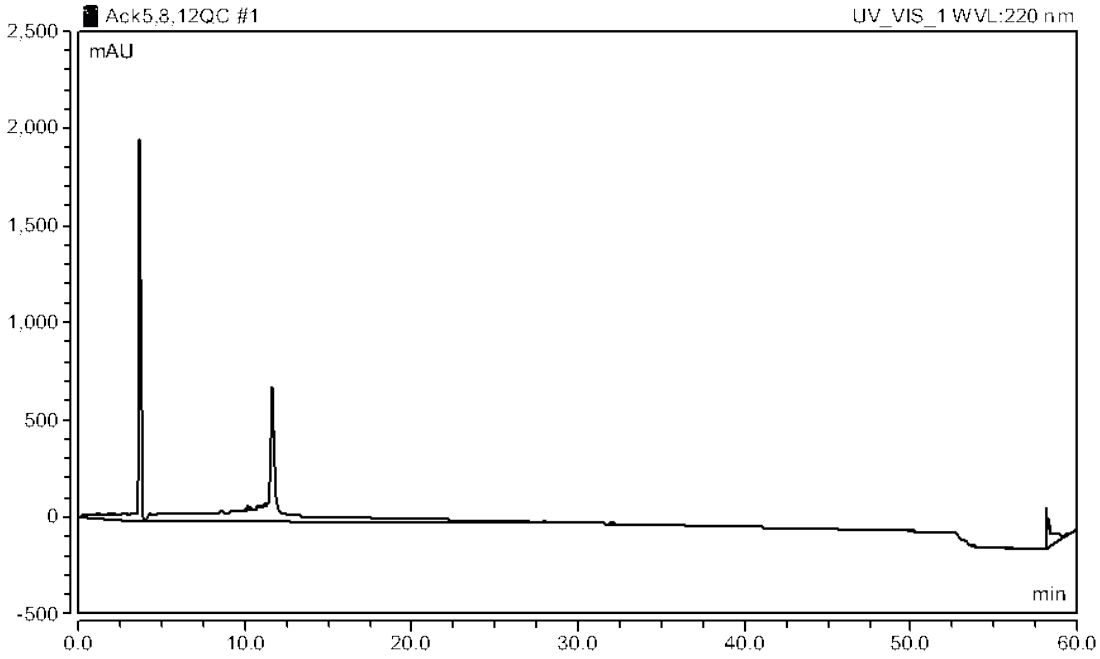

H2A.Z AcK4,7,11

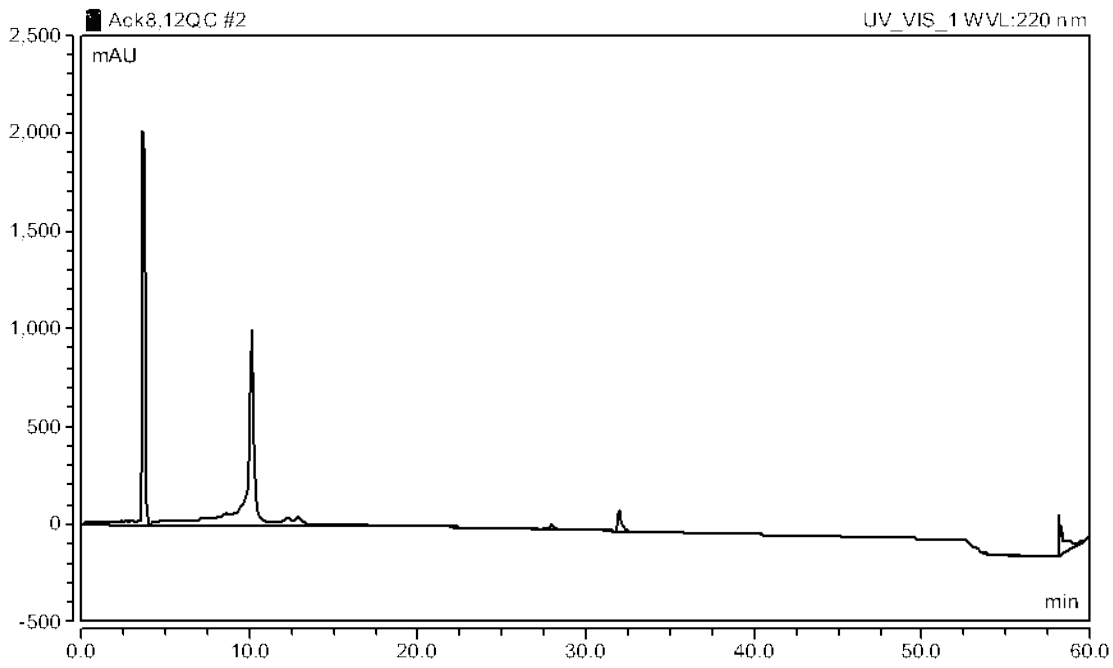

H2A.Z AcK7,11

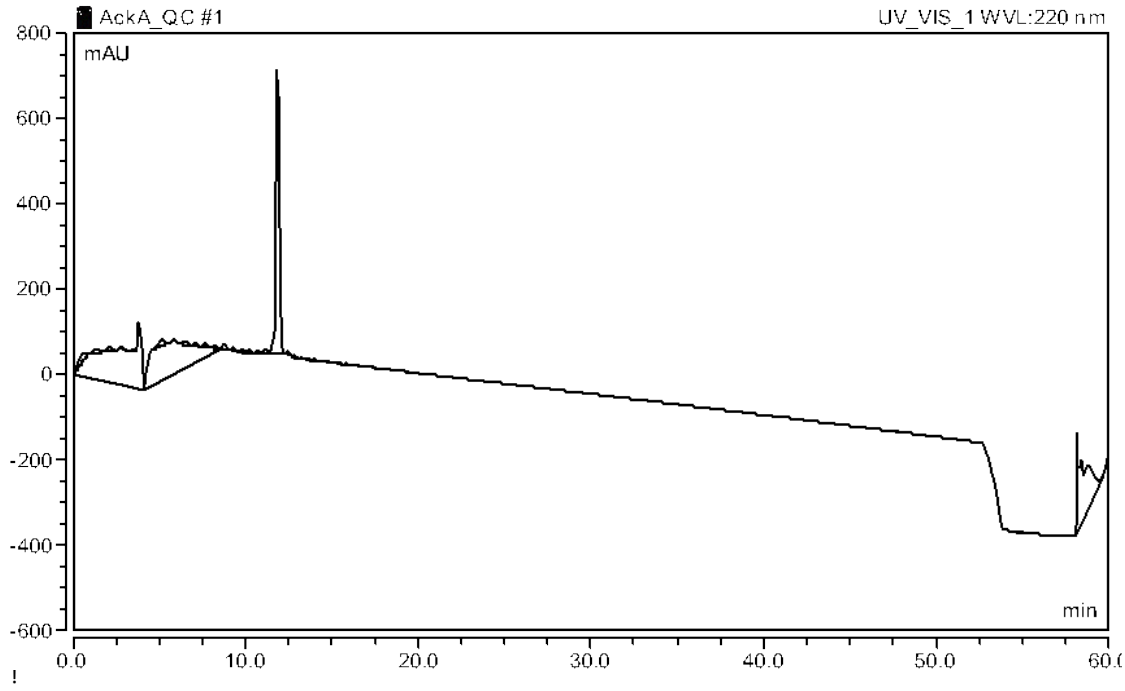

H2A.Z AcK4,7

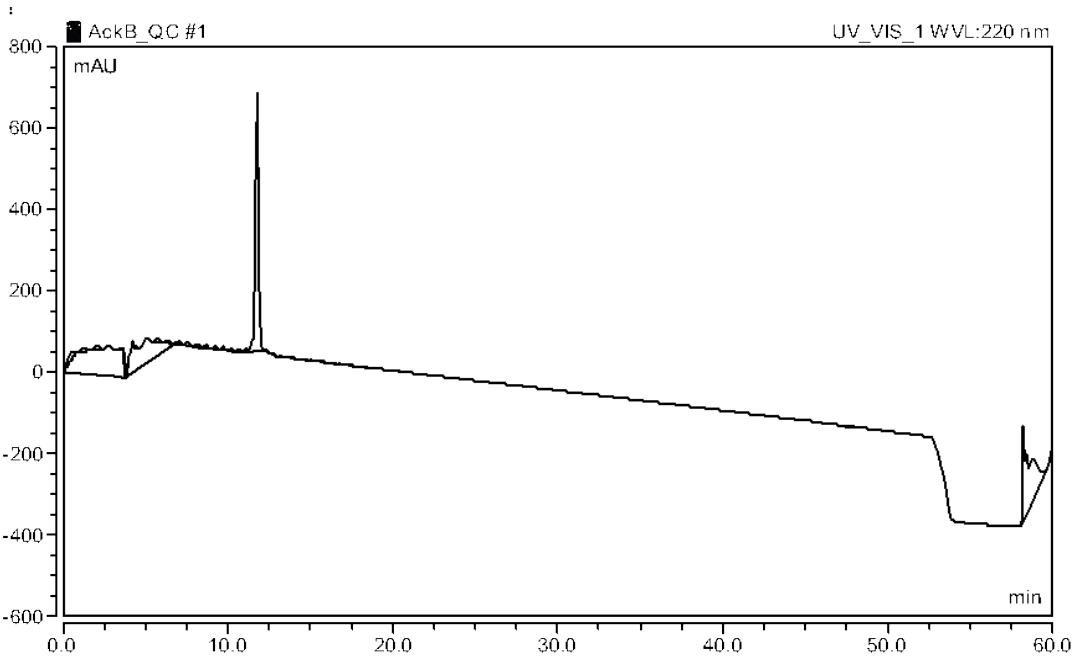

H2A.Z AcK4,11

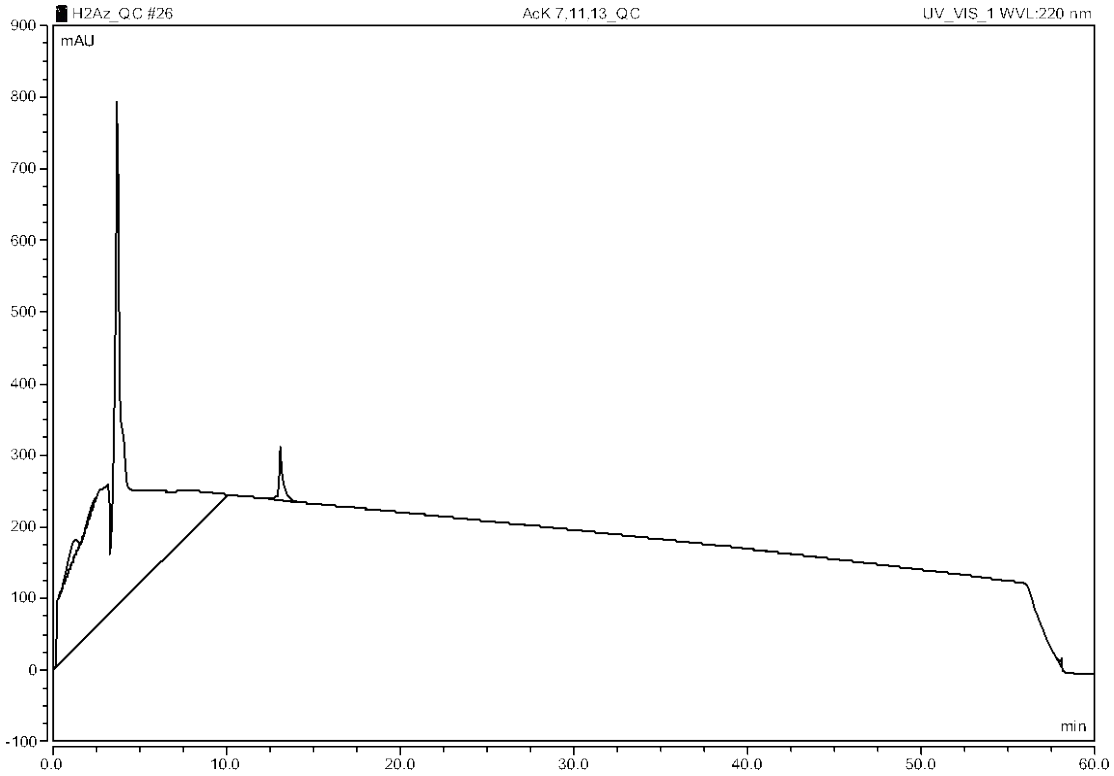

H2A.Z AcK7,11,13

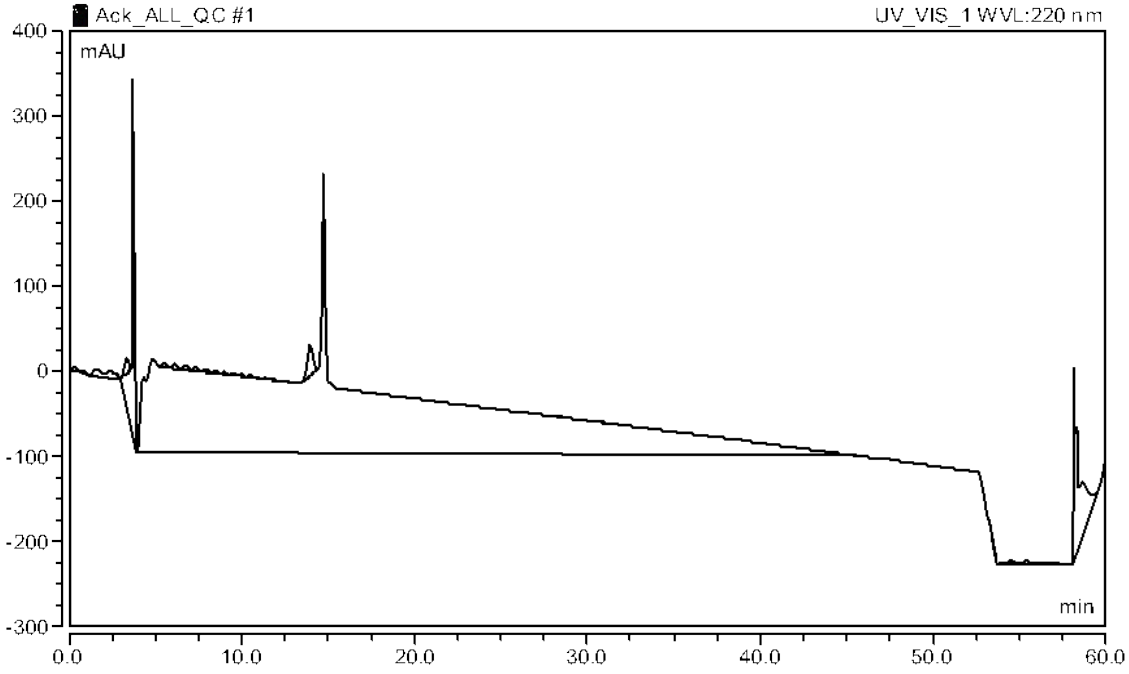

H2A.Z AcK4,7,11,13,15

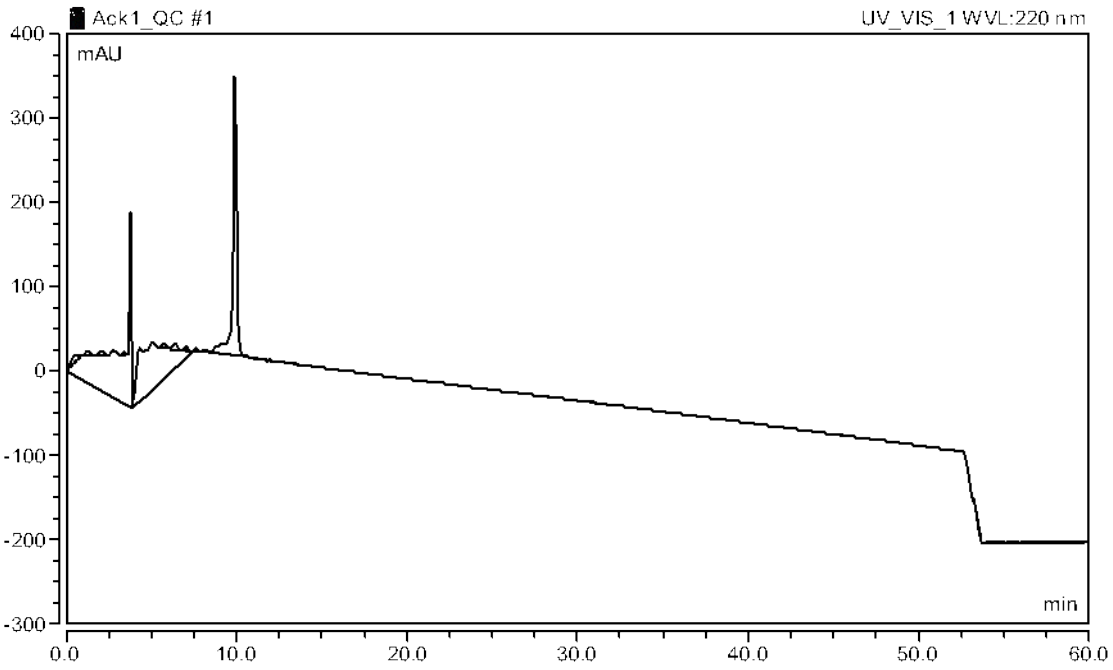
Ack1_QC #1
UV_VIS_1 WVL:220 nm
mAU
400
300
200
100
0
-100
-200
-300
min
0.0
10.0
20.0
30.0
40.0
50.0
60.0

H2A.Z AcK4

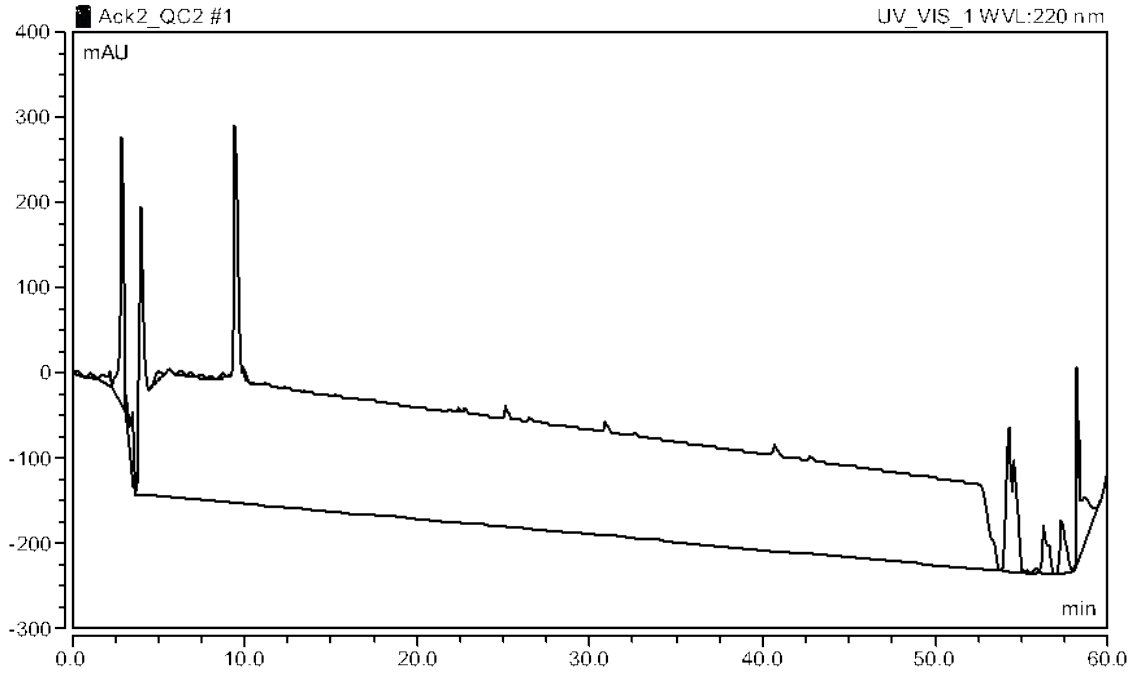

H2A.Z AcK7

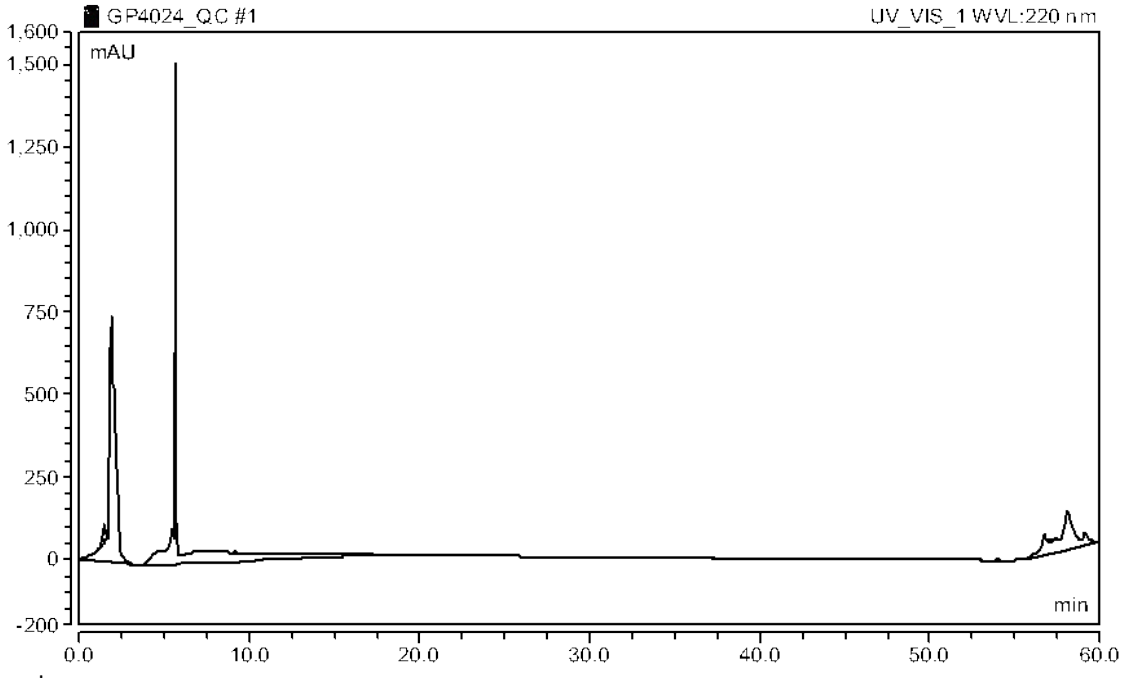

H4AcK16

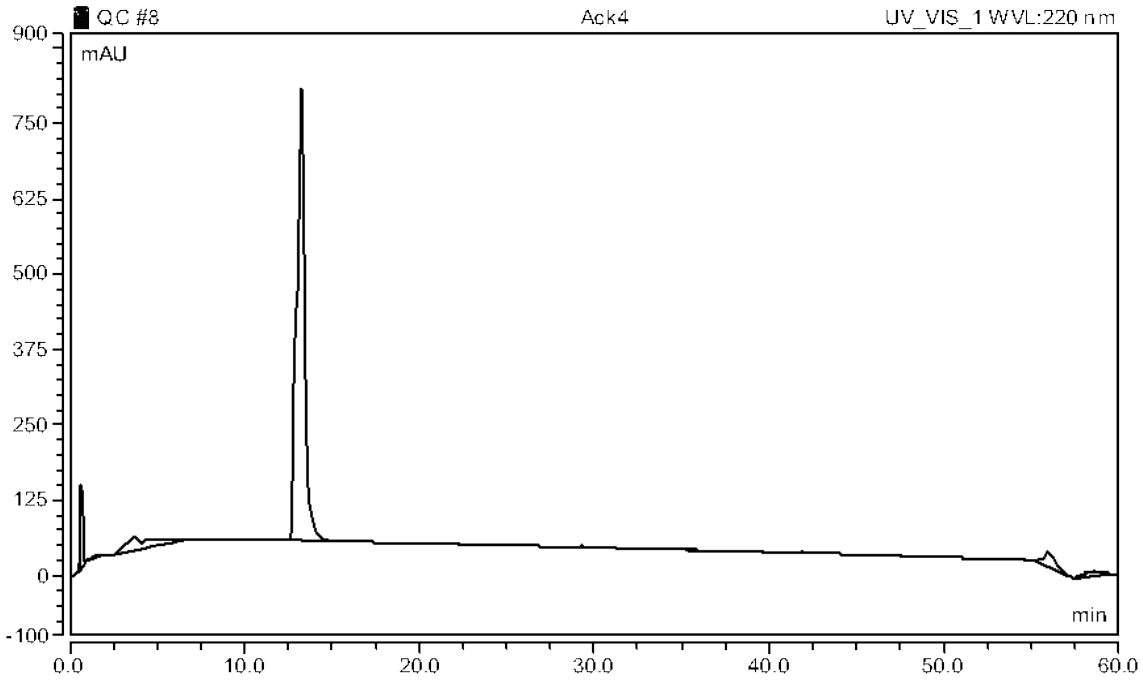
QC #8
Ack4
UV_VIS_1 WVL:220 nm
mAU
900
750
625
500
375
250
125
0
-100
min
0.0
10.0
20.0
30.0
40.0
50.0
60.0

H2A.Z AcK13

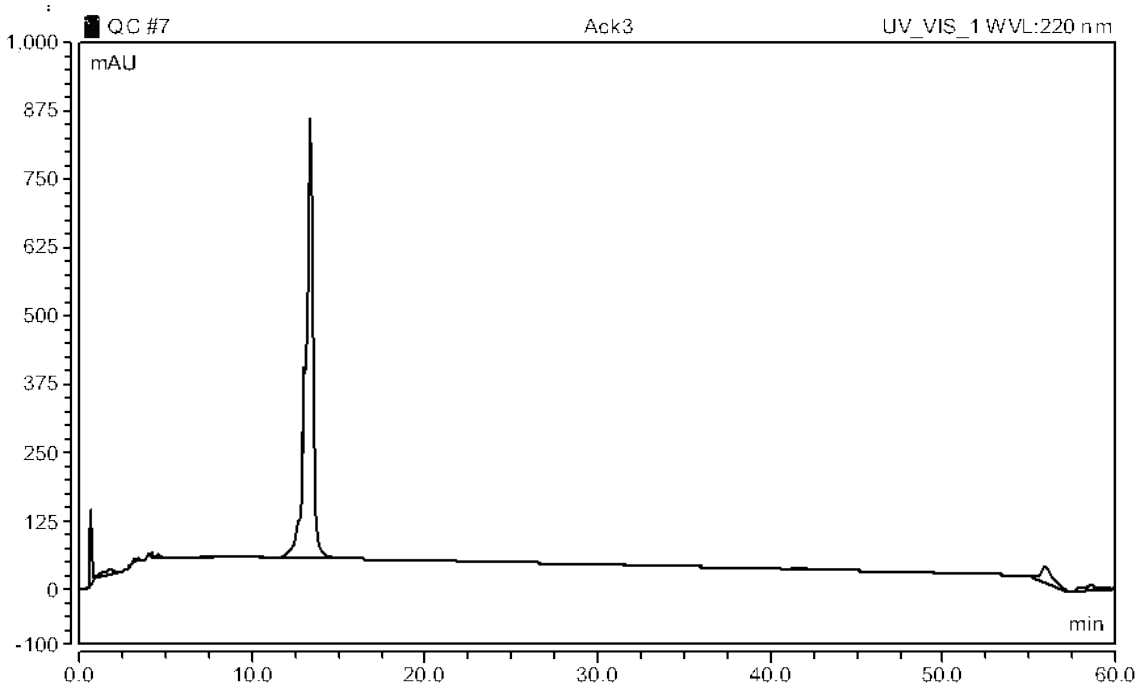
QC #7
Ack3
UV_VIS_1 WVL:220 nm
mAU
1,000
875
750
625
500
375
250
125
0
-100
min
0.0
10.0
20.0
30.0
40.0
50.0
60.0

H2A.Z AcK11

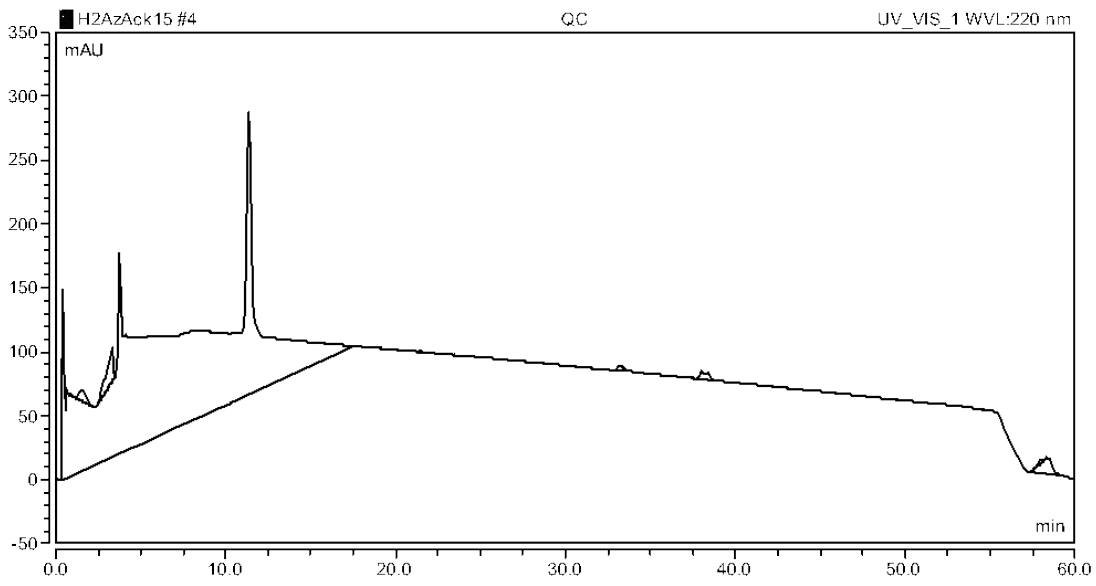

H2A.Z AcK15

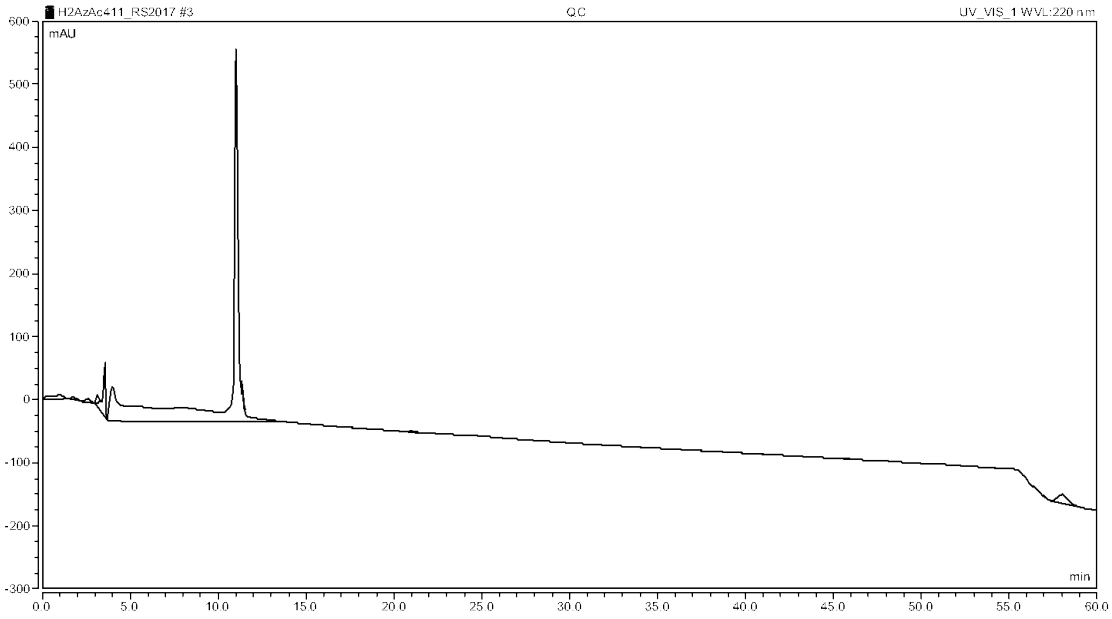

H2A.Z AcK4,11

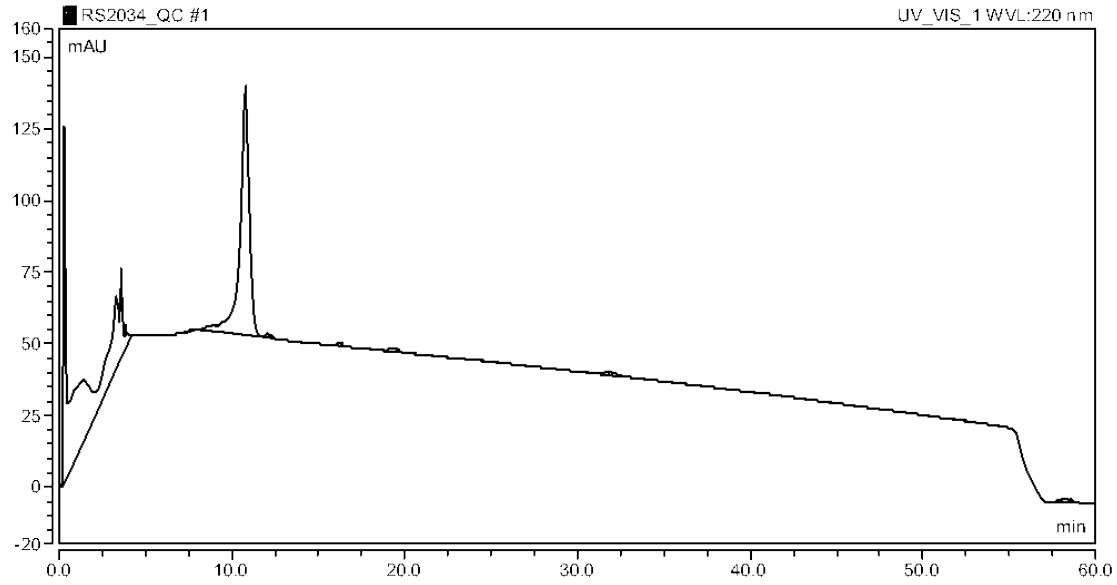

Biotin-βA-βA-YAGGKAGKDSGKAKTKAVSR

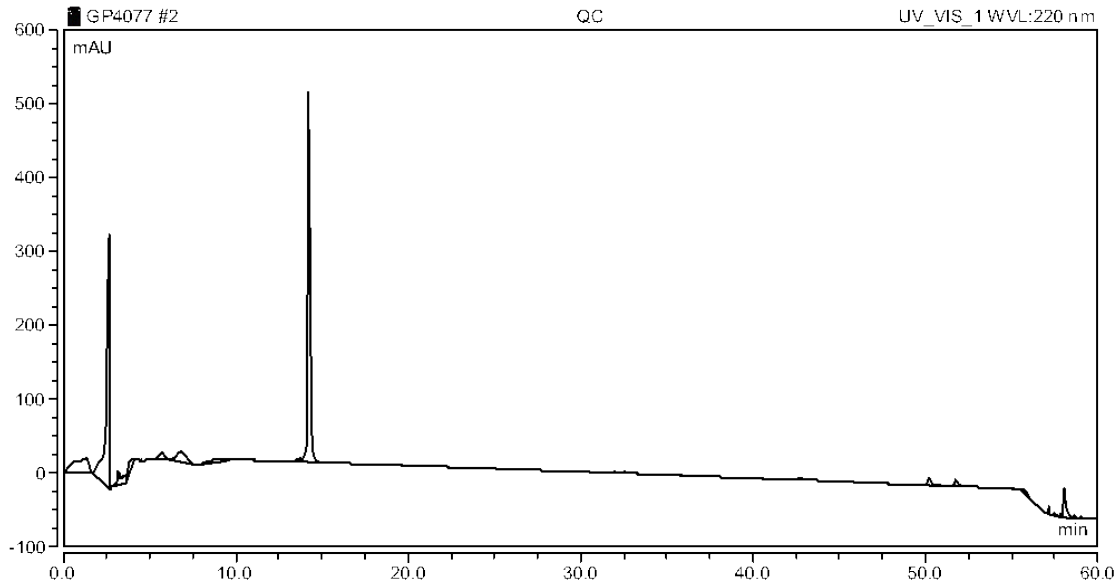

Biotin-βA-βA-YAGGKacAGKDSGKacAKTKAVSR

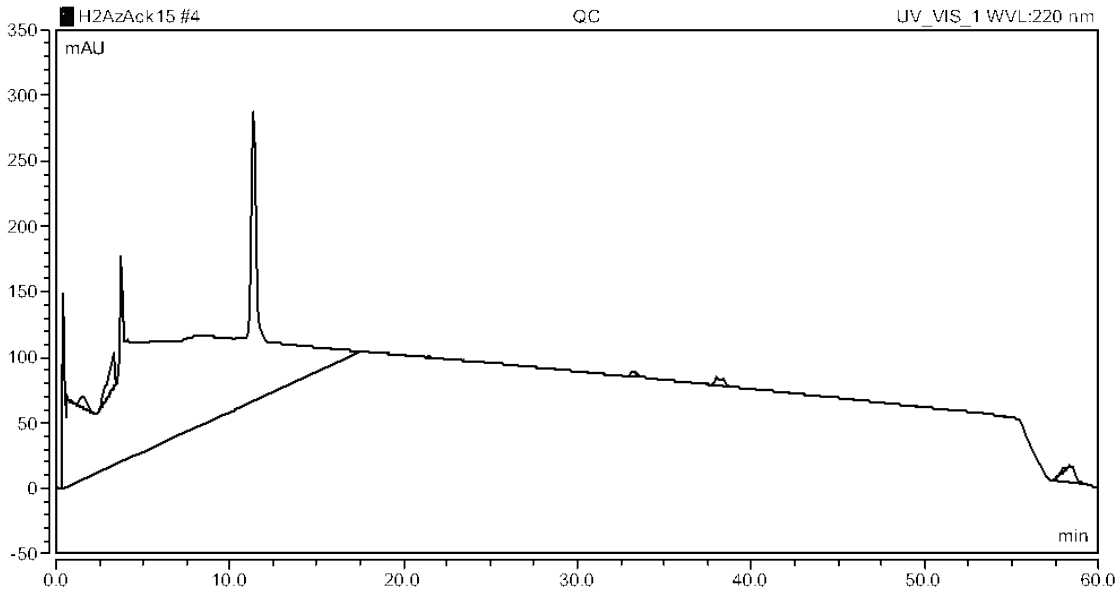

Biotin-βA-βA-YAGGKAGKDSGKAKTKacAVSR

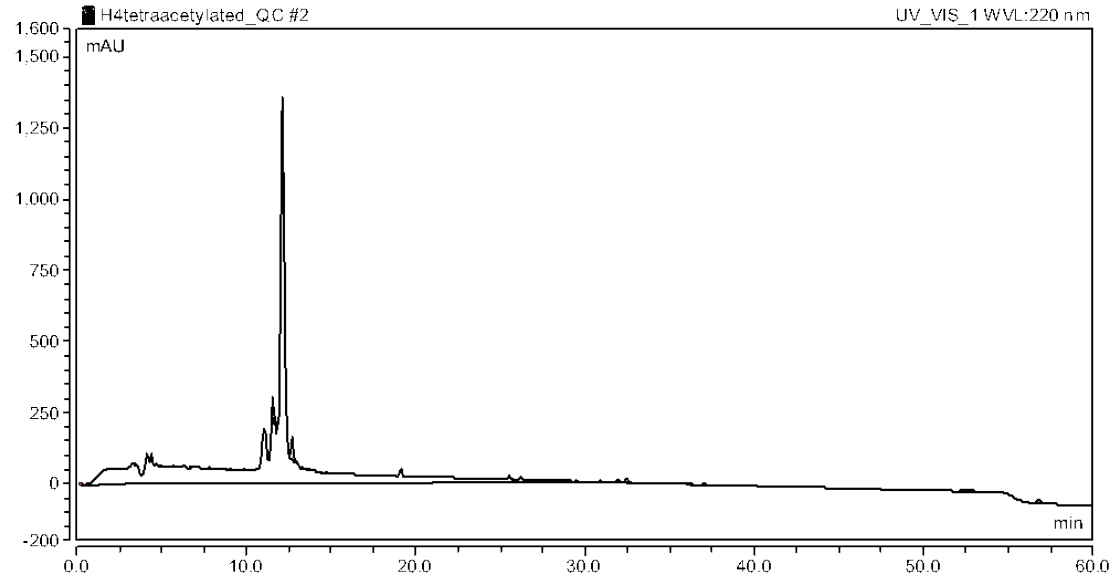

H4 Tetra-acetylated

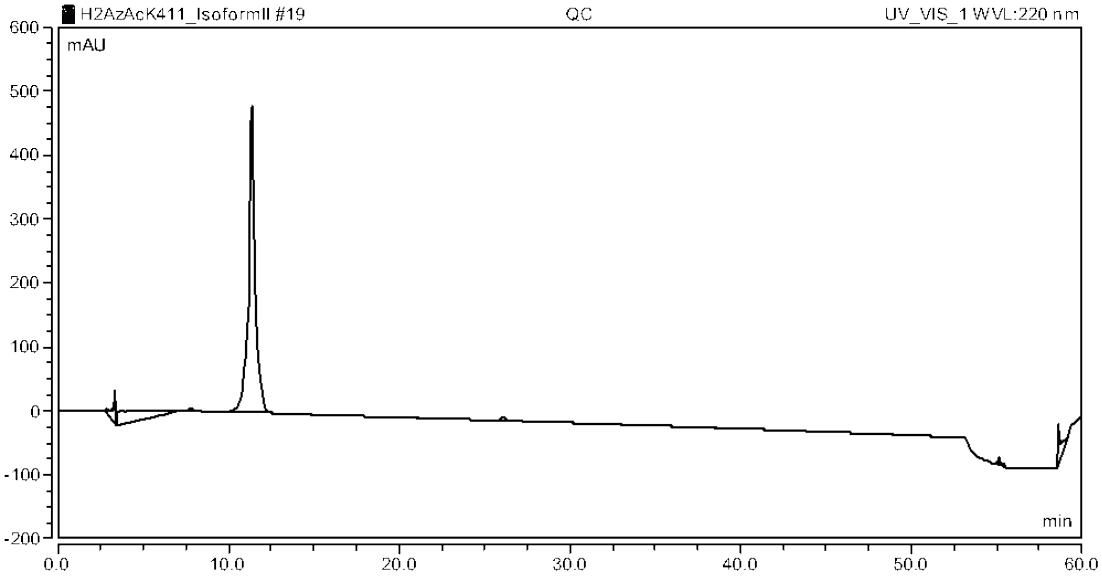

H2A.Z AcK4,11 Isoform II

5.2.7 Ongoing work evaluating histone peptide affinity towards BPTF

To further investigate high affinity histone ligands towards BPTF, we evaluated an H4 peptide. Using an AlphaScreen displacement assay, it has previously been reported that the H4 tetra-acetylated peptide (H4 AcK_4) binds BPTF with an IC_{50} = 14.4 μM.[288] A fluorescence polarization assay with TAMRA-H4AcK_4 identified a K_d = 126 μM.[279] We utilized the ^{19}F NMR platform to identify the binding affinity of H4 AcK_4 towards BPTF to be K_d = 69 ± 10 μM, **Figure 5.23**. Unlike H2A.Z, hyperacetylated H4 peptides appear to bind with higher affinity to BPTF.

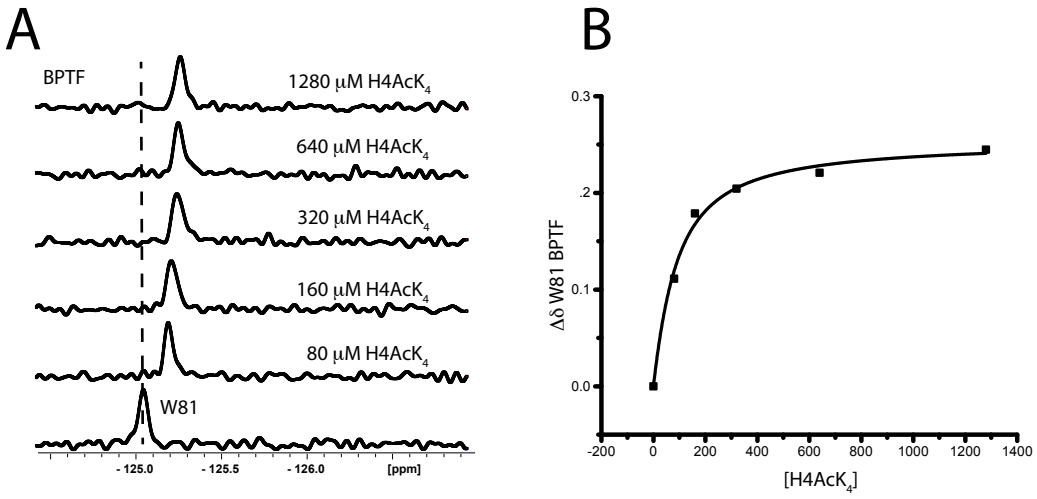

Figure 5.23 Using ^{19}F NMR to monitor H4 AcK_4 binding the 5FW-BPTF. A) Stacked NMR spectra with W81 fluorinated resonance on BPTF shifting with added ligand. B) Corresponding binding isotherm of the shift in W81 resonance with increasing H4 AcK_4 concentration, with a K_d = 69 ± 10 μM.

The variant of H2A.Z has two isoforms similar in sequence, with only a single amino acid difference within the N-terminal region, isoform II replaces a threonine with an alanine (H2A.Z I: AGGKAGKDSGKAKTKAVSR and H2A.Z II: AGGKAGKDSGKAKAKAVSR).[282,289,290] Two H2A.Z isoforms have been identified in

chicken DT40 cells to have similar function, as both are deposited by the SRCAP chromatin-remodeling complex.[291] However, differences in growth and gene expression were observed, indicating the isoforms have varying effects on chromatin structure. [291] While much of the literature focuses on isoform I, we wanted to further investigate if isoform II with the acetylation states at positions 4 and 11, binds BPTF as well. Following the same methods as indicated in Section 5.2, we used ^{19}F NMR to monitor the change in fluorinated W81 resonance with increasing equivalence of H2A.Z II. We observed a shift in the resonance to be within the fast exchange regime, and fit the data to a binding isotherm equation to afford a $K_d = 252 \pm 117$ μM, **Figure 5.24**. Compared to the isoform I variant, this binds significantly tighter. The slight change in sequence has a sizable effect on affinity for the H2A.Z variant. This is an initial step in further identifying how H2A.Z variants interact with bromodomains. Further evaluation on other acetylation sites as well as other bromodomains with H2A.Z may further elucidate the role histone variants play within epigenetics.

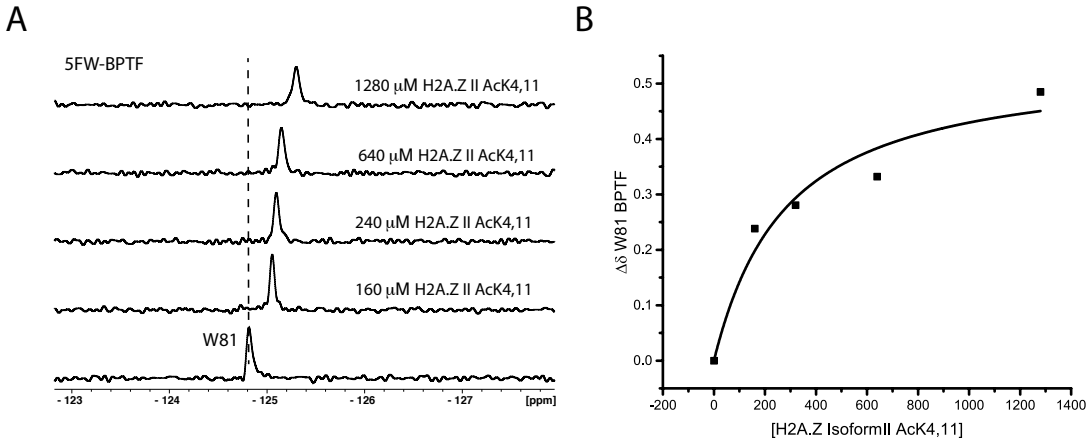

Figure 5.24 Using ^{19}F NMR to monitor H2A.Z II AcK4,11 binding the 5FW-BPTF. A) W81 fluorinated resonance on BPTF shifting with added H2A.Z II AcK4,11 ligand. B) Binding Isotherm of the shift in W81 resonance with increasing H2A.Z II AcK4,11 concentration, with a $K_d = 252 \pm 117$ μM.

Table 5.1 Peptides evaluated for binding towards BPTF

Peptide	Theoretical [M+H]	Observed [M+H]
H2A.ZAcK4,11 Iso II: YAGGKacAGKDSGKacAKAKAVSR	2034.15	2034.4
$H4AcK_4$: YSGRGKacGGKacGLGKacGGAKacRHRK	2323.36	2323.28

Table 5.2 H2A.Z peptides with varying acetylation sites and H4AcK16 were synthesized and characterized with an Ab-Sciex 5800 MALDI-MS.

Peptide	Theoretical [M/z]	Observed [M+H]
YAGGKacAGKacDSGKacAKTKAVSR	2104.2	2105.16
YAGGKAGKacDSGKacAKTKAVSR	2062.2	2063.14
YAGGKacAGKacDSGKAKTKAVSR	2062.2	2063.38
YAGGKacAGKDSGKacAKTKAVSR	2062.2	2063.4
YAGGKacAGKacDSGKacAKacTKAVSR	2146.2	2147.17
YAGGKAGKDSGKAKTKAVSR	1978.11	1979.17
YAGGKacAGKDSGKAKTKAVSR	2020.1	2021.16
YAGGKAGKacDSGKAKTKAVSR	2020.1	2021.14
YAGGKacAGKacDSGKacAKacTKacAVSR	2189.2	2189.13
YAGGKAGKDSGKacAKTKAVSR	2020.1	2021.28
YAGGKAGKDSGKAKacTKAVSR	2020.1	2021.14
YAGGKAGKDSGKAKTKacAVSR	2020.1	2021.12
YSGRGKGGKGLGKGGAKRHR	2196.3	2196.7
Biotin-$^{\beta}$A-$^{\beta}$A-YAGGKAGKDSGKAKTKacAVSR	2389.3	2390.3
Biotin-$^{\beta}$A-$^{\beta}$A-YAGGKacAGKDSGKacAKTKAVSR	2431.3	2432.6
Biotin-$^{\beta}$A-$^{\beta}$A-YAGGKAGKDSGKAKTKAVSR	2347.3	2348.6

5.3 **Efforts Towards Small Molecule Effects of Fluorinated CREB-Binding Protein in Collaboration with Professor Stuart Conway**

5.3.1 Introduction

Bromodomain containing proteins (BCPs) have a specific domain that bind post-translationally modified amino acids such as acetylated lysine and phosphorylated serine. Complex formation leads to altered chromosomal states which regulate gene expression. These adverse alterations lead to a variety of problems including neurodevelopmental disorders,[292] heart disease,[293] and cancer overexpression.[294] Cyclic AMP response element (CREB) binding protein (CBP) is an important transcriptional coactivator found to interact with several proteins including CREB, MLL, p300. Protein Kinase A (PKA) regulates the phosphorylation of Ser133 on CREB, which leads to the recruitment of KIX that activates cellular expression. Furthermore, acetylation of Lys136 on CREB stimulates interactions of the BRD of CBP, which leads to recruitment to the promotor.[292] CBP histone acetyl transferase is the main, if not the only protein that acetylates Lys136.[292] With both acetylated Lys136 and phosphorylated Ser133, a ternary complex with KIX, CREB, and CBP BRD has been observed. Disruption of the CREB:BRD complex have led to suppressed targeted cell expression. CBP-BRD interacts with acetylated lysine tails of histones. Targeting of only the CBP-BRD is a key challenge to suppress the specific transcriptional activity, as BRDs have similar homology. The lack of potent, selective bromodomain inhibitors is a key driving factor in the search for CBP BRD ligands. Several inhibitors have been evaluated including both small molecules and peptides with mid to low micromolar affinity, until recently Conway and colleagues identified a small molecule ligand with nanomolar affinity (MIB 411 with K_d = 390 nM, **Figure 5.25**).[295–298]

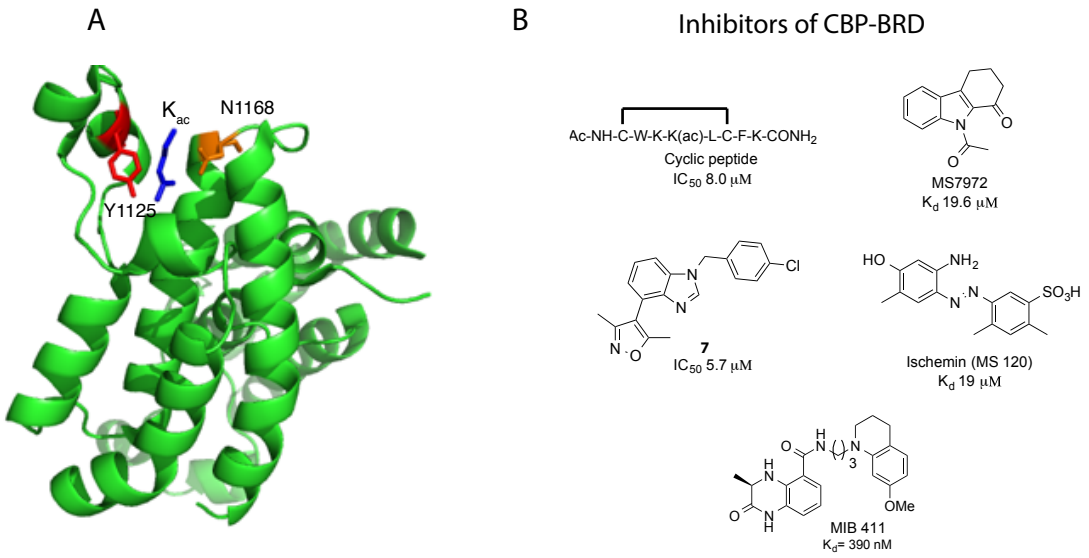

Figure 5.25 CBP-BRD (PDB: 3P1C) shown with acetylated lysine in the binding groove. N1168 and Y1125 stabilizes K_{ac} with hydrogen bonding. B. previously observed inhibitors of the CBP-BRD .[297,298]

BET bromodomains are the most investigated bromodomains to date, and have attracted attention due to their role in a variety of disease states. Both Brd4 and BrdT are part of the BET subclass of bromodomains. Brd4 regulates the transcription of c-Myc, an oncogenic protein, and has also been implicated in NUT midline carcinoma.[227] BrdT is a testis specific bromodomain involved in spermatogenesis; Suppression of BrdT is a promising avenue towards a male contraceptive. A few small molecule inhibitors have been identified to target BET bromodomains, including (+)-JQ-1[231] and I-BET762.[232] Both molecules contain a triazoloazepine scaffold able to engage with the K_{ac} binding pocket by mimicking both the hydrophobic and hydrophilic interactions of a native K_{ac} peptide. The inhibitor (+)-JQ-1 binds Brd4 and BrdT with mid-nanomolar affinity (K_d= 49 nM and 190 nM with ITC, respectively).[231] I-BET binds to Brd4 with 55 nM affinity, determined via

ITC.[232] While potent inhibitors, drug resistance has been observed for the triazoloazapine moiety in both small molecules.[299] To this end, a virtual screen has recently been carried out to identify dihydropyridopyridine scaffolds that have submicromolar affinity for both BrdT and BrD4, as identified by the Pomerantz and Georg labs.[300] The need to identify potent, selective bromodomain inhibitors is necessary. We therefore sought to help evaluate ligands of the CBP bromodomain using ^{19}F-NMR assay in collaboration with the Conway lab, based on their previous inhibitor MIB 411, **Figure 5.25**.

5.3.2 Results and Discussion

The research lab of Stuart Conway began their search for a more potent inhibitor with a non-selective BRD inhibitor, dimethylisoxazole.[298] Utilizing a fragment screen, they identified a variety of highly potent inhibitors of the CBP-BRD. Previous studies have identified MIB 411 to have a high binding affinity towards CBP, with K_d = 390 nM, as determined with ITC. This compound, identified through an AlphaScreen, can interact with R1173 on CBP through a cation-π interaction that is believed to stabilize the ligand with 3.2-4.7 kcal/mol, determined with DFT calculations, **Figure 5.26**.[298] In collaboration with the Conway lab, we evaluated a series of dihydroquinoxalinone compounds including MIB 411 that bind bromodomains CBP, Brd4 and BrdT with ^{19}F NMR and fluorescence polarization for both specificity and affinity. By incorporating fluorinated tryptophan resonances into the bromodomains, we are able to monitor the change in resonance with added ligand, as previously described.[190,191]

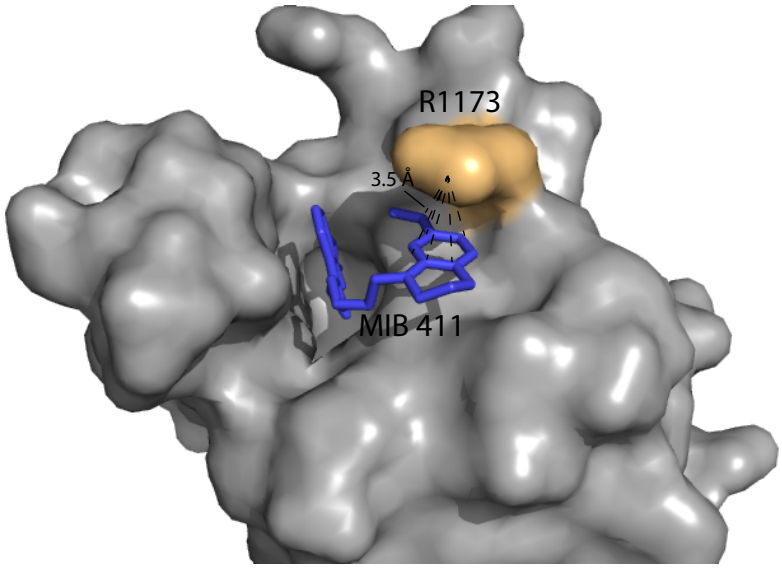

Figure 5.26 Solution structure of the CBP bromodomain interacting with MIB 411 (blue). The cation-π interaction is shown with the positive charge on R1173 (orange) and the tetrahydroquinoline of MIB 411 with a distance of 3.5-4.6 Å (PDB ID: 4NYX).

There are three tryptophan residues in CBP, leading to three fluorine resonances in the ^{19}F NMR spectrum. Perturbations were observed for the most downfield resonance at -123 ppm. Increasing concentration of ligand (0, 12.5, 25, and 50 μM) was titrated into 5FW-CBP to observe resonance perturbations. Slow (MIB310 and MIB197) to intermediate (MIB374 and MIB411) exchange was observed for four of the ligands, with the fifth ligand (MIB432) showing aggregation (**Figure 5.35**). To test the specificity, we analyzed how the ligands bind to the BET bromdomain, Brd4. Fluorination of the three tryptophan residues was incorporated using 5-Fluoroindole during the expression of the protein. ^{19}F NMR was again carried out with ligand titrations. In all cases, Trp-81 is perturbed the greatest, which is part of the WPF shelf within Brd4, **Figure 5.28**.

Intermediate to fast exchange was observed, consistent with low to mid-micromolar binders, but a specific K_d could not be extracted; therefore, a fluorescence polarization assay was utilized on Brd4, as well as another BET bromdomain, BrdT. Ligands were competed off with BI-BODIPY, a known binder of both BET bromodomains. A K_d value was obtained for Brd4 and BrdT to be 62.5 nM, and 380.9 nM, respectively, **Figure 5.29** and **Figure 5.37**. All ligands but the MIB 432, which again had aggregating issues **Figure 5.35**, had low micromolar affinity for both BET bromodomains. MIB 197 has the highest affinity towards Brd4 with a K_i value of 1.52 μM, with slightly higher affinity for BrdT, K_i = 6.11 μM, **Figure 5.28F**, **Figure 5.38**, and **Figure 5.32**.

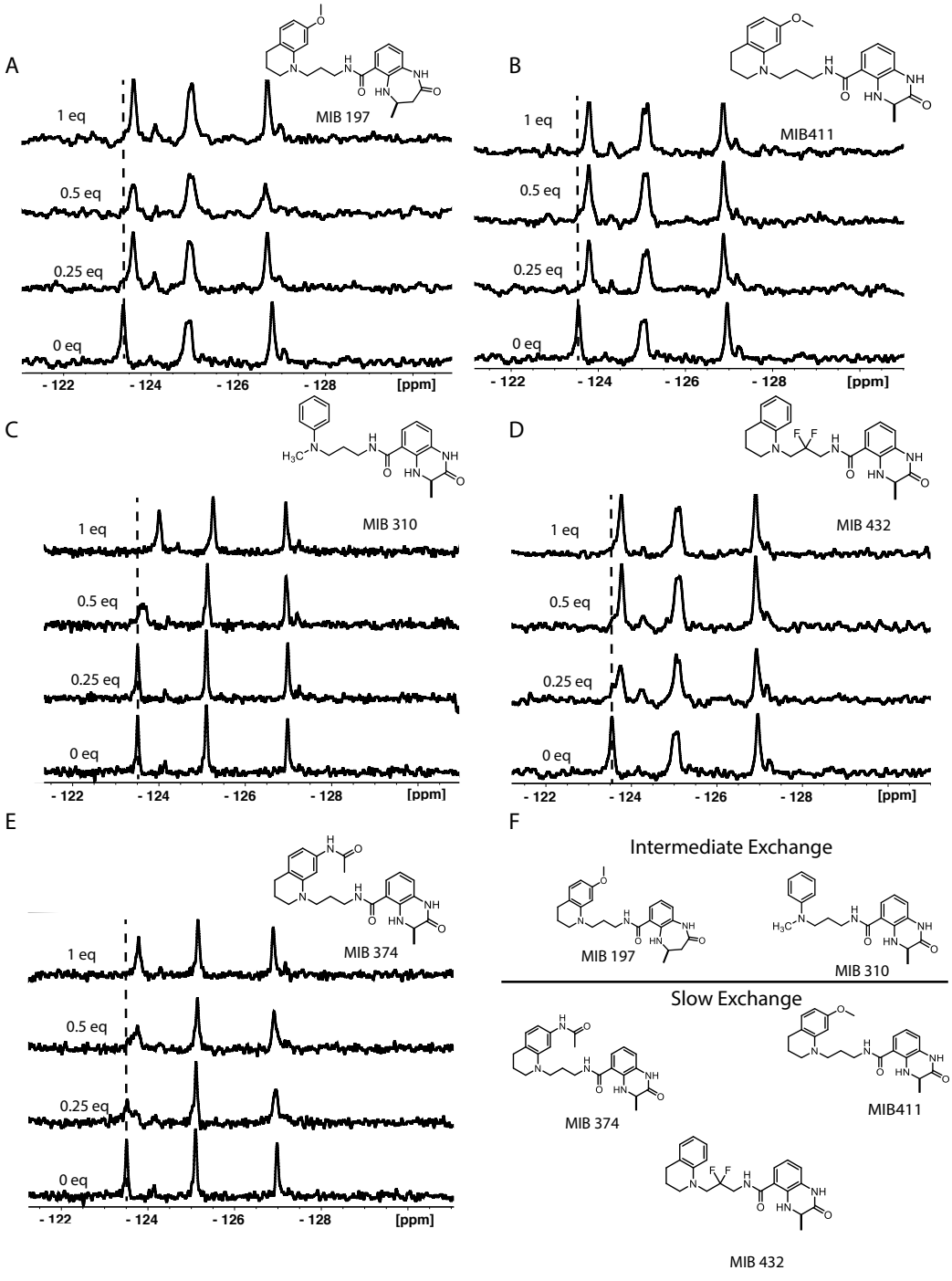

Figure 5.27 5FW-CBP 19F-NMR spectra overlays with increasing equivalence of 5 varied small molecule inhibitors, with 50 μM CBP. MIB 197 and MIB 310 show intermediate exchange, MIB 374 and MIB 411 show slow exchange; thus, MIB 411 and MIB 374 bind CBP with tighter affinity. MIB 432 displayed aggregation, leading to an unclear affinity.

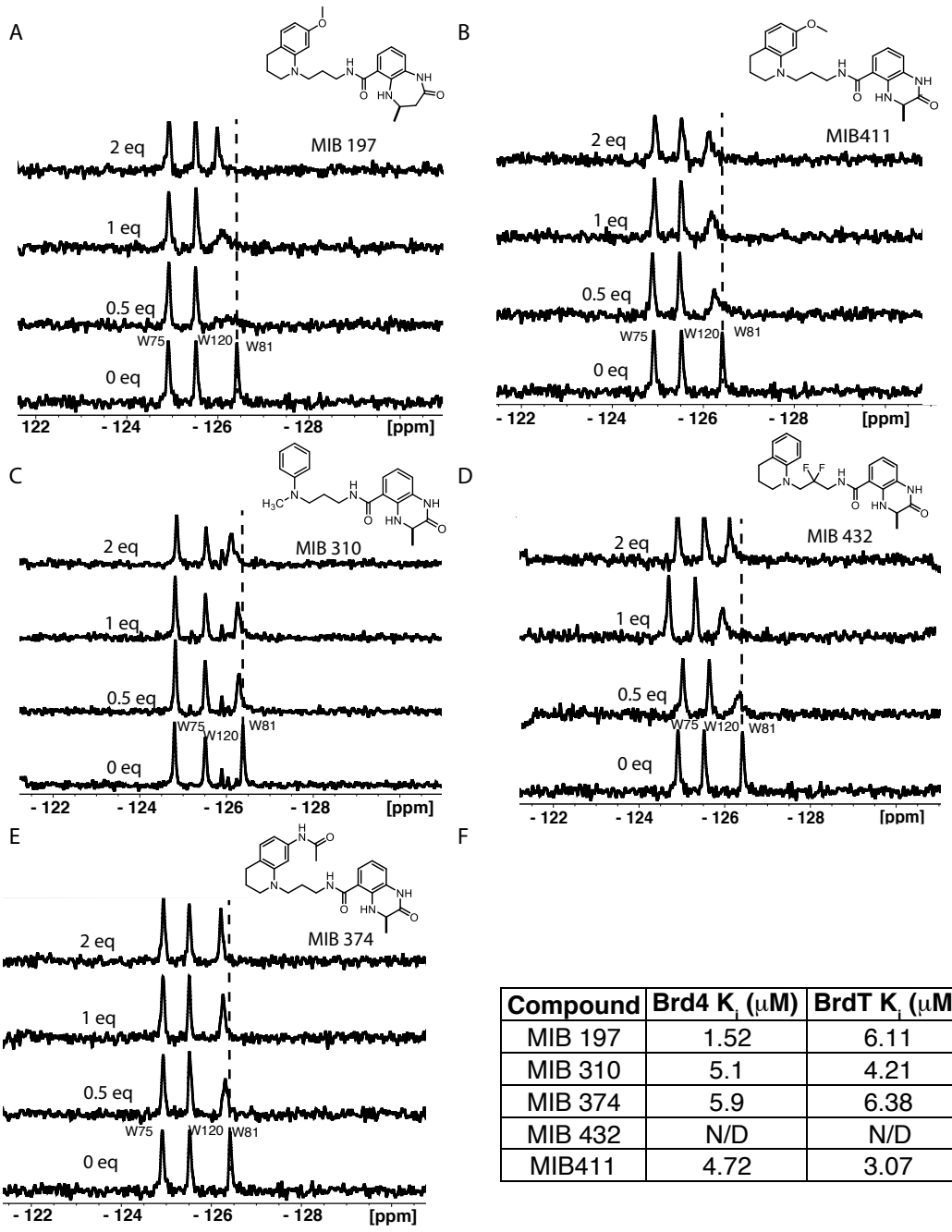

Compound	Brd4 K_i (μM)	BrdT K_i (μM)
MIB 197	1.52	6.11
MIB 310	5.1	4.21
MIB 374	5.9	6.38
MIB 432	N/D	N/D
MIB411	4.72	3.07

Figure 5.28 A-E. 19F-NMR of 5FW-Brd4 with increasing concentrations of 5 MIB compounds. F. Table of K_i values from fluorescence polarization assays with Brd4 and BrdT binding to 5 small molecule CBP-BRD inhibitors. Due to the aggregation, MIB 432 K_i values could not be determined (N/D).

5.3.3 Conclusion

The bromodomain of CBP is a targetable site for the suppression of a variety of diseased states. The few inhibitors available currently do not have high specificity or potency within BET bromodomains. Five small molecules were evaluated against three bromodomains: CBP, Brd4, and BrdT. 5FW-CBP has three resonant peaks that can be monitored for movement with added ligand. With little discovery towards CBP brodomodmain inhibitors, there is great utility of ^{19}F NMR assay for identifying ligands of the CBP bromodomain. Two molecules—MIB 197 and MIB 310 perturbed a fluorine resonance of 5FW-CBP within the intermediate exchange regime, but a binding curve could not be fit to the resonance move. We further evaluated these compounds with two BET bromdomains. MIB 197 has slight preference towards Brd4 with 1.52 μM, and MIB 411 has affinity towards the BrdT domain with 3.07 μM. This is a first step in understanding selective inhibitors against the CBP bromodomain to target diseases including heart disease as well as a variety of cancers.

5.4 **Materials and Methods**

5.4.1 Protein Expression Experimental

5FW-labeled CBP was expressed using *E. coli*/Bl21(DE3) cotransformed with the pRARE plasmid expressing tRNAs for rare codons. 5FW-labeled protein was expressed with LB media grown until an O.D. at 600 nm of 0.7 was reached. Cells were harvested and resuspended in defined media[1] which contained 5-fluoroindole (60 mg/L) in place of tryptophan[2]. Resuspended bacteria were incubated at 37 ^{o}C while shaking for 1.5 h. The

bacterial culture was cooled to 20 ^{o}C for 30 min. then induced with 1 mM IPTG for 18-20 h at 20 ^{o}C. Cells were pelleted and stored at -20 ^{o}C. Pellets were thawed to room temperature, and lysis buffer (50 mM Phsophate pH 7.4, 300 mM NaCl), PMSF (5 mM), and Egg White Lysozyme (1 mg/ml) were added followed by sonication and purified via FPLC using NTA-resin (Qiagen) and an imidazole gradient (0 to 400 mM). The yield following purification was 11 mg/L for 5FW-labeled CBP. Concentration of CBP was evaluated via absorbance at 280 nm.[3] 5FW-lableled was expressed as previously described.[4]

5.4.2 Protein Observed Fluorine NMR

Protein observed 1D ^{19}F NMR samples were obtained as previously described using a frequency window of -120 to -130 ppm, a D1 of 0.7 sec and an acquisition time of 0.05 sec. Small molecules stock solutions were prepared in DMSO at 20 mM. Small molecules were titrated into CBP or Brd4 (protein solutions at 50 μM in 50 mM TRIS, 100 mM NaCl, 5% D_2O, pH 7.4) at 0.25, 0.5, 1.0, and 2.0 equivalents of protein with a final concentration of 0.5% DMSO.

5.4.3 Fluorescence Anisotropy Direct Binding and Competition Experiments

Competitive inhibition experiments were carried with Brd4 and BrdT as previously described.[4] Serial dilutions were run in triplicate on a Tecan Infinite 500 plate reader using 384-well plates (Corning 3676). In competition experiments, Brd4 was held constant at 496 nM, and BrdT at 1.516 μM, equivalent to 80% bound tracer, BI-BODIPY (25 nM), as determined via direct binding experiments. The fluorescently tagged BI-BODIPY was

synthesized according to published methods.[5] K_i values were determined according to equation 1. A competition curve with known inhibitor BI2536[6] was used to estimate the baseline in cases where 100% inhibition could not be achieved with small molecule inhibitors.

$$y = c + (b - c) \times \frac{[(Kd+a+x)] - \sqrt{(Kd+a+x)^2 - 4ax}}{2a} \qquad \text{Eq. 1}$$

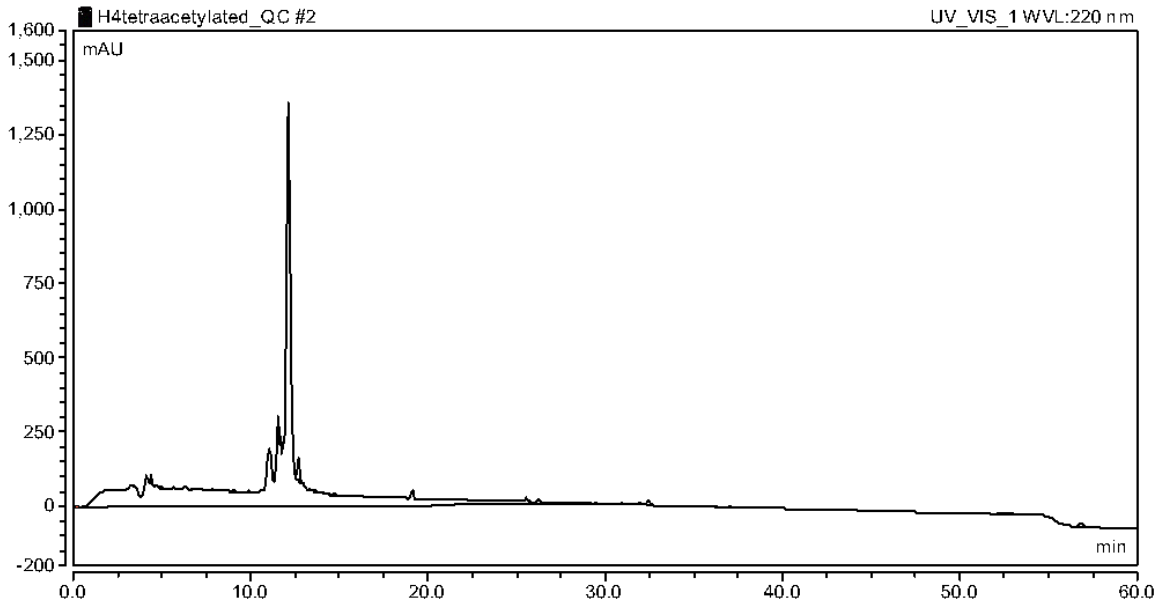

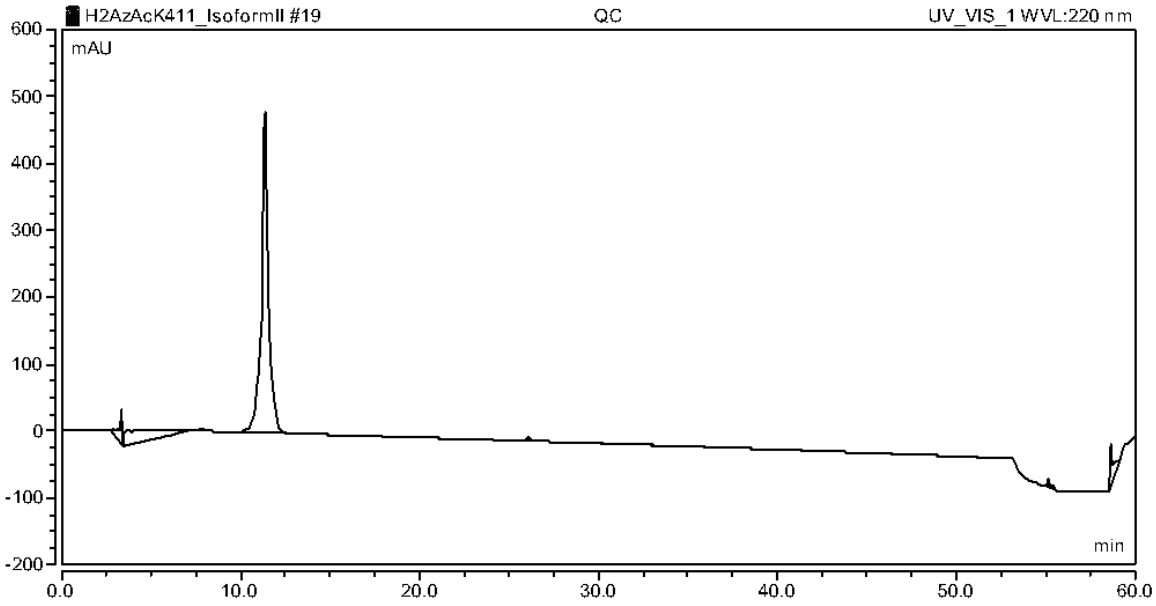
H2AzAcK411_IsoformII #19
QC
UV_VIS_1 WVL:220 nm
mAU
600
500
400
300
200
100
0
-100
-200
min
0.0
10.0
20.0
30.0
40.0
50.0
60.0

5.5 **Fluorescence Polarization binding curves**

Binding curves were constrained to the baseline of the self-competition anisotropy values, and used in determining the K_i values.

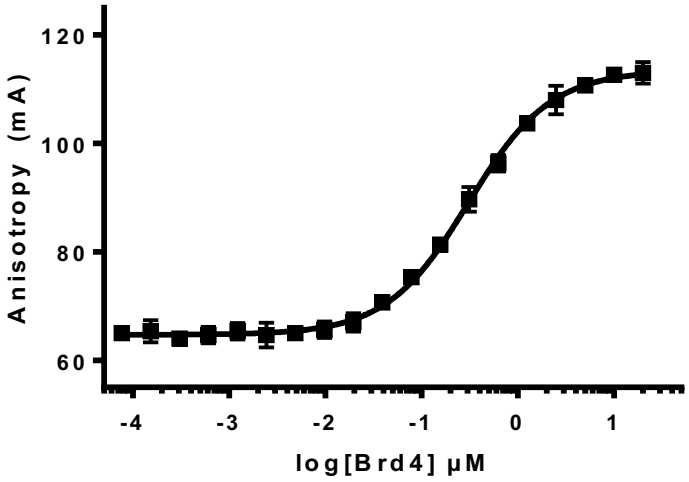

Figure 5.29 Direct Binding of Brd4 with BI-BOPIPY with Kd of 62.5 nM.

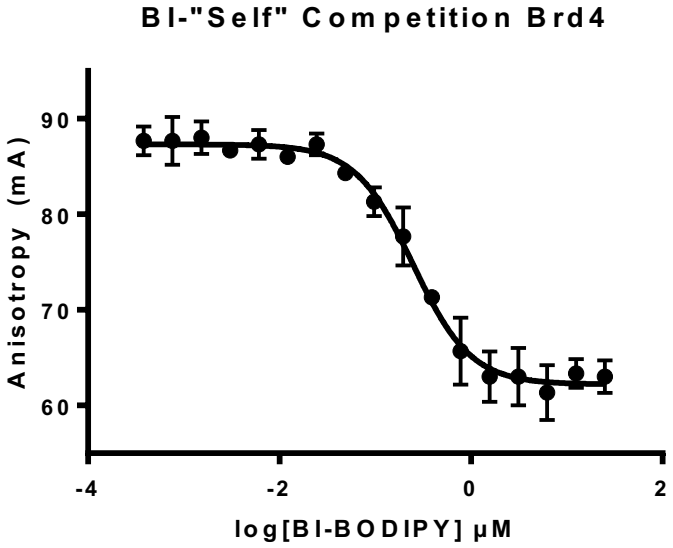

Figure 5.30 Self-competition of BI2536 with BI-BODIPY on Brd4.

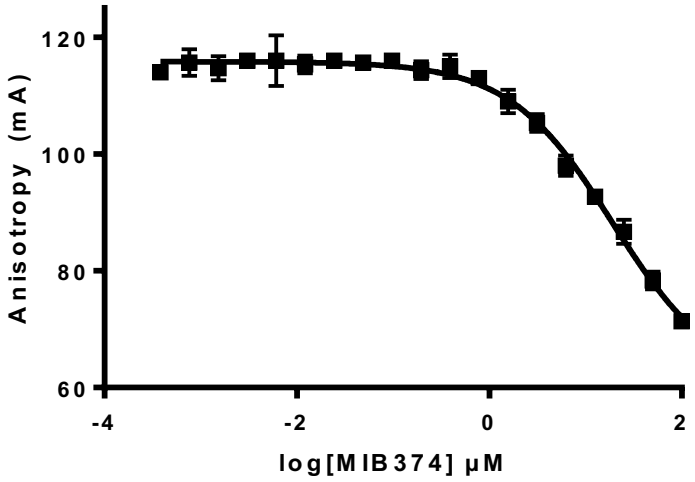

Figure 5.31 Competition of BI2536 with MIB 374 on Brd4 giving a constrained Ki of 5.90 µM.

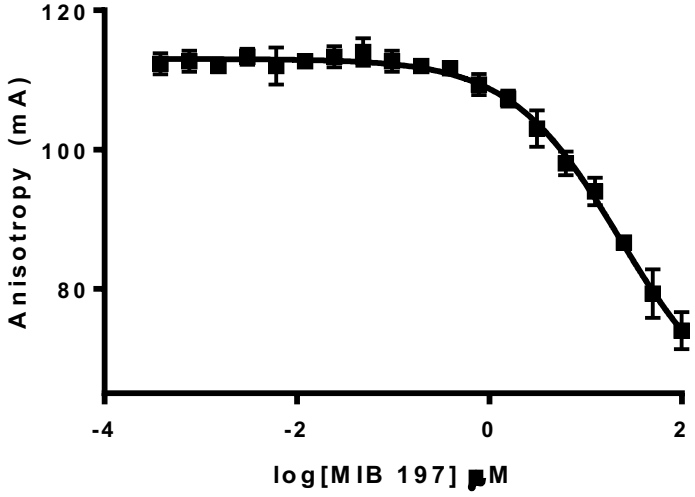

Figure 5.32 Competition of BI2536 with MIB 197 on Brd4 giving a constrained K_i of 1.52 µM at three different times. Longer equilibration times did not affect the K_i.

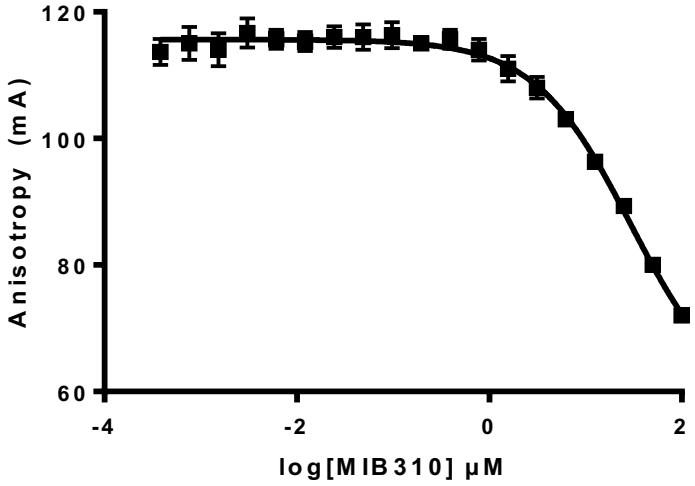

Figure 5.33 Competition of BI2536 with MIB 310 on Brd4 giving a constrained Ki of 5.10 µM**.**

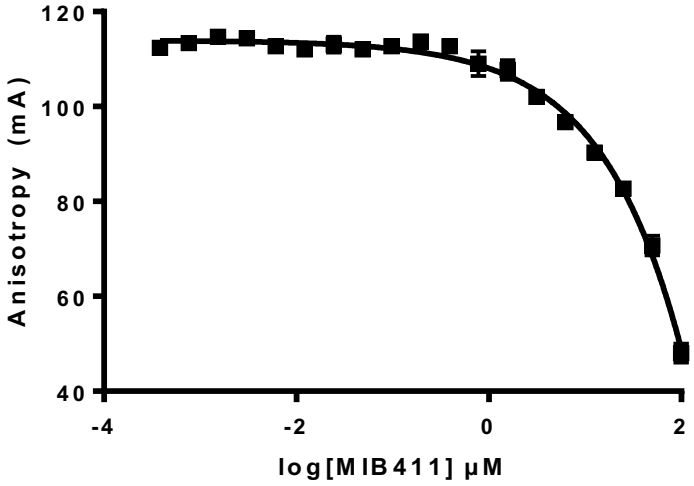

Figure 5.34 Competition of BI2536 with MIB 411 on Brd4 giving a constrained Ki of 4.72 µM.

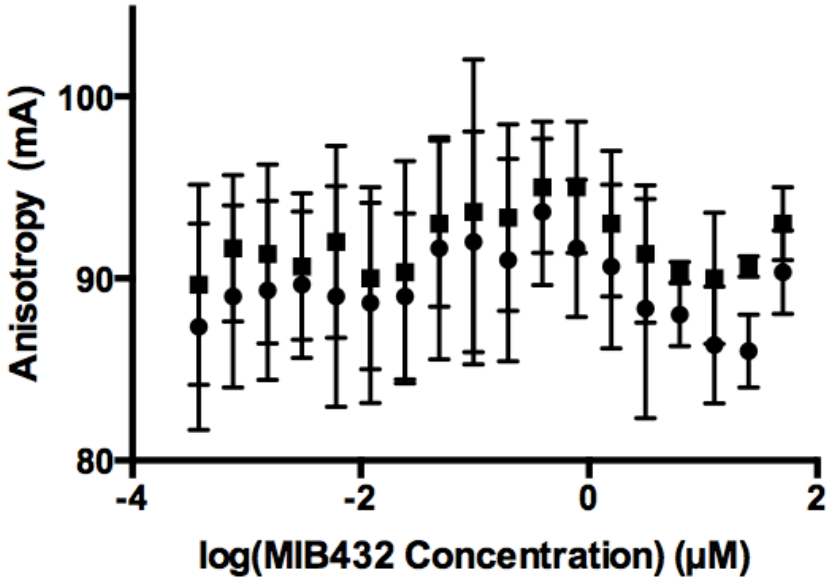

Figure 5.35 Competition of BI2536 with MIB 432 on Brd4. Aggregation led to an unclear competition curve.

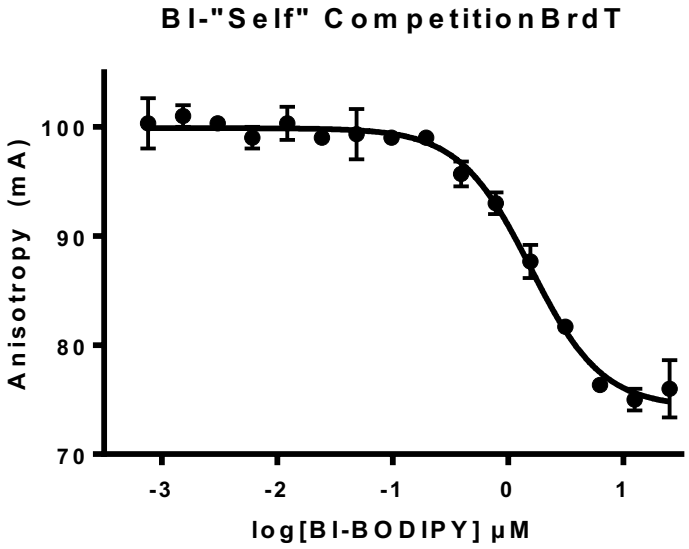

Figure 5.36 Self-competition of BI2536 with BI-BODIPY on BrdT.

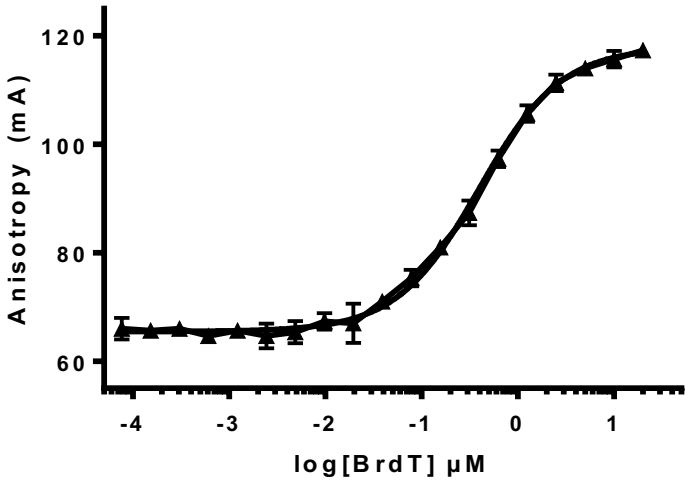

Figure 5.37 BI-BODIPY ligand FP binding assay with BrdT. A Kd of 380 nM was obtained for the previously identified high affinity ligand.

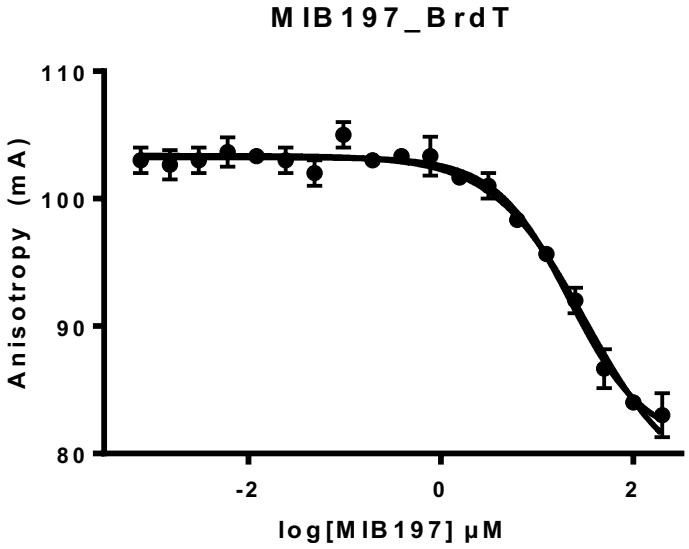

Figure 5.38 Competition of BI2536 with MIB 197 on BrdT.

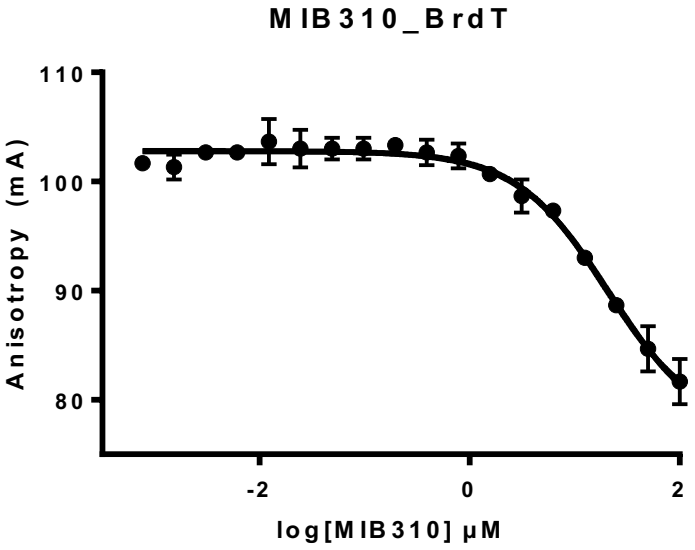

Figure 5.39 Competition of BI2536 with MIB 310 on BrdT.

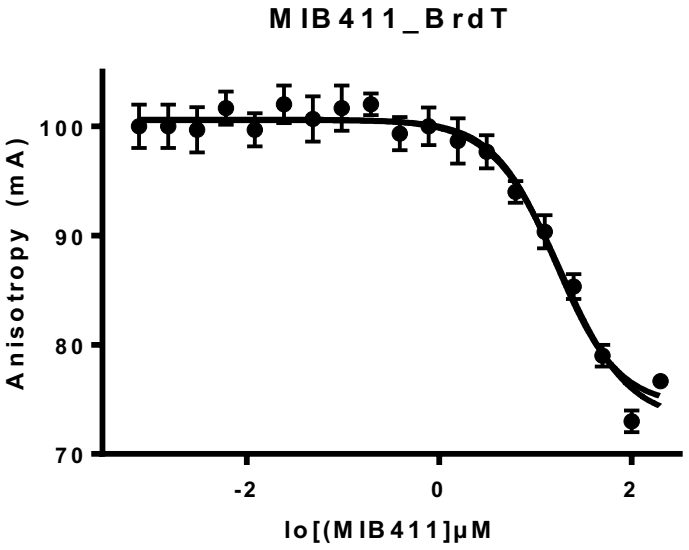

Figure 5.40 Competition of BI2536 with MIB 411 on BrdT.

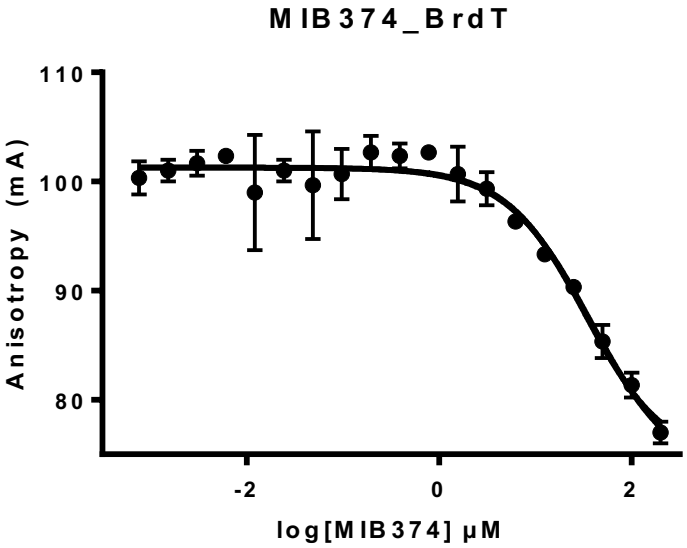

Figure 5.41 Competition of BI2536 with MIB 411 on Brd4.

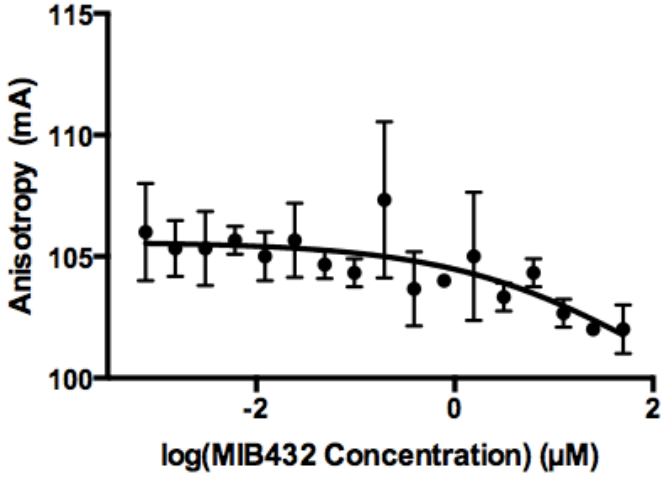

Figure 5.42 Competition of BI2536 with MIB 432 on Brd4. Aggregation led to poor

Chapter 6. References

(1) Stumpf, M. P. H.; Thorne, T.; Silva, E. De; Stewart, R.; An, H. J.; Lappe, M. Estimating the Size of the Human Interactome. *Proc. Natl. Acad. Sci. U. S. A.* **2008**, *105*, 6959–6964.

(2) Verdine, G. L.; Walensky, L. D. The Challenge of Drugging Undruggable Targets in Cancer: Lessons Learned from Targeting BCL-2 Family Members. *Clin. Cancer Res.* **2007**, *13*, 7264–7270.

(3) Jochim, A. L.; Arora, P. S. Assessment of Helical Interfaces in Protein-Protein Interactions. *Mol. Biosyst.* **2009**, *5*, 924–926.

(4) Smith, M. C.; Gestwicki, J. E. Features of Protein-Protein Interactions That Translate into Potent Inhibitors: Topology, Surface Area and Affinity. *Expert Rev. Mol. Med.* **2012**, *14*, e16.

(5) Clackson, T.; Wells, J. A. A Hot Spot of Binding Energy in a Hormone-Receptor Interface. *Science (80-.).* **1995**, *267*, 383–386.

(6) Babine, R. E.; Bender, S. L. Molecular Recognition of Protein−Ligand Complexes: Applications to Drug Design. *Chem. Rev.* **1997**, *97*, 1359–1472.

(7) Hopkins, A. L.; Groom, C. R. The Druggable Genome. *Nat. Rev. Drug Discov.* **2002**, *1*, 727–730.

(8) Russ, A. P.; Lampel, S. The Druggable Genome : An Update. *Drug Discov. Today* **2005**, *10*, 1607–1610.

(9) Bullock, B. N.; Jochim, A. L.; Arora, P. S. Assessing Helical Protein Interfaces for Inhibitor Design. *J. Am. Chem. Soc.* **2011**, *133*, 14220–14223.

(10) Kabsch, W.; Sander, C. Protein Secondary Structure: Pattern Recognition of Hydrogen-Bonded and Geometrical Features. *Biopolymers* **1983**, *22*, 2577–2637.

(11) Karle, I. L.; Flippen-Anderson, J. L.; Uma, K.; Balaram, P. Apolar Peptide Models for Conformational Heterogeneity, Hydration, and Packing of Polypeptide Helices: Crystal Structure of Hepta- and Octapeptides Containing α-Aminoisobutyric Acid. *Proteins Struct. Funct. Bioinforma.* **1990**, *7*, 62–73.

(12) Schafmeister, C. E.; Po, J.; Verdine, G. L. An All-Hydrocarbon Cross-Linking System for Enhancing the Helicity and Metabolic Stability of Peptides. *J. Am. Chem. Soc.* **2000**, *122*, 5891–5892.

(13) Miller, S. J.; Blackwell, H. E.; Grubbs, R. H. Application of Ring-Closing Metathesis to the Synthesis of Rigidified Amino Acids and Peptides. *J. Am. Chem. Soc.* **1996**, *118*, 9606–9614.

(14) Pace, C. N.; Scholtz, J. M. A Helix Propensity Scale Based on Experimental Studies of Peptides and Proteins. *Biophys. J.* **1998**, *75*, 422–427.

(15) Hilinski, G. J.; Kim, Y.-W.; Hong, J.; Kutchukian, P. S.; Crenshaw, C. M.; Berkovitch, S. S.; Chang, A.; Ham, S.; Verdine, G. L. Stitched α-Helical Peptides via Bis Ring-Closing Metathesis. *J. Am. Chem. Soc.* **2014**, *136*, 12314–12322.

(16) Kim, Y.-W.; Verdine, G. L. Stereochemical Effects of All-Hydrocarbon Tethers in i,i+4 Stapled Peptides. *Bioorganic Med. Chem. Lett.* **2009**, *19*, 2533–2536.

(17) Bernal, F.; Tyler, A. F.; Korsmeyer, S. J.; Walensky, L. D.; Verdine, G. L. Reactivation of the p53 Tumor Suppressor Pathway by a Stapled p53 Peptide. *J. Am. Chem. Soc.* **2007**, *129*, 2456–2457.

(18) Bird, G. H.; Bernal, F.; Pitter, K.; Walensky, L. D. Chapter 22 Synthesis and Biophysical Characterization of Stabilized α-Helices of BCL-2 Domains. In *Programmed Cell Death, The Biology and Therapeutic Implications of Cell Death, Part B*; Enzymology, B. T.-M. in, Ed.; Academic Press, 2008; Vol. Volume 446, pp. 369–386.
(19) Walensky, L. D.; Bird, G. H. Hydrocarbon-Stapled Peptides: Principles, Practice, and Progress. *J. Med. Chem.* **2014**, *57*, 6275–6288.
(20) Cromm, P. M.; Spiegel, J.; Grossmann, T. N. Hydrocarbon Stapled Peptides as Modulators of Biological Function. *ACS Chem. Biol.* **2015**, *10*, 1362–1375.
(21) Li, Y.-C.; Rodewald, L. W.; Hoppmann, C.; Wong, E. T.; Lebreton, S.; Safar, P.; Patek, M.; Wang, L.; Wertman, K. F.; Wahl, G. M. A Versatile Platform to Analyze Low-Affinity and Transient Protein-Protein Interactions in Living Cells in Real Time. *Cell Rep.* **2014**, *9*, 1946–1958.
(22) Walensky, L. D.; Kung, A. L.; Escher, I.; Malia, T. J.; Barbuto, S.; Wright, R. D.; Wagner, G.; Verdine, G. L.; Korsmeyer, S. J. Activation of Apoptosis in Vivo by a Hydrocarbon-Stapled BH3 Helix. *Science (80-.).* **2004**, *305*, 1466–1470.
(23) Chu, Q.; Moellering, R. E.; Hilinski, G. J.; Kim, Y.-W.; Grossmann, T. N.; Yeh, J. T.-H.; Verdine, G. L. Towards Understanding Cell Penetration by Stapled Peptides. *Med. Chem. Commun.* **2015**, *6*, 111–119.
(24) Labelle, J. L.; Katz, S. G.; Bird, G. H.; Walensky, L. D. A Stapled BIM Peptide Overcomes Apoptotic Resistance in Hematologic Cancers. *J. Clin. Invest.* **2012**, *122*.
(25) Okamoto, T.; Zobel, K.; Fedorova, A.; Quan, C.; Yang, H.; Fairbrother, W. J.; Huang, D. C. S.; Smith, B. J.; Deshayes, K.; Czabotar, P. E. Stabilizing the pro-Apoptotic BimBH3 Helix (BimSAHB) Does Not Necessarily Enhance Affinity or Biological Activity. *ACS Chem. Biol.* **2013**, *8*, 297–302.
(26) Bird, G. H.; Gavathiotis, E.; LaBelle, J. L.; Katz, S. G.; Walensky, L. D. Distinct BimBH3 (BimSAHB) Stapled Peptides for Structural and Cellular Studies. *ACS Chem. Biol.* **2014**, *9*, 831–837.
(27) van den Berg, A.; Dowdy, S. F. Protein Transduction Domain Delivery of Therapeutic Macromolecules. *Curr. Opin. Biotechnol.* **2011**, *22*, 888–893.
(28) Cantel, S.; Isaad, A. L. C.; Scrima, M.; Levy, J. J.; DiMarchi, R. D.; Rovero, P.; Halperin, J. a; D'Ursi, A. M.; Papini, A. M.; Chorev, M. Synthesis and Conformational Analysis of a Cyclic Peptide Obtained via I to i+4 Intramolecular Side-Chain to Side-Chain Azide-Alkyne 1,3-Dipolar Cycloaddition. *J. Org. Chem.* **2008**, *73*, 5663–5674.
(29) Bird, G. H.; Christian Crannell, W.; Walensky, L. D. Chemical Synthesis of Hydrocarbon-Stapled Peptides for Protein Interaction Research and Therapeutic Targeting. In *Current Protocols in Chemical Biology*; John Wiley & Sons, Inc., 2009.
(30) Azzarito, V.; Long, K.; Murphy, N. S.; Wilson, A. J. Inhibition of α-Helix-Mediated Protein–protein Interactions Using Designed Molecules. *Nat. Chem.* **2013**, *5*, 161–173.
(31) Galande, A. K.; Bramlett, K. S.; Burris, T. P.; Wittliff, J. L.; Spatola, A. F. Thioether Side Chain Cyclization for Helical Peptide Formation: Inhibitors of Estrogen

Receptor-Coactivator Interactions. *J. Pept. Res.* **2004**, *63*, 297–302.
(32) Jackson, D. Y.; King, D. S.; Chmielewski, J.; Singh, S.; Schultz, P. G. General Approach to the Synthesis of Short Alpha-Helical Peptides. *J. Am. Chem. Soc.* **1991**, *113*, 9391–9392.
(33) Dekan, Z.; Vetter, I.; Daly, N. L.; Craik, D. J.; Lewis, R. J.; Alewood, P. F. α-Conotoxin ImI Incorporating Stable Cystathionine Bridges Maintains Full Potency and Identical Three-Dimensional Structure. *J. Am. Chem. Soc.* **2011**, *133*, 15866–15869.
(34) Knerr, P. J.; Tzekou, A.; Ricklin, D.; Qu, H.; Chen, H.; van der Donk, W. A.; Lambris, J. D. Synthesis and Activity of Thioether-Containing Analogues of the Complement Inhibitor Compstatin. *ACS Chem. Biol.* **2011**, *6*, 753–760.
(35) Harrison, R. S.; Shepherd, N. E.; Hoang, H. N.; Ruiz-gómez, G.; Hill, T. A.; Driver, R. W.; Desai, V. S.; Young, P. R.; Abbenante, G.; Fairlie, D. P. Downsizing Human, Bacterial, and Viral Proteins to Short Water-Stable Alpha Helices That Maintain Biological Potency. *Proc. Natl. Acad. Sci. U. S. A.* **2010**, *107*, 11686–11691.
(36) Osapay, G.; Taylor, J. W. Multicyclic Polypeptide Model Compounds. 2. Synthesis and Conformational Properties of a Highly .alpha.-Helical Uncosapeptide Constrained by Three Side-Chain to Side-Chain Lactam Bridges. *J. Am. Chem. Soc.* **1992**, *114*, 6966–6973.
(37) Osapay, G.; Taylor, J. W. Multicyclic Polypeptide Model Compounds. 1. Synthesis of a Tricyclic Amphiphilic .alpha.-Helical Peptide Using an Oxime Resin, Segment-Condensation Approach. *J. Am. Chem. Soc.* **1990**, *112*, 6046–6051.
(38) Taylor, J. W. The Synthesis and Study of Side-Chain Lactam-Bridged Peptides. *Biopolymers* **2002**, *66*, 49–75.
(39) Chang, Y. S.; Graves, B.; Guerlavais, V.; Tovar, C.; Packman, K.; To, K.-H.; Olson, K. A.; Kesavan, K.; Gangurde, P.; Mukherjee, A.; et al. Stapled A−helical Peptide Drug Development: A Potent Dual Inhibitor of MDM2 and MDMX for p53-Dependent Cancer Therapy. *Proc. Natl. Acad. Sci.* **2013**, *110*, E3445–E3454.
(40) Moldoveanu, T.; Grace, C. R.; Llambi, F.; Nourse, A.; Fitzgerald, P.; Gehring, K.; Kriwacki, R. W.; Green, D. R. BID-Induced Structural Changes in BAK Promote Apoptosis. *Nat. Struct. Biol.* **2013**, *20*, 589–597.
(41) Leshchiner, E. S.; Braun, C. R.; Bird, G. H.; Walensky, L. D. Direct Activation of Full-Length Proapoptotic BAK. *Proc. Natl. Acad. Sci. U. S. A.* **2013**, *110*.
(42) Walensky, L. D. Direct BAKtivation. *Nat. Struct. Mol. Biol.* **2013**, *20*, 536–538.
(43) Cohen, N. a; Stewart, M. L.; Gavathiotis, E.; Tepper, J. L.; Bruekner, S. R.; Walensky, L. D. A Competitive Stapled Peptide Screen Identifies a Selective Small Molecule That Overcomes MCL-1-Dependent Leukemia Cell Survival. *Chem. Biol.* **2012**, *19*, 1175–1186.
(44) Stewart, M. L.; Fire, E.; Keating, A. E.; Walensky, L. D. The MCL-1 BH3 Helix Is an Exclusive MCL-1 Inhibitor and Apoptosis Sensitizer. *Nat Chem Biol* **2010**, *6*, 595–601.
(45) Moellering, R. E.; Cornejo, M.; Davis, T. N.; Del Bianco, C.; Aster, J. C.; Blacklow, S. C.; Kung, A. L.; Gilliland, D. G.; Verdine, G. L.; Bradner, J. E. Direct Inhibition of the NOTCH Transcription Factor Complex. *Nature* **2009**, *462*, 182–188.
(46) Grossmann, T. N.; Yeh, J. T.-H.; Bowman, B. R.; Chu, Q.; Moellering, R. E.;

Verdine, G. L. Inhibition of Oncogenic Wnt Signaling through Direct Targeting of β-Catenin. *Proc. Natl. Acad. Sci. U. S. A.* **2012**, *109*, 17942–17947.
(47) Kussie, P. H.; Gorina, S.; Marechal, V.; Elenbaas, B.; Moreau, J.; Levine, A. J.; Pavletich, N. P. Structure of the MDM2 Oncoprotein Bound to the p53 Tumor Suppressor Transactivation Domain. *Science (80-.).* **1996**, *274*, 948–953.
(48) Vassilev, L. T. In Vivo Activation of the p53 Pathway by Small-Molecule Antagonists of MDM2. *Science (80-.).* **2004**, *303*, 844–848.
(49) Chang, Y. S.; Graves, B.; Vassilev, L. T.; Sawyer, T. K.; Guerlavaisa, V.; Tovarb, C.; Packmanb, K.; Tob, K.-H.; Olsona, K. A.; Kesavana, K.; et al. Stapled α-Helical Peptide Drug Development: A Potent Dual Inhibitor of MDM2 and MDMX for p53-Dependent Cancer Therapy. *Proc. Natl. Acad. Sci. U. S. A.* **2013**, *110*, E3445-54.
(50) Baek, S.; Kutchukian, P. S.; Verdine, G. L.; Huber, R.; Holak, T. A.; Lee, K. W.; Popowicz, G. M. Structure of the Stapled p53 Peptide Bound to Mdm2. *J. Am. Chem. Soc.* **2012**, *134*, 103–106.
(51) Kim, W.; Bird, G. H.; Neff, T.; Guo, G.; Kerenyi, M. a; Walensky, L. D.; Orkin, S. H. Targeted Disruption of the EZH2-EED Complex Inhibits EZH2-Dependent Cancer. *Nat. Chem. Biol.* **2013**, 1–10.
(52) Long, Y.-Q.; Huang, S.-X.; Zawahir, Z.; Xu, Z.-L.; Li, H.; Sanchez, T. W.; Zhi, Y.; De Houwer, S.; Christ, F.; Debyser, Z.; et al. Design of Cell-Permeable Stapled Peptides as HIV-1 Integrase Inhibitors. *J. Med. Chem.* **2013**, *56*, 5601–5612.
(53) Chapuis, H.; Slaninová, J.; Bednárová, L.; Monincová, L.; Buděšínský, M.; Čeřovský, V. Effect of Hydrocarbon Stapling on the Properties of α-Helical Antimicrobial Peptides Isolated from the Venom of Hymenoptera. *Amino Acids* **2012**, *43*, 2047–2058.
(54) Phillips, C.; Roberts, L. R.; Schade, M.; Bazin, R.; Bent, A.; Davies, N. L.; Moore, R.; Pannifer, A. D.; Pickford, A. R.; Prior, S. H.; et al. Design and Structure of Stapled Peptides Binding to Estrogen Receptors. *J. Am. Chem. Soc.* **2011**, *133*, 9696–9699.
(55) Bhattacharya, S.; Zhang, H.; Debnath, A. K.; Cowburn, D. Solution Structure of a Hydrocarbon Stapled Peptide Inhibitor in Complex with Monomeric C-Terminal Domain of HIV-1 Capsid. *J. Biol. Chem.* **2008**, *283*, 16274–16278.
(56) Danial, N. N.; Walensky, L. D.; Zhang, C.-Y.; Choi, C. S.; Fisher, J. K.; Molina, A. J. A.; Datta, S. R.; Pitter, K. L.; Bird, G. H.; Wikstrom, J. D.; et al. Dual Role of Proapoptotic BAD in Insulin Secretion and Beta Cell Survival. *Nat Med* **2008**, *14*, 144–153.
(57) Green, B. R.; Klein, B. D.; Lee, H.-K.; Smith, M. D.; Steve White, H.; Bulaj, G. Cyclic Analogs of Galanin and Neuropeptide Y by Hydrocarbon Stapling. *Bioorg. Med. Chem.* **2013**, *21*, 303–310.
(58) Budwick, D. Aileron Therapeutics Successfully Completes First-Ever Stapled Peptide Clinical Trial http://www.aileronrx.com/pdf/Aileron-ALRN-5281Ph1PRFINAfor5713.pdf.
(59) Henchey, L. K.; Kushal, S.; Dubey, R.; Chapman, R. N.; Olenyuk, B. Z.; Arora, P. S. Inhibition of Hypoxia Inducible Factor 1-Transcription Coactivator Interaction by a Hydrogen Bond Surrogate Alpha-Helix. *J. Am. Chem. Soc.* **2010**, *132*, 941–943.

(60) Wang, D.; Liao, W.; Arora, P. S. Enhanced Metabolic Stability and Protein-Binding Properties of Artificial α Helices Derived from a Hydrogen-Bond Surrogate: Application to Bcl-xL. *Angew. Chemie Int. Ed.* **2005**, *44*, 6525–6529.
(61) Mahon, A. B.; Arora, P. S. Design, Synthesis and Protein-Targeting Properties of Thioether-Linked Hydrogen Bond Surrogate Helices. *Chem. Commun.* **2012**, *48*, 1416–1418.
(62) Boutureira, O.; Bernardes, G. J. L. Advances in Chemical Protein Modification. *Chem. Rev.* **2015**, *115*, 2174–2195.
(63) Fairlie, D. P.; Dantas de Araujo, A. Review Stapling Peptides Using Cysteine Crosslinking. *Biopolymers* **2016**, *106*, 843–852.
(64) Wang, Y.; Chou, D. H.-C. A Thiol-Ene Coupling Approach to Native Peptide Stapling and Macrocyclization. *Angew. Chem. Int. Ed. Engl.* **2015**, *54*, 10931–10934.
(65) Brunel, F. M.; Dawson, P. E. Synthesis of Constrained Helical Peptides by Thioether Ligation: Application to Analogs of gp41. *Chem. Commun.* **2005**, 2552–2554.
(66) Kumita, J. R.; Smart, O. S.; Woolley, G. A. Photo-Control of Helix Content in a Short Peptide. *Proc. Natl. Acad. Sci.* **2000**, *97*, 3803–3808.
(67) Nevola, L.; Martín-Quirós, A.; Eckelt, K.; Camarero, N.; Tosi, S.; Llobet, A.; Giralt, E.; Gorostiza, P. Light-Regulated Stapled Peptides to Inhibit Protein–Protein Interactions Involved in Clathrin-Mediated Endocytosis. *Angew. Chemie Int. Ed.* **2013**, *52*, 7704–7708.
(68) Micewicz, E. D.; Sharma, S.; Waring, A. J.; Luong, H. T.; McBride, W. H.; Ruchala, P. Bridged Analogues for p53-Dependent Cancer Therapy Obtained by S-Alkylation. *Int. J. Pept. Res. Ther.* **2016**, *22*, 67–81.
(69) Spokoyny, A. M.; Zou, Y.; Ling, J. J.; Yu, H.; Lin, Y.-S.; Pentelute, B. L. A Perfluoroaryl-Cysteine SNAr Chemistry Approach to Unprotected Peptide Stapling. *J. Am. Chem. Soc.* **2013**, *135*, 5946–5949.
(70) Brown, S. P.; Smith, A. B. Peptide/Protein Stapling and Unstapling: Introduction of S-Tetrazine, Photochemical Release, and Regeneration of the Peptide/Protein. *J. Am. Chem. Soc.* **2015**, *137*, 4034–4037.
(71) Goto, N. K.; Zor, T.; Martinez-Yamout, M.; Dyson, H. J.; Wright, P. E. Cooperativity in Transcription Factor Binding to the Coactivator CREB-Binding Protein (CBP). The Mixed Lineage Leukemia Protein (MLL) Activation Domain Binds to an Allosteric Site on the KIX Domain. *J. Biol. Chem.* **2002**, *277*, 43168–43174.
(72) Ansari, A. Z.; Reece, R. J.; Ptashne, M. A Transcriptional Activating Region with Two Contrasting Modes of Protein Interaction. *Proc. Natl. Acad. Sci. U. S. A.* **1998**, *95*, 13543–13548.
(73) Mapp, A.; Majmudar, C.; Wang, B.; Jenifer, L.; Håkansson, K. A High-Resolution Interaction Map of Three Transcriptional Activation Domains with a Key Coactivator from Photo-Cross-Linking and Multiplexed Mass Spectrometry. *Angew. Chem. Int. Ed. Engl.* **2009**, *48*, 7021–7024.
(74) Korkmaz, E. N.; Nussinov, R.; Haliloğlu, T. Conformational Control of the Binding of the Transactivation Domain of the MLL Protein and c-Myb to the KIX Domain of CREB. *PLoS Comput. Biol.* **2012**, *8*, e1002420.

(75) Ernst, P.; Jing, W.; Mary, H.; Richard H., G.; Stanley J., K. MLL and CREB Bind Cooperatively to the Nuclear Coactivator CREB-Binding Protein. *Mol. Cell. Biol.* **2001**, *21*, 2249–2258.
(76) Sakamoto, K. M.; Frank, D. a. CREB in the Pathophysiology of Cancer: Implications for Targeting Transcription Factors for Cancer Therapy. *Clin. Cancer Res.* **2009**, *15*, 2583–2587.
(77) Shankar, D. B.; Cheng, J. C.; Sakamoto, K. M. Role of Cyclic AMP Response Element Binding Protein in Human Leukemias. *Cancer* **2005**, *104*, 1819–1824.
(78) Giri, R.; Morrone, A.; Toto, A.; Brunori, M.; Gianni, S. Structure of the Transition State for the Binding of c-Myb and KIX Highlights an Unexpected Order for a Disordered System. *Proc. Natl. Acad. Sci. U. S. A.* **2013**, *110*, 14942–14947.
(79) Pagel, K.; Koksch, B. Following Polypeptide Folding and Assembly with Conformational Switches. *Curr. Opin. Chem. Biol.* **2008**, *12*, 730–739.
(80) Bock, J. E.; Gavenonis, J.; Kritzer, J. a. Getting in Shape: Controlling Peptide Bioactivity and Bioavailability Using Conformational Constraints. *ACS Chem. Biol.* **2013**, *8*, 488–499.
(81) Vakser, I. Protein-Protein Interfaces Are Special. *Structure* **2004**, *12*, 910–912.
(82) Radhakrishnan, I.; Pérez-Alvarado, G. C.; Parker, D.; Dyson, H. J.; Montminy, M. R.; Wright, P. E. Solution Structure of the KIX Domain of CBP Bound to the Transactivation Domain of CREB: A Model for Activator:coactivator Interactions. *Cell* **1997**, *91*, 741–752.
(83) Best, J. L.; Amezcua, C. a; Mayr, B.; Flechner, L.; Murawsky, C. M.; Emerson, B.; Zor, T.; Gardner, K. H.; Montminy, M. Identification of Small-Molecule Antagonists That Inhibit an Activator: Coactivator Interaction. *Proc. Natl. Acad. Sci. U. S. A.* **2004**, *101*, 17622–17627.
(84) Wagner, B. L. Stimulus-Specific Interaction between Activator-Coactivator Cognates Revealed with a Novel Complex-Specific Antiserum. *J. Biol. Chem.* **2000**, *275*, 8263–8266.
(85) Zor, T.; De Guzman, R. N.; Dyson, H. J.; Wright, P. E. Solution Structure of the KIX Domain of CBP Bound to the Transactivation Domain of c-Myb. *J. Mol. Biol.* **2004**, *337*, 521–534.
(86) Frangioni, J. V; LaRiccia, L. M.; Cantley, L. C.; Montminy, M. R. Minimal Activators That Bind to the KIX Domain of p300/CBP Identified by Phage Display Screening. *Nat. Biotechnol.* **2000**, *18*, 1080–1085.
(87) Brüschweiler, S.; Konrat, R.; Tollinger, M. Allosteric Communication in the KIX Domain Proceeds through Dynamic Re-Packing of the Hydrophobic Core. *ACS Chem. Biol.* **2013**.
(88) Shaywitz, A. J.; Greenberg, M. E. CREB: A Stimulus -Induced Transcription Factor Activated By A Diverse Array Of Extracellular Signals. *Annu. Rev. Biochem.* **1999**, 821–861.
(89) Hanahan, D.; Weinberg, R. A. Hallmarks of Cancer: The next Generation. *Cell* **2011**, *144*, 646–674.
(90) Cheng, J. C.; Kinjo, K.; Judelson, D. R.; Chang, J.; Wu, W. S.; Schmid, I.; Shankar, D. B.; Kasahara, N.; Stripecke, R.; Bhatia, R.; et al. CREB Is a Critical Regulator of Normal Hematopoiesis and Leukemogenesis. *Blood* **2008**, *111*, 1182–1192.

(91) Darnell, J. E. Transcription Factors as Targets for Cancer Therapy. *Nat. Rev. Cancer* **2002**, *2*, 740–749.
(92) Majmudar, C. Y.; Højfeldt, J. W.; Arevang, C. J.; Pomerantz, W. C.; Gagnon, J. K.; Schultz, P. J.; Cesa, L. C.; Doss, C. H.; Rowe, S. P.; Vásquez, V.; et al. Sekikaic Acid and Lobaric Acid Target a Dynamic Interface of the Coactivator CBP/p300. *Angew. Chemie Int. Ed.* **2012**, *51*, 11258–11262.
(93) Law, S. M.; Gagnon, J. K.; Mapp, A. K.; Brooks, C. L. Prepaying the Entropic Cost for Allosteric Regulation in KIX. *Proc. Natl. Acad. Sci.* **2014**, *111*, 12067–12072.
(94) Arai, M.; Dyson, H. J.; Wright, P. E. Leu628 of the KIX Domain of CBP Is a Key Residue for the Interaction with the MLL Transactivation Domain. *FEBS Lett.* **2010**, *584*, 4500–4504.
(95) De Guzman, R. N.; Goto, N. K.; Dyson, H. J.; Wright, P. E. Structural Basis for Cooperative Transcription Factor Binding to the CBP Coactivator. *J. Mol. Biol.* **2006**, *355*, 1005–1013.
(96) National Cancer Institute. SEER STAT Fact Sheets: Acute Myeloid Leukemia. http://seer.cancer.gov/statfacts/html/amyl.html.
(97) Howlader, N.; Noone, A.; Krapcho, M.; Neyman, N.; Aminou, R.; Waldron, W.; Altekruse, S.; Kosary, C.; Ruhl, J.; Tatalovich, Z.; et al. SEER Cancer Statistics Review 1975-2008 National Cancer Institute SEER Cancer Statistics Review 1975-2008 National Cancer Institute. *Cancer* **2011**, *2006*, 1992–2008.
(98) Explore Active Clinical Trials http://keynoteclinicaltrials.com/researchers (accessed Jun 4, 2017).
(99) Adult Acute Myeloid Leukemia Treatment https://www.cancer.gov/types/leukemia/patient/adult-aml-treatment-pdq#section/_73 (accessed Jun 4, 2017).
(100) Denis, C. M.; Chitayat, S.; Plevin, M. J.; Wang, F.; Thompson, P.; Liu, S.; Spencer, H. L.; Ikura, M.; LeBrun, D. P.; Smith, S. P. Structural Basis of CBP/p300 Recruitment in Leukemia Induction by E2A-PBX1. *Blood* **2012**, *120*, 3968–3977.
(101) Paulsen, C. E.; Carroll, K. S. Cysteine-Mediated Redox Signaling: Chemistry, Biology, and Tools for Discovery. *Chem. Rev.* **2013**, *113*, 4633–4679.
(102) Giles, N. M.; Watts, A. B.; Giles, G. I.; Fry, F. H.; Littlechild, J. A.; Jacob, C. Metal and Redox Modulation of Cysteine Protein Function. *Chem. Biol.* **2003**, *10*, 677–693.
(103) Moskovitz, J.; Bar-Noy, S.; Williams, W. M.; Requena, J.; Berlett, B. S.; Stadtman, E. R. Methionine Sulfoxide Reductase (MsrA) Is a Regulator of Antioxidant Defense and Lifespan in Mammals. *Proc. Natl. Acad. Sci.* **2001**, *98*, 12920–12925.
(104) Levine, R. L.; Berlett, B. S.; Moskovitz, J.; Mosoni, L.; Stadtman, E. R. Methionine Residues May Protect Proteins from Critical Oxidative Damage. *Mech. Ageing Dev.* **1999**.
(105) Reid, K. S. C.; Lindley, P. F.; Thornton, J. M. Sulphur-Aromatic Interactions in Proteins. *FEBS Lett.* **1985**.
(106) Tatko, C. D.; Waters, M. L. Investigation of the Nature of the Methionine-Pi Interaction in Beta-Hairpin Peptide Model Systems. *Protein Sci.* **2004**, *13*, 2515–2522.
(107) Viguera, A. R.; Serrano, L. Side-Chain Interactions between Sulfur-Containing

Amino Acids and Phenylalanine in ??-Helices. *Biochemistry* **1995**.
(108) Yamaotsu, N.; Moriguchi, I.; Hirono, S. Estimation of Stabilities of Staphylococcal Nuclease Mutants (Met32 → Ala and Met32 → Leu) Using Molecular Dynamics/free Energy Perturbation. *Biochim. Biophys. Acta - Protein Struct. Mol. Enzymol.* **1993**, *1203*, 243–250.
(109) Dougherty, D. A. The Cation-Pi Interaction. *Acc. Chem. Res.* **2013**.
(110) Kearney, P. C.; Mizoue, L. S.; Kumpf, R. A.; Forman, J. E.; McCurdy, A.; Dougherty, D. A. Molecular Recognition in Aqueous Media. New Binding Studies Provide Further Insights into the Cation-.pi. Interaction and Related Phenomena. *J. Am. Chem. Soc.* **1993**, *115*, 9907–9919.
(111) Salonen, L. M.; Ellermann, M.; Diederich, F. Aromatic Rings in Chemical and Biological Recognition: Energetics and Structures. *Angew. Chemie Int. Ed.* **2011**, *50*, 4808–4842.
(112) Tsuzuki, S. Interactions with Aromatic Rings BT - Intermolecular Forces and Clusters I. In; Wales, D. J., Ed.; Springer Berlin Heidelberg: Berlin, Heidelberg, 2005; pp. 149–193.
(113) Dougherty, D. A. Cation-Pi Interactions in Chemistry and Biology: A New View of Benzene, Phe, Tyr, and Trp. *Science (80-.).* **1996**.
(114) Tavares, X. D. S.; Blum, A. P.; Nakamura, D. T.; Puskar, N. L.; Shanata, J. A. P.; Lester, H. A.; Dougherty, D. A. Variations in Binding Among Several Agonists at Two Stoichiometries of the Neuronal, α4β2 Nicotinic Receptor. *J. Am. Chem. Soc.* **2012**, *134*, 11474–11480.
(115) Valley, C. C.; Cembran, A.; Perlmutter, J. D.; Lewis, A. K.; Labello, N. P.; Gao, J.; Sachs, J. N. The Methionine-Aromatic Motif Plays a Unique Role in Stabilizing Protein Structure. *J. Biol. Chem.* **2012**, *287*, 34979–34991.
(116) Zauhar, R. J.; Colbert, C. L.; Morgan, R. S.; Welsh, W. J. Evidence for a Strong Sulfur-Aromatic Interaction Derived from Crystallographic Data. *Biopolymers* **2000**.
(117) Pranata, J. Sulfur–Aromatic Interactions: A Computational Study of the Dimethyl Sulfide–Benzene Complex. *Bioorg. Chem.* **1997**.
(118) MORGAN, R. S.; McADON, J. M. PREDICTOR FOR SULFUR???AROMATIC INTERACTIONS IN GLOBULAR PROTEINS. *Int. J. Pept. Protein Res.* **1980**.
(119) Morgan, R. S.; Tatsch, C. E.; Gushard, R. H.; Mcadon, J. M.; Warme, P. K. CHAINS OF ALTERNATING SULFUR AND ?????BONDED ATOMS IN EIGHT SMALL PROTEINS. *Int. J. Pept. Protein Res.* **1978**.
(120) Viguera, A. R.; Serrano, L. Side-Chain Interactions between Sulfur-Containing Amino Acids and Phenyalanine in .alpha.-Helixes. *Biochemistry* **1995**, *34*, 8771–8779.
(121) Shechter, Y.; Burstein, Y.; Patchornik, A. Selective Oxidation of Methionine Residues in Proteins. *Biochemistry* **1975**.
(122) Hoshi, T.; Heinemann, S. Regulation of Cell Function by Methionine Oxidation and Reduction. *J Physiol* **2001**.
(123) Kim, G.; Weiss, S. J.; Levine, R. L. Methionine Oxidation and Reduction in Proteins. *Biochimica et Biophysica Acta - General Subjects*, 2014.
(124) Arakawa, T.; Kita, Y.; Timasheff, S. N. Protein Precipitation and Denaturation by

Dimethyl Sulfoxide. *Biophys. Chem.* **2007**.
(125) Scott, J.; Asami, M.; Tanaka, K. Novel Chromogenic, Guest-Sensitive Host Compounds. *New J. Chem.* **2002**.
(126) Rose, G. D.; Geselowitz, A. R.; Lesser, G. J.; Lee, R. H.; Zehfus, M. H. Hydrophobicity of Amino Acid Residues in Globular Proteins. *Science (80-.).* **1985**.
(127) Bogan, A. A.; Thorn, K. S. Anatomy of Hot Spots in Protein interfaces11Edited by J. Wells. *J. Mol. Biol.* **1998**, *280*, 1–9.
(128) Gottlieb, H. E.; Kotlyar, V.; Nudelman, A. NMR Chemical Shifts of Common Laboratory Solvents as Trace Impurities. *J. Org. Chem.* **1997**.
(129) Butterfield, S. M.; Patel, P. R.; Waters, M. L. Contribution of Aromatic Interactions to α-Helix Stability. *J. Am. Chem. Soc.* **2002**.
(130) Marqusee, S. Helix Stabilization by Glu-... Lys+ Salt Bridges in Short Peptides of de Novo Design. *Proc. Natl. Acad. Sci.* **1987**.
(131) Pearson, K. On Lines and Planes of Closest Fit to Systems of Points in Space. *London, Edinburgh, Dublin Philos. Mag. J. Sci.* **1901**.
(132) Yin, D.; Kuczera, K.; Squier, T. C. The Sensitivity of Carboxyl-Terminal Methionines in Calmodulin Isoforms to Oxidation by H2O2 Modulates the Ability to Activate the Plasma Membrane Ca-ATPase. *Chem. Res. Toxicol.* **2000**.
(133) Sacksteder, C. A.; Whittier, J. E.; Xiong, Y. J.; Li, J. H.; Galeva, N. A.; Jacoby, M. E.; Purvine, S. O.; Williams, T. D.; Rechsteiner, M. C.; Bigelow, D. J.; et al. Tertiary Structural Rearrangements upon Oxidation of methionine(145) in Calmodulin Promotes Targeted Proteasomal Degradation. *Biophys. J.* **2006**.
(134) Gao, J.; Yao, Y.; Squier, T. C. Oxidatively Modified Calmodulin Binds to the Plasma Membrane Ca-ATPase in a Nonproductive and Conformationally Disordered Complex. *Biophys. J.* **2001**.
(135) Gao, J.; Yin, D. H.; Yao, Y.; Sun, H.; Qin, Z.; Schoneich, C.; Williams, T. D.; Squier, T. C. Loss of Conformational Stability in Calmodulin upon Methionine Oxidation. *Biophys. J.* **1998**.
(136) Boschek, C. B.; Jones, T. E.; Smallwood, H. S.; Squier, T. C.; Bigelow, D. J. Loss of the Calmodulin-Dependent Inhibition of the RyR1 Calcium Release Channel upon Oxidation of Methionines in Calmodulin. *Biochemistry* **2008**.
(137) Bartlett, R. K.; Urbauer, R. J. B.; Anbanandam, A.; Smallwood, H. S.; Urbauer, J. L.; Squier, T. C. Oxidation of Met144 and Met145 in Calmodulin Blocks Calmodulin Dependent Activation of the Plasma Membrane Ca-ATPase. *Biochemistry* **2003**.
(138) Babu, Y. S.; Bugg, C. E.; Cook, W. J. Structure of Calmodulin Refined at 2.2 Å Resolution. *J. Mol. Biol.* **1988**.
(139) Kuboniwa, H.; Tjandra, N.; Grzesiek, S.; Ren, H.; Klee, C. B.; Bax, A. Solution Structure of Calcium-Free Calmodulin. *Nat. Struct. Biol.* **1995**.
(140) Mukherjea, P.; Maune, J. F.; Beckingham, K. Interlobe Communication in Multiple Calcium-Binding Site Mutants of Drosophila Calmodulin. *Protein Sci.* **1996**.
(141) Anbanandam, A.; Bieber Urbauer, R. J.; Bartlett, R. K.; Smallwood, H. S.; Squier, T. C.; Urbauer, J. L. Mediating Molecular Recognition by Methionine Oxidation: Conformational Switching by Oxidation of Methionine in the Carboxyl-Terminal Domain of Calmodulin. *Biochemistry* **2005**.

(142) Jeschke, G. DEER Distance Measurements on Proteins. *Annu. Rev. Phys. Chem.* **2012**.
(143) Ilardi, E. A.; Vitaku, E.; Njardarson, J. T. Data-Mining for Sulfur and Fluorine: An Evaluation of Pharmaceuticals To Reveal Opportunities for Drug Design and Discovery. *J. Med. Chem.* **2014**, *57*, 2832–2842.
(144) Vasquez, M.; Pincus, M. R.; Scheraga, H. A. Helix–coil Transition Theory Including Long-Range Electrostatic Interactions: Application to Globular Proteins. *Biopolymers* **1987**, *26*, 351–371.
(145) Greenfield, N. J. Using Circular Dichroism Collected as a Function of Temperature to Determine the Thermodynamics of Protein Unfolding and Binding Interactions. *Nat. Protoc.* **2007**.
(146) Fealey, M. E.; Gauer, J. W.; Kempka, S. C.; Miller, K.; Nayak, K.; Sutton, R. B.; Hinderliter, A. Negative Coupling as a Mechanism for Signal Propagation between C2 Domains of Synaptotagmin I. *PLoS One* **2012**.
(147) Horovitz, A. Double-Mutant Cycles: A Powerful Tool for Analyzing Protein Structure and Function. *Fold. Des.* **1996**.
(148) Horovitz, A.; Serrano, L.; Avron, B.; Bycroft, M.; Fersht, A. R. Strength and Co-Operativity of Contributions to Surface Salt Bridges to Protein Stability. *J. Mol. Biol.* **1990**.
(149) Serrano, L.; Bycroft, M.; Fersht, A. R. Aromatic-Aromatic Interactions and Protein Stability. Investigation by Double-Mutant Cycles. *J. Mol. Biol.* **1991**.
(150) Balog, E. M.; Lockamy, E. L.; Thomas, D. D.; Ferrington, D. A. Site-Specific Methionine Oxidation Initiates Calmodulin Degradation by the 20S Proteasome. *Biochemistry* **2009**.
(151) Klein, J. C.; Burr, A. R.; Svensson, B.; Kennedy, D. J.; Allingham, J.; Titus, M. a; Rayment, I.; Thomas, D. D. Actin-Binding Cleft Closure in Myosin II Probed by Site-Directed Spin Labeling and Pulsed EPR. *Proc. Natl. Acad. Sci. U. S. A.* **2008**.
(152) Etemadi, N.; Holien, J. K.; Chau, D.; Dewson, G.; Murphy, J. M.; Alexander, W. S.; Parker, M. W.; Silke, J.; Nachbur, U. Lymphotoxin α Induces Apoptosis, Necroptosis and Inflammatory Signals with the Same Potency as Tumour Necrosis Factor. In *FEBS Journal*; 2013.
(153) Frisch, M. J. et al. Gaussian 09, Revision D.01. *Gaussian 09, Revision D.01*, 2009.
(154) Boys, S.; Bernardi, F. The Calculation of Small Molecular Interactions by the Differences of Separate Total Energies. Some Procedures with Reduced Errors. *Mol. Phys.* **1970**.
(155) Zhao, Y.; Truhlar, D. G. A New Local Density Functional for Main-Group Thermochemistry, Transition Metal Bonding, Thermochemical Kinetics, and Noncovalent Interactions. *J. Chem. Phys.* **2006**.
(156) Reed, A. E.; Curtiss, L. a; Weinhold, F. Intermolecular Interactions from a Natural Bond Orbital, Donor-Acceptor Viewpoint. *Chem. Rev. (Washington, DC, United States)* **1988**.
(157) Mulliken, R. S. Electronic Population Analysis on LCAO–MO Molecular Wave Functions. I. *J. Chem. Phys.* **1955**.
(158) Cramer, C. J. *Essentials of Computational Chemistry Theories and Models*; 2004.
(159) Phillips, J. C.; Braun, R.; Wang, W.; Gumbart, J.; Tajkhorshid, E.; Villa, E.; Chipot,

C.; Skeel, R. D.; Kalé, L.; Schulten, K. Scalable Molecular Dynamics with NAMD. *Journal of Computational Chemistry*, 2005.
(160) Banner, D. W.; Darcy, A.; Janes, W.; Gentz, R.; Schoenfeld, H. J.; Broger, C.; Loetscher, H.; Lesslauer, W. Crystal Structure of the Soluble Human 55 Kd TNF Receptor- Human TNF-Beta Complex - Implications for TNF Receptor Activation. *Cell* **1993**.
(161) Jorgensen, W. L.; Chandrasekhar, J.; Madura, J. D.; Impey, R. W.; Klein, M. L. Comparison of Simple Potential Functions for Simulating Liquid Water. *J. Chem. Phys.* **1983**.
(162) MacKerell, A.; Bashford, D. All-Atom Empirical Potential for Molecular Modeling and Dynamics Studies of Proteins. *J. Phys. Chem. B* **1998**.
(163) MacKerell, A. D.; Feig, M.; Brooks, C. L. Improved Treatment of the Protein Backbone in Empirical Force Fields. *J. Am. Chem. Soc.* **2004**.
(164) Best, R. B.; Zhu, X.; Shim, J.; Lopes, P. E. M.; Mittal, J.; Feig, M.; MacKerell, A. D. Optimization of the Additive CHARMM All-Atom Protein Force Field Targeting Improved Sampling of the Backbone ??, ?? And Side-Chain ?? 1 and ?? 2 Dihedral Angles. *J. Chem. Theory Comput.* **2012**.
(165) Martyna, G. J.; Tobias, D. J.; Klein, M. L. Constant Pressure Molecular Dynamics Algorithms. *J. Chem. Phys.* **1994**.
(166) Jas, G. S.; Kuczera, K. Free-Energy Simulations of the Oxidation of C-Terminal Methionines in Calmodulin. *Proteins Struct. Funct. Genet.* **2002**.
(167) Darden, T.; Perera, L.; Li, L.; Lee, P. New Tricks for Modelers from the Crystallography Toolkit: The Particle Mesh Ewald Algorithm and Its Use in Nucleic Acid Simulations. *Structure* **1999**.
(168) Tuckerman, M.; Berne, G. J.; Martyna, B. J. Reversible Multiple Time Scale Molecular Dynamics. *J. Chem. Phys.* **1992**.
(169) Andersen, H. C. Rattle: A "velocity" version of the Shake Algorithm for Molecular Dynamics Calculations. *J. Comput. Phys.* **1983**.
(170) Lewis, A. K.; Dunleavy, K. M.; Senkow, T. L.; Her, C.; Horn, B. T.; Jersett, M. A.; Mahling, R.; McCarthy, M. R.; Perell, G. T.; Valley, C. C.; et al. Oxidation Increases the Strength of the Methionine-Aromatic Interaction. *Nat Chem Biol* **2016**, *12*, 860–866.
(171) Fry, D. C.; Vassilev, L. T. Targeting Protein-Protein Interactions for Cancer Therapy. *J. Mol. Med.* **2005**, *83*, 955–963.
(172) Bird, G. H.; Madani, N.; Perry, A. F.; Princiotto, A. M.; Supko, J. G.; He, X.; Gavathiotis, E.; Sodroski, J. G.; Walensky, L. D. Hydrocarbon Double-Stapling Remedies the Proteolytic Instability of a Lengthy Peptide Therapeutic. *Proc. Natl. Acad. Sci. U. S. A.* **2010**, *107*, 14093–14098.
(173) Verdine, G. L.; Hilinski, G. J. *Stapled Peptides for Intracellular Drug Targets.*; 1st ed.; Elsevier Inc., 2012; Vol. 503.
(174) Henchey, L. K.; Jochim, A. L.; Arora, P. S. Contemporary Strategies for the Stabilization of Peptides in the Alpha-Helical Conformation. *Curr. Opin. Chem. Biol.* **2008**, *12*, 692–697.
(175) Kalhor-Monfared, S.; Jafari, M. R.; Patterson, J. T.; Kitov, P. I.; Dwyer, J. J.; Nuss, J. M.; Derda, R. Rapid Biocompatible Macrocyclization of Peptides with

Decafluoro-Diphenylsulfone. *Chem. Sci.* **2016**, *7*, 3785–3790.
(176) Jo, H.; Meinhardt, N.; Wu, Y.; Kulkarni, S.; Hu, X.; Low, K. E.; Davies, P. L.; DeGrado, W. F.; Greenbaum, D. C. Development of α-Helical Calpain Probes by Mimicking a Natural Protein–Protein Interaction. *J. Am. Chem. Soc.* **2012**, *134*, 17704–17713.
(177) Bird, G. H.; Mazzola, E.; Opoku-Nsiah, K.; Lammert, M. A.; Godes, M.; Neuberg, D. S.; Walensky, L. D. Biophysical Determinants for Cellular Uptake of Hydrocarbon-Stapled Peptide Helices. *Nat Chem Biol* **2016**, *12*, 845–852.
(178) Wang, J.; Iwasaki, H.; Krivtsov, A.; Febbo, P. G.; Thorner, A. R.; Ernst, P.; Anastasiadou, E.; Kutok, J. L.; Kogan, S. C.; Zinkel, S. S.; et al. Conditional MLL-CBP Targets GMP and Models Therapy-related Myeloproliferative Disease. *EMBO J.* **2005**, *24*, 368 LP-381.
(179) Palazzesi, F.; Barducci, A.; Tollinger, M.; Parrinello, M. The Allosteric Communication Pathways in KIX Domain of CBP. *Proc. Natl. Acad. Sci.* **2013**, *110*, 14237–14242.
(180) Holland, H. L.; Andreana, P. R.; Brown, F. M. Biocatalytic and Chemical Routes to All the Stereoisomers of Methionine and Ethionine Sulfoxides. *Tetrahedron: Asymmetry* **1999**, *10*, 2833–2843.
(181) Schenck, H. L.; Dado, G. P.; Gellman, S. H. Redox-Triggered Secondary Structure Changes in the Aggregated States of a Designed Methionine-Rich Peptide. *J. Am. Chem. Soc.* **1996**, *118*, 12487–12494.
(182) Marenich, A. V; Cramer, C. J.; Truhlar, D. G. Generalized Born Solvation Model SM12. *J. Chem. Theory Comput.* **2013**, *9*, 609–620.
(183) Gunzburg, M. J.; Kulkarni, K.; Watson, G. M.; Ambaye, N. D.; Del Borgo, M. P.; Brandt, R.; Pero, S. C.; Perlmutter, P.; Wilce, M. C. J.; Wilce, J. A. Unexpected Involvement of Staple Leads to Redesign of Selective Bicyclic Peptide Inhibitor of Grb7. *Sci. Rep.* **2016**, *6*, 27060.
(184) Phillips, C.; Roberts, L. R.; Schade, M.; Bazin, R.; Bent, A.; Davies, N. L.; Moore, R.; Pannifer, A. D.; Pickford, A. R.; Prior, S. H.; et al. Design and Structure of Stapled Peptides Binding. *J. Am. Chem. Soc.* **2011**, *133*, 9696–9699.
(185) Speltz, T. E.; Fanning, S. W.; Mayne, C. G.; Fowler, C.; Tajkhorshid, E.; Greene, G. L.; Moore, T. W. Stapled Peptides with γ-Methylated Hydrocarbon Chains for the Estrogen Receptor/Coactivator Interaction. *Angew. Chemie Int. Ed.* **2016**, *55*, 4252–4255.
(186) Ernst, P.; Wang, J.; Huang, M.; Goodman, R. H.; Korsmeyer, S. J. MLL and CREB Bind Cooperatively to the Nuclear Coactivator CREB-Binding Protein. *Mol. Cell. Biol.* **2001**, *21*, 2249–2258.
(187) Kim, Y.-W.; Kutchukian, P. S.; Verdine, G. L. Introduction of All-Hydrocarbon i,i+3 Staples into Alpha-Helices via Ring-Closing Olefin Metathesis. *Org. Lett.* **2010**, *12*, 3046–3049.
(188) Checco, J. W.; Lee, E. F.; Evangelista, M.; Sleebs, N. J.; Rogers, K.; Pettikiriarachchi, A.; Kershaw, N. J.; Eddinger, G. A.; Belair, D. G.; Wilson, J. L.; et al. A/β-Peptide Foldamers Targeting Intracellular Protein-Protein Interactions with Activity in Living Cells. *J. Am. Chem. Soc.* **2015**, *137*, 11365–11375.
(189) Zhang, Q.; Jiang, F.; Zhao, B.; Lin, H.; Tian, Y.; Xie, M.; Bai, G.; Gilbert, A. M.;

Goetz, G. H.; Liras, S.; et al. Chiral Sulfoxide-Induced Single Turn Peptide α-Helicity. *Sci. Rep.* **2016**, *6*, 38573.
(190) Gee, C. T.; Koleski, E. J.; Pomerantz, W. C. K. Fragment Screening and Druggability Assessment for the CBP/p300 KIX Domain through Protein-Observed 19F NMR Spectroscopy. *Angew. Chem. Int. Ed. Engl.* **2015**, *54*, 3735–3739.
(191) Pomerantz, W. C.; Wang, N.; Lipinski, A. K.; Wang, R.; Cierpicki, T.; Mapp, A. K. Profiling the Dynamic Interfaces of Fluorinated Transcription Complexes for Ligand Discovery and Characterization. *ACS Chem. Biol.* **2012**, *7*, 1345–1350.
(192) Gee, C. T.; Arntson, K. E.; Urick, A. K.; Mishra, N. K.; Hawk, L. M. L.; Wisniewski, A. J.; Pomerantz, W. C. K. Protein-Observed 19F-NMR for Fragment Screening, Affinity Quantification and Druggability Assessment. *Nat. Protoc.* **2016**, *11*, 1414–1427.
(193) Jo, H.; Meinhardt, N.; Wu, Y.; Kulkarni, S.; Hu, X.; Low, K. E.; Davies, P. L.; DeGrado, W. F.; Greenbaum, D. C. Development of α-Helical Calpain Probes by Mimicking a Natural Protein-Protein Interaction. *J. Am. Chem. Soc.* **2012**, *134*, 17704–17713.
(194) Mitchell, D. J.; Steinman, L.; Kim, D. T.; Fathman, C. G.; Rothbard, J. B. Polyarginine Enters Cells More Efficiently than Other Polycationic Homopolymers. *J. Pept. Res.* **2000**, *56*, 318–325.
(195) Bertucci, C.; Domenici, E. Reversible and Covalent Binding of Drugs to Human Serum Albumin: Methodological Approaches and Physiological Relevance. *Curr Med Chem* **2002**.
(196) Basken, N. E.; Mathias, C. J.; Green, M. A. Elucidation of the Human Serum Albumin (HSA) Binding Site for the Cu-PTSM and Cu-ATSM Radiopharmaceuticals. *J. Pharm. Sci.* **2009**, *98*, 2170–2179.
(197) SUDLOW, G.; BIRKETT, D. J.; WADE, D. N. The Characterization of Two Specific Drug Binding Sites on Human Serum Albumin. *Mol. Pharmacol.* **1975**, *11*, 824 LP-832.
(198) Mishra, N. K.; Urick, A. K.; Ember, S. W. J.; Schönbrunn, E.; Pomerantz, W. C. Fluorinated Aromatic Amino Acids Are Sensitive 19F NMR Probes for Bromodomain-Ligand Interactions. *ACS Chem. Biol.* **2014**, *9*, 2755–2760.
(199) Richards, K. L.; Rowe, M. L.; Hudson, P. B.; Williamson, R. A.; Howard, M. J. Combined Ligand-Observe 19F and Protein-Observe 15N,1H-HSQC NMR Suggests Phenylalanine as the Key Δ-Somatostatin Residue Recognized by Human Protein Disulfide Isomerase. *Sci. Rep.* **2016**.
(200) Naik, P. N.; Chimatadar, S. A.; Nandibewoor, S. T. Interaction between a Potent Corticosteroid Drug – Dexamethasone with Bovine Serum Albumin and Human Serum Albumin: A Fluorescence Quenching and Fourier Transformation Infrared Spectroscopy Study. *J. Photochem. Photobiol. B Biol.* **2010**, *100*, 147–159.
(201) Ghuman, J.; Zunszain, P. A.; Petitpas, I.; Bhattacharya, A. A.; Otagiri, M.; Curry, S. Structural Basis of the Drug-Binding Specificity of Human Serum Albumin. *J. Mol. Biol.* **2005**, *353*, 38–52.
(202) Shao, Y.; Gan, Z.; Epifanovsky, E.; Gilbert, A. T. B.; Wormit, M.; Kussmann, J.; Lange, A. W.; Behn, A.; Deng, J.; Feng, X.; et al. Advances in Molecular Quantum Chemistry Contained in the Q-Chem 4 Program Package. *Mol. Phys.* **2015**, *113*,

184–215.
(203) Devlin, F. J.; Finley, J. W.; Stephens, P. J.; Frisch, M. J. Ab Initio Calculation of Vibrational Absorption and Circular Dichroism Spectra Using Density Functional Force Fields: A Comparison of Local, Nonlocal, and Hybrid Density Functionals. *J. Phys. Chem.* **1995**, *99*, 16883–16902.
(204) Becke, A. D. Density-Functional Exchange-Energy Approximation with Correct Asymptotic Behavior. *Phys. Rev. A* **1988**, *38*, 3098–3100.
(205) Lee, C.; Yang, W.; Parr, R. G. Development of the Colle-Salvetti Correlation-Energy Formula into a Functional of the Electron Density. *Phys. Rev. B* **1988**, *37*, 785–789.
(206) Becke, A. D. Density-functional Thermochemistry. III. The Role of Exact Exchange. *J. Chem. Phys.* **1993**, *98*, 5648–5652.
(207) Marenich, A. V; Jerome, S. V; Cramer, C. J.; Truhlar, D. G. Charge Model 5: An Extension of Hirshfeld Population Analysis for the Accurate Description of Molecular Interactions in Gaseous and Condensed Phases. *J. Chem. Theory Comput.* **2012**, *8*, 527–541.
(208) Holland, H. L.; Andreana, P. R.; Brown, F. M. Biocatalytic and Chemical Routes to All the Stereoisomers of Methionine and Ethionine Sulfoxides. *Tetrahedron: Asymmetry* **1999**, *10*, 2833–2843.
(209) Muchmore, D. C.; McIntosh, L. P.; Russell, C. B.; Anderson, D. E.; Dahlquist, F. W. Expression and Nitrogen-15 Labeling of Proteins for Proton and Nitrogen-15 Nuclear Magnetic Resonance. In; 1989; pp. 44–73.
(210) Pace, C. N.; Vajdos, F.; Fee, L.; Grimsley, G.; Gray, T. How to Measure and Predict the Molar Absorption Coefficient of a Protein. *Protein Sci.* **1995**, *4*, 2411–2423.
(211) Hu, K.; Sun, C.; Yang, D.; Wu, Y.; Shi, C.; Chen, L.; Liao, T.; Guo, J.; Liu, Y.; Li, Z. A Precisely Positioned Chiral Center in an I, I + 7 Tether Modulates the Helicity of the Backbone Peptide. *Chem. Commun.* **2017**, *53*, 6728–6731.
(212) Aimetti, A.; Shoemaker, R. K.; Lin, C.-C.; Anseth, K. S. On-Resin Peptide Macrocyclization Using Thiol-Ene Click Chemistry. *Chem. Commun.* **2010**, *46*, 4061–4063.
(213) Piccirillo, G.; Pepe, A.; Bedini, E.; Bochicchio, B. Photoinduced Thiol-Ene Chemistry Applied to the Synthesis of Self-Assembling Elastin-Inspired Glycopeptides. *Chem. – A Eur. J.* **2017**, *23*, 2648–2659.
(214) Kramer, J. R.; Deming, T. J. Glycopolypeptides with a Redox-Triggered Helix-to-Coil Transition. *J. Am. Chem. Soc.* **2012**, *134*, 4112–4115.
(215) Campos, L. M.; Killops, K. L.; Sakai, R.; Paulusse, J. M. J.; Damiron, D.; Drockenmuller, E.; Messmore, B. W.; Hawker, C. J. Development of Thermal and Photochemical Strategies for Thiol−Ene Click Polymer Functionalization. *Macromolecules* **2008**, *41*, 7063–7070.
(216) Chen, B.; Skoumbourdis, A. P.; Guo, P.; Bednarz, M. S.; Kocy, O. R.; Sundeen, J. E.; Vite, G. D.; Lett, A. T. A Facile Method for the Transformation of N-(Tert-Butoxycarbonyl) Alpha-Amino Acids to N-Unprotected Alpha-Amino Methyl Esters. *J. Org. Chem.* **1999**, 9294–9296.
(217) Salvatore, R. N.; Smith, R. a.; Nischwitz, A. K.; Gavin, T. A Mild and Highly Convenient Chemoselective Alkylation of Thiols Using Cs2CO3–TBAI.

Tetrahedron Lett. **2005**, *46*, 8931–8935.
(218) Cochrane, S. A.; Huang, Z.; Vederas, J. C. Investigation of the Ring-Closing Metathesis of Peptides in Water. *Org. Biomol. Chem.* **2013**, *11*, 630–639.
(219) Biron, E.; Kessler, H. Convenient Synthesis of N-Methylamino Acids Compatible with Fmoc Solid-Phase Peptide Synthesis. *J. Org. Chem.* **2005**, *70*, 5183–5189.
(220) Rogers, G. a; Shaltiel, N.; Boyer, P. D. Facile Alkylation of Methionine by Benzyl Bromide and Demonstration of Fumarase Inactivation Accompanied by Alkylation of a Methionine Residue. *J. Biol. Chem.* **1976**, *251*, 5711–5717.
(221) Kyte, J.; Degen, J.; Harkins, R. N. Purification of Peptides That Contain Methionine Residues. *Methods Enzymol.* **1983**, *91*, 367–377.
(222) Kornberg, R. D.; Thonmas, J. O. Chromatin Structure: Oligomers of the Histones. *Science (80-.).* **1974**, *184*, 865 LP-868.
(223) Sharma, S.; Kelly, T. K.; Jones, P. A. Epigenetics in Cancer. *Carcinogenesis* **2010**, *31*, 27–36.
(224) Kornberg, R. D.; Lorch, Y. Twenty-Five Years of the Nucleosome, Fundamental Particle of the Eukaryote Chromosome. *Cell* **1999**, *98*, 285–294.
(225) Martin, C.; Zhang, Y. The Diverse Functions of Histone Lysine Methylation. *Nat Rev Mol Cell Biol* **2005**, *6*, 838–849.
(226) Brown, Z. Z.; Müller, M. M.; Jain, S. U.; Allis, C. D.; Lewis, P. W.; Muir, T. W. Strategy for "Detoxification" of a Cancer-Derived Histone Mutant Based on Mapping Its Interaction with the Methyltransferase PRC2. *J. Am. Chem. Soc.* **2014**, *136*, 13498–13501.
(227) Prinjha, R. K.; Witherington, J.; Lee, K. Place Your BETs: The Therapeutic Potential of Bromodomains. *Trends Pharmacol. Sci.* **2017**, *33*, 146–153.
(228) Tamkun, J. W.; Deuring, R.; Scott, M. P.; Kissinger, M.; Pattatucci, A. M.; Kaufman, T. C.; Kennison, J. A. Brahma: A Regulator of Drosophila Homeotic Genes Structurally Related to the Yeast Transcriptional Activator SNF2 SWI2. *Cell* **1992**, *68*, 561–572.
(229) Ferri, E.; Petosa, C.; McKenna, C. E. Bromodomains: Structure, Function and Pharmacology of Inhibition. *Biochem. Pharmacol.* **2016**, *106*, 1–18.
(230) Sanchez, R.; Zhou, M.-M. The Role of Human Bromodomains in Chromatin Biology and Gene Transcription. *Curr. Opin. Drug Discov. Dev.* **2009**, *12*, 659–665.
(231) Filippakopoulos, P.; Qi, J.; Picaud, S.; Shen, Y.; Smith, W. B.; Fedorov, O.; Morse, E. M.; Keates, T.; Hickman, T. T.; Felletar, I.; et al. Selective Inhibition of BET Bromodomains. *Nature* **2010**, *468*, 1067–1073.
(232) Nicodeme, E.; Jeffrey, K. L.; Schaefer, U.; Beinke, S.; Dewell, S.; Chung, C.; Chandwani, R.; Marazzi, I.; Wilson, P.; Coste, H.; et al. Suppression of Inflammation by a Synthetic Histone Mimic. *Nature* **2010**, *468*, 1119–1123.
(233) Shi, J.; Vakoc, C. R. The Mechanisms behind the Therapeutic Activity of BET Bromodomain Inhibition. *Mol. Cell* **2014**, *54*, 728–736.
(234) Pan, L. N.; Lu, J.; Huang, B. HDAC Inhibitors: A Potential New Category of Anti-Tumor Agents. *Cell. Mol. Immunol.* **2007**, *4*, 337–343.
(235) Ruijter, A. J. M. de; Gennip, A. H. van; Caron, H. N.; Kemp, S.; Kuilenburg, A. B. P. van. Histone Deacetylases (HDACs): Characterization of the Classical HDAC Family. *Biochem. J.* **2003**, *370*, 737 LP-749.

(236) Grant, S.; Easley, C.; Kirkpatrick, P. Vorinostat. *Nat Rev Drug Discov* **2007**, *6*, 21–22.
(237) Talbert, P. B.; Henikoff, S. Histone Variants-Ancient Wrap Artists of the Epigenome. *Nat Rev Mol Cell Biol* **2010**, *11*.
(238) Iouzalen, N.; Moreau, J.; Méchali, M. H2A.ZI, a New Variant Histone Expressed during Xenopus Early Development Exhibits Several Distinct Features from the Core Histone H2A. *Nucleic Acids Res.* **1996**, *24*, 3947–3952.
(239) Zlatanova, J.; Thakar, A. H2A.Z: View from the Top. *Structure* **2008**, *16*.
(240) Obri, A.; Ouararhni, K.; Papin, C.; Diebold, M.-L.; Padmanabhan, K.; Marek, M.; Stoll, I.; Roy, L.; Reilly, P. T.; Mak, T. W.; et al. ANP32E Is a Histone Chaperone That Removes H2A.Z from Chromatin. *Nature* **2014**, *505*, 648–653.
(241) Mao, Z.; Pan, L.; Wang, W.; Sun, J.; Shan, S.; Dong, Q.; Liang, X.; Dai, L.; Ding, X.; Chen, S.; et al. Anp32e, a Higher Eukaryotic Histone Chaperone Directs Preferential Recognition for H2A.Z. *Cell Res* **2014**, *24*, 389–399.
(242) Petter, M.; Lee, C. C.; Byrne, T. J.; Boysen, K. E.; Volz, J.; Ralph, S. A.; Cowman, A. F.; Brown, G. V; Duffy, M. F. Expression of P. Falciparum Var Genes Involves Exchange of the Histone Variant H2A.Z at the Promoter. *PLOS Pathog.* **2011**, *7*, e1001292.
(243) Fan, Q.; An, L.; Cui, L. Plasmodium Falciparum Histone Acetyltransferase, a Yeast GCN5 Homologue Involved in Chromatin Remodeling. *Eukaryot. Cell* **2004**, *3*, 264–276.
(244) Srivastava, S.; Bhowmick, K.; Chatterjee, S.; Basha, J.; Kundu, T. K.; Dhar, S. K. Histone H3K9 Acetylation Level Modulates Gene Expression and May Affect Parasite Growth in Human Malaria Parasite Plasmodium Falciparum. *FEBS J.* **2014**, *281*, 5265–5278.
(245) Hardy, S.; Jacques, P. E.; Gevry, N.; Forest, A.; Fortin, M. E.; Laflamme, L.; Gaudreau, L.; Robert, F. The Euchromatic and Heterochromatic Landscapes Are Shaped by Antagonizing Effects of Transcription on H2A.Z Deposition. *PLoS Genet.* **2009**, *5*.
(246) Abbott, D. W.; Ivanova, V. S.; Wang, X.; Bonner, W. M.; Ausio, J. Characterization of the Stability and Folding of H2A.Z Chromatin Particles: Implications for Transcriptional Activation. *J Biol Chem* **2001**, *276*, 41945–41949.
(247) Santisteban, M. S.; Kalashnikova, T.; Smith, M. M. Histone H2A.Z Regulates Transcription and Is Partially Redundant with Nucleosome Remodeling Complexes. *Cell* **2000**, *103*, 411–422.
(248) Hu, G.; Cui, K.; Northrup, D.; Liu, C.; Wang, C.; Tang, Q.; Ge, K.; Levens, D.; Crane-Robinson, C.; Zhao, K. H2A.Z Facilitates Access of Active and Repressive Complexes to Chromatin in Embryonic Stem Cell Self-Renewal and Differentiation. *Cell Stem Cell* **2013**, *12*, 180–192.
(249) Subramanian, V.; Mazumder, A.; Surface, L. E.; Butty, V. L.; Fields, P. A.; Alwan, A.; Torrey, L.; Thai, K. K.; Levine, S. S.; Bathe, M.; et al. H2A.Z Acidic Patch Couples Chromatin Dynamics to Regulation of Gene Expression Programs during ESC Differentiation. *PLOS Genet.* **2013**, *9*, e1003725.
(250) Rudnizky, S.; Bavly, A.; Malik, O.; Pnueli, L.; Melamed, P.; Kaplan, A. H2A.Z Controls the Stability and Mobility of Nucleosomes to Regulate Expression of the

LH Genes. **2016**, *7*, 12958.
(251) Zhang, C.; Gao, S.; Molascon, A. J.; Liu, Y.; Andrews, P. C. Quantitative Proteomics Reveals Histone Modifications in Crosstalk with H3 Lysine 27 Methylation. *Mol. Cell. Proteomics* **2014**, *13*, 749–759.
(252) Barski, A.; Cuddapah, S.; Cui, K.; Roh, T. Y.; Schones, D. E.; Wang, Z.; Wei, G.; Chepelev, I.; Zhao, K. High-Resolution Profiling of Histone Methylations in the Human Genome. *Cell* **2007**, *129*, 823–837.
(253) Ku, M.; Jaffe, J. D.; Koche, R. P.; Rheinbay, E.; Endoh, M.; Koseki, H.; Carr, S. A.; Bernstein, B. E. H2A.Z Landscapes and Dual Modifications in Pluripotent and Multipotent Stem Cells Underlie Complex Genome Regulatory Functions. *Genome Biol.* **2012**, *13*, R85.
(254) Valdes-Mora, F.; Song, J. Z.; Statham, A. L.; Strbenac, D.; Robinson, M. D.; Nair, S. S.; Patterson, K. I.; Tremethick, D. J.; Stirzaker, C.; Clark, S. J. Acetylation of H2A.Z Is a Key Epigenetic Modification Associated with Gene Deregulation and Epigenetic Remodeling in Cancer. *Genome Res* **2012**, *22*, 307–321.
(255) Millar, C. B.; Xu, F.; Zhang, K.; Grunstein, M. Acetylation of H2AZ Lys 14 Is Associated with Genome-Wide Gene Activity in Yeast. *Genes Dev.* **2006**, *20*, 711–722.
(256) Vardabasso, C.; Gaspar-Maia, A.; Hasson, D.; Pünzeler, S.; Valle-Garcia, D.; Straub, T.; Keilhauer, E. C.; Strub, T.; Dong, J.; Panda, T.; et al. Histone Variant H2A.Z.2 Mediates Proliferation and Drug Sensitivity of Malignant Melanoma. *Mol. Cell* **2015**, *59*, 75–88.
(257) Vardabasso, C.; Gaspar-Maia, A.; Hasson, D.; Pünzeler, S.; Valle-Garcia, D.; Straub, T.; Keilhauer, E. C.; Strub, T.; Dong, J.; Panda, T.; et al. Histone Variant H2A.Z.2 Mediates Proliferation and Drug Sensitivity of Malignant Melanoma. *Mol. Cell* **2017**, *59*, 75–88.
(258) Yang, H. D.; Kim, P.-J.; Eun, J. W.; Shen, Q.; Kim, H. S.; Shin, W. C.; Ahn, Y. M.; Park, W. S.; Lee, J. Y.; Nam, S. W. Oncogenic Potential of Histone-Variant H2A.Z.1 and Its Regulatory Role in Cell Cycle and Epithelial-Mesenchymal Transition in Liver Cancer. *Oncotarget* **2016**, *7*, 11412–11423.
(259) Kobor, M. S.; Venkatasubrahmanyam, S.; Meneghini, M. D.; Gin, J. W.; Jennings, J. L.; Link, A. J.; Madhani, H. D.; Rine, J. A Protein Complex Containing the Conserved Swi2/Snf2-Related ATPase Swr1p Deposits Histone Variant H2A.Z into Euchromatin. *PLOS Biol.* **2004**, *2*, e131.
(260) Mizuguchi, G.; Shen, X.; Landry, J.; Wu, W.-H.; Sen, S.; Wu, C. ATP-Driven Exchange of Histone H2AZ Variant Catalyzed by SWR1 Chromatin Remodeling Complex. *Science (80-.).* **2004**, *303*, 343–348.
(261) Altaf, M.; Auger, A.; Monnet-Saksouk, J.; Brodeur, J.; Piquet, S.; Cramet, M.; Bouchard, N.; Lacoste, N.; Utley, R. T.; Gaudreau, L.; et al. NuA4-Dependent Acetylation of Nucleosomal Histones H4 and H2A Directly Stimulates Incorporation of H2A.Z by the SWR1 Complex. *J. Biol. Chem.* **2010**, *285*, 15966–15977.
(262) Raisner, R. M.; Hartley, P. D.; Meneghini, M. D.; Bao, M. Z.; Liu, C. L.; Schreiber, S. L.; Rando, O. J.; Madhani, H. D. Histone Variant H2A.Z Marks the 5` Ends of Both Active and Inactive Genes in Euchromatin. *Cell* **2005**, *123*, 233–248.

(263) Kusakabe, M.; Oku, H.; Matsuda, R.; Hori, T.; Muto, A.; Igarashi, K.; Fukagawa, T.; Harata, M. Genetic Complementation Analysis Showed Distinct Contributions of the N-Terminal Tail of H2A.Z to Epigenetic Regulations. *Genes to Cells* **2016**, *21*, 122–135.
(264) Landry, J. W.; Banerjee, S.; Taylor, B.; Aplan, P. D.; Singer, A.; Wu, C. Chromatin Remodeling Complex NURF Regulates Thymocyte Maturation. *Genes Dev.* **2011**, *25*, 275–286.
(265) Mayes, K.; Alkhatib, S. G.; Peterson, K.; Alhazmi, A.; Song, C.; Chan, V.; Blevins, T.; Roberts, M.; Dumur, C. I.; Wang, X.-Y.; et al. BPTF Depletion Enhances T-cell–Mediated Antitumor Immunity. *Cancer Res.* **2016**, *76*, 6183 LP-6192.
(266) Dai, M.; Lu, J.-J.; Guo, W.; Yu, W.; Wang, Q.; Tang, R.; Tang, Z.; Xiao, Y.; Li, Z.; Sun, W. BPTF Promotes Tumor Growth and Predicts Poor Prognosis in Lung Adenocarcinomas. *Oncotarget* **2015**, *6*, 33878–33892.
(267) Dar, A. A.; Nosrati, M.; Bezrookove, V.; de Semir, D.; Majid, S.; Thummala, S.; Sun, V.; Tong, S.; Leong, S. P. L.; Minor, D.; et al. The Role of BPTF in Melanoma Progression and in Response to BRAF-Targeted Therapy. *J. Natl. Cancer Inst.* **2015**, *107*, djv034-djv034.
(268) Chen, I.-Y.; Lypowy, J.; Pain, J.; Sayed, D.; Grinberg, S.; Alcendor, R. R.; Sadoshima, J.; Abdellatif, M. Histone H2A.z Is Essential for Cardiac Myocyte Hypertrophy but Opposed by Silent Information Regulator 2alpha. *J. Biol. Chem.* **2006**, *281*, 19369–19377.
(269) Richart, L.; Carrillo-de Santa Pau, E.; Río-Machín, A.; de Andrés, M. P.; Cigudosa, J. C.; Lobo, V. J. S.-A.; Real, F. X. BPTF Is Required for c-MYC Transcriptional Activity and in Vivo Tumorigenesis. *Nat. Commun.* **2016**, *7*, 10153.
(270) Richart, L.; Real, F. X.; Sanchez-Arevalo Lobo, V. J. C-MYC Partners with BPTF in Human Cancer. *Mol. Cell. Oncol.* **2016**, *3*, e1152346.
(271) Kim, K.; Punj, V.; Choi, J.; Heo, K.; Kim, J.-M.; Laird, P. W.; An, W. Gene Dysregulation by Histone Variant H2A.Z in Bladder Cancer. *Epigenetics Chromatin* **2013**, *6*, 34.
(272) Goldman, J. A.; Garlick, J. D.; Kingston, R. E. Chromatin Remodeling by Imitation Switch (ISWI) Class ATP-Dependent Remodelers Is Stimulated by Histone Variant H2A.Z. *J. Biol. Chem.* **2010**, *285*, 4645–4651.
(273) Filippakopoulos, P.; Picaud, S.; Mangos, M.; Keates, T.; Lambert, J.-P.; Barsyte-Lovejoy, D.; Felletar, I.; Volkmer, R.; Müller, S.; Pawson, T.; et al. Histone Recognition and Large-Scale Structural Analysis of the Human Bromodomain Family. *Cell* **2012**, *149*, 214–231.
(274) Ruthenburg, A. J.; Li, H.; Milne, T. A.; Dewell, S.; McGinty, R. K.; Yuen, M.; Ueberheide, B.; Dou, Y.; Muir, T. W.; Patel, D. J.; et al. Recognition of a Mononucleosomal Histone Modification Pattern by BPTF via Multivalent Interactions. *Cell* **2016**, *145*, 692–706.
(275) Arntson, K. E.; Pomerantz, W. C. K. Protein-Observed Fluorine NMR: A Bioorthogonal Approach for Small Molecule Discovery. *J. Med. Chem.* **2016**, *59*, 5158–5171.
(276) Norton, S. R.; Leung, W. E.; Chandrashekaran, R. I.; MacRaild, A. C. Applications of 19F-NMR in Fragment-Based Drug Discovery. *Molecules* **2016**, *21*, 860.

(277) Bruce, K.; Myers, F. A.; Mantouvalou, E.; Lefevre, P.; Greaves, I.; Bonifer, C.; Tremethick, D. J.; Thorne, A. W.; Crane-Robinson, C. The Replacement Histone H2A.Z in a Hyperacetylated Form Is a Feature of Active Genes in the Chicken. *Nucleic Acids Res* **2005**, *33*, 5633–5639.
(278) Urick, A. K.; Calle, L. P.; Espinosa, J. F.; Hu, H.; Pomerantz, W. C. K. Protein-Observed Fluorine NMR Is a Complementary Ligand Discovery Method to 1H CPMG Ligand-Observed NMR. *ACS Chem. Biol.* **2016**, *11*, 3154–3164.
(279) Sudhamalla, B.; Dey, D.; Breski, M.; Nguyen, T.; Islam, K. Site-Specific Azide-Acetyllysine Photochemistry on Epigenetic Readers for Interactome Profiling. *Chem. Sci.* **2017**, *8*, 4250–4256.
(280) Albert, I.; Mavrich, T. N.; Tomsho, L. P.; Qi, J.; Zanton, S. J.; Schuster, S. C.; Pugh, B. F. Translational and Rotational Settings of H2A.Z Nucleosomes across the Saccharomycescerevisiae Genome. *Nature* **2007**, *446*, 572–576.
(281) Babiarz, J. E.; Halley, J. E.; Rine, J. Telomeric Heterochromatin Boundaries Require NuA4-Dependent Acetylation of Histone Variant H2A.Z in Saccharomycescerevisiae. *Genes Dev.* **2006**, *20*, 700–710.
(282) Dryhurst, D.; Ishibashi, T.; Rose, K. L.; Eirín-López, J. M.; McDonald, D.; Silva-Moreno, B.; Veldhoen, N.; Helbing, C. C.; Hendzel, M. J.; Shabanowitz, J.; et al. Characterization of the Histone H2A.Z-1 and H2A.Z-2 Isoforms in Vertebrates. *BMC Biol.* **2009**, *7*, 86.
(283) Li, S.; Shogren-Knaak, M. A. The Gcn5 Bromodomain of the SAGA Complex Facilitates Cooperative and Cross-Tail Acetylation of Nucleosomes. *J. Biol. Chem.* **2009**, *284*, 9411–9417.
(284) Owen, D. J.; Ornaghi, P.; Yang, J.; Lowe, N.; Evans, P. R.; Ballario, P.; Neuhaus, D.; Filetici, P.; Travers, A. A. The Structural Basis for the Recognition of Acetylated Histone H4 by the Bromodomain of Histone Acetyltransferase Gcn5p. *EMBO J.* **2000**, *19*, 6141–6149.
(285) Hudson, B. P.; Martinez-Yamout, M. A.; Dyson, H. J.; Wright, P. E. Solution Structure and Acetyl-Lysine Binding Activity of the GCN5 bromodomain1 . *J. Mol. Biol.* **2000**, *304*, 355–370.
(286) Perell, G.; Staebell, R.; Hairani, M.; Cembran, A.; Pomerantz, W. C. K. Tuning Sulfur Oxidation States on Thioether-Bridged Peptide Macrocycles for Modulation of Protein Interactions. *ChemBioChem* **2017**, Accepted Author Manuscript.
(287) Crowley, P. B.; Kyne, C.; Monteith, W. B. Simple and Inexpensive Incorporation of 19F-Tryptophan for Protein NMR Spectroscopy. *Chem. Commun.* **2012**, *48*, 10681–10683.
(288) Philpott, M.; Yang, J.; Tumber, T.; Fedorov, O.; Uttarkar, S.; Filippakopoulos, P.; Picaud, S.; Keates, T.; Felletar, I.; Ciulli, A.; et al. Bromodomain-Peptide Displacement Assays for Interactome Mapping and Inhibitor Discovery. *Mol. Biosyst.* **2011**, *7*, 2899–2908.
(289) Coon, J. J.; Ueberheide, B.; Syka, J. E.; Dryhurst, D. D.; Ausio, J.; Shabanowitz, J.; Hunt, D. F. Protein Identification Using Sequential Ion/ion Reactions and Tandem Mass Spectrometry. *Proc Natl Acad Sci USA* **2005**, *102*.
(290) Ishibashi, T.; Dryhurst, D.; Rose, K. L.; Shabanowitz, J.; Hunt, D. F.; Ausio, J. Acetylation of Vertebrate H2A.Z and Its Effect on the Structure of the Nucleosome.

Biochemistry **2009**, *48*.
(291) Matsuda, R.; Hori, T.; Kitamura, H.; Takeuchi, K.; Fukagawa, T.; Harata, M. Identification and Characterization of the Two Isoforms of the Vertebrate H2A.Z Histone Variant. *Nucleic Acids Res.* **2010**, *38*, 4263–4273.
(292) Paz, J. C.; Park, S.; Phillips, N.; Matsumura, S.; Tsai, W.-W.; Kasper, L.; Brindle, P. K.; Zhang, G.; Zhou, M.-M.; Wright, P. E.; et al. Combinatorial Regulation of a Signal-Dependent Activator by Phosphorylation and Acetylation. *Proc. Natl. Acad. Sci.* **2014**, *111*, 17116–17121.
(293) Anand, P.; Brown, J. D.; Lin, C. Y.; Qi, J.; Zhang, R.; Artero, P. C.; Alaiti, M. A.; Bullard, J.; Alazem, K.; Margulies, K. B.; et al. BET Bromodomains Mediate Transcriptional Pause Release in Heart Failure. *Cell* **2013**, *154*, 569–582.
(294) Delmore, J. E.; Issa, G. C.; Lemieux, M. E.; Rahl, P. B.; Shi, J.; Jacobs, H. M.; Kastritis, E.; Gilpatrick, T.; Paranal, R. M.; Qi, J.; et al. BET Bromodomain Inhibition as a Therapeutic Strategy to Target c-Myc. *Cell* **2011**, *146*, 904–917.
(295) Hewings, D. S.; Rooney, T. P. C.; Jennings, L. E.; Hay, D. A.; Schofield, C. J.; Brennan, P. E.; Knapp, S.; Conway, S. J. Progress in the Development and Application of Small Molecule Inhibitors of Bromodomain–Acetyl-Lysine Interactions. *J. Med. Chem.* **2012**, *55*, 9393–9413.
(296) Gerona-navarro, G.; Mujtaba, S.; Frasca, A.; Patel, J.; Zeng, L.; Plotnikov, A. N.; Osman, R.; Zhou, M. Rational Design of Cyclic Peptide Modulators of the Transcriptional Coactivator CBP: A New Class of p53 Inhibitors. *J. Am. Chem. Soc.* **2011**, *133*, 2040–2043.
(297) Rooney, T. P. C.; Filippakopoulos, P.; Fedorov, O.; Picaud, S.; Cortopassi, W. A.; Hay, D. A.; Martin, S.; Tumber, A.; Rogers, C. M.; Philpott, M.; et al. A Series of Potent CREBBP Bromodomain Ligands Reveals an Induced-Fit Pocket Stabilized by a Cation–π Interaction. *Angew. Chemie Int. Ed.* **2014**, *53*, 6126–6130.
(298) Hay, D. A.; Fedorov, O.; Martin, S.; Singleton, D. C.; Tallant, C.; Wells, C.; Picaud, S.; Philpott, M.; Monteiro, O. P.; Rogers, C. M.; et al. Discovery and Optimization of Small-Molecule Ligands for the CBP/p300 Bromodomains. *J. Am. Chem. Soc.* **2014**, *136*, 9308–9319.
(299) Fong, C. Y.; Gilan, O.; Lam, E. Y. N.; Rubin, A. F.; Ftouni, S.; Tyler, D.; Stanley, K.; Sinha, D.; Yeh, P.; Morison, J.; et al. BET Inhibitor Resistance Emerges from Leukaemia Stem Cells. *Nature* **2015**, *525*, 538–542.
(300) Ayoub, A. M.; Hawk, L. M. L.; Herzig, R. J.; Jiang, J.; Wisniewski, A. J.; Gee, C. T.; Zhao, P.; Zhu, J.-Y.; Berndt, N.; Offei-Addo, N. K.; et al. BET Bromodomain Inhibitors with One-Step Synthesis Discovered from Virtual Screen. *J. Med. Chem.* **2017**.